SPECIFIC BIOMODELING AND ANALYSIS TECHNIQUES AT CELLULAR AND SYSTEMS LEVEL

A Dissertation presented to

The Faculty of the Graduate School

University of Missouri – Columbia

In Partial Fulfillment

of the Requirement for the Degree

Doctor of Philosophy

---

by

TAI SEUNG JANG

Dr. Satish S. Nair, Dissertation Supervisor

DECEMBER 2006

The undersigned, appointed by the Dean of the Graduate Faculty, have examined the dissertation entitled

SPECIFIC BIOMODELING AND ANALYSIS TECHNIQUES

AT CELLULAR AND SYSTEMS LEVEL

presented by Tai Seung Jang

a candidate for the degree of Doctor of Philosophy

and hereby certify that in their opinion it is worthy of acceptance.

_____

Dr. Satish S. Nair

_____

Dr. John B. Miles

_____

Dr. Roger Fales

_____

Dr. Jyotsna Nair

_____

Dr. Antonieta Lavin

ACKNOWLEDGEMENT

I would like to thank God first who gave me peace, joy, strength, and confidence throughout my life.

I'd like to thank my parents, Henry and Elisabeth Jang, my beautiful fiancé, Jung-sun, and my brother, Thomas for their unconditional support and love during my life.

I am especially grateful to Dr. Satish Nair for his encouragement and enthusiastic support, patience, and faith on me throughout the whole project and for his careful and critical supervision of this dissertation.

His wisdom, knowledge, kindness, and philosophy contributed greatly to my graduate program and my life.

I would like to extend my thanks to Dr. Antonieta Lavin of Medical University of South Carolina for her instructive cooperation and technical support in the electrophysiological aspects of computational neuroscience projects and Dr. Jyotsna Nair of Medical University of Missouri - Columbia for her close support in the clinical aspects of the brain disorder project.

I'd like to thank Dr. John Miles for his assistance in my research and for participating on my thesis advisory committee. I'd like to thank Dr. Fales for serving on my thesis advisory committee and his interest in my work.

I also would like to show my sincere appreciation to fellow Ph.D student members of our research group at the University of Missouri-Columbia for the wonderful team chemistry and for their multi-talents and interests in both research and extra scholarly activities. This partially includes Harvey Cline, John Gall, Anthony Iyoho, Guoshi Li, and Christie Pietarila.

SPECIFIC BIOMODELING AND ANALYSIS TECHNIQUES

AT CELLULAR AND SYSTEMS LEVEL

Tai Seung Jang

Dr. Satish S. Nair, Dissertation Supervisor

ABSTRACT

Computational models provide an effective avenue to test hypotheses regarding mechanisms that underlie the behavior of biological system, at all levels, including molecular, cellular, systems, and behavior levels, and to model emergent properties for such systems. Modeling approaches are developed for two different levels, cellular (Part I) and systems (Part II), and used to develop insights into system performance. The approaches are illustrated using two real-world example cases of systems that are nonlinear, large dimensional, and have significant parametric and unmodeled uncertainties.

PART I consists of three chapters focusing on computational neuroscience models at cellular level, each written in the form of a journal paper. Accurate modeling and analysis techniques are developed for the dynamics of single cell and networks of mammalian neurons for two different applications, and validated using experimental data. The mechanisms of action of a drug on prefrontal cortical cells are elucidated with two possible hypotheses, and a systematic methodology to study the excitability of cells under inhibitory post synaptic currents (IPSCs) is developed. For the second application, single cell models are developed for baroreceptor cells and it is shown to successfully model the conversion of an analog blood pressure signal to discrete firing patterns. Also, we investigate whether spike frequency adaptation is mediated by a pre- or post-synaptic

mechanism. Nucleus tractus solitarius (NTS) cells which receive the baroreceptor afferents are also modeled, and three specific network configurations of these are investigated as examples of the possible 'functional' circuitry that can implement the required 'signal transfer' from a pulse synchronous format (baroreceptors) at the input to one that lacks pulse-synchronocity in the network (NTS neurons), back to a pulse synchronous format at the output (NTS output neuron).

PART II focuses on mathematical models at the systems level. Specifically, thermal physiology models of the entire human body are developed using statistical and black box (artificial neural network, ANN) techniques.

MU 2-D Man is a human thermal model developed by our group at the University of Missouri (MU). The model has been developed for designing an automatic thermal comfort control strategy for NASA astronaut space suits and for the US Air Force warfighters in chemo-bio suits. It is a general purpose model and can be used to predict thermal responses of human beings under transient environmental conditions. The model has been enhanced using more accurate modeling of digits incorporating arterio-venous anastomoses (AVA) mechanisms that the fingers and toes use for better control of heat transfer. Also, a black box model has bee developed using ANN techniques to predict the thermal response of supine subjects to transient environmental conditions, using a US Army data set. A variation of this study was also published as a journal paper that is not included here.

TABLE OF CONTENTS

ACKNOWLEDGMENTS…… ii

ABSTRACT……. iii

LIST OF FIGURES…….. viii

LIST OF TABLES…… x

CHAPTER 1 INTRODUCTION AND OBJECTIVES…….. 1

1.1 Introduction and Objectives…… 1

1.2 Example Cases ……..…….……. 3

1.3 Objectives ……..…….…… 9

PART I **CELLULAR LEVEL MODELING**……...…… 15

CHAPTER 2 MODULATION OF PFC PYRAMIDAL CELL CEXCITABILITY BY CLONIDINE - A computational modeling study … 17

2.1 Abstract……. 17

2.2 Introduction ……..…… 19

2.3 Materials and methods…….. 20

2.5 Development of Computational Model..……..……. 22

2.7 Results …..……..……. 32

2.8 Discussion …..……...…… 39

2.9 References …..……...…… 41

2.8 Tables and Figures……..……...…… 44

CHAPTER 3 BAROREFLEX ARK: NUCLEUS TRACTUS SOLITARIUS 53

3.1 Abstract……. 53

3.2 Introduction ……..…… 53

3.3 Methods…….. 57

3.6 Results …..……..……. 61

3.7 Discussion …..……..…… 63

3.8 References …..……..…… 64

3.9 Tables and Figures……..……...…… 68

CHAPTER 4 COMPUTATIONAL MODEL OF THE BAROREFLEX ARK, NUCLEUS TRACTUS SOLITARIUS – NETWORK MODEL…….. 72

4.1 Abstract……. 72

4.2 Introduction ……..…… 72

4.3 Methods……..…….. 74

4.4 Results …..……..……. 78

4.6 References …..……..…… 79

4.7 Tables and Figures……..……..…… 82

PART II **SYSTEMS LEVEL MODELING** …… 89

CHAPTER 5 VARIATIONS IN THERMAL STRESS RESPONSE FOR SUPINE IN TRANSIENT ENVIRONMENTS …….. 91

5.1 Abstract…….…….. 91

5.2 Introduction …….. 91

5.3 Model Development……..……..…… 94

5.3.1 Modeling…… 95

5.3.2 Sensitivity Analysis……..… 96

5.4 Results and Discussion……..… 97

5.4.1 Observation From The Sensitivity Analysis…… 98

5.5 Conclusions…… 101

5.6 References…… 102

5.7 Tables…… 107

CHAPTER 6 HUMAN THERMAL MODEL WITH EXTREMITIES FOR ENVIRONMENTS…….…… 119

6.1 Introduction…… 119

6.2 Review of Human Thermal Models……

6.3 Proposed 2-D Model with Extremities…… 121

6.5 Results and Discussion…… 135

6.6 Conclusions…… 138

6.7 References…… 141

6.8 Figures…… 144

PART III **SUMMARY, CONTRIBUTIONS AND APPENDICES** …….
CHAPTER 7 CONCLUSIONS AND CONTRIBUTIONS……...… 147
7.1 Summary…….…… 147
7.2 Future Research……..…… 149
APPENDICES…… 151
1. Air Force Project Model – Users Manual…….. 152
2. SAE Journal Paper……... 167
3. Pediatric Study Journal Paper……. 183
4. Software Development …… 225
4.1 Genesis Programming for Cellular Modeling
4.1.1 ADHD Single Cell and Network Model
4.1.2 NTS Single Cell and Network Model
4.2 Artificial Neural Network Program for DOD Project
4.3 GUI for NASA Space Suit Project
4.4 Artificial Neural Network Program for Air Force Project
PUBLICATION…… 227
VITA…….…….. 229

LIST OF FIGURES

Figure		Page
1.1	Hippocampal pyramidal cell…….	3
1.2	A hyppocampal pyramidal cell and a simplified model ……...	5
1.3	A computational model of a Purkinje cell ……	5
1.4	Equivalent circuit for a compartmental model…….	6
1.5	Human Thermal Model in MALAB/SIMULINK software……..	8
2.1	Input resistance for PFC pyramidal cell ……	47
2.2	IPSC histograms and cumulative probability plots …….	47
2.3	IPSC for four different G peak conductances……	48
2.4	Direct modulation of IPSCs…….	49
2.5	Cumulative probability plots at different synaptic input rates ……..	50
2.6	Comparison of model predictions and experiments…….	51
3.1	Somatic action potential waveform from an A-Type nodose model……	67
3.2	1000 ms of model activity A-type ……	67
3.3	Somatic action potential waveform from a C-Type nodose model……...	69
3.4	1000 ms of model activity C-type ……	69
3.5	A type Nodose Neuron with different sensitivity responses……	70
3.6	C-type Nodose Neuron responses to a 5 Hz sinusoidal input …….	71
3.7	Current evoked responses from whole-cell patch clamped NTS cell …...	71

3.8	Current evoked responses from model NTS cell …….	71
4.1	Network of arterial baroreceptor circuitry in the NTS…….	82
4.2	Initial population model of architecture 1…….	83
4.3	Population model of architecture 2…….	86
4.4	Population model of architecture 3…….	88
5.1	Tskin data for members of Female Group 2……	116
5.2	Tcore data for members of Male Group 2……..	117
5.3	HR data for members of Male Group 2……..	118
6.1a	Cylindrical representation of the human form…….	144
6.1b	Concentric regions in each element……..	144
6.1c	Cross-sectional view of an element and nodal spacing…….	144
6.2a	Arm skin temperatures…….	145
6.2b	Leg skin temperatures……	145
6.3	Comparison of MU Model predictions and experimental results ……	145
6.4	Comparison: posterior skin temperature…….....	146
6.5	The effect of CIVD on finger temperature……	146
6.6	External auditory meatus temperature……..	146

LIST OF TABLES

Table		Page
2.1	Maximal conductances (in mS/cm^2)…….	44
2.2	IPSC characteristics for four different peak conductances……	46
3.1	Expression for Conductances of Ionic Channels…….	66
3.2	Maximal conductances (in mS/cm^2)…….	67
5.1	Details of the experimental dataset……..	107
5.2	Description of the parameters……	108
5.3	Average subject for each group…….	109
5.4	Regression Coefficients…….	110
5.5	Coefficients of correlation (R)……...	111
5.6a	Ranked and scaled sensitivity in Jungle and Desert-males……	112
5.6b	Ranked and scaled sensitivity in Jungle and Desert-females…….	113
5.7a	Ranked and scaled sensitivity in Neutral and Cold –males……...	114
5.7b	Ranked and scaled sensitivity in Neutral and Cold –females……	115

CHAPTER 1

INTRODUCTION AND OBJECTIVES

Control of a system requires that the system be understood 'adequately'. The term 'adequately' implies that the level of understanding of the system is related to the accuracy of control or understanding required. This requirement on control or understanding, typically takes the process of mathematical modeling, for most systems. A spectrum of models exists ranging from crude ones for human behavior and weather modeling, to very accurate models for aircraft and automobiles. Interestingly, the process of modeling is the same for all the models in the spectrum, except for the level of complexity and uncertainties involved. Several mathematical frameworks have been proposed to develop computational models. Computational models thus help transition from the 'real world' to the 'math world' where systems from all levels of the spectrum described above look similar. Thus, for systems and control engineers, the techniques of modeling and control are ubiquitous throughout nature, and seem similar.

Biological systems are increasingly being studied by systems engineers, and funding agencies such as the National Science Foundation and the National Institutes of Health, are encouraging interdisciplinary research involving engineers to understand biological systems across all scales ranging from genes to cells to tissue to organs to entire systems and behavior. This dissertation considers these modeling issues for two high order nonlinear example case biological systems:

(i) Cellular level modeling for neurons and networks, which is representative of complex nonlinear systems with multiple inputs and outputs.

Example Case I – cell modeling to study two types of neural circuits. One deals with a study of a single cell where the focus is on the mechanism of action of clonidine on prefrontal pyramidal cells. Clonidine is a drug used to treat attention deficit hyperactivity disorder (ADHD) patients. The second study deals with characterizing the neural circuitry involved in modulating the blood pressure, the nucleus tractus solitarius (NTS).

(ii) Systems physiology modeling for human thermal system, which represents a 'higher level' model, again with multiple inputs and outputs.

Example Case II –human thermal physiology modeling to better understand human thermal responses under transient environmental conditions and to develop automatic thermal control for astronauts during extra-vehicular activity (EVA).

All mathematical models considered for these systems are developed using nonlinear differential equations.

The two real-world example cases mentioned above are multi-input multi-output (MIMO), large dimensional, have significant nonlinearities and uncertainties (parametric uncertainties and unknown dynamics). There are no good models presently available for understanding how they work. The difference between two example cases is their scale and complexity. Example Case 1 systems are modeled at the cellular level, while Example Case 2 is modeled at the systems level. Both these example cases are described in detail next, followed by the objectives of the research.

1.1 Example Cases:

Two real world example cases have been considered to illustrate the proposed modeling and analysis tools:

1.1.1 Example Case I –– Cellular level Modeling to study mechanism of action of clonidine

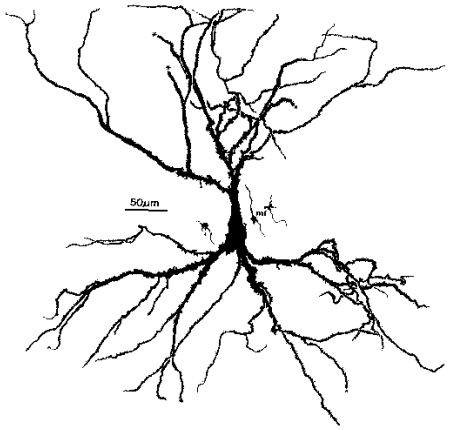

Figure 1: Hippocampal pyramidal cell.

An understanding of information processing at the level of individual nerve cells (e.g. of a hippocampal cell in Figure 1) requires detailed information about interactions between the anatomical structure, physiological properties, and synaptic inputs. Compartmental models have been used to explore ideas about current flows, voltage perturbations, and input-output relations, for cells which can be described as a capacitance with various variable resistances as will be explained shortly. In compartmental modeling, a cell is divided into sufficiently small compartments. One makes a negligibly small error by assuming that each compartment is isopotential and

spatially uniform in its properties. Non-uniformity in physical properties and differences in voltage occur between compartments rather than within them.

Throughout the cell, from an engineer's point of view, there are passive channels that remain partly open all the time, leading to a leakage resistance. An insulating cell membrane separates the conductive cytoplasm inside the cell from the extra cellular environment outside, giving rise to a membrane capacitance. As the cytoplasm has some resistance, there is an axial resistance along the dendrites and axon. To an engineer, a section of dendrite acts like a leaky cylindrical capacitor, coupled to neighboring sections with resistances.

If the goal is to understand the way that individual neurons "compute", rather than to implement some abstract model of "neural computation", one has to necessarily understand the method by which the dendritic structure processes its many inputs. After achieving this understanding with a structurally realistic model it might be possible to produce a simpler "ball and stick" model (Figure 2) that will function equivalently in a large network model. If one ultimately wants a simple, computationally efficient neuron model that can be used in simulations of very large neuronal networks, one should perform a model order reduction with careful consideration of the dynamics.

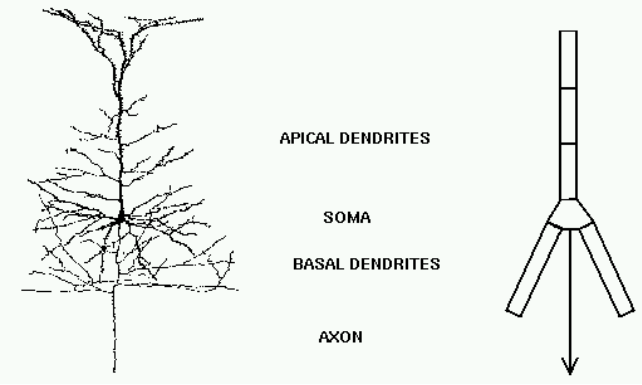

Figure 2: A hyppocampal pyramidal cell and a simplified model with a lumped parameter model in which the neuron is divided into a finite number of compartments containing resistances, capacitances and batteries to represent ionic equilibrium potentials.

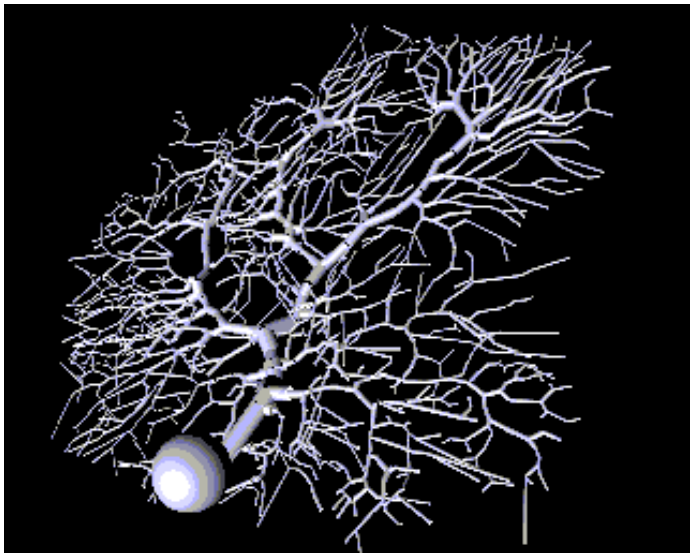

Figure 3: A computational model of a Purkinje cell from the cerebellum made with GENESIS by De Schutter and Bower. It has 4550 comparments and 8021 active channels

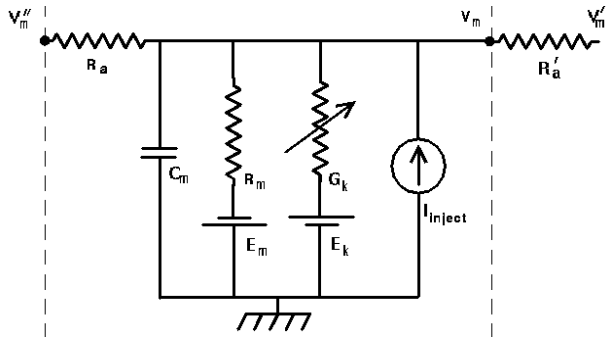

Figure 4: Equivalent circuit for a compartmental model

Figure 4 shows how a cell can be modeled as an equivalent circuit. In this diagram V_m represents the membrane potential at a point inside the compartment, relative to the "ground" symbol outside the cell. The membrane capacitance C_m can be charged or discharged as current flows into or out of the compartment, changing the value of V_m. This current can come from adjacent compartments, from the passage of ions through ion channels, or from a current 'injected' through an external probe as in electrophysiology experiments. Adjacent compartments have membrane potentials V_m' and V_m'', and the difference in potential across the axial resistances R_a and R_a' can cause current to enter or leave the compartment. The "leakage resistance" R_m and its associated equilibrium potential E_m represent the passive channels, and the resistor with the arrow through it represents one of the possible variable conductances that are specific to a particular ion or combination of ions. By convention, these are represented by a conductance G_k, rather than a resistance, $1/G_k$. Each one of these conductances has an associated equilibrium potential represented by the voltage E_k. The equilibrium potential (reversal potential) is the value of V_m at which there is no net flow of the ion through the conductance. Most neural simulation packages provide a way to calculate these from the Nernst equation [4]. Typically, there will be several of these variable resistances, with different conductances

and equilibrium potentials, corresponding to the different types of channels in the compartment. For example, the area near the region of the soma called the "axon hillock" may contain voltage dependent sodium and potassium channels, and regions in the dendrites are likely to contain channels that are chemically activated from synaptic connections. The index *k* is being used here to represent one of these various types of conductances.

A model is particularly valuable if it succeeds in reproducing, or predicting, behaviors in addition to those it was originally constructed to replicate [2]. For example the Hodgkin-Huxley model of voltage-gated currents was constructed to reproduce the properties of those currents as observed in experiments with each current isolated. That the model would, in addition, succeed in simulating an action potential was not evident *a priori*, and was of great significance.

Using the compartmental modeling approach, a single cell model along with a GABAergic interneuron has been developed to understand the effects of alpha2 agonist clonidine on working memory and ADHD. The model thus has applications in the area of drug discovery, in addition to providing a better understanding of the functioning of brain circuits for this disorder. This is collaborative project with Antonieta Lavin, MD, Ph.D., of the Medical University of South Carolina, Charleston, SC. In the other study, we develop both single cell and network models for baroreceptor and NTS cells to better characterize the functional circuitry involved in modulating the signals involved in the control of blood pressure.

1.1.2 Example Case II –– Modeling Human Thermal Physiology

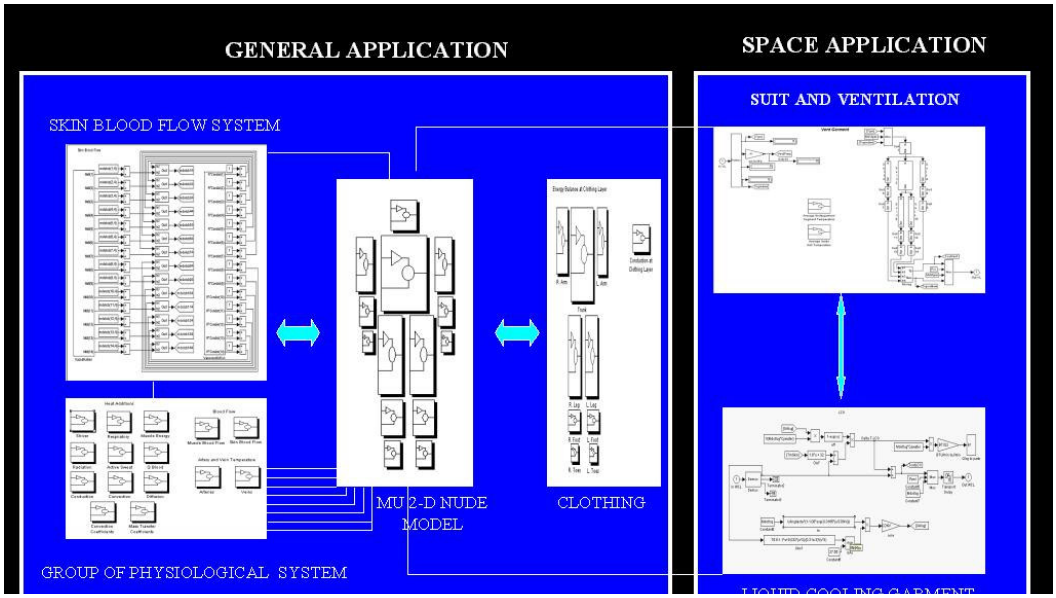

Figure 5: Human Thermal Model in MALAB/SIMULINK software for Space and General Application

Example Case II focuses on mathematical thermal physiology models of the entire human body, statistical models using artificial neural networks (ANN), belonging to the category of black box models), and the combined system of both models to enhance the limitations of the individual models.

MU 2-D Man is a human thermal model developed by our group at the University of Missouri (MU). The model has been developed for designing an automatic thermal comfort control strategy for NASA astronaut space suits and for the US Air Force warfighters in chemo-bio suits. It is a general purpose model and can be used to predict thermal responses of human beings under transient environmental conditions. It has two main components, one being the passive thermal system including the solid tissue

structure and circulatory system and the other being the active thermal system including the thermoregulation mechanisms.

Two statistical models using ANN have also been developed for the US Army and the US Air Force to predict individual human thermal responses under transient environmental conditions.

1.2 Objectives

The objectives of the dissertation are to study accurate modeling and analysis techniques for two classes of bio-systems: dynamics or brain circuits (single cell and network levels – Part I) for a psychiatric disorder, and human thermal system dynamics for heat stress tolerance and comfort control (Part II).

PART I CELLULAR LEVEL MODELING

(i) develop single cell and network modeling techniques including the various channels and afferent/efferent connections, and compare with experimental data from co-advisor at Medical University of South Carolina, Charleston, SC. (Chapters 2)

Details of Chapter 2: The executive function deficits observed in Attention Deficit Hyperactivity Disorder (ADHD) include short attention span, perseverance, impulse control, self-monitoring and working memory (WM), all attributed to the dorso-lateral prefrontal cortex (DLPFC). Increasing evidence indicates a central role of dysfunctional catecholaminergic systems in PFC in promoting the observed deficits. To study the mechanism of action of clonidine, an alpha 2 agonist used clinically to treat ADHD, a computational model of a single PFC pyramidal cell and a network model has been developed. A single, fast-acting GABAergic interneuron is also modeled to provide inhibition for the pyramidal cell in the form of negative feedback.

Details of Chapter 3: Cardiovascular homeostasis involves the complex interaction among key organs (ie. heart, blood vessels, kidney) which are under the control of autonomic circuits in the brain. Recent findings have indicated that alterations in autonomic brainstem circuits contribute to the development of cardiovascular disease, including hypertension and congestive heart failure. A better understanding of how the brain processes neural signals may provide new avenues for the therapeutic treatment of both neurological disorders, such as Alzhiemers disease, as well as cardiovascular diseases which impacts millions of Americans annually. The overall objective of this interdisciplinary project is to develop a predictive model of the arterial baroreceptor

reflex, and to identify the precise mechanisms underlying "information transfer" by the autonomic barosensitive circuit, including pathology leading to these disorders. Here we intend to reproduce the behavior of individual baroreceptors and nucleus tractus solitarii (NTS) neurons and understand effect of potassium channels.

The behavior of individual baroreceptors and nucleus tractus solitari (NTS) neurons is studied to understand their role in the autonomic circuit controlling systemic blood pressure. The electrical properties of these cells are characterized with particular focus on the role of potassium channels in modulating membrane potential. The computational model predictions matched experimental membrane potential traces for such cells reported in the literature

Details of Chapter 4: The network model is used to identify whether an alteration in GABAergic transmission in the NTS can mimic the reduction in baroreflex gain reported in hypertension.

We used the network based model to manipulate network architecture in such a manner as to predict the input-output characteristics of the NTS circuit. Baroreceptor afferent signals to the NTS, as well as output signals from the NTS, are pulsatile in nature. However, the discharge patterns of baosensitive NTS network neurons are generally not pulse-modulated. We have used our newly developed model to provide a working framework to explain this phenomenon.

PART II SYSTEMS LEVEL MODELING

As mentioned earlier, Part II focuses on systems level physiology using the human thermal system dynamics as the example case, representing a higher level, 'systems level' model, again with multiple inputs and outputs. Human thermal physiology modeling is important to better understand human thermal responses under transient environmental conditions, which will aid in the development of automatic thermal control for astronauts during extra-vehicular activity (EVA), and in characterizing heat stress tolerance times for war-fighters in extreme conditions (cold to desert) in chem-bio suits. A specific control technique, model predictive control is also investigated for EVA thermal comfort, is then proposed. The specific objectives for this part are listed below:

(ii) Develop techniques to model and characterize the role of various subsystems and quantify the uncertainties, in a human thermal system, to capture inter-subject variations, with the objective of better understanding variations in nominal (NASA astronauts) and extreme (warfighters and astronauts) among subjects. (Chapters 5-6)

Details of Chapter 5: The effect of individual differences on thermal stress response for semi-nude supine human subjects in transient environments is studied using an experimental data set. Two transient climatic parameters and seven individual characteristics are used as inputs to predict three thermal responses using a novel transient computational model. The model is developed using a neural network after ensuring generalization and also checking with results reported in the literature for predictions. A methodology is then proposed to identify the relative importance of the individual parameters and of environmental conditions on thermal stress, using a sensitivity analysis.

Details of Chapter 6: A new human thermal model has been developed that accounts for asymmetric environments and includes extremities. The model incorporates 2-dimensional (radial and circumferential) heat transfer along with arterial and venous countercurrent blood flow. To this model we add models for digits to predict heat transfer through toe and fingertip via arteriovenous anastomoses (AVAs) mechanisms, all of which are important in extremity discomfort.

Appendices 1-3 include other relevant material, including listing of the software code developed as part of this dissertation.

OTHER STUDIES: The author was also involved in other studies which are not included in this dissertation. One of these involved mathematical modeling of optimal triage in pediatric trauma care using advanced modeling techniques, which to date has resulted in two journal papers listed below:

- Burd, R. S., Jang, T., and Nair, S., "Evaluation of the relationship between mechanism of injury and outcome in pediatric trauma," *The Journal of Trauma* (accepted for publication).
- Burd, R. S., Jang, T. S., Nair, S. S., 2006, "Predicting hospital mortality among injured children using a national trauma database," *Journal of Trauma*, 60:792-801.

On the experimental side, he was a key member in a large scale human thermal experimental study involving 7 male and 7 female subjects for a US Air Force project. Using the data, he was the lead person for the development of a computer model to predict thermal responses in extreme conditions. All these have not been discussed in the dissertation, but mentioned here since it was performed during the author's Ph.D. program at MU.

REFERENCES

1. Bower J. and Beeman D., *The Book of GENESIS Exploring Realistic Neural Models with the GEneral NEural SImulation System*, Internet Edition, 2003.

2. Byrne J. and Roberts. J., *From molecules to networks, an introduction to cellular and molecular neuroscience* Academic Press, 2003:

3. Kandel E., Schwartz J., and Jessell T., *Principles of Neural Science*, Fourth Edition, Jessell. New York, McGraw-Hill Professional Publishing, 2000

4. Keener J. and Sneyd J., *Mathematical Physiology*, Springer-Verlag, New Yourk 2001.

5. Koch and Segev, *Methods in neuronal modeling: from ions to networks*, Second Edition, The MIT Press, Cambridge, Massachusetts, London, England, 2001.

6. Mays, C. D., Campbell, A. B., Nair, S. S., Miles, J. B., and Thomas, G., 2001, "Thermal Technologies for Space Suits," *ASHRAE Journal*, Vol. 43(1), pp. 25-36.

7. Parsons K. C., *Human Thermal Environments : the effects of hot, moderate, and cold environments on human health, comfort, and performance,* 2nd ed., London ; New York : Taylor & Francis, 2003.

8. Thornton, S. B. III, *Thermal Comfort and Control in Suited Environments: Theory and Experiments*, Ph.D Dissertation, Department of Mechanical and Aerospace Engineering, University of Missouri-Columbia, 2002.

PART I
CELLULAR LEVEL MODELING

Computational models provide an effective avenue to test hypotheses regarding mechanisms that underlie a system's behavior with applicability to the entire neuroscience spectrum including molecular, cellular, systems, and behavior levels. An improved understanding of the functional or physiological system/organ, organization typically requires connection of multiple levels, something that can be facilitated by computational models (Koch and Segev 2001,Terman et al. 2002). Koch and Segev (2001) predict that laboratories and researchers will rely on models and modeling software to check the significance and accuracy of their data, and that these models will enhance collaboration and communication within neuroscience.

PART I consists of three chapters focused at computational neuroscience models at cellular level, each written in the form of a journal paper. The objectives for this part are to develop accurate modeling and analysis techniques for the dynamics of single cell and networks of mammalian neurons for two different applications with collaborators who specialize in wet lab neuroscience experiments. The first application is to characterize the mechanism of action of a drug and the second is to characterize barosensitive circuits from a functional viewpoint. The models developed can be used to check prevalent ideas and competing theories, identify unknown relationships, i.e., to delineate 'gaps' in knowledge, and generate new possibilities.

In Chapter 2, a computational model of a PFC pyramidal cell and an interneuron is developed to study the mechanism of action of clonidine, an alpha 2 agonist, used clinically to treat patients with ADHD. Two specific hypotheses are tested and model

predictions are compared to experimental data from co-advisor Dr. Lavin of Medical University of South Carolina, Charleston, SC. Also, a novel methodology is reported to characterize the effects of IPSCs on PFC pyramidal cells.

In Chapter 3, single cell models of baroreceptor and NTS cells are developed with the objective of reproducing the behavior of individual baroreceptor cells and nucleus tractus solitari (NTS) cells and understand the effect of potassium channels. A and C –type baroreceptor models are used to develop a predictive model of the arterial baroreceptor reflex, and to identify the precise mechanisms underlying "information transfer" by the autonomic barosensitive circuit, including pathology in the circuits leading to conditions such as cardiovascular disease.

Extending the study in Chapter 3, Chapter 4 focuses on a network model to identify whether an alteration in GABAergic transmission in the NTS can mimic the reduction in baroreflex gain reported in hypertension. The model developed provides a working framework to explain these phenomena and study emergent properties of such computational circuits.

As mentioned earlier, each chapter is in the form of a self-contained journal paper.

CHAPTER2
MODULATION OF PFC PYRAMIDAL CELL EXCITABILITY BY CLONIDINE
- A computational modeling study

Abstract

In vitro data have shown that application of clonidine, an alpha-2 agonist, to cortical slices increases pyramidal cell excitability (Andrews et al. 2004). We propose two hypotheses, the first that GABA-mediated conductances underlie the increases in excitability elicited by activation of alpha 2 receptors, and the second that the closure of HCN channels results in the increased excitability. In order to test these hypotheses we developed a computational model consisting of a pyramidal cell connected to a fast spiking interneuron.

Model predictions show that the modulation of Ca^{2+} and K^{+} channels, including K_{ir}, by clonidine has little effect on the excitability of the pyramidal cell. The model also shows that activation of alpha-2 receptors can increase excitability of the pyramidal cell by decreasing the GABAergic inhibitory input from the interneuron. This theoretical result is consistent with experimental findings in slices (Andrews et al. 2004). However, GABAergic synaptic inputs to pyramidal cells are heterogeneous, thus, the underlying mechanisms (i.e., types of interneuron, subunit receptor composition, plasticity, desensitization, modulation, occupancy, and transmitter concentration and uptake) responsible for the change are not clear (Aradi et al. 2002). In a systematic study, we show how these mechanisms could lead to increased variance in the conductance or decay constant of IPSCs that could, in turn, modulate the firing rate of the pyramidal cell. Based on this analysis we develop regression models linking firing rate of pyramidal cells to IPSC characteristics such as mean IPSC amplitude,

charge transfer and variance. The simulation also showed that a closure of HCN channels could result in the observed increase in intrinsic excitability, confirming the second hypothesis. The actual mechanism could be a combination of the two effects, and possibly involve other channels also.

Keywords: Computational modeling, α-2NAR, norepinephrine, neuromodulators, IPSC, heterogeneity, PFC, ADHD

INTRODUCTION

The prefrontal cortex (PFC) is critically involved in cognitive processes underlying working memory (WM), attention, and inhibition of responses to non-relevant stimuli (Fuster, 2000; Goldman-Rakic, 1996). In this context, catecholaminergic inputs have proven to be critical for the regulation of these cognitive processes (Levitt *et al.*, 1984; Lewis *et al.*, 1987; Lewis and Morrison, 1989; Porrino and Goldman-Rakic, 1982). Indeed, dopamine (DA) and norepinephrine (NE) are involved in aspects of executive function (selective attention, response selection/control), as well as arousal (NE) that contribute to the efficiency of information processing. Numerous studies have focused on the role of DA in the PFC (Arnsten *et al.*, 1994, 1995; Castner *et al.*, 2000; Durstewitz *et al.*, 1999; Gao *et al.*, 2001; Gao and Goldman-Rakic, 2003; Goldman-Rakic, 1998; Goldman-Rakic *et al.*, 2000; Lavin and Grace, 2001; Lavin et al., 2005; Lewis and O'Donnell, 2000; Murphy *et al.*, 1996; Sawaguchi *et al.*, 1990; Williams and Goldman-Rakic, 1995; Yang and Seamans, 1996). However, DA is not the only catecholamine modulating PFC activity; the noradrenergic projection arising from the locus coeruleus (LC) also plays a very important role in the modulation of cortical activity (Berridge, *et al.*, 1993; Coull, 1994). Aston-Jones and Bloom (1981a, b) showed that the NE neurons located in LC and terminating in the PFC are

important in mediating selective and sustained attention and vigilance. Moreover, stimulation of the LC increases the discrimination of incoming external stimuli to the PFC by reducing the background noise, therefore enhancing the cortical signal-to-noise ratio (Aston-Jones *et al.*, 1985; Berridge and Waterhouse, 2003; Foote *et al.*, 1980, 1983; Waterhouse *et al.*, 1980; Robbins, 2000). More recently, several studies have shown that adrenergic agonists, especially specific alpha-2 agonists, are very effective in enhancing WM and attention. Indeed, administration of alpha-2 agonists can ameliorate some of the negative effects on cognition produced by NE depletion due to aging in monkeys (Arnsten and Goldman-Rakic, 1985; Arnsten *et al.*, 1988; Arnsten and Leslie, 1991) and improve performance in WM-related tasks in young monkeys with NE depletion (Arnsten and Goldman-Rakic, 1985; Cai *et al.*, 1993). Moreover, the therapeutic effects of the specific alpha-2 agonists, clonidine and guanfacine in treating disorders related to dysfunction of WM in patients have been proved (Fields *et al.*, 1988; Mair and McEntree 1986, 1988; Hunt *et al.*, 1985, 1990, 1995).

As a first step to further the understanding of the mechanisms involved in the catecholaminergic modulation of cortical activity, we have developed a computational model consisting of a single PFC pyramidal neuron, with a fast-acting GABAergic interneuron providing inhibition for the pyramidal cell in the form of negative feedback. Our goal is to use this model to predict the effects of activation of NE receptors on the cortical network. In particular, we will investigate two hypotheses about how clonidine would increase the intrinsic excitability of PFC pyramidal cells, the first hypothesis involving GABA IPSCs and the second hypothesis involving hyperpolarization-activated cation (HCN) channels.

MATERIALS AND METHODS

Electrophysiological experiments

Slice preparation and aCSF solutions: Infant, male Sprague-Dawley rats (P15-25) were deeply anesthetized with chloral hydrate (400 mg/kg ip) and rapidly decapitated. Surgical removal of the brain was quickly accomplished with the brain submerged in a near-frozen sucrose solution (in mM: sucrose, 200; KCl, 1.9; Na_2HPO_4, 1.2; $NaHCO_3$, 33; $MgCl_2$, 6; $CaCl_2$, 0.5; dextrose, 10; ascorbic acid, 0.4) aerated with a mixture of 5%CO_2/95%O_2. Coronal slices (300-350µm) were made to include infralimbic and prelimbic cortices using a Vibratome (Leica, VT1000). Slices were incubated for a minimum of 1h in a separate solution (containing in mM: NaCl 125; KCl 2.5; NaH_2PO_4, 1.25; $NaHCO_3$, 25; $MgCl_2$, 4; $CaCl_2$, 1; sucrose, 15; glucose 10; ascorbic acid, 0.4; osmolarity: 312 mOsmols) which was continuously aerated with 5%CO_2/95%O_2 mixture at 23-25°C. During recording, oxygenated aCSF (in mM: NaCl 125; KCl 2.5; $NaHCO_3$, 25; $MgCl_2$, 1.3; $CaCl_2$, 2; glucose 10; ascorbic acid, 0.4, osmolarity: 299 mOsmols) was perfused into the recording chamber at a rate of 1ml/min.

Electrophysiological Recording and Stimulation Protocol: Deep layer pyramidal neurons (layers V-VI) were targeted for recording by using a Leica DMLFSA microscope, equipped with a Nomarski differential interference contrast optics, infrared videoimaging camera (C2400, Hamamatsu) and fitted with an 40× water immersion objective. Whole-cell current-clamp recordings of targeted cells were made using microelectrodes (3-7 MOhms) pulled with an horizontal Flamming-Brown puller (model P97) from glass capillary tubing (Corming 7056; OD 1.5mm; ID 1.1mm) and filled with internal solution (in mM: K-Gluconate 125; KCl 20; HEPES 10; EGTA 1, $MgCl_2$ 2, ATP 4.0; GTP 0.3; pH 7.2-7.4, osmolarity: 298 mOsmols). The signal was amplified

using an AxoPatch 200B (Axon Instruments) and stored for off-line analysis using a custom-made, LabView based program.

In current-clamp mode, rectangular depolarizing pulses (25-300 pA, 1 sec duration) were delivered every 30 seconds (*intrinsic stimulation*). The intensity of current stimulation was adjusted to elicit an average of 3-4 action potentials. Once a minimum 5 minute stable baseline was established the drug was applied followed by a 5 min, non-recording perfusion period during which the drug was allowed to diffuse into the slice. Stimulation protocols were then reinstituted. The baseline holding membrane potential and the intensity of stimulating current were maintained throughout the experiment.

Stimulation (*synaptic stimulation*) was delivered via a concentric bipolar stimulating electrode placed in layer II/III, located approximately 300-500 µm diagonal from the recording cell. The duration of the stimulation pulse was 0.12 msec and the frequency was 2 Hz. In some experiments, stimulation intensity was adjusted to ½ of the ePSP maximum amplitude and that intensity was maintained throughout the experiment. The intensity of stimulation ranged from 0.3 to 1 mA.

Morphological examination: A subset of pyramidal cells were filled with 0.3% biocytin and fixed in a 4% paraformaldehyde solution for post-hoc immunohistochemical staining and morphological identification.

Drugs: All drugs were aliquoted and stored at -20 °C. Drugs were dissolved into the recording aCSF and bath-applied at a constant rate of 1ml/1min. The depth of the recorded cell in the slice varied between experiments thus altering the time of initial drug effect. All drugs used were Sigma products and were applied at 10 µM unless stated otherwise:

Statistics: The average number of spikes/pulse represents the average among all cells with each cell's mean being derived from results over time for that cell. All data are presented as X ± SE. For comparisons between two groups (e.g., control/drug) a paired t-test was used with a significance level of $p<0.05$ unless otherwise stated. For statistical analysis of 3 groups (e.g., control/antagonist/drug or drug/response curve) a one-way ANOVA with Fisher post-hoc test were used. The significance level was $p<0.05$ unless stated otherwise. The changes in excitability were evaluated individually for each cell using a paired Student's t-test ($p<0.05$ unless stated).

Development of the computational model

The computational model consists of a PFC pyramidal cell and an interneuron with the various conductances, and Ca^{2+} pools. These and the specifics of the ionic and synaptic currents are described next. We propose a mechanism to explain the transient hyperpolarization seen in the membrane upon immediate application of clonidine. The two hypotheses for modulation of intrinsic excitability by clonidine are then discussed.

PFC Pyramidal and fast-spiking GABAergic interneuron model. Multi-compartmental models were developed for a PFC pyramidal cell and a fast-spiking GABAergic interneuron. Simulations were run on a PC, using the GENESIS (GEneral NEural SImulation System, Bower and Beeman 2003) software package, with an integration time step dt=0.01 ms. The passive parameters for both pyramidal cell and a basket-type fast spiking Gabaergic interneuron were determined from published values.

The specific membrane resistance (Rm) of the pyramidal model was adjusted to 64 Kohm-cm^2 to reproduce the cell firing rate at a given injected current (15 pA) for an *in vitro* case (Andrews et al. 2004). The input resistance is 205 Mohms for control and 274 Mohms

during alpha 2 agonist activation which is within the range of recordings from pyramidal cell in vitro (319 ± 149 for control and 365.3 ± 219 Mohms during alpha 2 agonist activation).

Ionic currents. The biophysical models for currents were taken from the following sources: leakage current (I_L), a fast, spike-generating Na^+ current (I_{Na}), the delayed rectifier potassium current (I_{DR}), and persistent current (I_{NaP}) were from Durstewitz et al. (2000); the high-voltage activated Ca^{2+} current (I_{HVA}) from Brown et al. (1993); slow inactivating K current (I_{KS}) and a fast BK Ca and voltage-dependent C-type K current (I_C) were from Wang (1993); I_{AHP} from Warman et al. (1994); I_{IR} from Niesenbaum and Wilson (1995) and modified by the authors to account for the intracellular Ca^{2+} concentration; and the Ca^{2+} dependent cationic current (I_{CAT}) from Kang et al. The ionic currents are summarized below:

$$I_L = g_L(V - E_L) \quad (1\text{-}1)$$

$$I_{Na} = g_{Na} m^3 h(V - E_{Na}) \quad (1\text{-}2)$$

$$I_{DR} = g_{DR} n^4 (V - E_K) \quad (1\text{-}3)$$

$$I_{KS} = g_{KS} ab(V - E_K) \quad (1\text{-}4)$$

$$I_{IR} = g_{IR}(1 + \exp((V + 111.9)/6.5))^{-1}(V - E_K) \quad (1\text{-}5)$$

$$I_{HVA} = g_{HVA} u^2 v(V - E_{Ca}) \quad (1\text{-}6)$$

$$I_C = g_C c^2 (V - E_K) \quad (1\text{-}7)$$

$$I_{AHP} = g_{AHP} q(V - E_K) \quad (1\text{-}8)$$

$$I_H = g_H h(V - E_H) \quad (1\text{-}9)$$

$$I_{cat} = g_{cat} m_{cat}(V - E_{cat}) \quad (1\text{-}10)$$

where V can be V_s or V_d, the reversal potentials for Na^+ and K^+ are $E_{Na} = 55$ mV and $E_k =$ 25 x $\ln([K^+]_o/[K^+]_i)$ where $[K^+]_o$=3.82 mmol/l and $[K^+]_i$=140mmol/l (Durstewitz et al. 2000). E_H was set at – 80 while E_{cat} was set at -42 mV for the reversal potential of mixed cationic channel and the cationic channel respectively. E_{cat} was set at -42 mV for the reversal

potential of the cationic channel. The kinetic equation for each of the gating variables *m*, *h*, *n*, *a*, *b*, *u, v, c* and *q* takes the form

$$\frac{dx}{dt} = \frac{x_\infty(V,[Ca^{2+}]_i) - x}{\tau_x(V,[Ca^{2+}]_i)} \quad (2)$$

where $[Ca^{2+}]_i$ is the intracellular Ca^{2+} concentration, x_∞ is the voltage- (or Ca^{2+}-) dependent steady state and τ_x is a voltage- (or Ca^{2+}-) dependent time constant. x_∞ and τ_x are given by the rate functions, α_x and β_x, for the gating variables *m*, *h*, *n* and *r*

$$x_\infty = \alpha_x/(\alpha_x + \beta_x) \quad (3)$$
$$\tau_x = 1/(\alpha_x + \beta_x) \quad (4)$$

For the gating variables *c* and *q*, x_∞ is given by Eq (3) and τ_x is either a constant or a function of α_x and β_x in a form different from Eq (4). For the remaining gating variables *a*, *b*, *u*, and *v*, x_∞ and τ_x are directly given. All the rate functions, steady state x_∞ and time constant τ_x are listed in Table 1.

Fast-spiking (FS) GABAergic interneurons were modeled using two compartments based on the one in Durstewitz et al. (2000). FS interneurons provide most of the inhibition to the PFC cell. A fast, spike-generating Na^+ current (I_{Na}), the delayed rectifier potassium current (I_{DR}), the high-voltage activated Ca^{2+} current (I_{HVA}), a fast BK Ca^{2+} and voltage-dependent C-type K current (I_C), I_{AHP}, I_{IR} included in the somatic and dendritic compartment. The kinetics of Na^+ and K^+ channels differs from those of the pyramidal neuron so as to reproduce the much shorter spike duration in interneurons as compared to the pyramidal cells. All conductance kinetics are summarized in Table 1.

Modeling the I_{IR} current. The model for the inward rectifying potassium current, I_{IR}, was modified from the one in Niesenbaum and Wilson (1995) to account for its dependency on

intracellular and extracellular calcium concentration, and placed both on the dendrites and soma of pyramidal neuron and interneuron (Takigawa and Alzheimer 1999, Kitano et al. 2002). I_{IR} activates at hyperplarization around and below a potassium equilibrium potential E_k=-80 mV. It contributes to both depolarization and repolarization of the action potential and is significant in the maintenance of the resting membrane potential by opposing the depolarizing effect of the leakage current (I_L) at low voltage (Torres et al. 2004). The modified kinetics reflect dependency of I_{IR} on intercellular calcium concentration (Grabov et. al., 1999).

$$I_{IR} = G_{IR\_Peak}(1/(1+\exp((V_m - E_h / E_{cir}))\zeta([Ca^{2+}]_i)(V_m - E_K([K^+]_o)) \quad (5)$$

where E_{cir} characterizes the curvature of the I-V relation. E_{cir} is a slope factor and was held constant at 10mV. V_m is the membrane potential, E_h is the half-activation voltage and was equal to E_k-15 mV. E_k = 25 x ln($[K^+]_o/[K^+]_i$) where $[K^+]_o$=3.82 mmol/l and $[K^+]_i$=140mmol/l (Durstewitz et al. 2000). A shift in E_k shift from -70 mV to -110 mV leads to a corresponding shift in the hyperpolarizing direction. E_{cir}, which determines the degree of slope, the curvature of the I-V relation, is set to 10. The sigmoid function $\zeta([Ca^{2+}]_i)$ which represents a steep dependence curve on $[Ca^{2+}]i$ above resting $[Ca^{2+}]i$ levels (Grabov and Blatt 1999) is as follows,

$$\zeta([Ca^{2+}]_i) = [1/(1+\exp(([Ca^{2+}]i\text{-}Ca_h)/Ca_{ir})) \quad (6)$$

where $[Ca^{2+}]i$ is set at 50 nmol initially (Durstewitz 2000). In simulation runs, $[Ca^{2+}]_i$ varied from 50 to 100 nmol for soma, 50 to 210 nmol for both proximal and basal dendrites and 50 to 81 nmol for distal dendrites. Ca_h is the value at which G/G_{max} = ½ and its value was set at 0.06. Ca_{ir} was set at 0. 002 and G_{IR_Peak} at 0.4 mS (Kitano et al. 2002). The I_{IR} current was

open at resting Vm and increased during injection of a depolarizing current. As $[Ca^{2+}]i$ was increased Kir deactivated because the inactivation curve decreased significantly as $[Ca^{2+}]i$ moved closer to inactivation threshold. The current I_{IR} is not involved in modulating pyramidal cell excitability during the action potential period since it is inactivated but it is active before and after activation potential period and contributes to maintaining the resting potential around E_k.

Modeling synaptic currents: EPSCs and IPSC

AMPA-like synaptic and NMDA currents were modeled by a double exponential function as in Durstwitz (2000). Random background synaptic activity is provided to GABAergic cells. IPSC due to GABA is modeled as

$$I_{IPSC}(V,t) = g_{IPSC}(t)(V - E_{gaba,}), \quad (7)$$

where the time course of the synaptic conductance is:

$$g_{IPSC}(t) = A(g_{IPSC,\max}/(\tau_{rise} - \tau_{decay}))(\exp(-t/\tau_{decay}) - \exp(-t/\tau_{rise})) \text{ for } \tau_1 > \tau_2, \quad (8)$$

where the normalization constant A is chosen so that g_{syn} reaches a maximum value of $g_{IPSC,\max}$,

$$A = -1/((\tau_{rise}/\tau_{decay})^{\tau decay/(\tau decay-\tau rise)} - (\tau_{rise}/\tau_{decay})^{\tau rise/(\tau decay-\tau rise)}) \quad (9)$$

The parameters $g_{IPSC,\max}$, τ_{decay}, and E_{gaba} were varied to study their effects on variances in IPSC phase and frequency. Background excitatory synaptic inputs were placed on all dendritic compartments of pyramidal cells and interneurons, while inhibitory inputs are limited to the soma where cortical pyramidal cells receive most of their inhibitory input.

Calcium Dynamics. Based on the description in Warman et al. (1994), two different Ca^{2+} pools are modeled, one mediating the activation of I_C ($[Ca^{2+}]_{i1}$) and the other mediating the activation of I_{AHP} ($[Ca^{2+}]_{i2}$). This permits I_C to deactivate rapidly following an action

potential to generate the fast AHP, while I_{AHP} can activate gradually after each spike to produce the slow AHP (Warman et al. 1994). Extracellular calcium is assumed to be constant ($[Ca^{2+}]_o = 2$ mmol/l), while intracellular calcium in the dendrite compartment is regulated by a simple first-order differential equation of the form (Warman et al. 1994)

$$\frac{d[Ca^{2+}]_{ij}}{dt} = -f_j \frac{I_{Ca}}{wzFA} + \frac{[Ca^{2+}]_{rest} - [Ca^{2+}]_{ij}}{\tau_{Caj}} \qquad (10)$$

where $j = 1$ or 2 to represent the first or second calcium pool, f_j is the fraction of the Ca^{2+} influx ($f_1 = 0.7$; $f_1 = 0.024$), w is the shell thickness (1μm), A is the dendritic area, F is the Faraday constant, τ_{Caj} is the Ca^{2+} removal rate of the jth pool ($\tau_{Ca1} = 1$ ms and $\tau_{Ca2} = 500$ ms).). In our study I_{HVA} is the total CA^{2+} current for the soma and dendrite. The resting Ca^{2+} concentration is $[Ca^{2+}]_{rest} = 50$ nmol/l, which is the same as the initial concentration (Durstewitz et al. 2000). In Eq (3), the unit of the Ca^{2+} concentration is μm/l. In Eq. (2-8), the reversal potential of Ca^{2+} current is determined by the Nernst equation

$$E_{Ca} = 12.5 \times \ln([Ca^{2+}]_o / [Ca^{2+}]_{i1}) \qquad (11)$$

$I_{Na}, I_{DR}, I_{CAT}, I_{NaP}, I_{HVA}, I_{KS}, I_C, I_{AHP}$, and I_{Leak} were placed in soma, proximal, basal, and distal dendrites of the pyramidal cell and I_{IR} was only placed in proximal and distal dendrites of the pyramidal cell. $I_{Na}, I_{DR}, I_{HVA}, I_C, I_{IR}$, and I_{Leak} were placed on both soma and dendrite compartment of the interneuron. I_{GABA_A} placement was limited to the soma of the pyramidal and interneuron while I_{AMPA} and I_{NMDA} were placed in all dendrites compartments of the pyramidal cell and interneuron (Durstweitz et al. 2000).

Experiments in the Lavin lab (REF) showed that the frequency of sIPSCs measured in the PFC cell decreased with the application of clonidine. This provides the basis for our first

hypothesis that GABA-mediated conductances underlie the increases in excitability of the PFC cell, i.e., GABA synaptic input to the pyramidal cell was decreased due to stimulation of alpha 2 NAR located in interneurons leading to decreased inhibition on the PFC cell.

Spontaneous IPSCs reflect a scenario more analogous to basal conditions of inactivity. It is important to note that sIPSCs are a mixture of quantal release of neurotransmitter (miniature IPSCs) and the neurotransmitter release from intrinsic spontaneous stimulation (in this case enhanced interneuron activation by increasing external K^+ concentration). The latter form of release requires the influx of Ca^{2+}, and clonidine, known to inhibit voltage-gated calcium channels, would be expected to cause a decrease in sIPSCs but its mechanism of action is not well understood presently.

Modeling IPSC variations. Pyramidal neuron traces for control and clonidine cases were obtained and compared with experimental data, for the same depolarizing injection current of 20 pA. The IPSC maximum conductance was 2.4 nS and rise and decay times were 2.5 and 10.5 ms respectively (Aradi et al. 2002). The maximum conductance of the Kir channel was set at 0.3 mS/cm^2 for control and 0.4 mS/cm^2 for the clonidine case (Wolf et al. 2005, Kitano et al. 2002) while for the calcium current I_{HVA} it is 0.65 mS/cm^2 for proximal and basal dendrites and 0.327 mS/cm^2 for soma and distal dendrite. The increased conductance of Kir channels in the pyramidal cell due to the activation of clonidine caused an increased in hyperpolarized membrane potential by 5 mV compared to controls. The decreased high voltage activated channel, I_{HVA} conductance actually suppressed excitability leading to a decrease in the number of action potentials by 2 spikes, over control. Therefore, without decreased $GABA_A$ synaptic inhibition on pyramidal cell, the activation by clonidine would

eventually hyperpolarize the both interneuron and the pyramidal cell through increased hyperpolarizing potassium and calcium channels. The decreased synaptic inhibition on pyramidal cell through GABAergic interneuron was simulated by decreasing the interneuron excitability or decreased GABA release to pyramidal cell assuming the release was activity-dependent. Interneuron excitatory input through AMPA/NMDA was decreased and so was its GABA release. As a result, the alteration in IPSC is a key mechanism in modulating pyramidal cell excitability, which we consider as hypothesis 1. To study this mechanism in the presence of considerable GABA synaptic diversity, we develop a systematic methodology in the next section for this hypothesis, by focusing on IPSC modulation of pyramidal cell excitability through GABAergic interneuron while maintaining the increase of Kir channels and I_{HVA} channel at a low level.

Modeling modulation of pyramidal cell firing rate by clonidine via GABA mediated IPSCs – first hypothesis

Synaptic input diversity or heterogeneity in pyramidal cell and its mechanism are not well understood. The activation of synaptic $GABA_A$ receptors produces an inhibitory postsynaptic current (IPSC) shaped by the properties and number of receptors and by the magnitude and duration of the GABA transient. It is known that the number of synaptic $GABA_A$ receptors is subject to large alterations during neuronal plasticity and development (Fritschy et al. 2003). The factors underlying the diversity of inhibitory neurotransmission through $GABA_A$ receptors can be many including subunit composition which affect decay kinetics (Sieghart et al. 2002), localization, activation, number and phosphorylation states,

variance of GABA concentration in the synaptic cleft, and some of the presynaptic factors regulating GABA release (Mody et al. 2004).

At the level of the postsynaptic cells, the diversity of the presynaptic interneuronal populations is reflected as the heterogeneity in the synaptic GABAergic inputs, which can be detected electro physiologically as variances in the conductance, or decay of sIPSCs (Aradi et al. 2002). Using the computational model described earlier, a systematic study of the effect of GABA related IPSCs on the excitability of the cell is explored. This is done in simulation with the IPSCs initiated by an interneuron which in turn was excited by random synaptic inputs as stated below. This is based on the hypothesis that clonidine might modulate the pyramidal neuron excitability through GABAergic interneurons. Decay time constants, peak GABA conductance, and synaptic input rate have been altered systematically.

Modeling modulation of pyramidal cell firing rate by closure of HCN channels – second hypothesis

We also investigated a second hypothesis to explain the increase in excitability mediated by clonidine blocking hyperpolarization-activated/cyclic nucleotide gated cation (HCN) channels. These channels have the ability to generate rhythmic cellular activity known as h currents (I_h) and allow neuronal cells to be rhythmically active over precise intervals of time. As a result, they function as pacemakers. HCN channels regulate synaptic integration (Magee, 1999) and influence factors such as resting membrane potential, input resistance, and membrane time and length constants. These channels are activated (opened) by hyperpolarizing currents and are deactivated (or closed) by depolarizing currents. When activated, HCN channels decrease the efficacy of

synaptic inputs and dampen cellular response to inhibitory stimuli. Activation of cAMP serves to enhance the opening of the HCN channels (Ulens and Siegelbaum, 2003) on the dendritic spines. This contributes to the observed impairment of PFC function associated with the activation of the adenylyl cyclase-cAMP-PKA pathway. In the PFC, HCN channels are co-localized with post-synaptic alpha 2A receptors on dendritic spine necks and spine heads. Alpha 2A receptor-activation-induced inhibition of adenylyl cyclase-cAMP-protein kinase A (PKA) therefore, indirectly deactivates the HCN channels enhancing the ability of PFC to modulate inhibiting and interfering stimuli and, as a result, strengthening the main impulses.

Based on separate spikes/pulse experiments, following administration of I_H blocker and then clonidine I_H current was blocked.

The signal to noise ratio was also increased due to the presence of Clonidine.

The role of Kir channel remains same as its main role was to hyperpolarize the membrane potential initially. The hyperpolarization-activation cationic current, I_H, was modeled by a continuous and bell-shaped function of membrane potential, with the slowest rate of activation (time constant around 1s) occurring at -80mV.

The activation curve was represented by the following equation.

$$h_\infty = 1/(1+\exp^{((V-75)/13.5)}) \qquad (13)$$

I_H does not inactivate, even with prolonged (minutes) hyperpolaization (McCormick 1990, Hugenard 1992). For control case h_{max} was set at 20 nS well within the experimental range (15-30 nS; McCormick 1990) while with clonidine, h_{max} was set zero simulating the blocking of I_H by the presence of clonidine. Our reversal potential was set at -67 mV lower than the

reported values which range form -24 to -50 mV (Halliwell and Adams 1982; Spain et al. 1987; van Ginnken and Giles 1991) to account for net outward current during control case.

RESULTS

Input Resistance. The specific membrane resistance (Rm) and the axial membrane resistance of the pyramidal model were adjusted to 64 Kohm/cm^2 and 1.8 Kohm-cm respectively to reproduce the cell firing rate at a given injected current (15~20pA) for an *in vitro* case (Andrews et al. 2004) for both hypotheses. The inwardly rectifying potassium current conductance and Gabaergic inhibitory synaptic conductance variations accounted for the significant change in input resistance of control and clonidine cases where it was 205 Mohms for control and 274 Mohms with clonidine which is within the range of recordings from pyramidal cell in vitro (319 ± 149 for control and 365.3 ± 219 Mohms after application of clonidine). See Figure 1.

Transient depression in membrane potential with clonidine. The conventional Kir model (Niesenbaum and Wilson 1995) showed that an increase in Kir conductance totally or partially suppressed the pyramidal cell's excitability failing to produce more spikes. The conventional Kir model does not include dependency on $[Ca^{2+}]_i$ but a recent study showed that I_{ir} is strongly dependent on $[Ca^{2+}]_i$ in inactivating I_{ir} (Grabov et al. 1999). A steep dependence curve on $[Ca^{2+}]_i$ above resting $[Ca^{2+}]_i$ levels (left) and modified Kir channel considering $[Ca^{2+}]_i$ and membrane potential dependency were considered in the modified Kir model. This modified Kir model successfully reproduced then experimental data, showing the same transient depression in resting membrane potential of 5 mV with the application of

clonidine. The next section considers the modulation of pyramidal cell firing rate by clonidine.

Modulation of pyramidal cell firing rate by clonidine via GABA-mediated IPSCs – first hypothesis

The GABA synaptic regulation was modeled as being dependent on interneuron activity so that each spike that the interneuron generates sends a signal to GABA channel to activate according to the kinetics described in Eq. (7). This activation is modeled using NMDA and AMPA receptors. Pyramidal cells excite interneurons, along with inputs from other regions, and since precise excitation profiles are difficult to determine, the study used a range of frequencies as input to the interneuron instead for varying peak GABA conductance and decay time systematically. The interneuron receives this input through AMPA/NMDA channels. At low frequencies, the interneuron was less excited and released relatively small amount of GABA transmitter to pyramidal cell. Its inhibitory effect on pyramidal cell resulted in increased spikes. We altered $g_{IPSC,\max}$ and decay time systematically and showed that same pc firing rate could be obtained with a different combination of $g_{IPSC,\max}$ and the decay time constants and the interneuron excitation. With a $g_{IPSC,\max}$ and the decay time constant fixed at 6.4 nS and 2.5 ms, respectively and with the frequency range of 35 to 50 Hz to the interneuron for example, the pyramidal cell showed 3 to 4 spikes, and at higher frequencies, it showed lesser number of spikes as interneuron was excited and released more GABA to the pyramidal cell. Larger events of IPSCs were clearly seen in pyramidal cells for control, but rarely seen during the activation of alpha-2 agonist shown in the histogram and cumulative probability plot in Fig. 2.

The computational model shows that despite of the existence of diversity of GABAergic synaptic input and heterogeneity of interneuron types, IPSC characteristics such as a total charge transfer (area under the IPSC-time curve), mean IPSC amplitude, IPSC standard deviation among others could be used as an indicator of pyramidal cell firing rate. For instance, using a fixed $g_{IPSC,\max}$ value of 4.4 nS, different pyramidal firing rates ranging from 0 to 7 action potentials were obtained as shown in Fig. 2 along with experimental results. Fig 7 shows the IPSC histograms and cumulative probability plots. In the case of the alpha 2 agonist, lesser events of IPSC were seen yielding lower charge transfer and lower maximum IPSC amplitude, compared to the control case.

In Fig. 3, four different IPSC traces for different $g_{IPSC,\max}$ values (with the same rise and decay time constants and an injection current of 15 pA) yield the same pyramidal cell firing rate of 4 action potentials (these are shown in Fig. 4) each in the duration shown. Table 2 shows the IPSC characteristics including total charge transfer and interneuron firing rates for the four $g_{IPSC,\max}$ values. Interestingly, a large total charge transfer or the area under the IPSC curve did not necessarily imply the largest inhibitory effect on pyramidal excitability. This observation was same with minimum IPSC amplitude. It seemed that pyramidal excitability was more of a combined effect of a total charge transfer, standard deviation for IPSC amplitudes and other possible factors.

We also considered the case where the IPSCs were manipulated directly (without taking it as the output of the interneuron) to consider the trends involved, and found predictions similar to the ones discussed. These are shown in Figures 4 and 5. As Fig. 4A shows, increasing synaptic input rate from 10 to 140 Hz in 14 steps resulted in an increased inhibitory effect on the pyramidal cell. In Fig. 4B, the decay time was varied from 1.5 ms to

146 ms while its rise time was kept constant. The synaptic input was kept at 100 Hz (indicated by the letter "B" in Fig. 4A). A normalized charge transfer or normalized total area under the curve of IPSC for each pyramidal firing rate form Fig. 4A was calculated and shown in Fig. 4C. An approximate linear relationship can be observed in this particular case when mean IPSC conductance was increased gradually except when the pyramidal cell excitability is completely suppressed. The function increasing IPSC peak conductance ($g_{IPSC,\max}$) was shown in Fig. 2D where synaptic input was kept at 30 Hz as indicated by the letter "D" in Fig. 4A. The cumulative plots of IPSC amplitudes obtained from Fig. 4A for different synaptic inputs are shown in Fig. 5. It was observed that the lower the synaptic input, the larger the slope of the curve in this particular case where synaptic input increased monotonically.

These findings complement some of the results reported by Aradi and colleges (Aradi et al. 2002 and 2003) since both studies deal with the modulation of cell firing rates by GABAergic heterogeneity inputs. However, our study focuses on understanding IPSC characteristics as a result of the heterogeneous nature of the fast, $GABA_A$, synaptic inputs.

Multi-linear regression model for pyramidal cell firing rate. We believed that after observing the simulation data the IPSC characteristics might determine pyramidal cell firing rate when the external injection current to pyramidal cell kept constant during the simulation period. A multiple regression approach is used to determine the IPSC characteristics that could explain the variation in pyramidal cell excitability. The data was obtained from the simulation results of 58 different runs where GABA peak conductance ($g_{IPSC,\max}$) was varied from 0.8 to 12.4 nS for each pyramidal cell firing rate value that ranged from 0 to 8 Hz. The pyramidal cell firing rate was then taken as the dependent variable in the analysis, with the independent

variables being the IPSC characteristics for one step period of depolarizing current (1000 ms in our study; 58 runs). These independent variables were mean IPSC amplitude ($MEAN_{IPSC}$), standard deviation of IPSC (SD_{IPSC}) , variance, and the coefficient of variance of IPSC (CV_{IPSC} =SD/Mean). The inter-correlation of all variables (17 variables including charge transfer-area under the IPSC curve, mean conductance of IPSC, standard deviation of IPSC conductance, variance of conductance, delay time constant, interneuron firing rate, and synaptic input rate among them) was tested and used to avoid multicollinearity of the input variables. Next the regression analysis was performed stepwise to select the salient variables in the multiple regression model. We used forward stepwise regression. At each step it added the most statistically significant term (the one with the highest F statistic or lowest p-value) until there was none left.

Finally two multiple regression models were developed chosen from 17 variables that represent IPSC characteristics. In the first model, only the IPSC parameters were used to investigate how much of the variability could be explained by them. This model is shown as Eqn. 11 with

$$Firing\ rate = 12.8809 + 0.548716 * MEAN_{IPSC} + 0.0014048 * VAR_{IPSC} \qquad (11)$$

where $\boldsymbol{MEAN}_{\mathrm{IPSC}}$, $\boldsymbol{VAR}_{\mathrm{IPSC}}$ are the mean and variance of IPSC. In this model, only the IPSC parameters were used to see how much these variables can explain the variability in firing rates. This model yielded an adjusted R^2 value of 0.793, thus accounting for 79% of the variability in the pyramidal cell firing rates. The F statistic of about 104.868 and its p-value < 0.000001 indicated that it was highly unlikely that all of the regression coefficients were zero. T-tests for $\boldsymbol{MEAN}_{\mathrm{IPSC}}$ and $\boldsymbol{VAR}_{\mathrm{IPSC}}$ were 14.0576 and 7.1400 respectively with p-value < 0.0001 for all three variables. In the second regression model, the cell conductance

parameters were also used along with IPSC parameters, to yield a prediction given by Eqn. 12,

$$Firing\ rate = 11.5734 + 0.358144 * MEAN_{IPSC} + 0.00116 * VAR_{IPSC} - 0.75869 * MEAN_{COND} \quad (12)$$

where $MEAN_{IPSC}$, VAR_{IPSC} ,and $MEAN_{COND}$ are the mean and variation of IPSC and mean of conductance. This model yielded an adjusted R^2 value of 0.94, accounting for 94% of the variability in the pyramidal cell firing rates. The F statistic of about 240.4 and its p-value < 0.0001 indicated that it was highly unlikely that all of the regression coefficients were zero. T-tests yielded values of 12.1053, 9.9197, and -10.0418, respectively with p-values < 0.0001 for all three variables. This regression model was validated using a separate test data set of 20 cases. The result showed that the model was able to interpolate and extrapolate with the same accuracy as for the training patterns.

Modulation of pyramidal cell firing rate by HCN channels – second hypothesis

A second possible explanation for the increase in excitability mediated by clonidine was that alpha 2 agonists block IH (HCN) currents in the pyramidal cell. No IH channels are present in the interneuron model for this case.

Voltage clamp studies done by Lavin's group demonstrated that clonidine inhibited a hyperplarizaton activated inward current with similar characteristics to the current sensitive to the HCN channel blocker ZD7288. By increasing R_{in}, inhibition of HCN channels enhanced the amplitude and duration of the response to a burst of excitatory synaptic input.

Deactivation of HCN channels by distal EPSPs result in a snet outward current that opposes subsequent EPSPs, resulting in sublinear summation of EPSP trains. According to Dr.Lavin, inhibition of these channels prevents this sublinear summation and increases the probability that a train of excitatory input will bring the neuron to pike threshold. By increasing Rin , inhibition of HCN channels enhances the amplitude and duration of the response to a burst of excitatory synaptic input.

The role of Kir channel remains the same as its main role was to hyperpolarize the membrane potential initially. The result is shown in figure 6E. The conductance was 0 nS for clonidine and 8.4 nS for control respectively.

DISCUSSION

A computational model of a single pyramidal cell connected to a single fast spiking interneuron was used to study the mechanism of action of clonidine, an in particular two hypothesis. The predictions compared well with in-vitro experimental data, including the transient depression of membrane potential with application of clonidine. The first hypothesis on the mechanism of action was that the increase in excitability of the pyramidal cell occurs via a decrease in GABAergic inhibition on the cell by the interneuron. A systematic study of this hypothesis forms the main part of the paper. In the process, we developed a general methodology for studying the effect of IPSCs on the excitability of a cell, with applicability to any cell type with IPSCs. This was done by systematically varying the IPSC characteristics of mean and standard deviation, an indirect means of modeling the diversity of GABA-ergic inputs to a cell.

For the pyramidal cell studied, Ca^{2+} and K^{+}, including the K_{ir} channel, were found to have little effect on modulation of excitability. It is known that an increased variance in the conductance or decay of IPSCs could modulate the firing rate of the postsynaptic cell. However, since GABAergic synaptic inputs to principal cells are heterogeneous in terms of their anatomical , molecular and physiological properties, underlying mechanisms (eg., types of interneuron, GABAa receptor composition, plasticity, desensitization, modulation, occupancy, and in transmitter concentration and uptake) are not clear. We used the reverse engineering method to study how IPSC currents modulate the excitability of a pyramidal cell. IPSC characteristics were varied systematically to generate data which was then used to generate a multiple regression relationship between IPSC characteristics and the cell firing rate. The process helped identify the important IPSC characteristics such as $\boldsymbol{MEAN}_{IPSC}$ and $\boldsymbol{SD}_{IPSC}$, and $\boldsymbol{VAR}_{IPSC}$, and also reveal how the same firing rate could be obtained with different, but non-intuitive, combinations of these characteristics. For instance, a larger IPSC area doesn't necessarily translate to a larger inhibitory effect on the postsynaptic cell. The variance around IPSC conductance plays an important role to tune the firing rate, for the same charge transfer or IPSC area. The variability in pyramidal cell firing rates could thus be explained by a few IPSC characteristics despite the possibility of significant diversity in GABA synaptic inputs. Thus, the complexities and uncertainties involved with GABA synaptic heterogeneity were simplified by focusing on IPSC characteristics as regulatory factors in the modulation of cell excitability.

In the second hypothesis we were also able to show that the excitably could have been easily modulated by blocking the I_H channel simulating the effect of an alpha 2 agonist. In

this case uncertainty was relatively small and no additional analysis was necessary as in the first hypothesis.

The study also illustrates how a computational model can be used to investigate several possible hypotheses *in silico* complementing wet lab experiments, determining possible emergent properties, and also providing new ideas for wet lab experiments.

REFERENCES

1. Andrews, H., and Lavin, A., Alpha2 noradrenergic agonist increases intrinsic excitability of prefrontal cortical pyramidal neurons in vitro. Poster at the Annual meeting of the Society for Neuroscience, 2004.
2. Aoki C, Go CG, Venkatesan C, Kurose H., Perikaryal and synaptic localization of alpha 2A-adrenergic receptor-like immunoreactivity. *Brain Res* 650 (2):18˜1204, 1994.
3. Aradi, I., Santhakumar, V., Chen, K., and Soltesz, I. Postsynaptic effects of GABAergc synaptic diversity: regulation of neuronal excitability by changes in IPSC variance. *Neuropharmacology* 43 (2002) 511-522.
4. Aradi, I., Santhakumar, V., and Soltesz, I. Impact of Heterogeneous Perisomatic IPSC Populations on Pyramidal Cell Firing Rates. *J Neurophysiology* 91: (2004) 2849-2858.
5. Arnsten AFT, Cai JX, Goldman-Rakic PS., The alpha-2 adrenergic agonist guanfacine improves memory in aged monkeys without sedative or hypotensive side effects: Evidence for alpha -2 receptor subtypes. *J Neurosci* 8:428˜74297, 1988.
6. Arnsten, A., Steere, J.C., Hunt, R.D. The contribution of alpha sub 2-noradrenergic mechanisms to prefrontal cortical cognitive function: potential significance for attention-deficit hyperactivity disorder. *Archives of General Psychiatry*, Vol. 54, pp. 448-455, 1996.
7. Arnsten, A. Catecholamine modulation of prefrontal cortical cognitive function. *Trends in Cognitive Sciences,* Vol. 2, No. 11, pp. 436-447, 1998.
8. Berridge, C. W. and B. D. Waterhouse. The locus coeruleus-noradrenergic system: modulation of behavioral state and state-dependent cognitive processes. Brain Res Brain Res Rev 42(1): 33-84.2003.
9. Bower JM, Beeman D (2003) The book of GENESIS: Exploring realistic neural models with the GEneral NEural SImulation System, Internet Edition.
10. Brown, A.M., Schwindt, P.C., and Crill, W. E. Voltage dependence and activation kinetics of pharmacologically defined components of the high-threshold calcium current in rat neocortical neurons. *J. Neurophysiol*. 70:1530-1543, 1993.
11. Brunel Nicolas and X.J. Wang. What determines the frequency of fast network oscillations with irregular neural discharges? I. synaptic dynamics and excitation-inhibition balance. *J Neurophsiol.* 90: 415-430, 2003.

12. Casey, B.J., Castellanos, F.X., Giedd, J.N. Implication of right frontostriatal circuitry in response inhibition and attention-deficit/hyperactivity disorder. *Journal of the American Academy of Child and Adolescent Psychiatry,* Vol. 36, pp. 374-383, 1997.
13. Castellanos, F.X. Toward a pathophysiology of Attention Deficit/Hyperactivity Disorder. *Clinical Pediatrics*, Vol. 36, pp. 381-393, 1997.
14. Chen K, Aradi I, Thon N, Eghbal-Ahmadi M, Baram TZ, and Soltesz I. Pesitently modified h-channels after complex febrile seizures convert the seizure-induced enhancement of inhibition to hyperexcitability. *Nat Med* 7:331 337, 2001
15. Durstewitz, D., Seamans, J.K., and Sejnowski, T.J. Dopamine-mediated stabilization of delay-period activity in a network model of prefrontal cortex. *Journal of Neurophysiology*, Vol. 83, pp. 1733-1750, 2000.
16. Fritschy, J-M. and I. Brunig. Formation and plasticity of GABAergic synapses: physiological mechanisms and pathophysiological implications. *Pharmacology & Therpeutics,* 98, 299-323, 2003.
17. Goldman-Rakic, P.S. Regional and cellular fractionation of working memory. *Proceedings of the National Academy of Science USA*, Vol. 93, pp. 13473-13480, 1996.
18. Grabov, A. and M.R. Blatt. A steep dependence of inward-rectifying potassium channels on cytosolic free calcium concentration increase evoked by hyperpolarization in guard cells. *Plant Physiology*, Vol. 119, pp. 277-287, 1999.
19. Kang, Y., Okada, T., Ohmor, H., A phenytoin-sensitive cationic current participates in gnerating afterdepolarization and burst afterdischarge in rat neocortical pyramidal cells. *Eur. J. Neurosci.* 10 1363-1375, 1998
20. Kawaguchi, Y. Groupings of nonpyramidal and pyramidal cells with specific physiological and morphological characteristics in rat frontal cortex. *J. Neurophysiol*. 69: 416-431, 1993.
21. Kitano, K., H. Cateau, K. Kaneda, A. Nambu, M. Takada, and T. Fukai. Two-state membrane potential transitions of striatal spiny neurons as evidenced by numerical simulations and electrophysiological recordings in awake monkeys. *J. Neurosci*. Vol.22. RC230, 2002.
22. Levy, F., Farrow, M. Working Memory in ADHD: Prefrontal/Parietal Connections. *Current Drug Targets*, Vol. 2, pp. 347-352, 2001.

23. Levy, F. Swanson, J.M. Timing, space and ADHD: the dopamine theory revisited. *Australian and New Zealand Journal of Psychiatry*, Vol. 35, pp. 504-511, 2001.
24. Niesenbaum, E.S. and C.J. Wilson. Potassium currents responsible for inward and outward rectification in rat neostriatal spiny projection neurons. *J. Neuroscience*, 15(6): 4449-4463.1995.
25. Wynn, P.H.T., Yang, S.Y., and Lin, S.K. Neurochemical Interaction Between Dopaminergic and Noradarenergic Neurons in the Medial Prefrontal Cortex. *Synaps.* Vol. 53, pp. 44-52, 2004.
26. Wang X.J. Calcium coding and adaptive temporal computation in cortical pyramidal neurons. *J. Neurophysiol* 79:1549-1566, 1998.
27. Warman, E.N., Durand, D. M., and Yuen, G.L.F. Reconstruction of hippocampal CA1 pyramidal cell electrophysiology by computer simulation. *J. Neurophysiol*. 71: 2033-2045, 1994
28. Wilson, F.A.W., Scalaidhe, S.P.O., and Goldman-Rakic, P.S. Functional synergism between pytative gama-aminobuttyrate-containing neurons and pyramidal neurons in prefrontal cortex. *Proc. Natl. Acad. Sci.* USA 91: 4009-4013, 1994
29. Wolf,J.A., J.T.Moyer, M.T.Lazarewicz, D.Contreras, M.Benoit-Marand, P.O'Donnell, and L.H. Finkel. NMDA/AMPA ratio impacts state transitions and entrainment to oscillations in a computational model of the nucleus accumbens medium spiny projection neuron. J.Neurosci. 25(40):9080-9095, 2005.
30. Wynn, P.H.T., Yang, S.Y., and Lin, S.K. "Neurochemical Interaction B etween Dopaminergic and Noradarenergic Neurons in the Medial Prefrontal Cortex." *Synapse,* Vol. 53, pp. 44-52, 2004.

Tables and Figures

Table 1. Maximal conductances (in mS/cm^2) and compartment dimensions (in µm)

	Maximal conductance densities (mS/cm^2)	Compartment dimensions (µm)
Basic Properties	$R_M = 65000$ Ohm/cm^2; $Ra = 1800$ Ohm cm *c_bdend=1.2 * 1.92 mu F/cm^2* *c_soma=1.2 mu F/cm^2* *c_pdend=1.2 * 1.92 mu F/cm^2* *c_ddend=1.2 * 1.92 mu F/cm^2*	
Basal	$g_{Na} = 36.4$; $g_{NaP} = 1.0$ $g_{DR} = 9.2$; $g_{KS} = 0.24$; $g_{IR} = 0.4$; $g_{HVA} = 0.67$; $g_{Cat} = 0.01$; $g_C = 3.8$; $g_{AHP} = 0.02$	$d = 16.0$; $l = 150$
Soma	$g_{Na} = 111.8$; $g_{NaP} = 2.2$; $g_{DR} = 33.8$; $g_{KS} = 0.14$; $g_H = 5(Control)$; $g_{HVA} = 0.323$; $g_{Cat} = 5.0$; $g_C = 2.2$; $g_{AHP} = 0.02$	dendrite: $d = 23$; $l = 23$
Proximal	$g_{Na} = 36.4$; $g_{NaP} = 1.0$; $g_{DR} = 9.2$ $g_{KS} = 0.24$; $g_{IR} = 0.4$; $g_{HVA} = 0.67$ $g_{Cat} = 0.01$; $g_C = 3.8$; $g_{AHP} = 2$	$d = 2.6$ $l = 400$
Distal	$g_{Na} = 36.4$; $g_{NaP} = 1.0$; $g_{DR} = 9.2$ $g_{KS} = 0.24$; $g_{IR} = 0.4$; $g_{HVA} = 0.323$ $g_{Cat} = 0.01$; $g_C = 2.2$; $g_{AHP} = 0.02$	$d = 2.6$ $l = 400$
Interneuron	$Rm = 100000.0$ Ohm/cm^2 $Ra = 150.0$ Ohm cm *c_soma=2.2 mu F/cm^2* *c_dend=3.8 mu F/cm^2*	
Soma	$g_{Na} = 100.0$; $g_{DR} = 40.0$;; $g_{IR} = 0.4$ $g_{HVA} = 0.323$; $g_C = 2.2$	soma: $d = 15$; $l = 15$
Dendrite	$g_{Na} = 20.0$; ; $g_{DR} = 8.0$;; $g_{IR} = 0.4$ $g_{HVA} = 0.323$; $g_{Cat} = 0.01$; $g_C = 3.8$	dendrite: $d = 10$; $l = 150$
Synaptic currents		
AMPA	$g_{AMPA} = 15.1392$ $\tau_{RISE} = 0.55$ $\tau_{DECAY} = 2.2$	
GABA	$g_{NMDA} = 0.0912$ $\tau_{RISE} = 10.6$ $\tau_{DECAY} = 285.0$	
NMDA	$g_{GABA} = 8.4$ $\tau_{RISE} = 1.5$ $\tau_{DECAY} = 2.5$	

Rate functions, steady states and time constants of the pyramidal cell model

$$\alpha_m = \frac{-0.2816(V+28)}{\exp(-(V+28)/9.3)-1}$$

$$\beta_m = \frac{0.2464(V+1)}{\exp((V+1)/6)-1}$$

$$\alpha_h = 0.098 \times \exp(-(V+43.1)/20)$$

$$\beta_h = \frac{1.4}{\exp(-(V+13.1)/10)+1}$$

$$\alpha_n = \frac{-0.018(V-13)}{\exp(-(V-13)/25)-1}$$

$$\beta_n = \frac{0.0054(V-23)}{\exp((V-23)/12)-1}$$

$$\alpha_c = \frac{-0.00642V_m - 0.1152}{\exp(-(V_m+18)/12)-1}$$

$$\beta_c = 1.7 \times \exp(-(V_m+152)/30)$$

$$V_m = V + 40\log_{10}([Ca]_{i1})$$

$$\tau_c = \max(1/(\alpha_c+\beta_c), 1.1)$$

$$\alpha_q = \frac{0.0048}{\exp(-(10\log[Ca^{2+}]_{i2}-35)/2)}$$

$$\beta_q = \frac{0.012}{\exp((10\log[Ca^{2+}]_{i2}+100)/5)}$$

$$\tau_q = 48 \text{ ms}$$

$$a_\infty = \frac{1}{\exp(-(V+34)/6.5)-1}$$

$$\tau_a = 6.0 \text{ ms}$$

$$b_\infty = \frac{1}{\exp((V+65)/6.6)+1}$$

$$\tau_b = 200 + \frac{3200}{\exp(-(V+63.6)/4)+1}$$

$$u_\infty = \frac{1}{\exp(-(V+24.6)/11.3)+1}$$

$$\tau_u = 1.25 \times \sec h(-0.031(V+37.1))$$

$$v_\infty = \frac{1}{\exp((V+12.6)/18.9)+1}$$

$$\tau_v = 420.0 \text{ ms}$$

$$h_\infty = 1/(1+\exp^{((V-75)/5.5)})$$

Rate functions of the Gabaergic interneuron model

$$\alpha_m = 4.2 \times \exp((V + 34.5)/11.57)$$
$$\beta_m = 4.2 \times \exp(-(V + 34.5)/27)$$
$$\alpha_h = 0.09 \times \exp(-(V + 45)/33)$$
$$\beta_h = 0.09 \times \exp((V + 45)/12.2)$$
$$\alpha_n = 0.3 \times \exp((V + 35)/10.67)$$
$$\beta_n = 0.3 \times \exp(-(V + 35)/42.68)$$
$$\alpha_c = \frac{-0.00642V_m - 0.1152}{\exp(-(V_m + 18)/12) - 1}$$
$$\beta_c = 1.7 \times \exp(-(V_m + 152)/30)$$
$$V_m = V + 40\log_{10}([Ca]_{i1})$$
$$\tau_c = \max(1/(\alpha_c + \beta_c), 1.1)$$
$$u_\infty = \frac{1}{\exp(-(V + 24.6)/11.3) + 1}$$
$$\tau_u = 1.25 \times \sec h(-0.031(V + 37.1))$$
$$v_\infty = \frac{1}{\exp((V + 12.6)/18.9) + 1}$$

Table 2. IPSC characteristics for four different peak conductances yielding same PC firing rate from 1000 ms runs (Case 2)

PC rate (Hz)	Peak Conductanc (nS)	Decay constan (ms)	Charge Transfer (fq)	Mean Amplitude (pA)	Minimum Amplitude (pA)	SD	CV abs ((SD/Mean))	IPSC frequenc (Hz)	Mean conductance (nS)	IN Firing Rate (Hz)
4	12.4	2.5	-20903	-19.003	-703.16	48.32	2.5	40	2.68	44
4	8.4	2.5	-15350	-13.954	-167.42	26.2	1.87	44	1.848	44
4	4.4	2.5	-15384	-13.9856	-216.719	21.73	1.55	68	1.503	67
4	1.4	2.5	-14710	-13.373	-284.23	16.52	1.24	145	1.3849	155

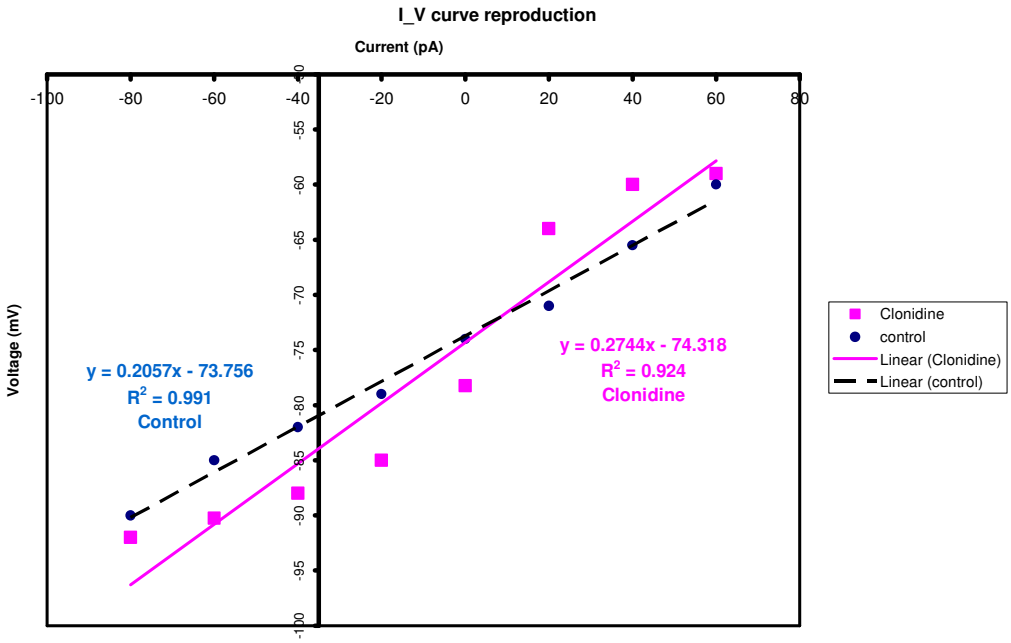

Figure 1: Input resistance for PFC pyramidal cell with current injection, Clonidine vs. control. The application of Clonidine to a subset of total cells did not produce significant changes in input resistance.

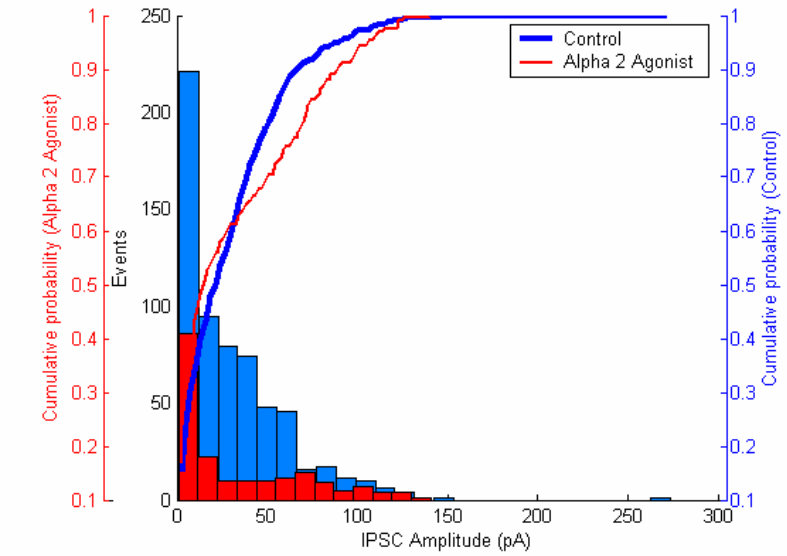

Figure 2. IPSC histograms and cumulative probability plots for both control and alpha 2 agonist cases obtained from model predictions, using hypothesis 1. Smaller events of low IPSC amplitudes were seen during the activation of alpha-2 agonist as a result of increased GABAergic synaptic input.

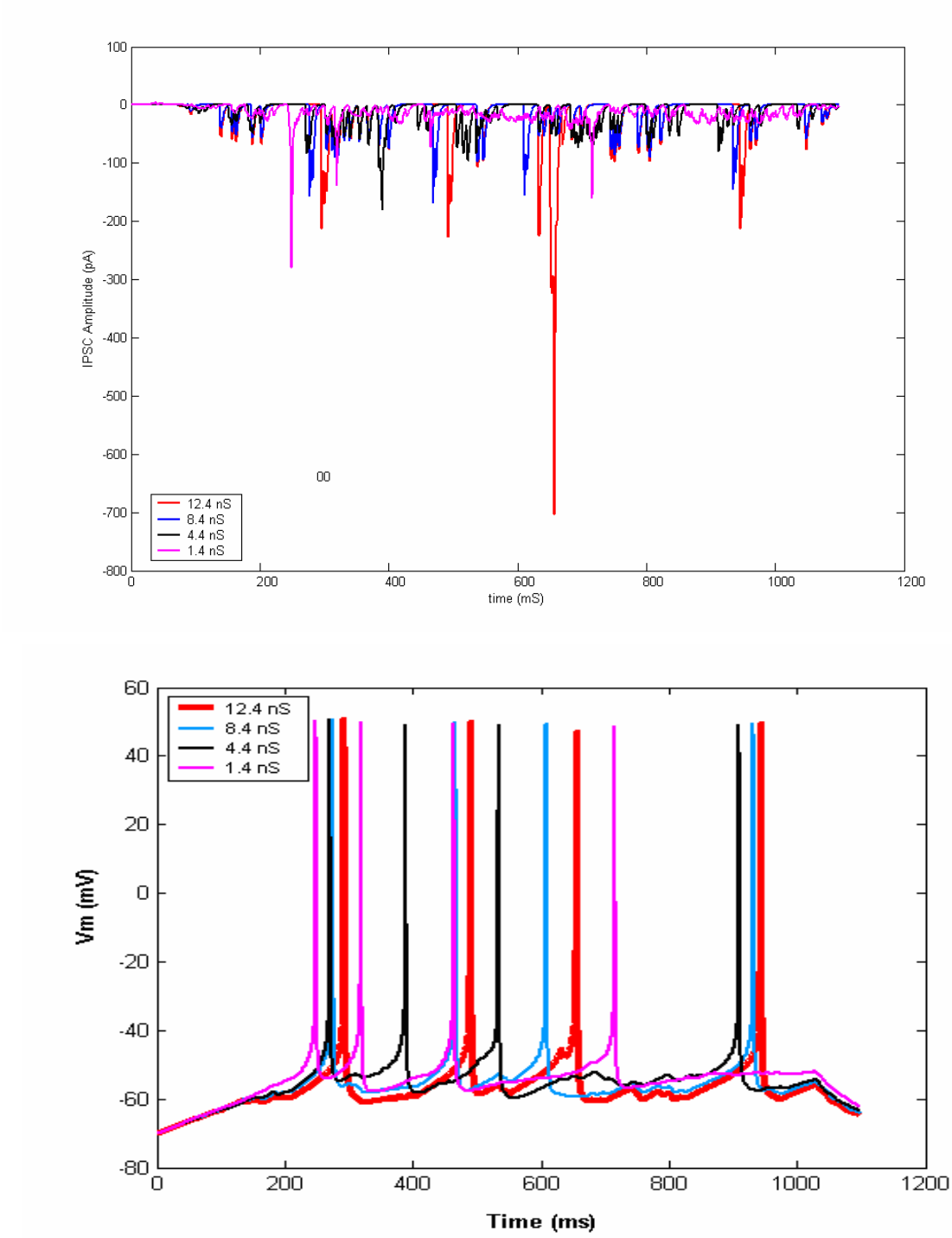

Figure 3. Top: IPSC for four different G peak conductances yielding same PC firing rate of 4 spikes; Bottom: Pyramidal traces plot for four different G peak conductances yielding same PC firing rate of 4 spikes.

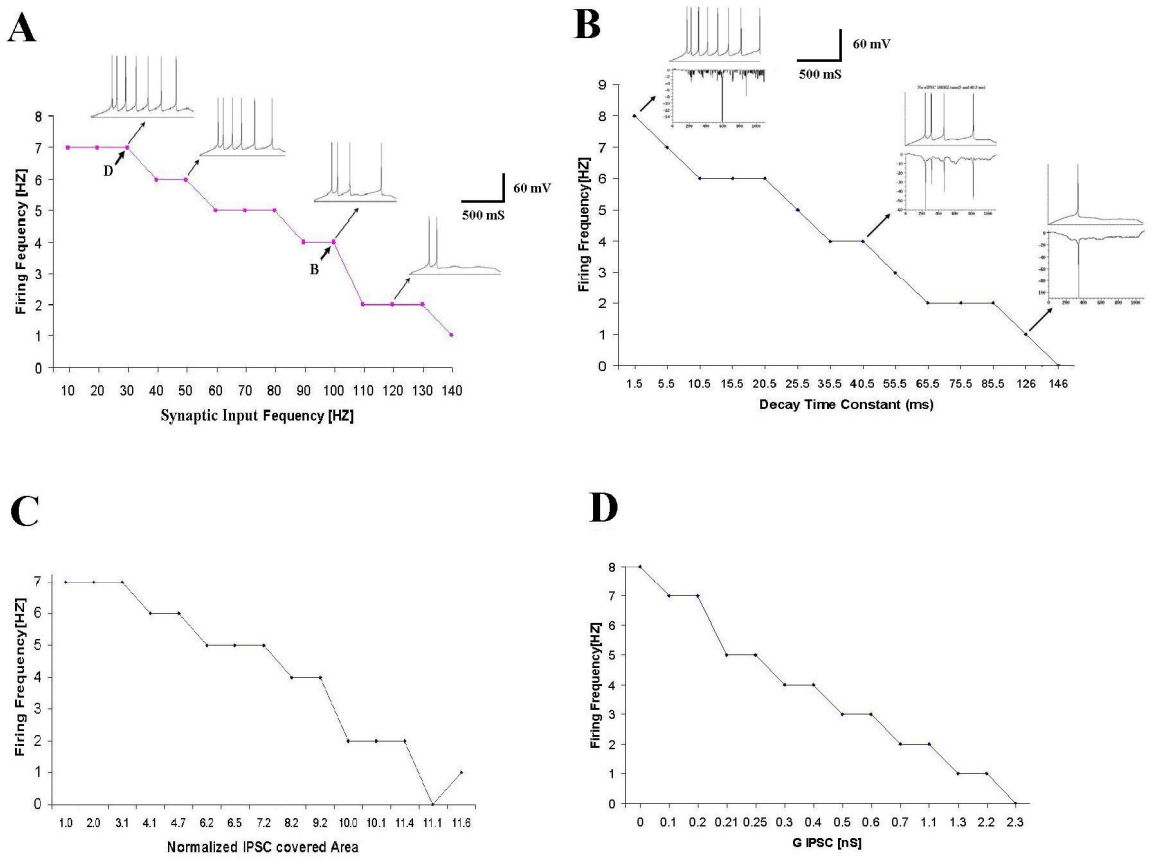

Figure 4. Direct modulation of IPSCs seen by the pyramidal cell, without the interneuron present.

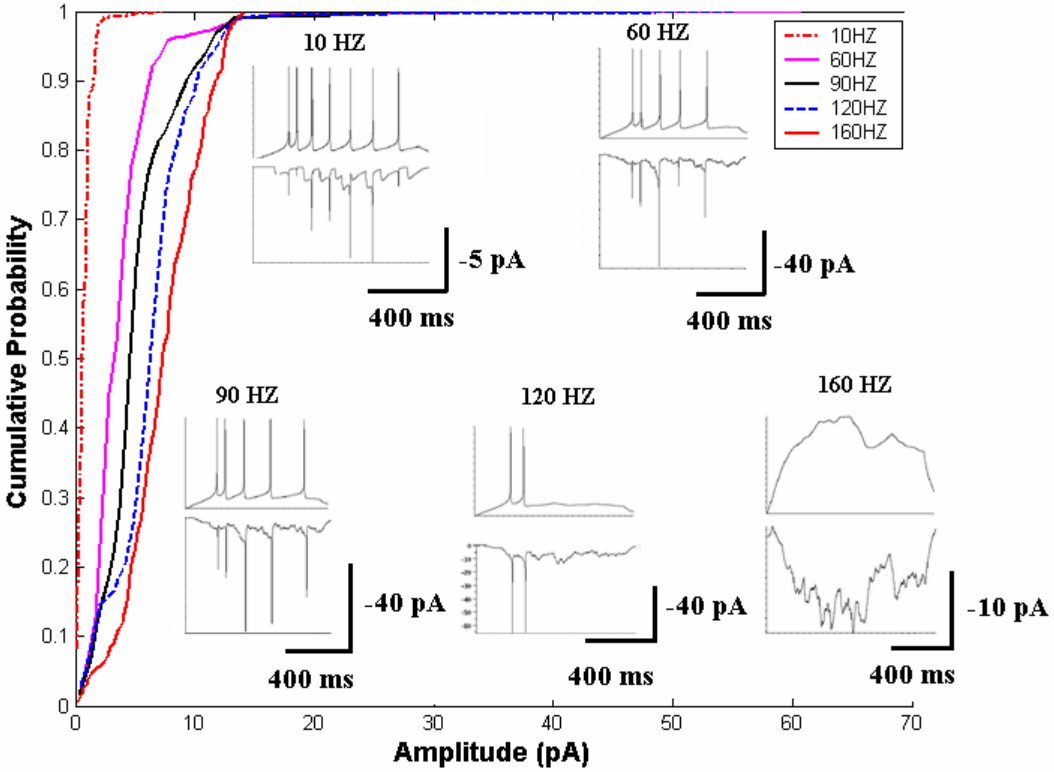

Figure 5. Cumulative probability plots at different synaptic input rates and pyramidal cell firing plots along with IPSC traces obtained from the simulation studies.

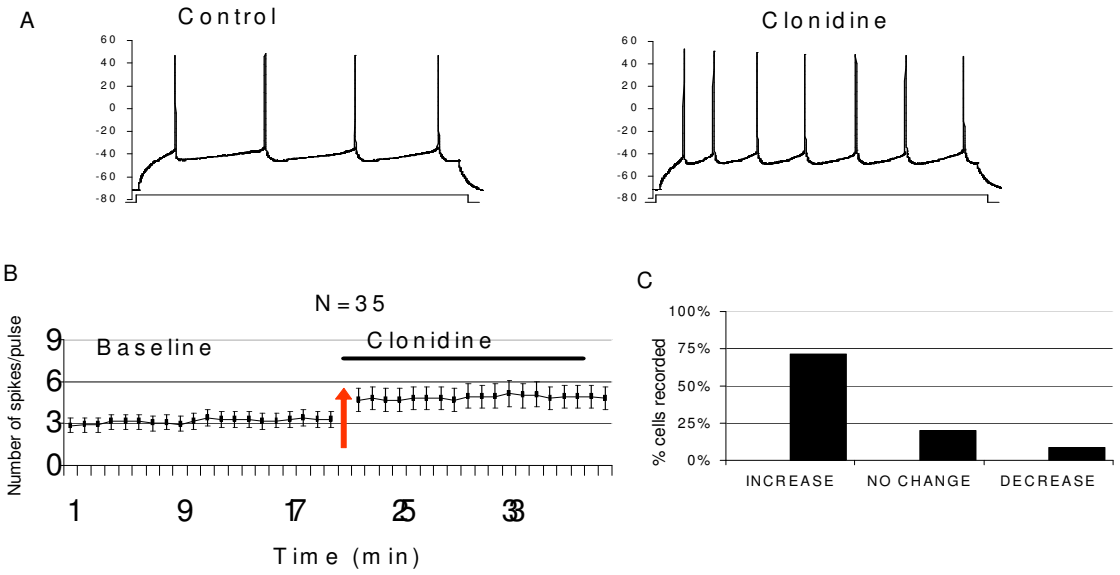

D. Traces of model predictions (control and after clonidine administration) during a single depolarizing period of 15 pA

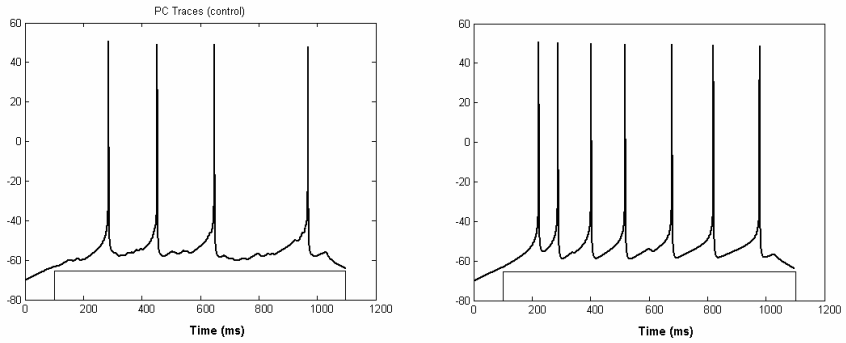

E. Traces of model predictions (control and after clonidine administration) during a single depolarizing period of 15 pA by blocking IH channel

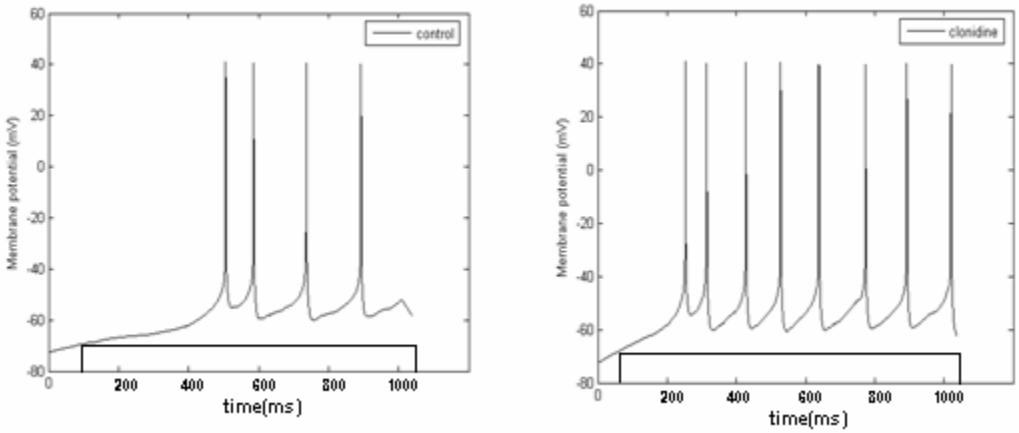

Figure 6. Comparison of model predictions and experiments for effects of the α-2 agonist clonidine on pyramidal cells, using hypothesis 2. A) EXPTL- Representative traces of intrinsic excitability in control and clonidine cases. B) EXPTL - Histogram shows the average increase in intrinsic excitability produced by clonidine administration (10 μM) to the population of pyramidal cells sampled (n=35). C) EXPTL - Bar graph indicates the percentage of cells that exhibited significant increases, no changes or significant decreases following clonidine administration. The arrow indicates clonidine administration. In this figure, the data are presented as mean ± SE. The current trace represents 500 pA. D) MODEL –First hypothesis: Traces of simulated single pyramidal cell model (control and after clonidine administration) during a single depolarizing period of 15pA with peak IPSC conductance of 6.5 nS and a decay time of 2.5 ms (***Case 2***). E) MODEL – Second hypothesis: Traces of simulated single pyramidal cell model (control and after clonidine administration). Clonidine blocks IH channel and the excitability of pyramidal cell is increased.

CHAPTER 3

Computational model of the baroreflex arc, Nucleus tractus solitarius – Cellular models

Abstract.

The behavior of individual baroreceptors and nucleus tractus solitari (NTS) neurons is studied to understand their role in the autonomic circuit controlling systemic blood pressure. The electrical properties of these cells are characterized with particular focus on the role of potassium channels in modulating membrane potential. The computational model predictions matched experimental membrane potential traces for such cells reported in the literature.

Introduction

Cardiovascular homeostasis involves complex interactions among key organs such as heart, blood vessels and the kidney, which are under the control of autonomic circuits in the brain. Recent findings have indicated that alterations in autonomic brainstem circuits contribute to the development of cardiovascular disease, including hypertension and congestive heart failure. A better understanding of how the brain processes neural signals may provide new avenues for the therapeutic treatment of both neurological disorders, such as Alzhiemers disease, as well as cardiovascular diseases which impacts millions of Americans annually. The overall goal of the project is to develop a predictive model of the arterial baroreceptor reflex is developed to identify the precise mechanisms

underlying “information transfer” by the autonomic barosensitive circuit, including pathology leading to these disorders.

The arterial baroreceptor reflex is the essential controller for short-term and longer-term changes in systemic blood pressure. Primary baroreceptor afferents project to the nucleus tractus solitarius (NTS) and synapse onto a complex system of network interneurons. In the mammalian brain, the NTS contains 600 – 900 barosensitive neurons that contain either excitatory or inhibitory neurotransmitters. Some of these neurons receive input from primary baroreceptor afferents (second order cells), some project to target nuclei which generate autonomic motor command signals (output neurons), while the remainders are network interneuons which form reciprocal synaptic contacts with other NTS neurons. Currently, we do not have the electrophysiological tools to study a large number of barosensitive neurons simultaneously or to predict network behavior. Therefore, it is essential to establish a network based model of barosensitive circuits that could then be used to guide new experimentation into the mechanisms involved in information transfer in the NTS. Currently, there are a very limited number of computational models for barosensitive circuits and these have focused exclusively on the intrinsic properties of second order neurons and their synaptically evoked responses.

Single cell models of barosensitive second order NTS neurons have previously been reported (Schild et al., 1993; Schwaber et al., 1993; Rogers et al., 2000). These models are based on a typical, one-compartment neuron of the Hodgkin-Huxley type consisting of a membrane capacitance shunted by time- and voltage-dependent ion-selective channels, in addition to ion pumps, exchangers and other background currents. These models have been successful in simulating several of the intrinsic properties and synaptic

responses of second order barosensitive neurons. However, they have failed to include network and output neurons in their models. Moreover, there is a virtual absence of information regarding the intrinsic and synaptic properties of network and output neurons. This has resulted in a significant gap in our understanding the role of NTS neurons in baroreceptor neurotransmission. This application will provide a complete network model of neural circuits responsible for processing and transmitting baroreceptor signals in the NTS.

The medial NTS is the first relay site in the baroreceptor pathway and receives substantial afferent input on a second-to-second basis. Information transfer between primary baroreceptor afferents and second order NTS cells has been extensively examined. Of these studies, it has been shown that the second order neuron acts as a low-frequency filter limiting its degree of excitation. Consequently, there is a paucity of NTS cells which exhibit pulse-synchronous discharges in relation to baroreceptor discharge. While the NTS is a heterogeneous population of neurons that encode a variety of sensory inputs, their cellular properties may be segregated by cell morphology.

Changes in ionic conductance can alter the action potential discharge pattern of neurons and its associated network. Potassium (K+) channels are vital for information transfer in the nervous system because of their ability to set the resting membrane potential (RMP), control action potential duration, terminate periods of activity, and time the interspike intervals during repetitive firing. The contribution of these channels to neuronal activity depends not only on the current subtype (i.e., voltage or calcium-dependent, etc.), but also on where the channels are expressed. Second-order cells can be characterized as receiving either A- or C-type baroreceptor inputs based on the presence

or absence of A-type K+ currents. The presence of an A-type current significantly modulates the firing properties of NTS neurons. For instance, removing inactivation of these channels significantly increases the delay of action potential firing; a property termed “delayed excitation”. Calcium entry during a spike can induce calcium-activated K currents (I_{KCa}), which are known to modulate action potential/post-burst afterhyperpolarization as well as spike frequency adaptation. The importance of these currents in the NTS (cells and network) has recently been modeled and suggests I_{KCa} has a significant impact on network activity

The importance of understanding the role a particular ion channel plays in cardiovascular disease in underlined by the increasing number of identified channelopathies. For instance, mutations in the potassium channel gene Kv1.1 are associated with human episodic ataxia type 1 (EA-1) syndrome characterized by continuous myokymia, exercise, and stress-induced episodic attacks of ataxia, spastic contractions of skeletal muscles, and partial epilepsy (Zuberi et al., 1999; Benatar, 2000). The association of ataxic episodes with exercise or emotional stress suggests a prominent role for the autonomic nervous system, including the NTS. Previously, we have demonstrated in mice deletion of this K+ subunit significantly alters sensory fiber discharge and neurotransmitter release in the NTS.

This paper reports computational biophysical models for baroreceptor and NTS cell types and comparison of their predictions with experimental data. Using the single cell models, one of the objectives is to determine whether spike frequency adaptation is mediated by a pre- or post-synaptic mechanism. Spike frequency adaptation is a

recognized property of most NTS neurons. However, the precise mechanism has not been established.

The details pertaining to the model are listed in the next section 'Methods'.

Methods

Baroreceptor afferent model: We have completed the development of preliminary models for A- and C-type baroreceptors based on the structure reported in Durstwitz et al (2000), Schilds et al (1994) and Rogers et al. (2000).

Ionic currents. The biophysical models for currents were taken from the pyramidal cell model used in Chapter 2. : leakage current (I_L), a fast, spike-generating Na^+ current (I_{Na}), the delayed rectifier potassium current (I_{DR}), and persistent current (I_{NaP}) were from Durstewitz et al. (2000); the high-voltage activated Ca^{2+} current (I_{HVA}) from Brown et al. (1993); slow inactivating K current (I_{KS}) and a fast BK Ca and voltage-dependent C-type K current (I_C) were from Wang (1993); I_{AHP} from Warman et al. (1994); I_{IR} from Niesenbaum and Wilson (1995) and modified by the authors to account for the intracellular Ca^{2+} concentration; and the Ca^{2+} dependent cationic current (I_{CAT})from Kang et al. The details of all channel characteristics are listed in the previous chapter.

The passive properties and the maximal conductance of channels of the A and C type baroreceptors were tuned to match the experimental data such as resting potential (V_{rest}). In addition, the baroreceptors reproduced the basic properties of spiking behavior of these neurons (Fig. 1-4).

A type nodose show faster and more repetitive action potential dynamics.

Current injections into the soma of A type nodose model elicited repetitive spikes at a relatively low activation threshold (-50mV).

C type nodose neurons exhibit slower and more complicated action-potential dynamics with a distinct "hump" during repolarization. To account this characteristic dynamics the maximal conductance of transient sodium current I_{NaP} were set at 55% of the maximum conductance used in Durstewitz et al (2000) while membrane capacity was set at 70 $\mu F / cm^2$. Threshold for firing is slightly higher in the C type cell than the A type cell and in the presence of a strong depolarizing stimulus neither C types cells nor the model fired repetitively while the C type model elicits only a single action potential.

In the presence of identical step depolarization from rest membrane potential , the A type nodose model fires repetitively. All other parameters are listed in the table 1-2.

Single NTS cell model

The single cell neuron model has six ion channels. The expression used for conductances of these channels (g_i), their steady state values ($m_{\infty i}$ and $h_{\infty i}$) and time constants (τ_{mi} and τ_{hi}) are listed in Table 1.

As representative examples of the six currents modeled, we list the mathematical expressions for two currents here, the fast sodium and calcium-activated potassium currents. The sodium current is modeled using the standard Hodgkin-Huxley equation, Eqn. 1,

$$I_{Na} = g_{Na} m^3 h (V - E_{Na}) \qquad (1)$$

where V is the membrane potential, maximum conductance g_{Na} = 3 μS; reversal potential E_{Na} = 55 mV (Rogers 2000). Similarly, a representative calcium-activated current is the potassium AHP current $I_{K,Ca}$, which is modeled as Eqn. 2,

$$I_{K,Ca} = g_{K,Ca} q^2 (V - E_K) \tag{2}$$

where, again, V is the membrane potential, maximum conductance $g_{K,Ca}$ = 0.15 μS; reversal potential E_K = -94 mV. The kinetic equation for each of the gating variable x in the various current equations, e.g., m, h in Eqn. 1 and q in Eqn. 2, take the form

$$\frac{dx}{dt} = \frac{x_\infty(V,[Ca^{2+}]_i) - x}{\tau_x(V,[Ca^{2+}]_i)} \tag{3}$$

where $[Ca^{2+}]_i$ is the intracellular Ca^{2+} concentration, x_∞ is the voltage- (or Ca^{2+}) dependent steady state and τ_x is a voltage- (or Ca^{2+}-) dependent time constant. The expressions for x_∞ and τ_x for the gating variables are given in terms of the rate functions, α_x and β_x

$$x_\infty = \alpha_x / (\alpha_x + \beta_x) \tag{4a}$$

$$\tau_x = 1/(\alpha_x + \beta_x) \tag{4b}$$

For the sodium current, I_{Na}, the rate functions are

$\alpha_m = 0.91(V+38)/(1-\exp(-(V+38)/5))$, $\beta_m = 0.062(V+38)/\exp((V+38)/5) - 1$,

$\alpha_h = 0.016\exp(-(V+55)/15)$, $\beta_h = 2.07/(1+\exp(\text{-}(\text{v} - 17)/21))$. For the calcium-dependent potassium current, $I_{K,Ca}$, q_∞ is given directly as

$q_\infty = 1.25e8 * [Ca_i^{2+}]^2 (1.25e8 * [Ca_i^{2+}]^2 + 2.5)$ and $\tau_q = 1000/(1.25e8 * [Ca_i^{2+}]^2 + 2.5)$.

Concentration of the calcium pool inside the cell, $[Ca_i^{2+}]$, is modeled using a first order

equation, assuming the external concentration to be constant, with details omitted here due to space considerations.

GABAergic interneuron model:

A basket-type fast spiking (FS) neocortical aspiny interneuron was implemented based on a description by Durstewitz (2000). Passive membrane properties were as follows: the membrane capacity was set at 6 and 8 $\mu F / cm^2$ for dendrite and soma respectively. Membrane resistance and cytoplasmatic receptivity were 90 $k\Omega \cdot cm^2$ and 150 $\Omega \cdot cm$. The leakage current (I_L), a fast, spike-generating Na^+ current (I_{Na}), the delayed rectifier potassium current (I_{DR}) were from Durstewitz et al. (2000); the high-voltage activated Ca^{2+} current (I_{HVA}) from Brown et al. (1993); slow inactivating K current (I_{KS}) and a fast BK Ca and voltage-dependent C-type K current (I_C) were from Wang (1993); I_{IR} from Niesenbaum and Wilson (1995); and the Ca^{2+} dependent cationic current (I_{CAT})from Kang et al. The ionic currents and maximum conductance for each channel are summarized in Table 2.

The GABAergic interneuron was then tuned to trigger action potentials when it receives synaptic inputs through AMPA and NMDA. AMPA-like synaptic currents were modeled by a double exponential function as described by Durstewitz. AMPA and NMDA synapses then were placed in the dendrite compartment only while GABA synapse was placed in soma only. The values for these synapses were summarized in Table 2.

Modeling sysnaptic currents: EPSCs and IPSC

AMPA-like synaptic and NMDA currents were modeled by a double exponential function as in Durstwitz (2000). Random background synaptic activity is provided to GABAergic cells. IPSC due to GABA is modeled as

$$I_{IPSC}(V,t) = g_{IPSC}(t)(V - E_{gaba,}), \tag{7}$$

where the time course of the synaptic conductance is:

$$g_{IPSC}(t) = A \bullet (g_{IPSC,\max}/(\tau_{rise} - \tau_{decay})) \bullet (\exp(-t/\tau_{decay}) - \exp(-t/\tau_{rise})) \quad \text{for } \tau_1 > \tau_2, \tag{8}$$

where A is a normalization constant chosen so that g_{syn} reaches a maximum value of $g_{IPSC,\max}$.

$$A = -1/((\tau_{rise}/\tau_{decay})^{\tau decay/(\tau decay - \tau rise)} - (\tau_{rise}/\tau_{decay})^{\tau rise/(\tau decay - \tau rise)}) \tag{9}$$

Background excitatory synaptic inputs were placed on all dendritic compartments of interneurons, while inhibitory inputs are limited to the soma where cortical pyramidal cells receive most of their inhibitory input.

$I_{Na}, I_{DR}, I_{CAT}, I_{NaP}, I_{HVA}, I_{KS}, I_C, I_{AHP}$, and I_{Leak} were placed in the somatic compartment of the A and C-type baroreceptors. $I_{Na}, I_{DR}, I_{HVA}, I_C$, and I_{Leak} were placed on both soma and dendrite compartment of the interneuron. I_{GABA_A} I_{AMPA} and I_{NMDA} were placed in the somatic compartment of the baroreceptor and NTS nodose neuron while for interneuron I_{AMPA} and I_{NMDA} were placed in a dendrite compartment and I_{GABA_A} in a soma (Durstweitz et al. 2000).

Results

Single cell baroreceptors The membrane potential spike dynamics for the A-Type nodose model with a 2-ms current pulse of 400 pA is shown in Figure 1. The model is capable to reproducing the rapid dynamic characteristic of A-type nodose neurons. Such neurons

exhibit relatively low activation threshold (-50 mV) and resting potential (-59 mV) and fire repetitively in response to a step depolarization with a current injection of 40 pA as seen in Figure 2.

Our C-Type nodose neuron model required a 2-ms current pulse of 860 pA. This value is higher than the value of 450 pA used by Schilds et al. (2000) but still within the experimental range (400 ~ 900 pA). The model is capable of reproducing the slower and more complicated action-potential dynamics with a distinct "hump" during repolarization (Fig.3). C-type nodose neurons do not fire repetitively in the model, in the presence of a step depolarization with a current injection of 60 pA for a period of 1000 ms (Fig 4.). This agrees well with experimental and simulation results obtained by Schilds (2000).

Coding the pressure signal using A-type baroreceptors. We report a technique to model the pressure thresholds of the individual A-type baroreceptors by tuning the membrane capacitance of each neuron, *Cm* from 5 to 70 *pF*. The baroreceptor with the smallest Cm has the highest sensitivity to arterial pressure waveform firing action potentials repetitively with higher frequency. This technique works well for our case as shown in Figures 5 which shows the responses of the five baroreceptors of type-A with different input thresholds simulating arterial pressure thresholds. The arterial pressure frequency oscillations were mimicked by injecting a 3500ms-long, 5-Hz sinusoidal function $I_0 + A_0 \bullet (\sin(2\pi \cdot f \cdot t))$ where f=5 HZ and A_0 =*20 pA*. I_0 was gradually increased from 0 until the maximum injected current reached 85 pA. The generation of baroreceptor spikes is adaptive and contains a *dP/dt* sensitivity, as real baroreceptors do.

The response of C-type baroreceptors to a pressure signal is shown in Fig 6.

NTS neuron model. Figures 7 and 8 show the membrane potential predictions for NTS neuron and experimental data, for different depolarizing step inputs ranging from 40 to 200 pA. The NTS neuron is capable of reproducing the spike frequency for different step depolarization currents.

Discussion

Our study successfully reproduced the dynamic behaviors of A and C type baroreceptors and NTS neurons. In particular a methodology was developed to successfully replicate the coding of pressure signal by A-type baroreceptors.

The role of potassium (K+) channels in this process needs to be studied systematically since they set the resting membrane potential, control action potential duration, terminate periods of activity, and time interspike intervals during repetitive firing, all of which are vital to information transfer in the nervous system. This part will be completed later.

References

Durstewitz, D., Seamans, J.K., and Sejnowski, T.J. Dopamine-mediated stabilization of delay-period activity in a network model of prefrontal cortex. *Journal of Neurophysiology*, Vol. 83, pp. 1733-1750, 2000.

Hutcheon B, Miura RM, Puil E (1996) Models of subthreshold membrane resonance in neurocortical neurons, Journal of Neurophysiology 76(2):698-714.

Goaillard JM, Marder E. Dynamic clamp analyses of cardiac, endocrine, and neural function. Physiology (Bethesda). 2006 Jun;21:197-207.

Kang, Y., Okada, T., Ohmor, H., A phenytoin-sensitive cationic current participates in gnerating afterdepolarization and burst afterdischarge in rat neocortical pyramidal cells. *Eur. J. Neurosci.* 10 1363-1375, 1998

Kawaguchi, Y. Groupings of nonpyramidal and pyramidal cells with specific physiological and morphological characteristics in rat frontal cortex. *J. Neurophysiol*. 69: 416-431, 1993.

Kitano H (2002) Computational systems biology, Nature 420:206-210.

Koch C, Segev I (2001) Methods in Neuronal Modeling- From Ions to Networks, The MIT Press.

Kubo T, Kihara M (1988) Evidence for gamma-aminobutyric acid receptor-mediated modulation of the aortic baroreceptor reflex in the nucleus tractus solitarius of the rat. Neurosci Lett 89:156-160.

Kubo T, Kihara M (1987) Evidence for the presence of GABAergic and glycine-like systems responsible for cardiovascular control in the nucleus tractus solitarius of the rat. Neurosci Lett 74:331-336.

Kumada M, Terui N, Kuwaki T (1990) Arterial baroreceptor refles: its central and peripheral neural mechanisms. pp 331-361.

Leblois A, Boraud T, Meissner W, Bergman H, Hansel D (2006) Competition between Feedback Loops Underlies Pathological Dynamics in the Basal Ganglia, Journal of Neuroscience 26(13):3567-3583.

Lien CC, Jonas P. (2003) Kv3 potassium conductance is necessary and kinetically optimized for high-frequency action potential generation in hippocampal interneurons.

J Neurosci. 23(6):2058-68

Manuel M, Meunier C, Donnet M, Zytnicki D. (2005How much afterhyperpolarization conductance is recruited by an action potential? A dynamic-clamp study in cat lumbar motoneurons. J Neurosci. Sep 28;25(39):8917-23.

Miura M, Okada J, Takayama K, Jingu H (1996) Barosensitive and chemosensitive neurons in the rat medulla: a double labeling study with c-Fos/glutamate, GAD, PNMT and calbindin. J Auton Nerv Sys 61:17-25.

Rogers RF, Rybak IA, Schwaber JS (2000) Computational modeling of the baroreflex arc: nucleus tractus solitarius. Brain Res Bull 51:139-150.

Schild JH, Clark JW, Canavier CC, Kunze DL, Andresen MC (1995) Afferent synaptic drive of rat medial nucleus tractus solitarius neurons: dynamic simulation of graded vesicular mobilization, release, and non-NMDA receptor kinetics. J Neurophysiol 74:1529-1548.

Schild JH, Clark JW, Hay M, Mendelowitz D, Andresen MC, Kunze DL (1994) A- and C-type rat nodose sensory neurons: model interpretations of dynamic discharge characteristics. J Neurophysiol 71:2338-2358.

Schild JH, Khushalani S, Clark JW, Andresen MC, Kunze DL, Yang M (1993) An ionic current model for neurons in the rat medial nucleus tractus solitarii receiving sensory afferent input. J Physiol 469:341-363.

Wang X.J. Calcium coding and adaptive temporal computation in cortical pyramidal neurons. *J. Neurophysiol* 79:1549-1566, 1998.

Warman, E.N., Durand, D. M., and Yuen, G.L.F. Reconstruction of hippocampal CA1 pyramidal cell electrophysiology by computer simulation. *J. Neurophysiol*. 71: 2033-2045, 1994

Wilson, F.A.W., Scalaidhe, S.P.O., and Goldman-Rakic, P.S. Functional synergism between pytative gama-aminobuttyrate-containing neurons and pyramidal neurons in prefrontal cortex. *Proc. Natl. Acad. Sci.* USA 91: 4009-4013, 1994

Table 1. Expression for Conductances of Ionic Channels Explored in NTS Neuron Models

Channel	Conductance, g	Parameters
Fast sodium, Na_{fast}	$g_{Na} = g_{Na} \times m^3_{Na} \times h$	$m_{\infty Na} = \frac{0.091(V+38)/(1-\exp(-(V+38)/5)}{0.091(V+38)/(1-\exp(-(V+38)/5)+0.062(V+38)/(\exp(((V+38)/5)-1)}$ $\tau_{mNa} = 1/(0.91 \times (V+38)/(1-\exp(-(V+38)/5)+0.062(V+38)/(\exp((V+38)/5)-1))$ $h=_{\infty Na} = \frac{0.016\exp(-(V+55)/15)}{0.016(\exp(-(V+55)/15)+2.07/(1+\exp(-(V-17)/21)}$ $\tau_{hNa} = 1/(0.016\exp(-(V+55)/15)+2.07/(1+\exp(-(V-17)/21))$
Potassium delayed rectifier, K_{DR}	$g_{dr} = g_{dr} \times m^4_{dr}$	$m_{\infty DR} = \frac{0.01(V+45)/(1-\exp(-(V+45)/5)}{0.01(V+45)/(1-\exp(-(V+45)/5)+0.17\exp(-(V+50)/40)}$ $\tau_{mDR} = 1/(0.01(V+45)/(1-\exp(-(V+45)/5)+0.17\exp(-(V+50)/40))$
Transient potassium-A, K_A	$g_A=g_A x(0.6m^4_{A1}xh_{A1}+0.4xm^4_{A2}xh_{A2})$	$m_{\infty A1} = 1/(1+\exp(-(V+60)/8.5))$ $\tau_{mA1} = 1/((\exp(V+35.82)/19.69)+\exp(-(V+79.69)/12.7)+0.37)$ $h=_{\infty A1} = 1/(1+\exp(-(V+78)/6)$ τ_{hA1} = if V<-63,1/(1+exp((V+46.05)/5)+exp(-(V+238.4)/37.45)) else 19.0 $m_{\infty A2} = 1/(1+\exp(-(V+36)/20))$ $\tau_{mA2} = 1/((\exp(V+35.82)/19.69)+\exp(-(V+79.69)/12.7)+0.37)$ $h=_{\infty A2} = 1/(1+\exp(-(V+78)/6)$ τ_{hA2} = if V<-73,1/(1+exp((V+46.05)/5)+exp(-(V+238.4)/37.45)) else 60.0
Calcium-dependent potassium, K_{Ca+2}	$g_{cak} = g_{cak} \times m^2_{Cak}$	$m_{\infty AHP} = 1.25*10^8*[cai]^2/(1.25*10^8*[cai]^2 +2.5)$ $\tau_{mAHP} = 1000/(1.25*10^8*[cai]^2 +2.5)$
High-threshold calcium, Ca_L	$g_{cal} = g_{cal} \times m^3_{cal}$	$m_{\infty cal} = 1.6/(1 +\exp(-0.072 * (V - 5))))/((1.6/(1 + \exp(-0.072 * (V _ 5))))$ $+ (0.02 * (V -1.31)/(\exp((V - 1.31)/5.36) - 1)))$ $\tau_{mcal} = 1.0/((1.6/(1 + \exp(-0.072 * (V - 5))))$ $+ (0.02 (V * 1.31)/(\exp((V -1.31)/5.36) - 1))$

Table 2. Maximal conductances (in mS/cm^2) and compartment dimensions (in µm) of interneuron used in simulation

	Maximal conductance densities (mS/cm^2)	**Compartment dimensions (µm)**
Interneuron	$Rm = 100000.0$ Ohm/cm^2 $Ra = 150.0$ Ohm cm *c_soma=1* *mu F/cm^2* *c_dend=1* *mu F/cm^2*	
Soma	$g_{Na} = 100.0$; $g_{DR} = 40.0$;; $g_{IR} = 0.4$ $g_{HVA} = 0.323$; $g_C = 2.2$	soma: $d = 15$; $l = 15$
Dendrite	$g_{Na} = 20.0$; ; $g_{DR} = 8.0$;; $g_{IR} = 0.4$ $g_{HVA} = 0.323$; $g_{Cat} = 0.01$; $g_C = 3.8$	dendrite: $d = 10$; $l = 150$
Synaptic currents for NTS nodose neuron, Baroreceptors, and Interneuron		
AMPA	$g_{AMPA} = 15.1392$ $\tau_{RISE} = 0.55$ $\tau_{DECAY} = 2.2$	
GABA	$g_{NMDA} = 0.0912$ $\tau_{RISE} = 10.6$ $\tau_{DECAY} = 285.0$	
NMDA	$g_{GABA} = 8.4$ $\tau_{RISE} = 1.5$ $\tau_{DECAY} = 2.5$	

Figures

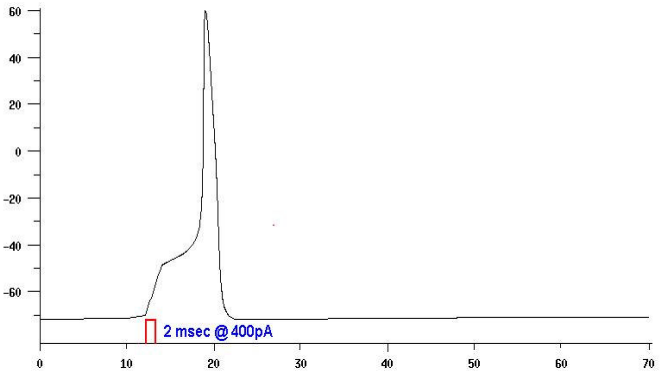

Figure 1. Somatic action potential waveform from an A-type nodose model, using a 2-ms current pulse from near rest potential.

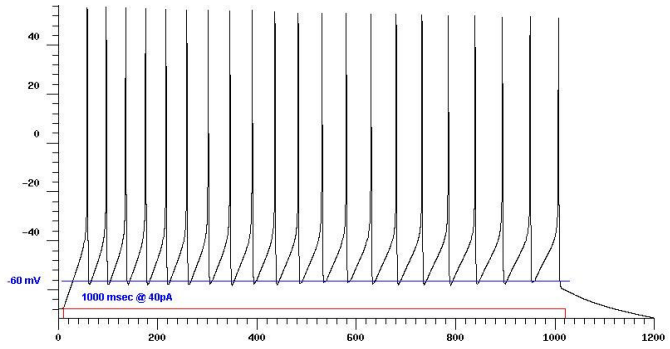

Figure 2. 1000 ms of model activity using a depolarizing step current injection.

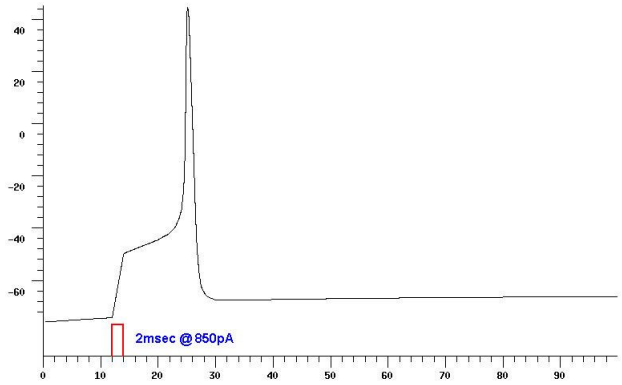

Figure 3. Somatic action potential waveform from an c-Type nodose model using a 2-ms current pulse from near rest potential.

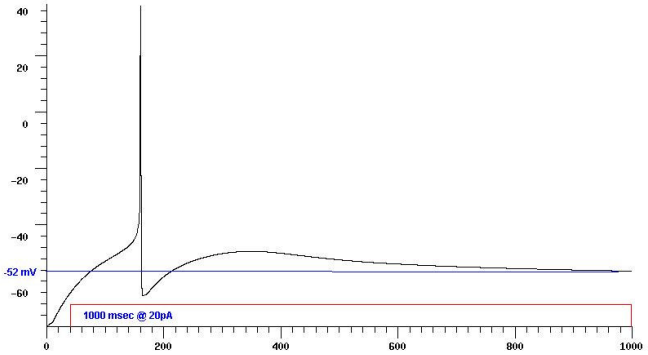

Figure 4. 1000 ms of model activity using a depolarizing step current injection.

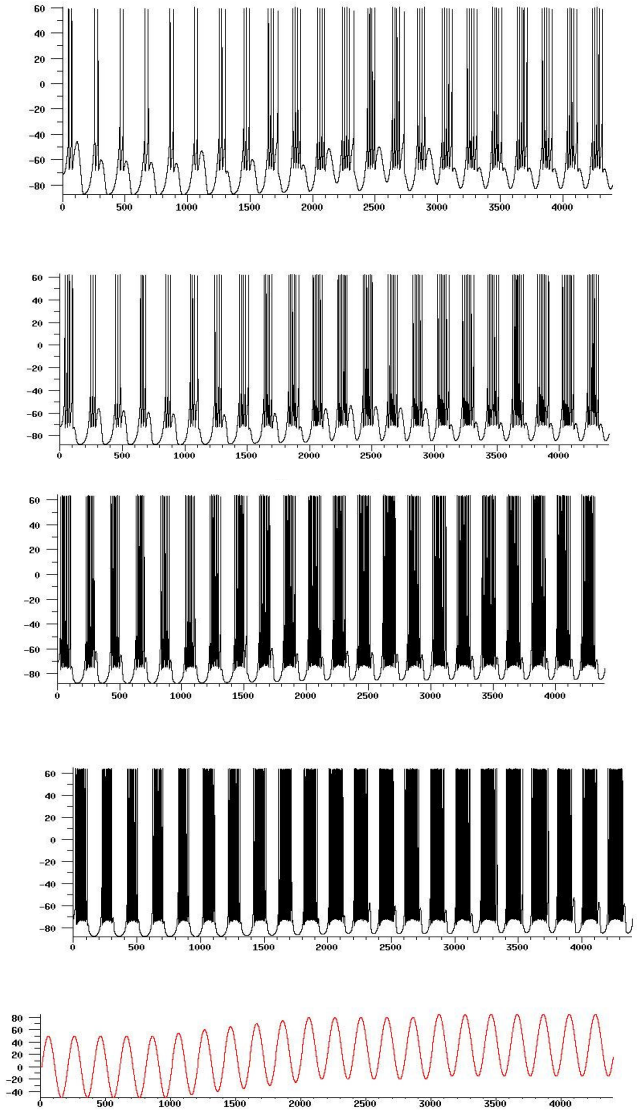

Figure 5. A type Nodose Neuron with different sensitivity responses to same sinusoidal input simulating elevated arterial pressure. From the bottom to top membrane capacity (*Cm*) of each nodose neuron was set at 70, 30, 25, 10, and 5 *pF* respectively.

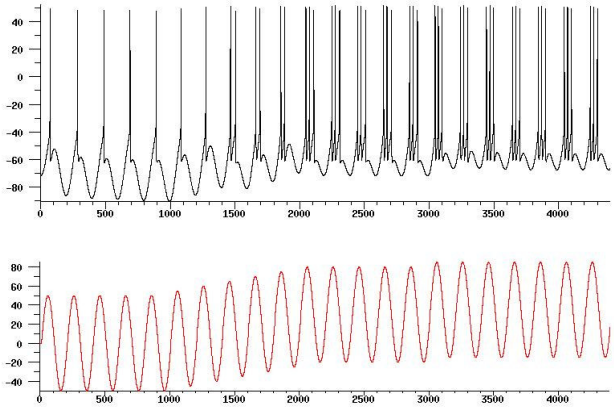

Figure 6. C type Nodose neuron responses to a 5 Hz sinusoidal input simulating elevated arterial pressure. The membrane capacity (*Cm*) of C-type nodose neuron was set at 70 *pF*.

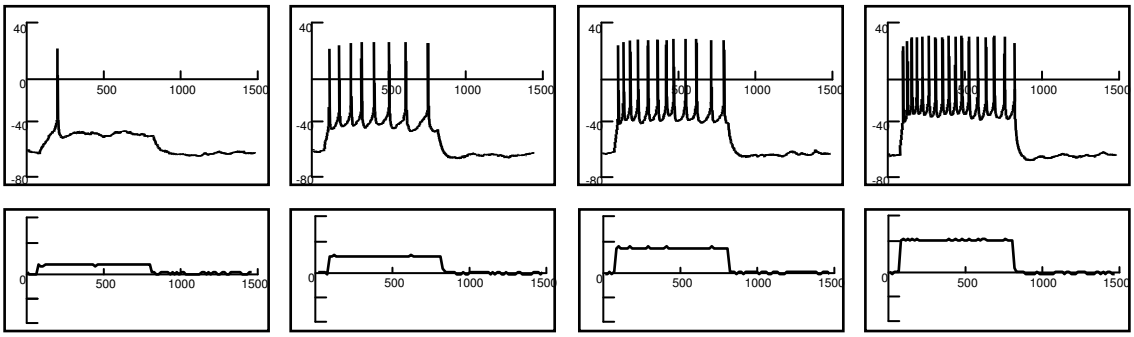

Figure 7. Current evoked responses from whole-cell patch clamped NTS cell

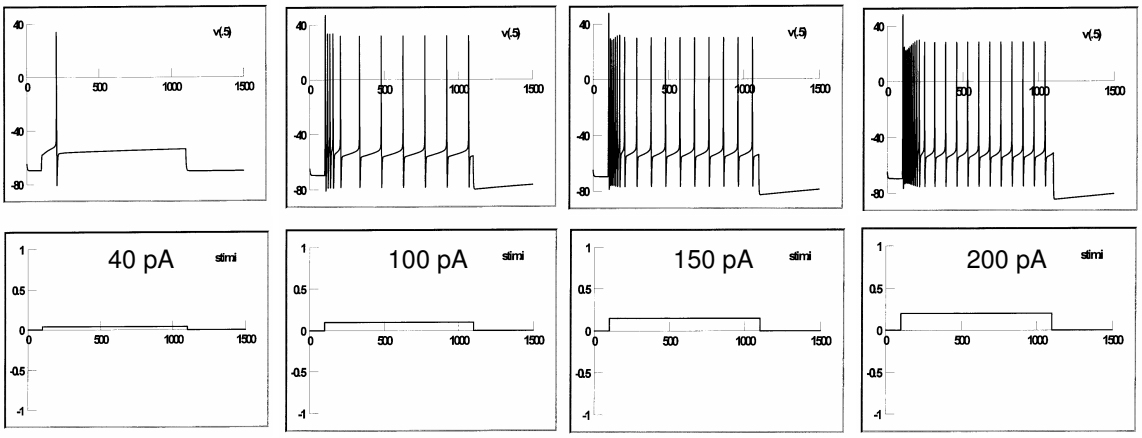

Figure 8. Current evoked responses from model NTS cell

CHAPTER 4

Computational model of the baroreflex arc, Nucleus tractus solitarius – Network model

Abstract.

Baroreceptor afferent signals to the NTS, as well as output signals from the NTS, are pulsatile in nature. However, the discharge patterns of baosensitive NTS network neurons are generally not pulse-modulated. Using single cell models for baroreceptor and NTS neurons that are validated using experimental data, a computational model of the NTS network is developed to mapt its input-output characteristics and to further investigate functional details of the circuitry. We also investigate whether an alteration in GABAergic transmission in the NTS can mimic the reduction in baroreflex gain reported in hypertension.

Introduction

The NTS network receives pulse-synchronous input from arterial baroreceptor afferents and transmits pulse-synchronous output to brainstem target nuclei (such as the CVLM). However, NTS cells generally lack pulse modulated activity based on direct recording from barosensitive neurons. The lack of pulse synchronicity may result from network inputs (i.e., from both excitatory and inhibitory interneuons) onto barosensitive neurons. There is a need to develop a comprehensive network model that can accurately predict the pulse synchronous input-output characteristics of the NTS network, as well as the asynchronous activity of barosensitive NTS neurons. Development of such a network

model would provide a powerful platform to test hypotheses regarding sensory neurotransmission in the NTS.

Arterial Baroreflex and Network Properties

The arterial baroreceptor reflex provides rapid compensation for changes in systemic pressure by regulating cardiovascular organs in a negative-feedback manner. Arterial baroreceptors are sensory neurons that discharge phasically with each pulse pressure generated by the heart. These pulse synchronous signals are transmitted to the nucleus tractus solitarius (NTS) which is the termination site for thinly myelineated A-type and unmyelinated C-type baroreceptors originating from arterial baroreceptors, in addition to a variety of cardiorespiratory receptors. The NTS contains a network of barosensitive neurons that integrate and process baroreceptor signals in a manner that retains pulse-synchronous output to central targets such as the caudal ventrolateral medulla (Schreihofer and Guyenet, 2003). However, despite the phasic nature, baroreceptor activity into and out of the NTS, barosensitive NTS neurons lack pulse-synchronousity. This suggests that NTS circuit neurons are more then simple relay neurons and are involved in dramatically altering sensory neurotransmission. Although the functional properties of the arterial baroreflex are well characterized, the synaptic mechanism(s) and network architecture by which this afferent information is integrated in the NTS is poorly understood.

The cytoarchitecture of the NTS is highly complex and consists of a heterogeneous distribution of neurons (Kumada et al., 1990;Van Giersbergen et al., 1992). Glutamatergic transmission plays an important role of sensory transmission in the NTS. Blockade of ionotropic glutamate receptors with kyurenic acid (non-selective glutamate receptor antagonist) or NBQX (selective AMPA receptor antagonist) blocked

excitatory post-synaptic conductance in second order NTS cells . This suggests that fast glutamatergic transmission between a primary baroreceptor afferent and the second order NTS cell is mediated by non-NMDA glutamate receptors. In addition to glutamatergic transmission, GABAergic neurons are densely distributed throughout the NTS. Anatomical studies have demonstrated that the NTS contains a high density of both GABAergic terminals and somata (Izzo et al., 1992; Sved, 1994; Kawai & Senba, 1996; Stornetta & Guyenet, 1999; Tanaka et al., 2003). In addition, physiological studies have shown that local depolarization of NTS neurons evokes GABA release (Kubo & Kihara, 1987; Sved, 1994) and that GABAergic inhibition alters baroreceptor neurotransmission in the NTS (Miura et al., 1996;Kubo and Kihara, 1988;Kubo and Kihara, 1987). *In vivo* experiments have reported that activation of NTS neurons by electrical stimulation of the aortic depressor nerve, carotid sinus nerve, or cardiopulmonary vagal afferents was strongly inhibited by GABA application (Bennett et al., 1987; Jordan et al., 1988; McWilliam & Shepheard, 1988). The inhibitory effect of GABA was prevented by pre-application of $GABA_A$ receptor antagonists. Together, these studies provide strong evidence that GABA inhibition in the NTS modulates the transmission of inputs from cardiovascular afferents.

To date, no attempt has been made to develop a predictive model of the arterial baroreflex system that includes network, interneurons and output neurons. This paper attempts to propose a network-based predictive model of arterial baroreceptor circuitry in the NTS and to characterize the circuitry from a functional perspective (see Fig 1).

Methods

The number of neurons in each NTS population was initially based on data from Rogers et al (2000), as well as loosely on the relative proportion of excitatory and inhibitory barosensitive NTS neurons. The probability of synaptic connections between each population is listed. Model 1 represented the architecture proposed by Rogers et al (2000) using single compartment cell representation. The architecture presented in Model 2 was based on the finding that second order NTS neurons receive long latency excitatory input from NTS circuit following tract stimulation. Finally, the architecture in Model 3 was based on the following findings: i) a moderate percentage of second order cells receive long latency inhibitory input from NTS circuit neurons following tract stimulation, and ii) a recent finding that some inhibitory second order NTS cells receive monosynaptic excitatory input from tract stimulation.

Further refinement of the model will be based on numerical fits to quantitative voltage- and current-clamp data obtained from *in vitro* brainstem slice experiments and the discharge patterns of barosensitive neurons to physiological activation from in situ experiments. Similar to the single cell model, a sensitivity analysis is performed with each model to identify the importance of each of the channels (e.g., K+) and connectivity parameter (e.g., synaptic weights, probability of connections) on for instance, the property of asynchronous firing. The study will reveal the effect of the number of cells within a population on the overall function, i.e., what effect does an increase in the number of baroreceptors from 30 to 50, or the second order cells from 100 to 200 have on overall network behavior. The network model also permits a systematic evaluation of the existence of functional sub-circuits relevant to the overall function of NTS circuitry such

has been reported in gain control in the visual cortex and short term memory in prefrontal cortex (Wilson 2003).

The paper considers three network architectures. The schematic for the first network we consider is presented in the top of Fig. 2. The model consists of two populations of baroreceptors, each with 10 cells. The Type A-baroreceptors have lower pressure thresholds and greater pressure sensitivity than the Type C baroreceptors. The two baroreceptor populations provide fully-connected input exclusively to two populations provide fully-connected input exclusively to two populations of NTS cells, each with 10 cells. The NTS(C) neurons (i.e., those receiving only Type C baroreceptor inputs) provide fully connected excitatory inputs to the population of inhibitory neurons, which in turn provide a fully connected inhibitory connection to the NTS(A) (i.e., those receiving only Type A baroreceptor inputs) population. Finally, the synaptic weights and delays are Gaussian distributed with a variance of 50% and 20% between connected populations, but with a different mean for each connection. Figure 2 shows the responses by the cells of all neurons to an arterial pressure increase. Two main responses types are evident. Both the inhibitory population and the NTS(C) neurons yield monotonic responses to increases in arterial pressure. The NTS neurons driven by Type A baroreceptors respond to increases in pressure with an increase, followed by a decrease in firing frequency due to the increased inhibition received from GABAergic interneurons.

Another proposed structure is given in the top of Fig. 3. In this model, 10 baroreceptors of each type provide input to a common poll of 30 NTS second-order neurons, each with the same active membrane kinetics. These neurons are reciprocally connected to a population of 10 inhibitory interneurons, none of which receive direct

baroreceptor input. Aside from the differences in circuit arrangement, this model differs from the previous model in its connectivity distribution. In this model, both the number and strength of inputs is randomized by the following probability of connectivity specifications: Baroreceptor → NTS (p=0.25); NTS → Inhibitory (p=1.0), Inhibitory → NTS (p=0.10). These are the probabilities of connection between the different populations. The weights and delays of each individual neuronal connection are randomized. For example, any individual NTS second-order neuron receives 2 to 3 total baroreceptor inputs, each of random strength and type (A vs. C).

The network architecture #3 is shown in Fig 4. In this network, 10 baroreceptors of each type provide input to both pools of 30 NTS second order neurons and a pool of 10 inhibitory neurons. The NTS second order neurons then provide inputs to a network of 30 NTS neurons. The network of NTS neurons then provides inputs to 30 NTS output network and reciprocally, to the pool of NTS second order neurons.

The interneurons also receive inputs from the NTS second order neurons.
In this model, both the number and strength of inputs is randomized by the following probability of connectivity specifications: Baroreceptor → NTS second order(p=0.25); Baroreceptor → inhibitory (p=0.60); NTS second order → NTS network (p=0.25); NTS network → NTS second order (p=0.25); NTS network → NTS output network (p=0.25); NTS second order→ Inhibitory (p=1.0), Inhibitory → NTS second order (p=1.0); Inhibitory → NTS second order (p=1.0). Finally, the synaptic weights and delays are Gaussian distributed with a variance of 30~40% and 70% respectively between connected populations, but with a different mean (i.e., weights (0.2~0.5) and delays (2~20ms) for each connection.

In this configuration the baroreceptors and interneurons were monotonically excited to increase to the arterial pressure.

Sensitivity analysis: Selected model parameters, such as maximal conductance and time constant for each current will be systematically increased and decreased by a fixed percentage while noting its effect on the membrane potential and firing pattern. Such an analysis will help identify the importance of each parameter on a given current, and will provide finer insights into the dynamics of the NTS cell types,

Reduced membrane analysis: We will "turn off" the spike producing Na+ and K+ currents, and will study the dynamics of the 'reduced membrane' as performed by Hutcheon, et al. (1996) using dynamic clamp ideas. This will provide further insights into the parameters of each current that contribute to known properties of NTS cells, such as delayed excitation (DE) and spike frequency adaptation (SFA), and should assist in the generation of hypotheses for testing using dynamic clamp techniques in the Kline lab. Again, we will perform such analyses for all the different cell types investigated.

Results

Initial model runs focused on replicating the asynchronous firing pattern of barosensitive NTS neurons to pulsatile baroreceptor input and the reconstitution of pulse-synchronous activity by NTS output neurons adjusted in order to simulate the electrical behavior of these NTS populations. The arterial pressure frequency oscillations were modeled by injecting a 3500ms-long, 5-Hz sinusoidal current $I_0 + A_0 \bullet (\sin(2\pi \cdot f \cdot t))$ where f=5 Hz and $A_0 = 20\ pA$. I_0 was gradually increased from 0 until the maximum injected current reached 85 pA.

In the case of network #2, the NTS second order neurons did monotonically excited to arterial blood increase suggesting that GABAergic inhibition from interneuron was not strong enough to suppress NTS neuron's excitability.

In the case of network #3, the NTS second order neurons however were monotonically less excited due to the strong inhibition received from interneurons. As NTS second order neurons provided fewer inputs to next network of NTS network neurons, these neurons were also inactivated. It is not hard to imagine that a model with greater structural variability would be capable of reproducing a wider range of responses to arterial pressure increases including all those that have been observed *in vivo*. The response type of any given neuron is determined by its connectivity and the architecture of the network.

Sensitivity and other studies will be added, to the extent possible.

References

Durstewitz, D., Seamans, J.K., and Sejnowski, T.J. Dopamine-mediated stabilization of delay-period activity in a network model of prefrontal cortex. *Journal of Neurophysiology*, Vol. 83, pp. 1733-1750, 2000.

Hutcheon B, Miura RM, Puil E (1996) Models of subthreshold membrane resonance in neurocortical neurons, Journal of Neurophysiology 76(2):698-714.

Goaillard JM, Marder E. Dynamic clamp analyses of cardiac, endocrine, and neural function. Physiology (Bethesda). 2006 Jun;21:197-207.

Kang, Y., Okada, T., Ohmor, H., A phenytoin-sensitive cationic current participates in gnerating afterdepolarization and burst afterdischarge in rat neocortical pyramidal cells. *Eur. J. Neurosci.* 10 1363-1375, 1998

Kawaguchi, Y. Groupings of nonpyramidal and pyramidal cells with specific physiological and morphological characteristics in rat frontal cortex. *J. Neurophysiol*. 69: 416-431, 1993.
Kitano H (2002) Computational systems biology, Nature 420:206-210.
Koch C, Segev I (2001) Methods in Neuronal Modeling- From Ions to Networks, The MIT Press.
Kubo T, Kihara M (1988) Evidence for gamma-aminobutyric acid receptor-mediated modulation of the aortic baroreceptor reflex in the nucleus tractus solitarius of the rat. Neurosci Lett 89:156-160.
Kubo T, Kihara M (1987) Evidence for the presence of GABAergic and glycine-like systems responsible for cardiovascular control in the nucleus tractus solitarii of the rat. Neurosci Lett 74:331-336.
Kumada M, Terui N, Kuwaki T (1990) Arterial baroreceptor refles: its central and peripheral neural mechanisms. pp 331-361.
Leblois A, Boraud T, Meissner W, Bergman H, Hansel D (2006) Competition between Feedback Loops Underlies Pathological Dynamics in the Basal Ganglia, Journal of Neuroscience 26(13):3567-3583.
Lien CC, Jonas P. (2003) Kv3 potassium conductance is necessary and kinetically optimized for high-frequency action potential generation in hippocampal interneurons. J Neurosci. 23(6):2058-68
Manuel M, Meunier C, Donnet M, Zytnicki D. (2005How much afterhyperpolarization conductance is recruited by an action potential? A dynamic-clamp study in cat lumbar motoneurons. J Neurosci. Sep 28;25(39):8917-23.
Miura M, Okada J, Takayama K, Jingu H (1996) Barosensitive and chemosensitive neurons in the rat medulla: a double labeling study with c-Fos/glutamate, GAD, PNMT and calbindin. J Auton Nerv Sys 61:17-25.
Rogers RF, Rybak IA, Schwaber JS (2000) Computational modeling of the baroreflex arc: nucleus tractus solitarius. Brain Res Bull 51:139-150.
Schild JH, Clark JW, Canavier CC, Kunze DL, Andresen MC (1995) Afferent synaptic drive of rat medial nucleus tractus solitarius neurons: dynamic simulation of graded vesicular mobilization, release, and non-NMDA receptor kinetics. J Neurophysiol 74:1529-1548.

Schild JH, Clark JW, Hay M, Mendelowitz D, Andresen MC, Kunze DL (1994) A- and C-type rat nodose sensory neurons: model interpretations of dynamic discharge characteristics. J Neurophysiol 71:2338-2358.

Schild JH, Khushalani S, Clark JW, Andresen MC, Kunze DL, Yang M (1993) An ionic current model for neurons in the rat medial nucleus tractus solitarii receiving sensory afferent input. J Physiol 469:341-363.

Wang X.J. Calcium coding and adaptive temporal computation in cortical pyramidal neurons. *J. Neurophysiol* 79:1549-1566, 1998.

Warman, E.N., Durand, D. M., and Yuen, G.L.F. Reconstruction of hippocampal CA1 pyramidal cell electrophysiology by computer simulation. *J. Neurophysiol*. 71: 2033-2045, 1994

Wilson, F.A.W., Scalaidhe, S.P.O., and Goldman-Rakic, P.S. Functional synergism between pytative gama-aminobuttyrate-containing neurons and pyramidal neurons in prefrontal cortex. *Proc. Natl. Acad. Sci.* USA 91: 4009-4013, 1994

Figures

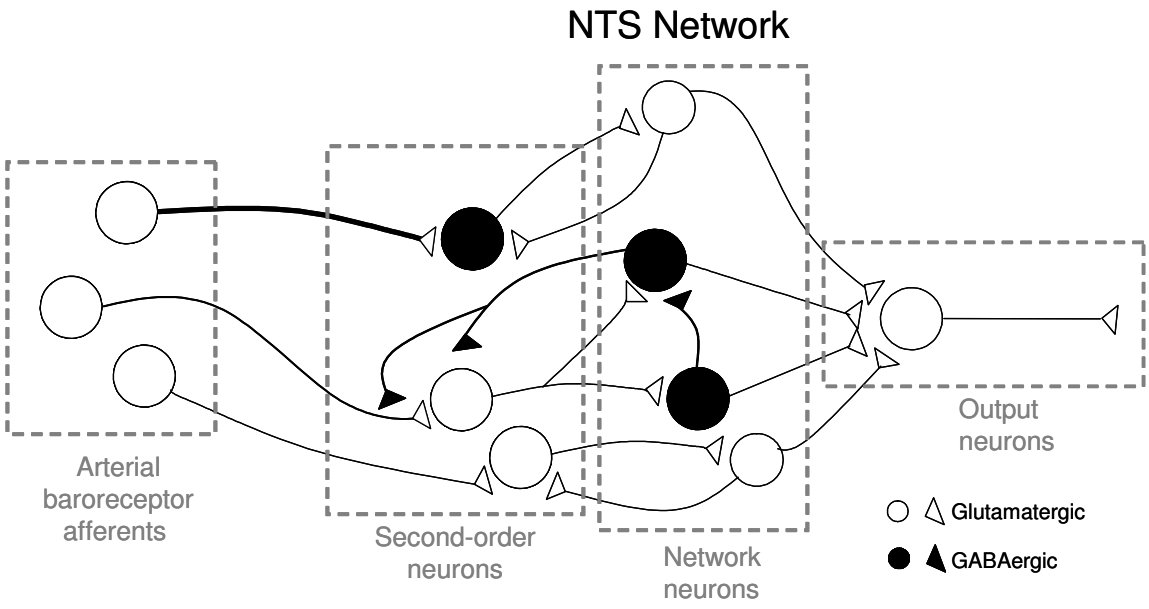

Figure 1. Network of arterial baroreceptor circuitry in the NTS.

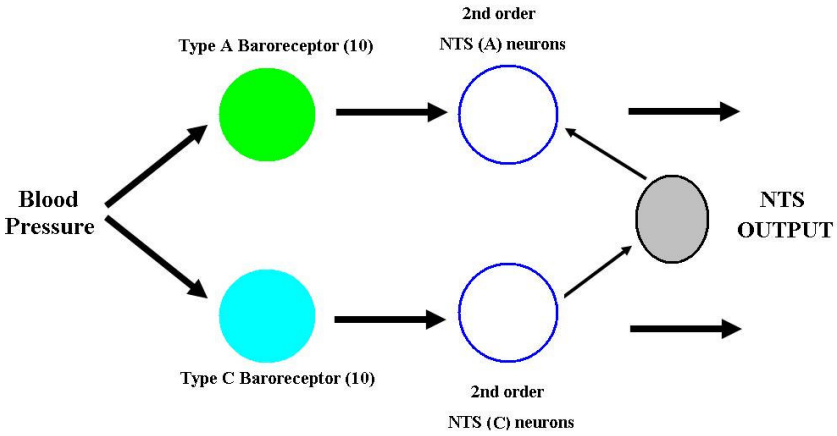
2nd order
Type A Baroreceptor (10)
NTS (A) neurons
Blood
Pressure
NTS
OUTPUT
Type C Baroreceptor (10)
2nd order
NTS (C) neurons

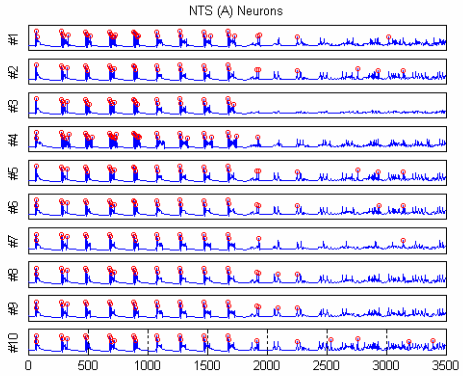
NTS (A) Neurons
#1
#2
#3
#4
#5
#6
#7
#8
#9
#10
0
500
1000
1500
2000
2500
3000
3500

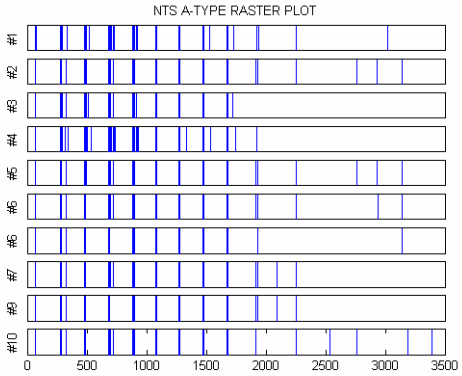
NTS A-TYPE RASTER PLOT
#1
#2
#3
#4
#5
#6
#7
#9
#10
0
500
1000
1500
2000
2500
3000
3500

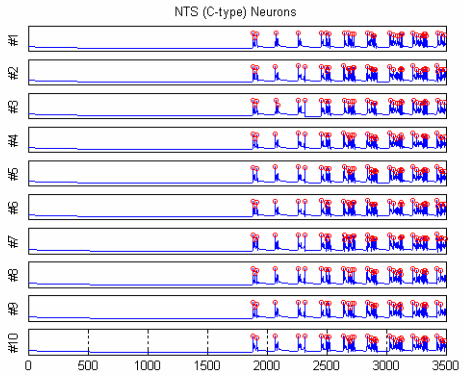
NTS (C-type) Neurons
#1
#2
#3
#4
#5
#6
#7
#8
#9
#10
0
500
1000
1500
2000
2500
3000
3500

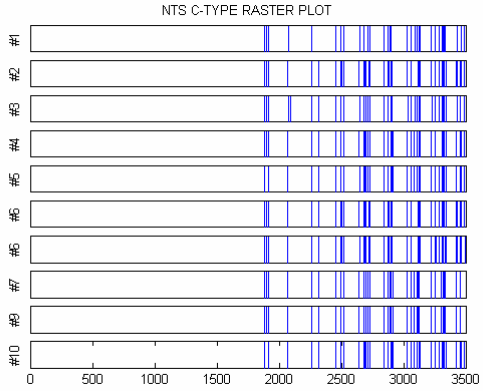
NTS C-TYPE RASTER PLOT
#1
#2
#3
#4
#5
#6
#7
#9
#10
0
500
1000
1500
2000
2500
3000
3500

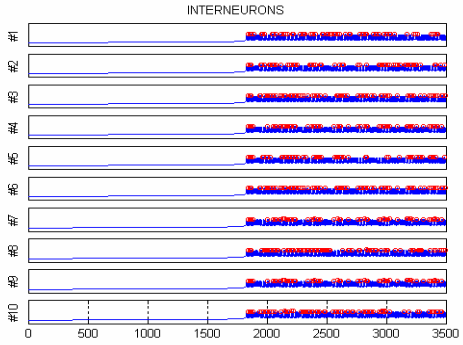
INTERNEURONS
#1
#2
#3
#4
#5
#6
#7
#8
#9
#10
0
500
1000
1500
2000
2500
3000
3500

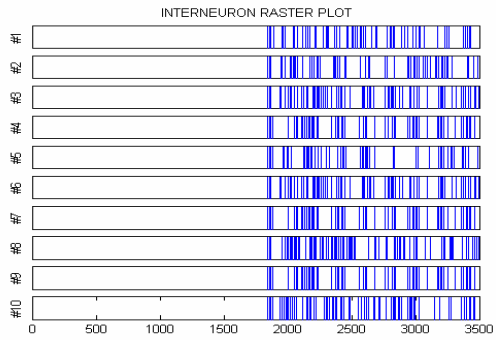
INTERNEURON RASTER PLOT
#1
#2
#3
#4
#5
#6
#7
#8
#9
#10
0
500
1000
1500
2000
2500
3000
3500

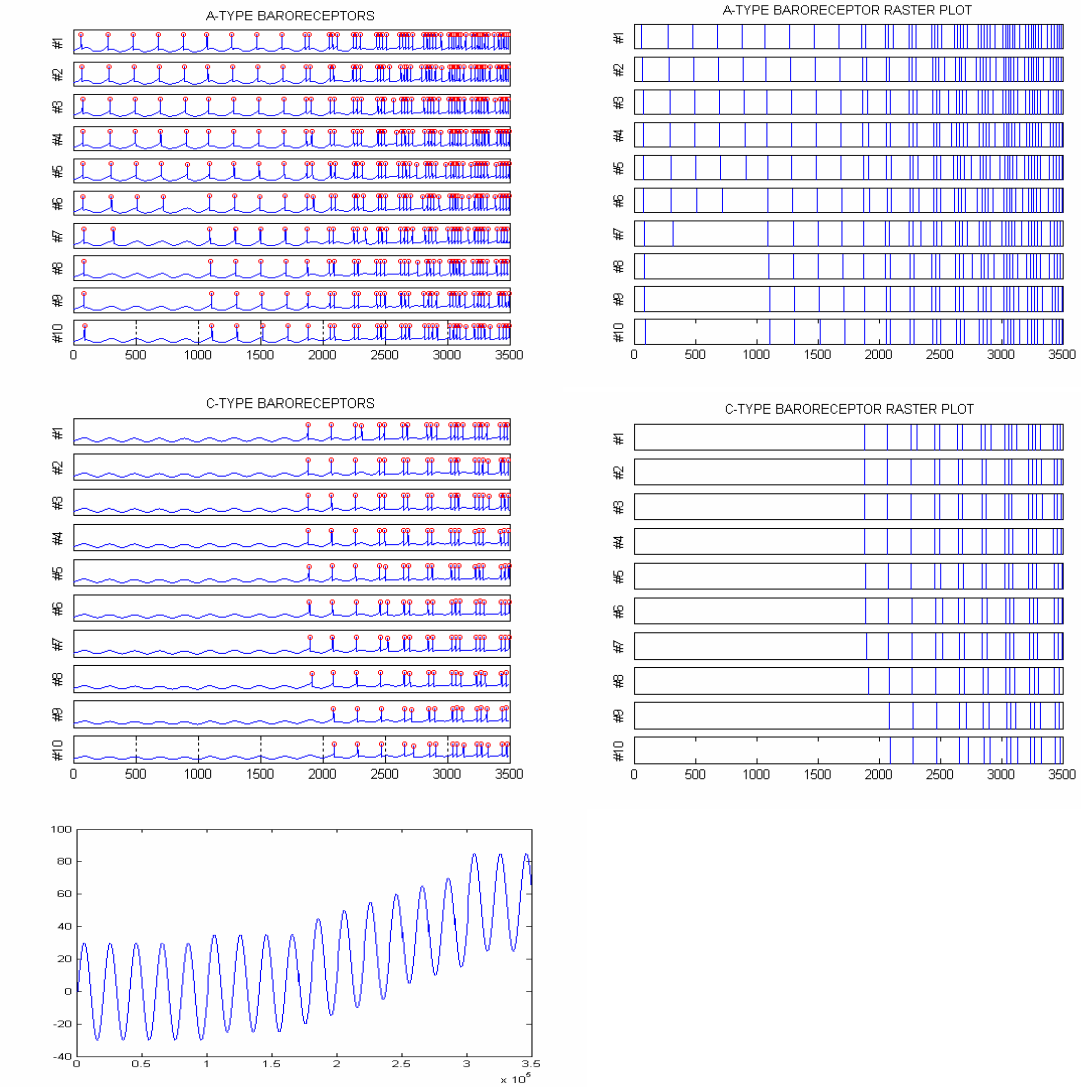

Figure 2. Initial population model of architecture 1 proposed to explain variability of nucleus tractus solitarius (NTS) neuronal responses to arterial pressure increases. Top: network architecture showing “labeled lines” for processing A and C type baroreceptor inputs. Bottom_left: plots of membrane traces generated by each of the neuron model in the network to an increase of arterial pressure. Red marks indicate spike packs above 0 mV. Bottom-right: raster plots of action potentials generated by each neuron with a threshold of 0 mV.

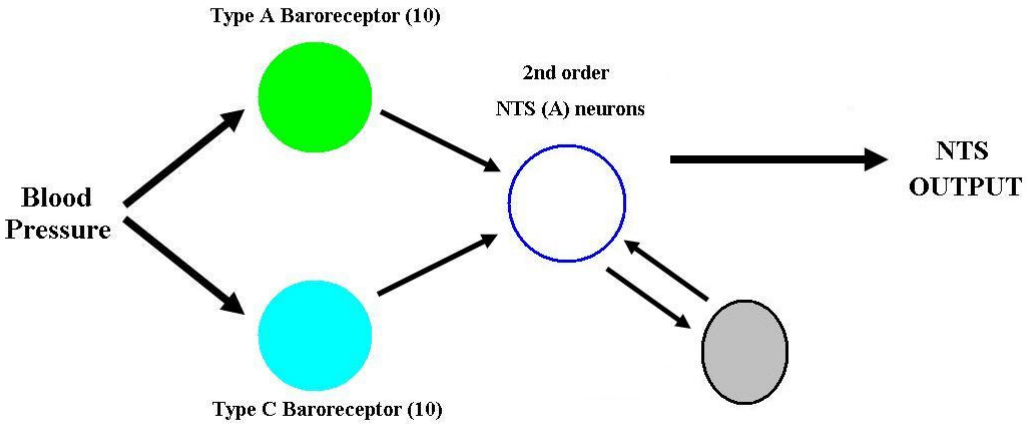
Type A Baroreceptor (10)
2nd order
NTS (A) neurons
NTS
OUTPUT
Blood
Pressure
Type C Baroreceptor (10)

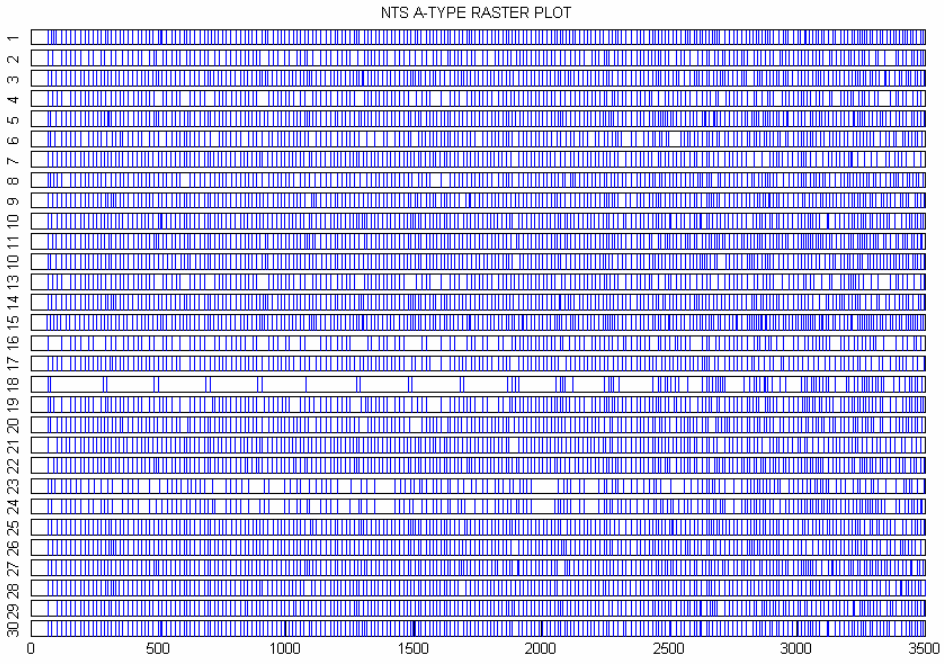
NTS A-TYPE RASTER PLOT
1
2
3
4
5
6
7
8
9
10
11
10
13
14
15
16
17
18
19
20
21
22
23
24
25
26
27
28
29
30
0
500
1000
1500
2000
2500
3000
3500

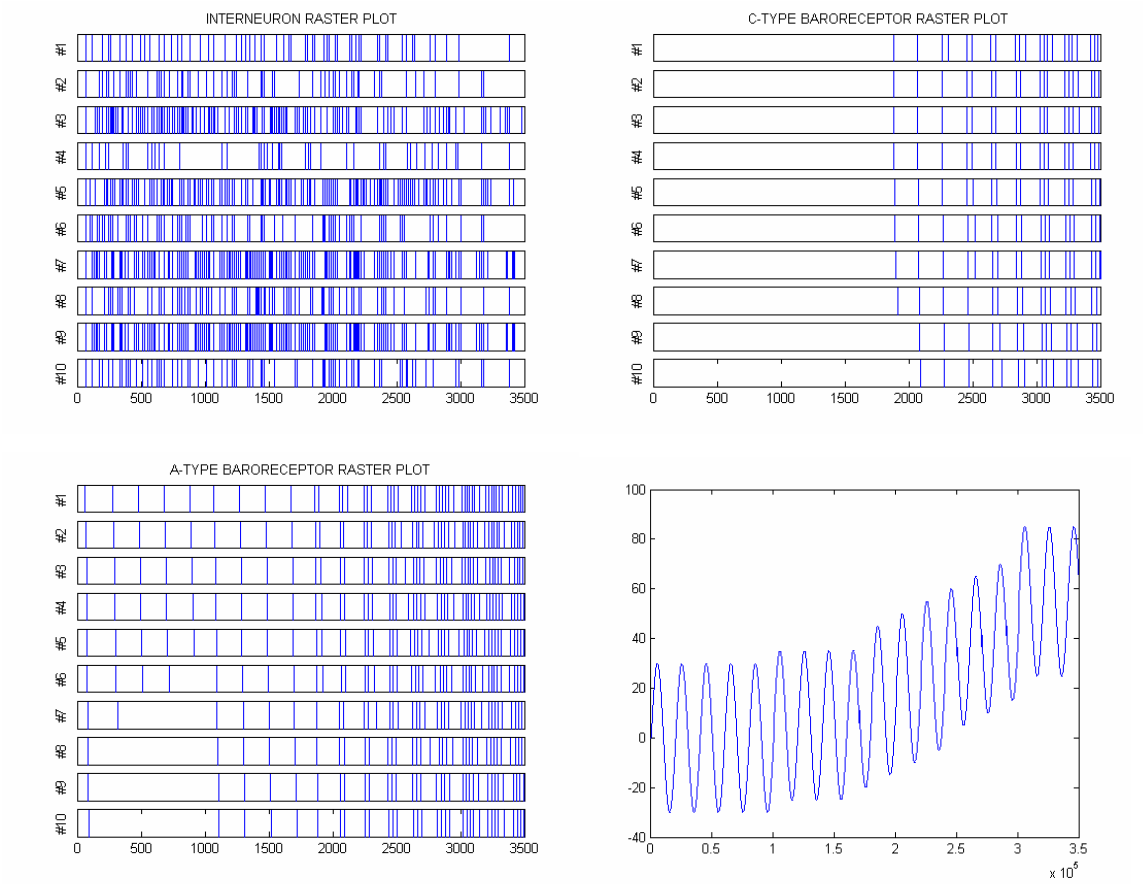

Figure 3. Population model of architecture 2 proposed to explain variability of nucleus tractus solitarius (NTS) neuronal responses to arterial pressure increases. Top: network architecture showing "labeled lines" for processing A and C type baroreceptor inputs. Bottom: raster plots of action potentials generated by each neuron with a threshold of 0 mV. GABAergic inhibition was not strong enough to suppress NTS neurons excitability. NTS neurons became more excited as arterial blood pressure increased.

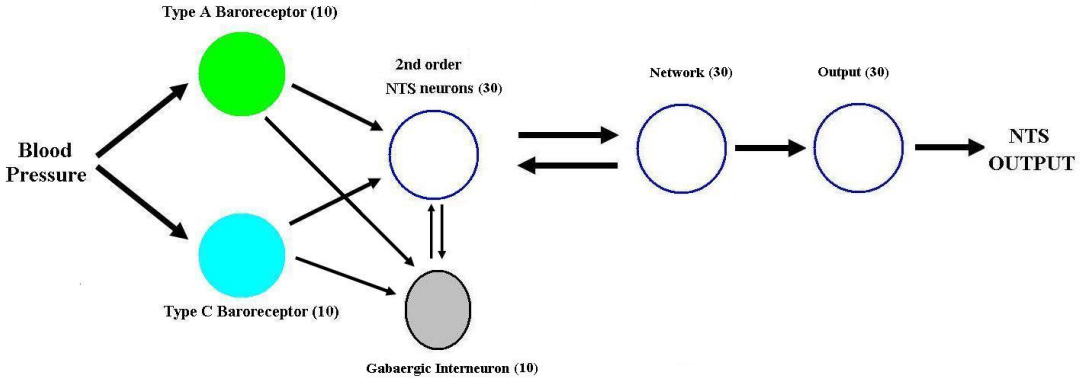
Type A Baroreceptor (10)
2nd order
NTS neurons (30)
Network (30)
Output (30)
Blood
Pressure
NTS
OUTPUT
Type C Baroreceptor (10)
Gabaergic Interneuron (10)

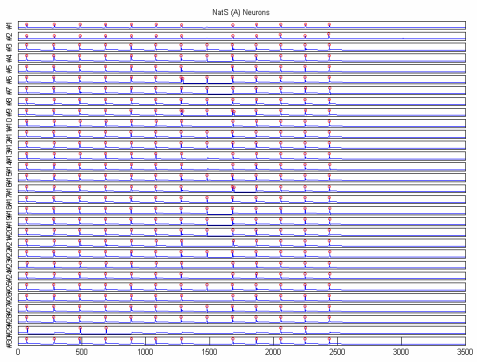
NatS (A) Neurons

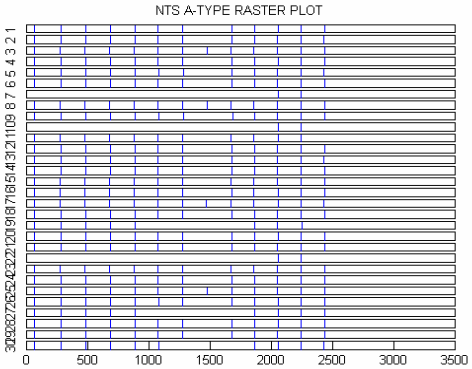
NTS A-TYPE RASTER PLOT

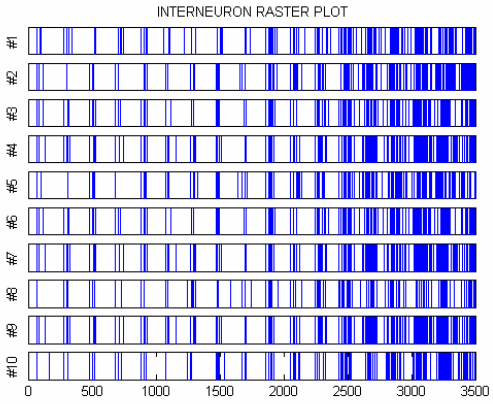
INTERNEURON RASTER PLOT
#1
#2
#3
#4
#5
#6
#7
#8
#9
#10
0
500
1000
1500
2000
2500
3000
3500

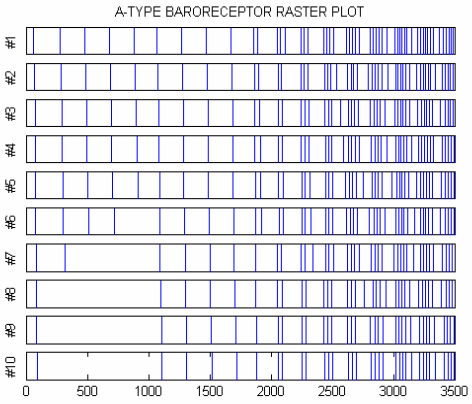
A-TYPE BARORECEPTOR RASTER PLOT
#1
#2
#3
#4
#5
#6
#7
#8
#9
#10
0
500
1000
1500
2000
2500
3000
3500

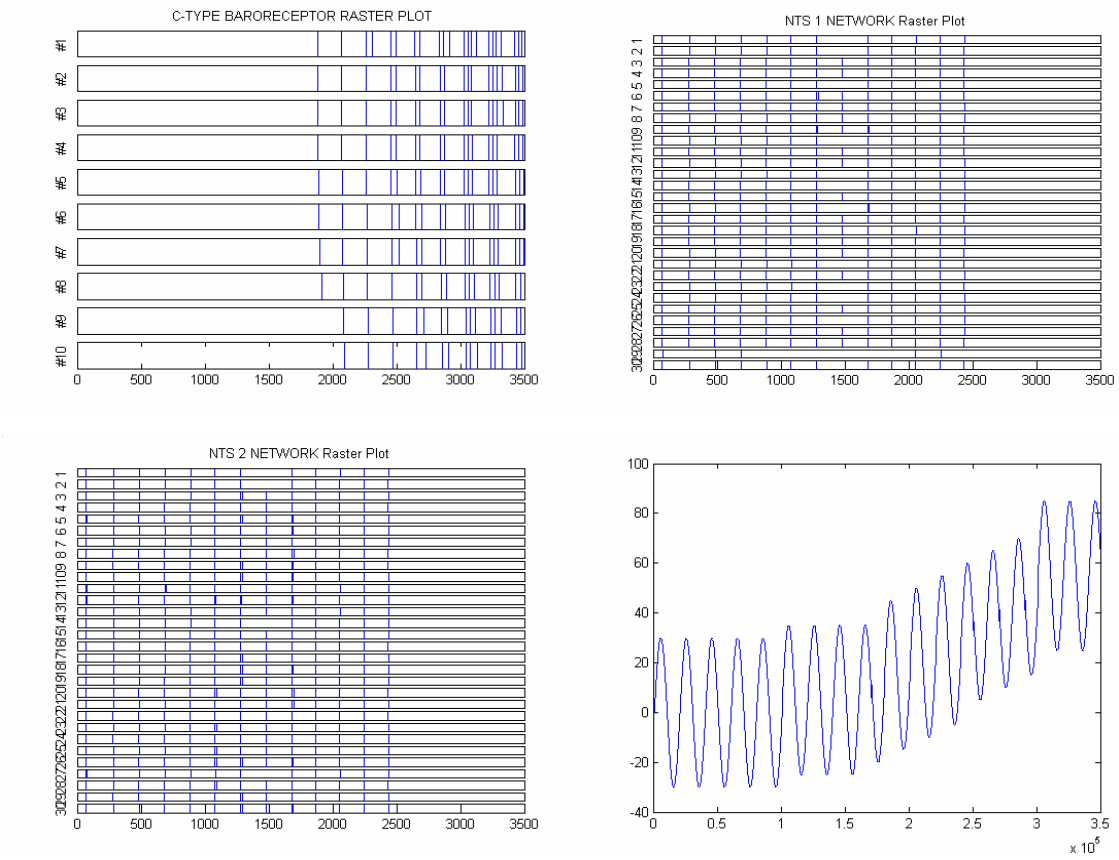

Figure 4. Population model of architecture 3 proposed to explain variability of nucleus tractus solitarius (NTS) neuronal responses to arterial pressure increases. Top: network architecture showing “labeled lines” for processing A and C type baroreceptor inputs. Bottom: raster plots of action potentials generated by each neuron with a threshold of 0 mV. GABAergic inhibition was strong enough to suppress NTS neurons excitability. NTS neurons became less excited as arterial blood pressure increased.

PART II

SYSTEMS LEVEL MODELING

Part II focuses on systems level physiology using the human thermal system dynamics as the example case, representing a 'higher level' model, again with multiple inputs and outputs. Human thermal physiology modeling is important to better understand human thermal responses under transient conditions, to facilitate development of automatic thermal control for astronauts during extra-vehicular activity (EVA), and in characterizing heat stress tolerance times for war-fighters in extreme conditions (cold to desert) in chem-bio suits. A specific control technique, model predictive control is also investigated for EVA thermal comfort, is then proposed. The details in each of the chapters is listed below.

In Chapter 5, the effect of individual differences on thermal stress response for semi-nude supine human subjects in transient environments is studied using an experimental data set. Two transient climatic parameters and seven individual characteristics are used as inputs to predict three thermal responses using a novel transient computational model. The model is developed using a neural network after ensuring generalization and also checking with results reported in the literature for predictions.

In Chapter 6, a new human thermal model has been developed that accounts for asymmetric environments and includes extremities. To this model we add models for

digits of toes to predict heat transfer through toe and fingertip via arteriovenous anastomoses (AVAs) mechanisms, all of which are important in extremity discomfort.

As mentioned earlier, each chapter is in the form of a self-contained journal paper.

CHAPTER 5

MODELING INDIVIDUAL VARIATIONS IN THERMAL STRESS RESPONSE FOR HUMANS IN TRANSIENT ENVIRONMENTS

Abstract

The effect of individual differences on thermal stress response for semi-nude supine human subjects in transient environments is modeled using an experimental data set. Two transient climatic parameters and seven individual characteristics are used as inputs to predict three thermal responses using a novel transient computational model. The model is developed using a neural network after ensuring generalization and also checking with results reported in the literature for predictions. It reliably predicts core temperature, skin temperature and heart rate in transient environmental conditions for individual subjects. A methodology is then proposed to identify the relative importance of the individual parameters and of environmental conditions on thermal stress, using a sensitivity analysis. The results have applications for heat stress monitoring, and other biomedical applications.

Keywords: individual differences in heat stress; heat stress prediction; heat tolerance time limit

INTRODUCTION

Researchers have developed thermal computational models using different approaches such as analytical, statistical, empirical, and physiological, to forecast and to better understand human thermal responses under different environmental conditions (Bue et

al.; Campbell et al. 1994; French et al. 1997; Fu et.al 1995; Gonzalez et al. 1997; Gonzalez et al. 2001; Guan et al. 2003; Hsu et al. 1971; -17; Pennes 1948; Stolwijk 1971; Tanabe et al. 2002; Wissler 1971). However, due to the complexity of human thermoregulation including interactions with the environment, the suitability of such models to real world applications has been limited. Better characterization of the uncertainties involved, including physiological mechanisms and parameter variations will be important as we seek improved understanding of human thermophysiology related to heat stress.

One of the earliest human thermal efforts was the development of a steady-state model to analyze heat transfer in a resting human forearm by Pennes in 1948 (Pennes 1948). This cylindrical model served as the basis for a more advanced model by Wissler (Wissler 1971) and is still being used for the prediction of temperature elevation during hyperthermia (Frank et al. 1999). Subsequent advances in computing technology and increased experimental data on human physiology helped researchers in developing more sophisticated human thermal models. In the 1960s, early versions of the well-known Wissler (1961), Stolwijk models were being developed. Later human thermal models derive their ideas largely from these three mathematical models.

Various research teams (Fu 1995, Huizenga 2001, Iyoho 2002) have developed models in the past decade to be used in environments that range from steady state to transient and non-uniform cases. Examples of models that are being improved include the Wissler model, a detailed finite element model (Fu 1995), a model by Huizenga (2001), and one by the authors' group. All these models include heat transfer within the body as well as between the body and its environment, as well as sweating, shivering, and

vasomotor functions. The authors' group has also been investigating human thermal dynamic modeling issues (Campbell et al.1994;Iyoho 2002; Thornton et al 2000 and 2002) and are developing an advanced 2-D human thermal model, as part of a larger goal to design an automatic thermal controller for astronauts during extra vehicular activities (Iyoho 2002, Thornton et al 2002).

Quantitative comparisons among human thermoregulation models have been difficult due to the individual characteristics of each model in particular environmental conditions (Campbell et al 2002, Gonzalez et al 2001, Guan et al. 2003). From a user point of view, it has not been clear which of the models would be best suited for a particular environment and application. From a physiology point of view, many aspects of the human active (thermoregulatory/control) thermal system are still not well understood. The passive thermal system (conduction through body regions, etc.) has been modeled with more success, but the effect of uncertainties such as intra-subject and inter-subject variations in thermal parameters, continue to be poorly understood. Hence, although human thermal models predict core and mean skin temperature fairly accurately, they fail to predict other thermal responses such as sweat production, and metabolic heat production, particularly in extreme conditions. Important indicators for the thermal risk such as heart rate, and dehydration level due to the excess sweating are not typically considered explicitly in the models. Perturbations such as fast transient and widely disparate environmental conditions, individual physiological differences, altitude, clothing, and terrain level also cause problems for such models. As an example, causes for large variations in thermal responses and tolerance time limits among individuals continue to be poorly understood.

A neural network model has been developed by our team to predict heat stress, using transient experimental thermal data from a group of subjects, details of which are provided in the next section. The inputs to the model are prior values of core temperature (Tcore), heart rate (HR), skin temperature (Tsk) and seven 'individual' parameters, and the model outputs are future predictions of Tcore, HR and Tsk. The seven parameters considered to characterize individual differences are gender, age, height, weight, maximal oxygen consumption (VO2max), basal metabolic rate (Minitial), and initial heart rate (HRinitial). A methodology is then proposed to identify the relative importance of 'individual' parameters on heat stress variables such as core temperature and heart rate, using a sensitivity analysis. A method to calculate the relative importance of environmental conditions on those variables is also reported.

MODEL DEVELOPMENT

The dataset used to develop the neural network was provided by Dr. Richard Gonzalez of US Army Research Institute of Environmental Medicine (USARIEM), Natick, MA, and contains thermal observations for 35 healthy male and female subjects ranging in age from 8 to 67 years. The data were collected in compliance with appropriate guidelines. For each subject, in a resting supine position through the experiment, 10 variables are measured for 140 minutes, in still air, with transient environmental conditions (from 9°C to 50°C and from dry to humid environments). After an initial period of 30 min at Ta 30° C, the chamber temperature was increased at the rate of 1.5°C min^{-1} rising rapidly for the first 20 min and leveling off at 50° C. Following a 30 min hot-dry exposure, the dew point temperature was raised to 32° C and responses were observed for another 25 minutes after which the chamber temperature

was lowered falling rapidly and leveling off at 10^{o} C . For more details refer to Gonzalez et al. 1980. The data set is divided into eight groups by age and gender as shown in Table 1. Since the subjects are resting, the metabolic rate is considered constant for each subject, with a term added separately if shivering occurs.

Modeling. Three separate models are developed, two gender based models (male and female using male and female datasets respectively), and one 'general' combined model with gender as an input (using the entire dataset). The general combined model has nine inputs which includes two environmental parameters (Ta, Pa) and seven individual characteristics (Age, Gender, VO2max, Weight, Height, Minitial, and HRinitial; see Table 2 for symbols and description) for the subjects with only gender variable being omitted in the two gender-based models. The potential user thus has to provide only the environmental conditions and the individual characteristics as inputs. The outputs of the model are Tsk, Tcore, and HR. Esophageal temperature, Tes, and rectal temperature, Trec, were used to represent Tcore in the training process. A feedforward neural network architecture is used for the models with an input layer, two hidden layers, and an output layer, using a back-propagation algorithm for update, with a mean square error performance function. The architecture has feedback of one time-delayed value for each of the three outputs, making it a dynamic model. The structure of the net for the combined model is 12 x 12 x 14 x 3, while for gender based models it is 11 x 10 x 10 x 3. The dataset provided 4759 patterns for training, each separated in time by one minute. An early stopping method [Amari et al. 1997, Pennes et al. 1948] is used to prevent over-fitting and ensure generalization, with the data divided into three subsets 50% for training, 25% for validation, and 25% for testing subsets. From the six models, the one

with the least mean square error (mean square error, MSE) for the testing data set is selected. The weights, biases and number of epochs for the network are then used to train the final model with the entire dataset.

Sensitivity analysis. We perform a sensitivity analysis with mean skin temperature (Tsk) and core temperature (Tcore) as outputs, and the individual parameters (Age, VO2max, HRinitial, Minitial, HRinitial, height, weight) as inputs. The sensitivity derivative is defined as □ *(output)/* □ *(parameter)* and this derivative is calculated by perturbing each input by one standard deviation of its value within the group, and noting its effect on the steady state value of the output. Taking the ratio of the change in output to the change in input provides the sensitivity derivative. This analysis is carried out for each input, one at a time, keeping the others constant, in four environmental conditions. An 'average' subject from each group is chosen as the representative subject for the sensitivity analyses (Table 3). This value is then scaled by the largest magnitude in the column to provide a ranked estimate of its relative importance. This results in the largest value in each column having a magnitude of 1 and the magnitudes and signs for each parameter provide an indication of its relative importance. Sensitivity analysis provides further insights into system characteristics by permitting to rank the importance of the 'inputs' on influencing the 'outputs'. Sensitivity analysis also serves as an additional tool to check whether the model has generalized adequately since it can be checked against known trends reported in the literature.

RESULTS AND DISCUSSION

The neural network structures for our models were chosen based on extensive statistical analysis of the data and a review of the literature. These analyses included correlations, ANOVA, and development of linear regression models. Havenith et al. (1990) have shown that Ta, vapor pressure, and metabolic rate can explain 96% of the variance in mean skin temperature with Ta being the largest contributor. This finding coincides with our multiple regression analysis of the dataset which gives a value 92% for the same check. Havenith (1990) shows that a multiple regression analysis using Ta, Pa, M, % Fat, and sweating set point can explain 71% of the variance in Tcore. Regression analysis performed with our dataset showed that 61% of the variance could be explained when Tsk, HR, Evg, and age group were included along with Ta, Pa. Moran et.al showed that 77 to 88% of the variance in heart rate can be explained by initial heart rate, metabolic rate, maximum evaporative rate, required evaporative rate, and time of exposure in minutes. Our data analysis showed (Table 4) that Tsk, Tes, Evg, Ta, Pa, and age group could explain 64% of the variance. For the variance in heat storage rate, S, 92 % could be explained by Ta, Pa, M, %Fat, A_d, VO2max, and sweating gain (Havenith et al. 1990).

Predictions of the models developed using a representative 'average' for each group (Table 3) compared well with actual data, some of which are shown in Figures 1-3. Actual data for all the subjects are superimposed in the figures with the prediction for a representative subject in the group with average properties. The correlation coefficients between predicted values and experimental values are shown in Table 5 for each of the

subjects, for all the three outputs, showing good overall performance using gender-based models. Several other similar investigations were performed which are not described due to space limitations, and the observations from the study are summarized next. The model is found to successfully predict Tcore, HR and Tskin, given only two environmental variables and seven individual parameters as inputs to forecast three thermal response outputs. Tcore and HR are two of the most important thermal predictors of thermal risk and they are products of complex internal and external interactions with the surrounding environment and within the body.

Observations from sensitivity analysis

Sensitivity analysis is systematically performed using all three models under four different environmental conditions: normal (Ta=20, Pa=24), jungle (Ta=40, Pa=30), desert (Ta=43, Pa=10), and cold (Ta=5, Pa=10). The dataset used for the first model has been categorized into four age groups for each gender. From each age group an average subject is generated to test how well the model generalizes. This average subject in each group has a mean value for each input (Table 3). As mentioned earlier, Figures 1-3 show that the model has generalized well without over-fitting, since the thermal responses of these average subjects lie within the range of thermal outputs of the group, in transient environmental conditions. Results of the sensitivity analyses are provided as ranked values of the scaled sensitivity derivatives(□ (*output*)/ □ (*parameter*)) in Tables 6 and 7.

Many interesting observations can be noted, some of which are described next, and they agree with findings reported in the literature. For instance, Havenith et.al suggested that part of the variance in Tcore could be explained by the A_d/mass relationship for the subjects, with 'big' subjects who are characterized by large values of A_d (body surface area as a function of height and weight) and low A_d/mass having a lower Tcore. One

physiological explanation is that subjects with high A_d have a larger surface area for heat loss to the environment and have higher heat storage capacity. Havenith et al. found a positive correlation between A_d/mass ratio and core temperature not only for a warm-humid or jungle, but also for a neutral and a hot-dry (desert) climate. The positive correlation was highest in the warm-humid climate or jungle, however, implying that big subjects have the most marked advantage in the jungle or warm-humid climate. Our sensitivity analysis yielded the same results. As seen in Tables 6 and 7, an increase in weight, implying a smaller A_d/mass ratio, causes Tcore to decrease in most of subjects (negative value for the scaled derivative), with the largest effect visible in jungle and desert environments. And the increase in height implying a larger A_d causes an increase in Tcore in most of the male groups but this was not true for female group 1. With regard to the effect of fitness on thermoregulation, Gonzalez et al. showed that a higher value of gain in the rate of the total change in evaporative heat loss (ΔE_{SK}) to the change in mean body temperature (ΔT_b) indicates a greater ease in handling heat stress by increased evaporation of sweat without incurring excessive excursions of internal body temperature. And there was a significant positive correlation between $\Delta E_{SK}/\Delta T_b$ and the maximum aerobic capacity (VO2max). The effect of VO2max on Tcore was confirmed in our sensitivity analysis where the increase of VO2max leads to a decrease in Tcore in all models in most environmental conditions. There were two cases with a positive increase in Tcore in desert conditions for male groups 1 and 3, using the male model. Age by itself does not seem to be a factor in thermoregulation since the sensitivity analysis shows no major effect on Tcore, Tskin and HR due to age.

Havenith et. al, report that VO_{2max}, A_d, and % body fat were responsible for 62 % of the variance in linear regression model for Tskin. Their data set was obtained from 27 subjects (19 men and 8 women) engaged in ergometer exercise in a warm humid climate (35 C, 80% humidity) for one hour. The data are different from ours where the subjects are seminude, in a supine resting position in transient environmental conditions. However, our sensitivity study is consistent with this result. Also, there was a gender-based difference in terms of parameter contribution to Tskin. In males, VO_{2max} was a main parameter with a negative impact on Tskin, implying partial acclimation, improved sweating and skin cooling. However, in females, height and weight were the main parameters representing the heat loss capacity of the female body. But overall contributions of these parameters to Tskin were very small as Tair and Pa are the main driving factors in our data set.

Heart rate variation accounts for some of the gender-based differences in heat stress responses. Women are reported to have higher heart rates than men (Stephenson et al. 1993) since, on average, they have a greater surface area to body mass ratio (Nunneley et al. 1978), lower sweat rates (Frye et al. 1981), higher fat percentage, and lower aerobic fitness (Shapiro et al. 1980). In a study presented by Wells et al. (1973), the authors noted that independent of other stresses, heat raised HR by 6.5 beats per minute for women. Possibly the higher heart rate, elevated respiration and metabolic requirements occurring in female subjects implies an inadequacy of circulatory transport of oxygen for women in hot conditions (Havenith et al. 1990). Havenith (1990) notes that the increase in HR needed is smaller for a higher A_d as it provides more heat loss surface, resulting in improved cooling and thus efficient heat removal from core to skin (McArdle et al.1991). Our findings indicate that the group with old women shows a negative effect on HR with

increase of A_d (by increasing height by one standard deviation) in all four conditions, but the other female groups do not. There are many such trends that can be determined from the sensitivity results in Tables 6 and 7, and we have discussed only some representative ones here. It is also noted that we have not considered the effect of different exercise levels, and of factors such as hydration level, and non-thermal factors such as smoking, medication, and menstrual cycle, and these can be considered in future studies.

CONCLUSIONS

A novel transient predictive thermal model is reported for resting semi-nude supine individuals, to reliably predict Tcore, Tskin, and HR in transient environmental conditions for individual subjects. The model was then used to determine the relative importance of individual parameters on thermal stress variables, using a proposed sensitivity method. An important contribution of the reported study is to demonstrate that the predictive thermal model development methodology using neural networks is viable for human thermal response studies and can identify the relative importance of the individual parameters and environmental inputs. The model is validated by demonstrating prediction trends that are consistent with the literature. The ranking of the relative importance of the inputs in Tables 6 and 7 for various conditions provide 'fine-grained' insights into the thermal stress response phenomena. Some such insights are: fitness level is very important for predicting thermal risk but age is not; subjects with large A_d will have an advantage in handling heat stress in jungle and desert conditions; the effect of gender on the handling of thermal stress was not obvious from the model, but it seems that women usually have higher core temperature even if their individual physiological characteristics are matched with that of male, and this is something that needs further study. The sensitivity results in Tables 6 and 7 can be used for numerous other comparison studies,

depending on the application. For instance, one can compare between environments (jungle, desert, neural, cold), between outputs, and between groups of individuals (Table 3).

The data set we have used was limited to 35 semi-nude subjects resting in a supine position and it will be interesting to determine trends with larger datasets, in varying environmental conditions and exercise levels. Our study does, however, demonstrate that the proposed methodology for modeling and sensitivity analysis using neural networks has the potential to model and also discern the relative importance of the environmental and individual parameters on thermal stress responses in different conditions.

Acknowledgment

This research was supported in part by grant # DAAD16-03-P-0119, from US Army Research Institute of Environmental Medicine, Natick, MA. The authors also gratefully acknowledge the numerous insights provided by Richard Gonzalez of USARIEM.

REFERENCES

Amari S, Murata, N, Muller K –R, Finke M, and Yang HH. Asymptotic statistical theory of overtraining and cross-validation. *IEEE Transactions on Neural Networks*, 8(5): 985-996, 1997.

Bue GC. "Computer program documentation: 41-node transient metabolic man program," Lockheed Engineering and Sciences Company, Houston, TX, Tech. Rep.

Campbell AB, Nair SS, and Miles JB. Modeling the sweat regulation mechanism. 24th International Conference on Environmental Systems and 5th European Symposium on Space Environmental Control Systems. Friedrichsafen, Germany, June 20-23, 1994

Frank SM, Raja SN, Bulcao CF, and Goldstein. Relative contribution of core and cutaneous temperatures to thermal comfort and autonomic responses in humans. *Journal of Applied Physiology* 86(5): 1588-93, 1999.

French JD, Viswanath AD, Nair SS, Miles JB, and Lin CH. Parameters and assumptions in human thermal modeling for EVA applications. *SAE Transactions, Journal of Aerospace*, vol. 106, pp. 579-586, SAE 972320, 1997.

Frye AJ, Kamon E. Responses to dry heat of men and women with similar aerobic capacities. *Journal of Applied Physiology* 50(1): p. 65-70, 1981.

Fu G. A Transient, three-Dimensional mathematical thermal model for the clothed human. *Ph.D. Thesis*, Kansas State University, 1995.

Gonzalez RR, Berglund LG, and Stolwijk JAJ. Thermoregulation in humans of different ages during thermal transients. *Advances in Physiological Sciences*. Chapt.32. Contributions to Thermal Physiology, Pergamon Press, 560, 1981.

Gonzalez RR, McLellan TM, Withey WR, Chang SK, and Pandolf KB. Heat strain models applicable for protective clothing systems: comparison of core temperature response. *Journal of Applied Physiology* 83(3): 1017-1032, 1997.

Gonzalez RR. Problems of heat exchange and exercise during long term space operations: Use of a Thermoregulatory Model to Describe Physiologic Response. *Society of Automotive Engineers*, 2001.

Guan Y, Hosni M, Jones B, and Gielda T. Literature review of the advances in thermal comfort Modeling. *ASHRAE Transactions* 2003.

Haslam RA and Parsons KC. Computer-based models of human responses to the thermal environment: Are their predictions accurate enough for practical use?. in *Thermal Physiology*, J.B. Mercer, Ed., 763-768, 1989.

Havenith G and van Middendorp H. The relative influence of physical fitness, acclimatization state, anthropometrics measures and gender on individual reactions to heat stress. *European Journal of Applied Physiology* 61: 419-427, 1990

Hsu F. Modeling, simulation, and optimal control of the human thermal system, *Ph.D. Thesis*, Kansas State University, 1971.

Huizenga C, Zhang H, and Arens E. A model of human physiology and comfort for assessing complex thermal environments. *Building and Environment*, vol. 36: 691-699, 2001.

Hwang CL and Konz SA. Engineering models of the human thermoregulatory system: a review. *IEEE Transactions on Biomedical Engineering* 24(4): 309-325, 1977.

Iyoho A. Development of a two-dimensional human thermal model for EVA Applications, *MS Thesis*, Department of Mechanical and Aerospace Engineering, University of Missouri-Columbia.

McArdle WD, Katch FI, Katch VL. Exercise Physiology: Energy, Nutrition, and Human Performance, Philadelphia: Lea & Febiger, 1991.

Moran DY, Epstein A, Laor A, Vitalis, and Shapiro Y. Predicting heart rate response to various metabolic rates, environments, and clothing. *American Physiological Society*. 0161-7567, 1995.

Mungcharoen T, and Wissler E. A new two-dimensional human thermal model. *AIChE Symposium Series*, 85(269) :394-399, 1989.

Nunneley S. Physiological responses of women to thermal stress: a review. *Medicine and Science in Sports and Exercise*, 10: 250-255, 1978.

Pennes HH. Analysis of tissue and arterial blood temperatures in the resting human forearm. *Journal of Applied Physiology* 1(2): 93-122, 1948.

Prechelt L. Early stopping – But when? In: Orr, G.B., and Mueller, K.-R., eds., Neural Networks: Tricks of the Trade. Berlin: Springer, 55-69, 1998.

Shapiro Y, Pandolf KB, Avellini BA, Pimental NA, and Goldman RF. Physiological responses of men and women to humid and dry heat. *Journal of Applied Physiology* 49: 1-8, 1980.

Stephenson LA and Kolka MA. Thermoregulation in women. *Exercise and Sports Science Reviews*, 21:231-262, 1993.

Stolwijk JAJ. A mathematical model of physiological temperature regulation in man. Tech. Rep. CR-1855, NASA, Washington, DC,1971.

Tanabe S, Kobayashi K, Nakano J, Ozeki Y, and Konishi M. Evaluation of thermal comfort using combined multi-node thermoregulation (65MN) and radiation models and computational fluid dynamics (CFD). *Energy and Buildings* 34: 637-646, 2002.

Thornton SB, Xu Wenwei, and Nair SS. Thermal control of an advanced space suit. *Transactions of the Society of Automotive Engineers, Journal of Aerospace*: 69 -77, 2002.

Thornton SB and Nair SS. Parametric studies of human thermal mechanisms and measurements. *IEEE Transactions on Biomedical Engineering*, 47(4): 444-451, 2000.

Wells CL, Horvath SM. Metabolic and Thermoregulatory responses of women to exercise in two thermal environments. *Medicine and Science in Sports*, 6(1): 8-13, 1973.

Wissler EH. A mathematical model of the human thermal system. Bulletin of Mathematical Biophysics, 26: 147-166, 1964.

Wissler EH. Comparison of computed results obtained from two mathematical models: A simple 14-node model and a complex 250-node model. *Journal de Physiologie*, 63(3)P: 455-458, 1971.

Wyss CR, Brengelmann GL, Johnson JM, Rowell LB, and Niederberger M. Control of skin blood flow, sweating, and heart rate: role of skin vs. core temperature. *Journal of Applied Physiology* 36(6), June 1974.

TABLES

Table1. Details of the experimental dataset.

Gender	Group	N° of Subjects	Age (years)	Surface Area to mass ratio ($Cm^2 Kg^{-1)}$	Maximum Aerobic Capacity(VO2 max) ml/(min-kg)
Female	F1	5	11.7 ± 1.6	321.3 ± 21.4	43.8 ± 1.3
	F2	5	22.5 ± 2.3	307.3 ± 36.4	49.8 ± 1.3
	F3	3	40.0 ± 6.0	279.3 ± 11.1	35.8 ± 1.3
	F4	2	61.8 ± 2.0	290.3 ± 9.4	30.9 ± 1.3
Male	M1	5	11.8 ± 2.8	319.3 ± 35.9	47.8 ± 2.4
	M2	5	22.3 ± 2.9	270.3 ± 14.2	47.1 ± 2.1
	M3	5	34.0 ± 5.6	252.3 ± 11.9	44.4 ± 2.2
	M4	5	60.2 ± 5.0	253.3 ± 18.6	27.7 ± 1.5

Table 2. Description of the parameters.

	Variables	Description	Unit
Individual Characteristics	**Subject**	Identifier	
	Group	1 to 4	
	Age	Age of a subject	Years
	A_d	Surface area	m^2
	Gender	Male or Female	
	VO_2 Max	Max. aerobic capacity	ml/(min-kg)
	Height		Inches
	Weight		Kg
	M initial	Initial Metabolic Rate	$W*m^{-2}$
	HR initial	Initial Heart Rate	Beat/min
Controlled Variables	**Time**	A total of 140 min	Min
	Ta	Air Temperature	C
	Pa	Ambient Vapor Pressure	In-Hg
Measured Variables	**Tsk**	Skin Temperature	C
	Tes	Core Temperature (esophageal)	C
	HR	Heart Rate	Beat/min
	Evg	Evaporative Loss	g/min
	m_s	Sweating rate sweat capsule	$mg/(min*cm^2)$
	K_{chest}	Skin Conductance in Chest	$W/(m^2C)$
	K_{arm}	Skin Conductance	$W/(m^2C)$
	M	Metabolic Free Energy production	$W*m^{-2}$
	Disc	Discomfort Index	
	Tsens	Temperature Sensation Magnitude	
Calculated Variables	**Esk**	Heat Transfer via evaporation from the skin surface	$W*m^{-2}$
	Tb	Mean body temp.	C
	w	Skin wettedness	
	R+C	Dry Heat Loss	$W*m^{-2}$
	$\Delta Tb / \min$	Mean body temp. rate	$W*m^{-2}$
	S	Body Heat Storage Rate	$W*m^{-2}$
	Req Esk	Required Evaporative Heat Loss	$W*m^{-2}$
	ET	Effective Temp.	C
	HRR	Heart Rate Ratio	

Table 3. Average subject for each group, with mean individual parameters.

Male	**Average Male of group 1**	**SD**	**Average Male of group 2**	SD	**Average Male of group 3**	**SD**	**Average Male of group 4**	**SD**
Age (yrs)	11	2.58	22	3.69	34	6.22	60	5.56
VO_2 Max ($W*m^{-2}$)	48.55	6.29	47.11	5.93	46.08	7.61	27.6	3.94
M initial (ml/(min-kg)	54.027	4.42	49.06	5.23	54.6	6.42	51.05	5.60
HR initial (bpm)	72	8.64	73.6	5.16	76.5	4.56	83.46	3.82
Height (inches)	57.38	6.34	70.9	2.68	73.13	3.32	66.85	2.40
Weight (Kg)	39.1	12.65	70.24	8.04	77.21	4.63	72.61	2.76
Female	**Average Female of group 1**	**SD**	**Average Female of group 2**	SD	**Average Female of group 3**	**SD**	**Average Female of group 4**	**SD**
Age (yrs)	12	1.14	23	2.5	39	4.94	62	2.82
VO_2 Max ($W*m^{-2}$)	43.86	3.05	47.35	7.22	37	8.98	30.4	10.60
M initial (ml/(min-kg)	50.88	6.92	46.32	11.48	47.66	1.26	41.25	7.99
HR initial (bpm)	84	3.31	74	8.64	74.66	2.82	80	5.65
Height (inches)	60.75	7.87	64.37	2.04	64.70	0.61	61.12	0.17
Weight (Kg)	43.25	4.68	51.13	4.17	59.21	8.36	51	3.53

SD: standard deviation of each group

Table 4. Regression Coefficients for various physiological heat stress reactions with environmental, heat production and individual's parameters from Havenith et al. study (13).

Dependent Variables	**Ta** (°C)	**PH_2O** (kPa)	**M** (kW)	**% Fat**	**Surf:mass** (m^2kg^{-1})	**VO_{2max}**	**% VO_{2max}**	**Sweating**		**S**	**R^2** (%)	**R'^2** (%)
								set point	gain			
S (J/g)	x	x	x								88	
S (J/g)	x	x	x	x	x	x			x		92	33
Rectal Temperature (°C)	x	x	x	x							38	
Rectal Temperature (°C)	x	x	x	x	x	x		x			60	37
Skin	x	x	x	x							96	
Temperature (°C)												
HR (bpm)	x	x	x	x							75	
HR (bpm)	x	x	x	x			x				88	46

Ta, Ambient temperature; PH_2O, water vapor pressure; VO_2 max, maximal oxygen uptake; r^2, total variance explained by the equation; r'^2, the fraction of the residual variance left after introduction of climatic and work rate parameters in the prediction equation, which is explained by individual's parameters.

Table 5. Coefficients of correlation (R) of predicted values against experimental values for each output for all groups using gender-based models.

Group1	Male1	Male2	Male3	Male4	Male5	Female1	Female2	Female3	Female4	Female5
Tsk	0.985	0.983	0.9728	0.993	0.999	0.9262	0.9715	0.9566	0.9825	0.9819
Tcore	0.742	0.853	0.8720	0.778	0.942	0.7843	0.8188	0.9344	0.8504	0.8811
HR	0.9207	0.8995	0.8757	0.9019	0.8732	0.9041	0.9225	0.8776	0.8998	0.9086
Group2	Male1	Male2	Male3	Male4	Male5	Female1	Female2	Female3	Female4	Female5
Tsk	0.9850	0.9922	0.9881	0.9930	0.9850	0.9851	0.9843	0.9917	0.9478	
Tcore	0.8705	0.7580	0.9322	0.7390	0.7772	0.8920	0.8561	0.9193	0.7759	
HR	0.9552	0.8983	0.9669	0.8838	0.8428	0.9135	0.8886	0.8893	0.7959	
Group3	Male1	Male2	Male3	Male4	Male5	Female1	Female2	Female3	Female4	Female5
Tsk	0.9971	0.9963	0.9920	0.9900	0.9912	0.9870	0.9835	0.9748		
Tcore	0.9140	0.8381	0.8452	0.8141	0.8274	0.7921	0.8912	0.8798		
HR	0.9285	0.8334	0.7425	0.8433	0.8246	0.9262	0.8925	0.8574		
Group4	Male1	Male2	Male3	Male4	Male5	Female1	Female2	Female3	Female4	Female5
Tsk	0.9843	0.9661	0.9783	0.9520	0.9800	0.9761	0.9750			
Tcore	0.8812	0.8203	0.8672	0.8460	0.8392	0.947	0.9192			
HR	0.9470	0.8437	0.8011	0.9054	0.8283	0.9318	0.8373			

Table 6. Ranked and scaled sensitivity derivatives in Jungle and Desert conditions for 'average' subject from each group.

6a. Males

JUNGLE

	Male Group 1		Male Group 2		Male Group 3		Male Group 4	
Skin	'Height'	-1.0000	'VO2max'	-1.0000	'VO2max'	-1.0000	'Height'	-1.0000
		(0.0307)		(0.0499)		(0.0402)		(0.0358)
	'VO2max'	-0.8168	'Height'	-0.6403	'Height'	-0.9099	'HR '	0.4420
	'Weight'	-0.5168	'HR '	0.5607	'HR '	0.5445	'age '	-0.3815
	'HR '	0.4580	'age '	-0.3570	'age '	-0.3629	'VO2max'	-0.3348
	'M '	0.1808	'M '	0.2425	'Weight'	-0.3210	'M '	-0.1268
	'age '	-0.0729	'Weight'	-0.1791	'M '	0.1272	'Weight'	0.1177
Core	'Height'	-1.0000	'VO2max'	-1.0000	'VO2max'	-1.0000	'Height'	1.0000
		(0.0208)		(0.0456)		(0.0345)		(0.0186)
	'VO2max'	0.6244	'M '	0.6592	'M '	0.6557	'M '	0.4067
	'Weight'	-0.5352	'Height'	0.5426	'Height'	0.6164	'age '	0.3757
	'HR '	-0.5329	'Weight'	-0.4719	'Weight'	-0.4187	'Weight'	-0.3748
	'M '	0.3199	'HR '	0.3152	'HR '	0.3391	'HR '	-0.1680
	'age '	-0.0128	'age '	0.0543	'age '	0.1024	'VO2max'	-0.0047
HR	'Height'	1.0000	'VO2max'	-1.0000	'VO2max'	-1.0000	'Height'	1.0000
		(0.6435)		(1.6084)		(1.1731)		(0.4831)
	'VO2max'	0.6887	'M '	0.6686	'M '	0.7125	'Weight'	-0.6204
	'Weight'	-0.6825	'Weight'	-0.5244	'Weight'	-0.5661	'M '	0.5774
	'HR '	-0.5687	'Height'	0.4324	'HR '	0.4910	'age '	0.4706
	'M '	0.2964	'HR '	0.3781	'Height'	0.4096	'VO2max'	0.0639
	'age '	0.0407	'age '	0.0388	'age '	0.1027	'HR '	-0.0028

DESERT

	Male Group 1		Male Group 2		Male Group 3		Male Group 4	
Skin	'Height'	-1.0000	'Weight'	-1.0000	'Weight'	-1.0000	'Height'	1.0000
		(0.1226)		(0.0384)		(0.1588)		(0.1146)
	VO2max'	-0.6771	'Height'	-0.9929	'HR '	-0.8961	'VO2max'	0.7765
	'age '	-0.1032	VO2max'	-0.7021	'VO2max'	-0.4687	'age '	-0.5112
	'M '	-0.0824	'age '	-0.1229	'M '	-0.3690	'M '	-0.1242
	'Weight'	-0.0797	'M '	-0.0891	'age '	0.1485	'HR '	-0.0624
	'HR '	0.0289	'HR '	-0.0148	'Height'	-0.0679	'Weight'	0.0616
Core	'Height'	1.0000	'Height'	1.0000	'Weight'	1.0000	'VO2max'	-1.0000
		(0.0667)	'VO2max'	(0.0192)		(0.0536)		(0.0127)
	'VO2max'	-0.6832	'Weight'	0.7685	'HR '	0.8775	'Height'	-0.9101
	'HR '	0.0712	'HR '	0.6059	'VO2max'	0.6373	'HR '	0.3905
	'M '	0.0539	'age '	-0.1172	'M '	0.3704	'M '	0.3741
	'Weight'	0.0512	'M '	0.0431	'Height'	0.2671	'Weight'	0.3580
	'age '	-0.0173		0.0119	'age '	-0.1984	'age '	0.1439
HR	'VO2max'	-1.0000	'Weight'	-1.0000	'Weight'	-1.0000	'Height'	1.0000
		(0.8082)		(0.8205)		(1.2349)		(0.7449)
	'Height'	-0.9513	'age '	0.6184	'age '	0.6460	'VO2max'	0.8327
	'age '	0.8146	VO2max'	0.5288	'Height'	-0.2815	'Weight'	-0.3591
	'Weight'	-0.5613	'HR '	-0.2391	VO2max'	0.1717	'M '	0.2020
	'HR '	-0.2875	'M '	0.0714	'HR '	-0.1112	'age '	-0.1281
	'M '	0.0845	'Height'	0.0368	'M '	0.0678	'HR '	0.0783

6b. Females

JUNGLE

	Female Group 1		Female Group 2		Female Group 3		Female Group 4	
Skin	'Height'	1.0000	'HR '	1.0000	'Height'	1.0000	'HR '	1.0000
		(0.2052)		(0.0839)		(0.2052)		(0.0839)
	'VO2max'	-0.0792	'Height'	0.2866	'VO2max'	-0.0792	'Height'	0.2866
	'Weight'	-0.0422	VO2max'	-0.2551	'Weight'	-0.0422	VO2max'	-0.2551
	'HR '	-0.0383	'Weight'	-0.0998	'HR '	-0.0383	'Weight'	-0.0998
	'M '	0.0152	'M '	0.0254	'M '	0.0152	'M '	0.0254
	'age '	0.0070	'age '	0.0046	'age '	0.0070	'age '	0.0046
Core	'Height'	-1.0000	'VO2max'	-1.0000	'Height'	-1.0000	'VO2max'	-1.0000
		(0.0074)		(0.0767)		(0.0074)		(0.0767)
	'VO2max'	-0.7913	'Height'	0.7765	'VO2max'	-0.7913	'Height'	0.7765
	'Weight'	-0.4197	'Weight'	-0.3896	'Weight'	-0.4197	'Weight'	-0.3896
	'HR '	-0.3538	'HR '	0.0527	'HR '	-0.3538	'HR '	0.0527
	'M '	0.1738	'age '	0.0461	'M '	0.1738	'age '	0.0461
	'age '	0.0582	'M '	0.0047	'age '	0.0582	'M '	0.0047
HR	'Height'	1.0000	'HR '	1.0000	'Height'	1.0000	'HR '	1.0000
		(4.0794)		(2.9869)		(4.0794)		(2.9869)
	'VO2max'	-0.0464	'VO2max'	0.8947	'VO2max'	-0.0464	'VO2max'	0.8947
	'Weight'	-0.0257	'Height'	-0.6043	'Weight'	-0.0257	'Height'	-0.6043
	'HR '	-0.0183	'Weight'	0.3455	'HR '	-0.0183	'Weight'	0.3455
	'M '	0.0110	'age '	-0.0492	'M '	0.0110	'age '	-0.0492
	'age '	0.0034	'M '	0.0217	'age '	0.0034	'M '	0.0217

DESERT

	Female Group 1		Female Group 2		Female Group 3		Female Group 4	
Skin	'Height'	-1.0000	'HR '	-1.0000	'Weight'	-1.0000	'HR '	-1.0000
		(0.1737)		(0.0969)		(0.2013)		(0.1002)
	'Weight'	-0.5117	'Height'	-0.6465	'M '	-0.1653	'VO2max'	-0.6901
	'M '	0.4560	'Weight'	-0.4915	'HR '	0.1031	'M '	-0.3525
	'HR '	0.4544	'M '	-0.3519	'Height'	0.0783	'Weight'	-0.0950
	'VO2max'	-0.3486	'age '	0.1297	VO2max'	0.0686	'age '	0.0926
	'age '	0.0033	'VO2max'	-0.0638	'age '	0.0681	'Height'	0.0846
Core	'Height'	-1.0000	'Height'	1.0000	'Weight'	-1.0000	'Height'	1.0000
		(0.2101)		(0.0888)		(0.0507)		(0.2851)
	'VO2max'	-0.3828	'HR '	-0.6387	'Height'	0.8240	'HR '	-0.1692
	'M '	0.3810	'VO2max'	-0.5965	'VO2max'	-0.5391	'Weight'	-0.1195
	'Weight'	-0.2437	'Weight'	-0.4501	'HR '	-0.2055	'VO2max'	-0.1001
	'HR '	0.2225	'M '	0.0513	'M '	0.0592	'age '	0.0207
	'age '	-0.0396	'age '	0.0464	'age '	0.0520	'M '	0.0202
HR	'M '	1.0000	'Height'	-1.0000	'Height'	-1.0000	'Height'	-1.0000
		(0.9551)		(3.7397)		(1.2761)		(10.9790)
	'HR '	0.7674	'HR '	0.5831	'VO2max'	0.8468	'HR '	0.1449
	'VO2max'	-0.5548	VO2max'	0.4943	'HR '	0.7491	'Weight'	0.1163
	'Height'	-0.3551	'Weight'	0.2906	'Weight'	-0.1037	'age '	-0.0186
	'Weight'	-0.3133	'M '	-0.0351	'M '	-0.0921	VO2max'	0.0183
	'age '	-0.0079	'age '	-0.0186	'age '	0.0340	'M '	-0.0015

Table 7. Ranked and scaled sensitivity derivatives in Neutral and Cold conditions for an 'average' subject from each group.

7a. Males

NEUTRAL

	Male Group 1		Male Group 2		Male Group 3		Male Group 4	
Skin	'VO2max'	-1.0000	'VO2max'	-1.0000	'VO2max'	-1.0000	'VO2max'	-1.0000
		(0.0596)		(0.0943)		(0.0915)		(0.0761)
	'M '	0.7546	'M '	0.5339	'Weight'	-0.5862	'HR '	0.7357
	'HR '	0.6593	'HR '	0.4549	'M '	0.4256	'M '	0.6903
	'age '	0.3512	'Weight'	-0.3209	'age '	-0.1335	'Height'	-0.2913
	'Weight'	-0.2115	'age '	-0.1890	'HR '	0.1155	'Weight'	-0.2654
	'Height'	-0.0608	'Height'	-0.0288	'Height'	0.0658	'age '	-0.1324
Core	'VO2max'	-1.0000	'M '	1.0000	'M '	1.0000	'Height'	1.0000
		(0.0494)		(0.0346)		(0.0535)		(0.0619)
	'M '	0.9818	'HR '	0.7116	'HR '	0.8582	'age '	-0.3773
	'HR '	0.7320	'VO2max'	-0.5670	'VO2max'	-0.5472	'M '	0.2728
	'Weight'	-0.2322	'Height'	0.2015	'age '	-0.1770	'VO2max'	0.2440
	'age '	-0.1995	'Weight'	-0.1186	'Height'	0.1097	'Weight'	0.1029
	'Height'	0.0992	'age '	-0.1130	'Weight'	0.0093	'HR '	0.0431
HR	'VO2max'	-1.0000	'M '	1.0000	'M '	1.0000	'VO2max'	-1.0000
		(1.7602)		(1.1042)		(1.6003)		(1.6833)
	'M '	0.9260	'VO2max'	-0.8093	'HR '	0.8076	'M '	0.6670
	'HR '	0.6919	'HR '	0.7340	'VO2max'	-0.6502	'HR '	0.6355
	'Weight'	-0.2702	'Weight'	-0.2925	'Weight'	-0.2326	'Weight'	-0.2567
	'age '	-0.2027	'Height'	0.1750	'age '	-0.1512	'Height'	-0.2002
	'Height'	0.1044	'age '	-0.1177	'Height'	0.0669	'age '	-0.0601

COLD

	Male Group 1		Male Group 2		Male Group 3		Male Group 4	
Skin	'VO2max'	-1.0000	'VO2max'	-1.0000	'VO2max'	-1.0000	'Height'	1.0000
		(0.1254)		(0.0916)		(0.1099)		(0.0864)
	'M '	0.6508	'M '	0.9661	'M '	0.8237	'M '	0.7971
	'HR '	0.4718	'HR '	0.7239	'Weight'	-0.5119	'VO2max'	-0.5506
	'Weight'	-0.3122	'Weight'	-0.3813	'HR '	0.4979	'HR '	0.5298
	'age '	-0.2065	'age '	-0.2169	'Height'	0.2050	'age '	-0.4803
	'Height'	0.1588	'Height'	0.1440	'age '	-0.1843	'Weight'	-0.3115
Core	'M '	1.0000	'M '	1.0000	'HR '	1.0000	'VO2max'	-1.0000
		(0.0108)	'VO2max'	(0.0044)		(0.0093)		(0.0260)
	'HR '	0.8668	'HR '	-0.8247	'M '	0.8360	'M '	0.7896
	VO2max'	-0.8210	'Height'	0.6706	'Weight'	0.5040	'HR '	0.5192
	'Weight'	-0.2639	'Weight'	0.4811	'VO2max'	-0.3730	'Height'	-0.2338
	'Height'	0.1094	'age '	0.0732	'age '	-0.1399	'Weight'	-0.1972
	'age '	-0.0298		-0.0485	'Height'	0.0718	'age '	0.0144
HR	'VO2max'	-1.0000	'VO2max'	-1.0000	'M '	1.0000	'VO2max'	-1.0000
		(0.9350)		(0.6525)		(0.7283)		(0.9646)
	'M '	0.6692	'M '	0.9854	'VO2max'	-0.9832	'M '	0.8780
	'HR '	0.5025	'HR '	0.7294	'HR '	0.8712	'HR '	0.6396
	'Weight'	-0.3224	'Weight'	-0.3266	'Weight'	-0.2380	'Weight'	-0.3306
	'Height'	0.1524	'Height'	0.2299	'age '	-0.1957	'Height'	-0.0959
	'age '	-0.1220	'age '	-0.1688	'Height'	0.1582	'age '	-0.0489

7b. Females

NEUTRAL

	Female Group 1		Female Group 2		Female Group 3		Female Group 4	
Skin	'Height'	-1.0000	'HR '	1.0000	'M '	1.0000	'Height'	1.0000
		(0.4401)		(0.0379)		(0.0145)		(0.0691)
	'HR '	0.1941	'Height'	0.4880	'Height'	-0.9927	'VO2max'	-0.7113
	'M '	0.1908	'M '	-0.4250	'HR '	0.9741	'HR '	0.4191
		-0.0468	'VO2max'	-0.3696	'Weight'	0.3912	'M '	0.2255
	'VO2max'	0.0060	'Weight'	0.1242	'age '	0.1264	'Weight'	-0.1747
	'age '	-0.0024	'age '	0.0596	'VO2max'	0.1055	'age '	0.0765
	'Weight'							
Core	'Height'	-1.0000	'Height'	-1.0000	'Height'	1.0000	'Height'	1.0000
		(0.2805)		(0.0919)		(0.0331)		(0.3721)
	'HR '	0.1273	'VO2max'	0.6874	'VO2max'	-0.6904	'Weight'	-0.1253
	'M '	0.1246	'HR '	-0.3885	'HR '	-0.5064	'VO2max'	-0.0920
		-0.0501	'Weight'	0.3716	'Weight'	-0.2698	'HR '	-0.0688
	'VO2max'	-0.0267	'age '	-0.0661	'M '	0.1636	'age '	0.0284
	'Weight'	-0.0001	'M '	0.0546	'age '	0.0627	'M '	0.0103
	'age '							
HR	'HR '	1.0000	'Height'	1.0000	'HR '	1.0000	'Height'	-1.0000
		(0.5884)		(3.4201)		(1.1482)		(14.1845)
	'Height'	-0.9977	'HR '	0.8945	'Height'	-0.9973	'HR '	0.1828
	'M '	0.9580	'VO2max'	-0.7080	'VO2max'	0.8577	'Weight'	0.1232
		-0.2107	'Weight'	0.4223	'Weight'	0.3942	'VO2max'	0.0477
	'VO2max'	-0.1902	'M '	-0.0703	'M '	0.1622	'M '	0.0248
	'Weight'	0.1173	'age '	0.0537	'age '	-0.0050	'age '	-0.0240
	'age '							

COLD

	Female Group 1		Female Group 2		Female Group 3		Female Group 4	
Skin	'Height'	-1.0000	'Height'	-1.0000	'Height'	-1.0000	'HR '	-1.0000
		(0.5384)		(0.3751)		(0.3742)		(0.2593)
	'Weight'	0.1941	'HR '	-0.5662	'Weight'	0.9927	'VO2max'	-0.9295
	'M '	0.1908	'VO2max'	-0.2842	'M '	0.9741	'Height'	0.1834
	'HR '	0.0468	'Weight'	-0.1759	'age '	-0.3912	'M '	0.1763
	'age '	-0.0060	'M '	0.0929	'VO2max'	-0.1264	'Weight'	0.1172
		0.0024	'age '	-0.0589	'HR '	-0.1055	'age '	-0.0612
	'VO2max'							
Core	'Height'	-1.0000	'VO2max'	-1.0000	'VO2max'	-1.0000	'Height'	1.0000
		(0.2581)		(0.0906)		(0.0249)		(0.4716)
	'HR '	0.1273	'HR '	-0.9480	'HR '	-0.6904	'HR '	-0.1713
	'M '	0.1246	'Height'	0.4039	'Height'	-0.5064	'VO2max'	-0.1411
	'Weight'	0.0501	'Weight'	-0.3758	'M '	0.2698	'Weight'	-0.1178
	'age '	-0.0267	'M '	0.0584	'Weight'	-0.1636	'age '	0.0245
		-0.0001	'age '	0.0445	'age '	-0.0627	'M '	0.0117
	'VO2max'							
HR	'HR '	1.0000	'Height'	-1.0000	'Height'	-1.0000	'Height'	-1.0000
		(0.7461)		(3.5811)		(1.7732)		(17.0163)
	'M '	0.9977	'VO2max'	0.6936	'HR '	0.9973	'Weight'	0.1329
	'Height'	0.9580	'HR '	0.6396	'VO2max'	0.8577	'HR '	0.0898
	'Weight'	0.2107	'Weight'	0.4979	'Weight'	0.3942	'M '	0.0310
		-0.1902	'M '	0.1032	'M '	0.1622	'age '	-0.0309
	'VO2max'	-0.1173	'age '	-0.0772	'age '	-0.0050	'VO2max'	-0.0064
	'age '							

FIGUERS

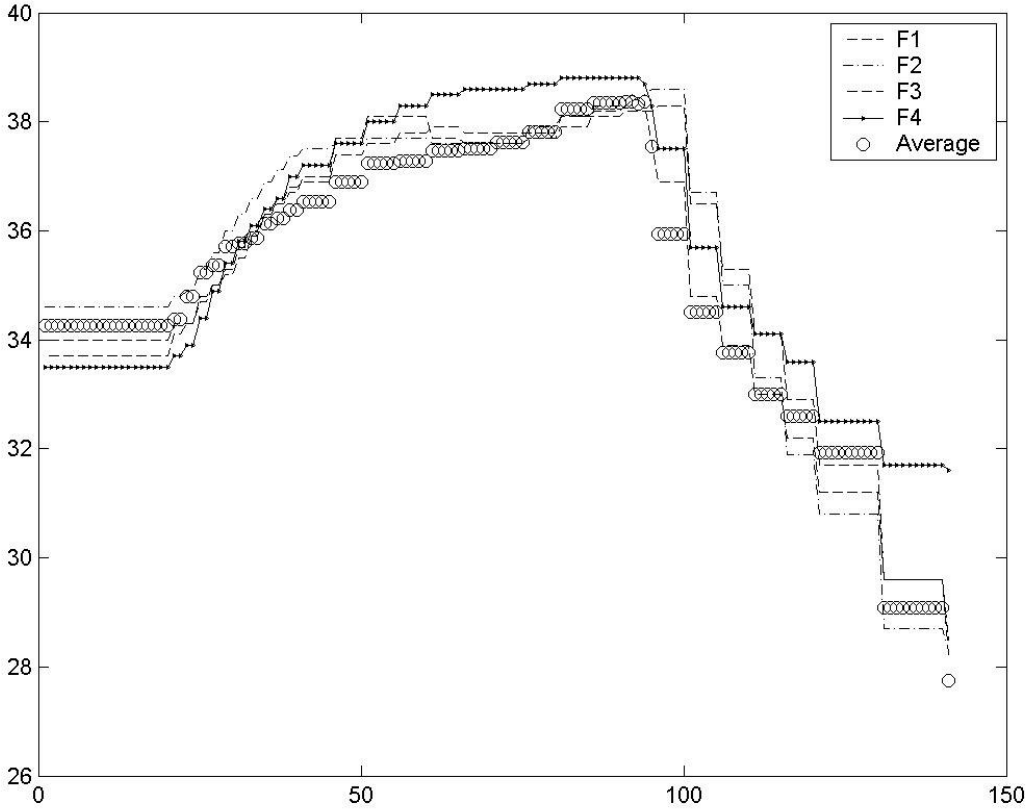

Figure 1. Experimental Tskin data for members of Female Group 2 and predictions for the ‘average’ person in that group.

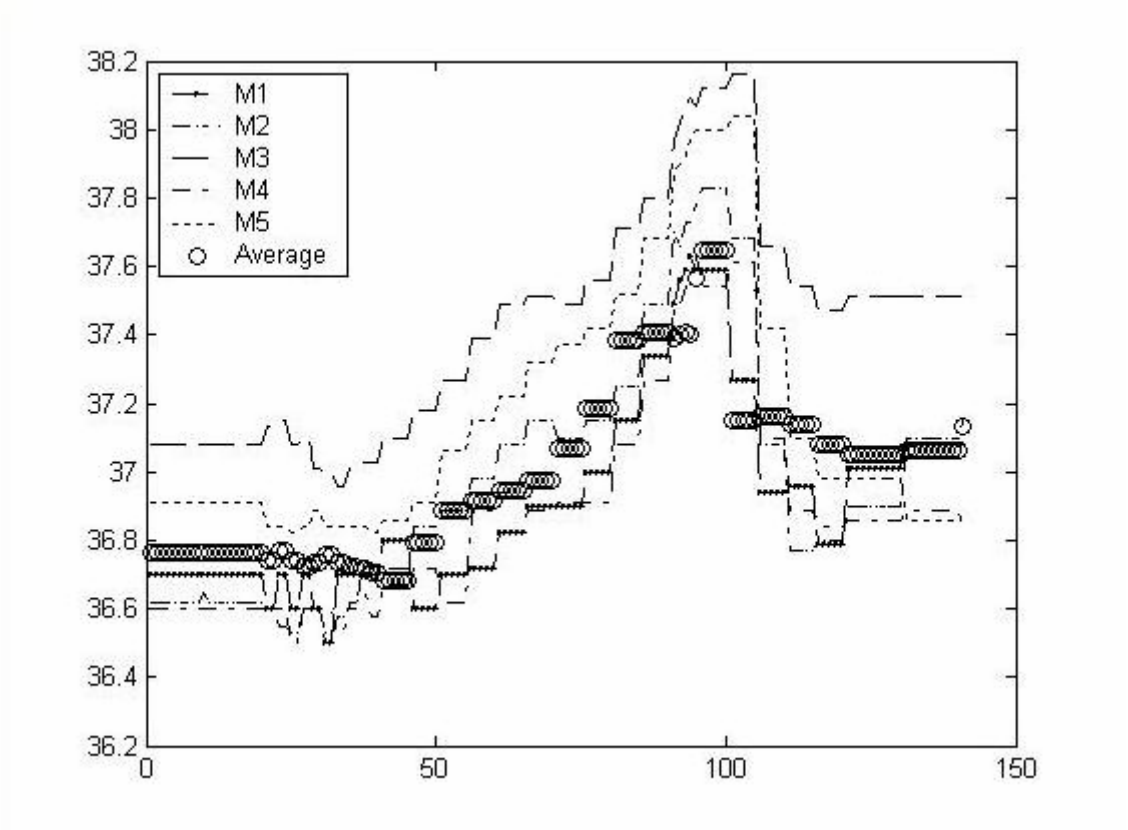

Figure 2. Experimental Tcore data for members of Male Group 2 and predictions for the 'average' person in that group.

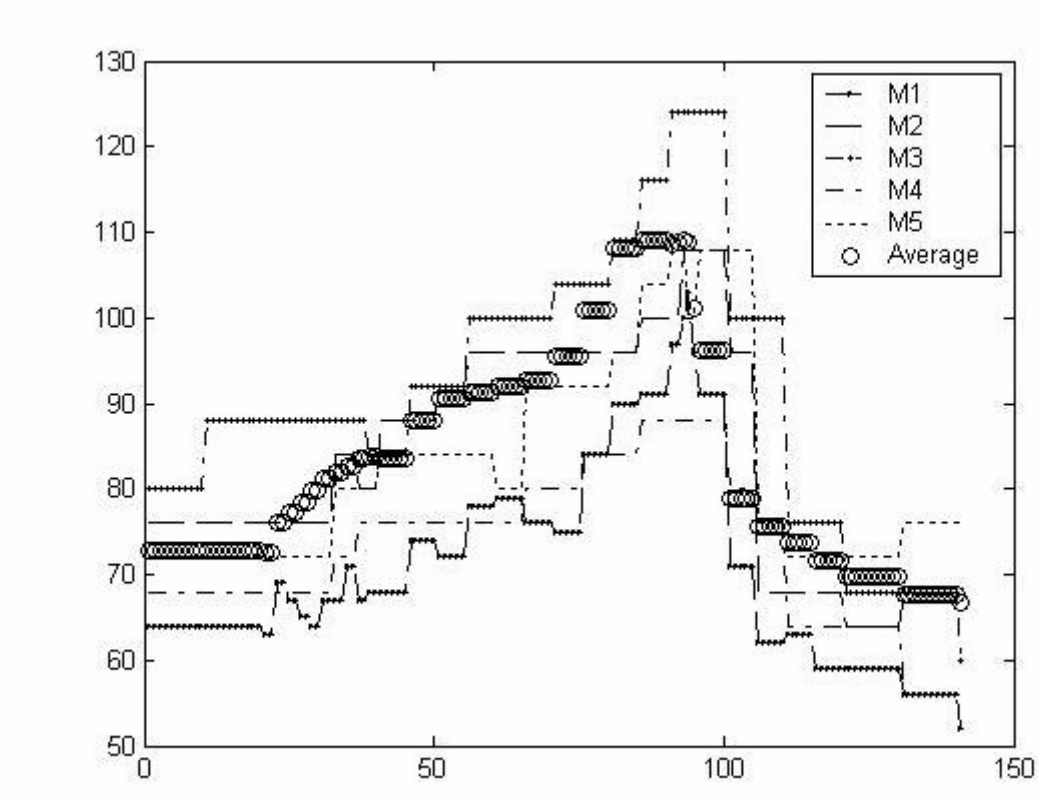

Figure 3. Experimental HR data for members of Male Group 2 and predictions for the 'average' person in that group.

CHAPTER 6

HUMAN THERMAL MODEL WITH EXTREMITIES FOR ASYMMETRIC ENVIRONMENTS

Abstract. A new computational model of the human thermal system is developed that accounts for asymmetric environments and includes extremities is reported. The model incorporates 2-dimensional (radial and circumferential) heat transfer along with arterial and venous countercurrent blood flow. Digits to predict toe and fingertip are modeled as well as arteriovenous anastomoses (AVAs), all of which are important in extremity discomfort.

I. INTRODUCTION

Humans are poor judges of their thermal state, and so are not able to control their thermal comfort well. As an example, the authors have been working with NASA to automate thermal control in astronaut spacesuits. NASA found during the first space flight that sufficient cooling of an astronaut could not be accomplished via air convection in the suit due to ventilation, and have since been using a liquid cooling garment (LCG) to circulate water for cooling the astronaut during space walks. In the present arrangement, the astronaut controls the temperature of the water flowing through the LCG by manually adjusting the temperature control valve (TCV) located on the front of the space suit. However, manually manipulating the TCV setting can dramatically reduce the productivity of the astronaut, distracting them from the extra-vehicular activity (EVA) mission at hand; and since an astronaut's attention is focused on other things during EVA, there are time lags in the application of temperature control. This can cause

overheating or overcooling; placing unneeded thermal stress on the astronaut, and degrading EVA performance. Human thermal models are needed to accurately describe the transient heat transfer processes and predict the thermal response within an acceptable band of accuracy before an automatic controller can be designed. Such human thermal models are also relevant for various other applications involving fire fighters, combat pilots, hazardous waste workers, and other industries where comfort in a thermally stressful environment needs to be insured.

The development of mathematical models for human thermoregulation started in the early 20th century [44]. Early models used simple representations for the human thermal system. However, in the 1960s, more detailed models were developed that incorporated our increased understanding of human thermoregulation, as these complexities became known, to improve accuracy [20, 44, 16]. Although many aspects of the human active thermal system are is still not understood well. The passive thermal system has been computationally better modeled although the parametric and model approximates do present challenges. The latter is due to unaccounted parameter variations between human subjects (inter-subject variations) and effects influencing the individual at different times (intra-subject variations). It is advantageous for a modeler to identify important parameters of the passive thermal system and quantify their effect on the model's response to gain a better understanding of modeling issues and limitations.

Numerous human thermal models have been developed and used in many practical applications for the past sixty years, starting with the development of a steady-state model to analyze heat transfer in a resting human forearm by Pennes in 1948 [10]. This cylindrical model served as the basis for a more advanced model by Wissler [7] and it is still widely used for prediction of temperature elevation during hyperthermia [22, 23]. Subsequent advances in computing technology and increased experimental data on human physiology helped researchers

in developing better and more sophisticated human thermal models. In the 1960s, early versions of the well-known Wissler [20], Stolwijk [14], and Gagge [3] models were being developed. All later human thermal models for the most part, are probably extensions of these three mathematical models.

However, due to the natural complexity of human thermoregulation, it has been difficult to study the issue of accuracy for such models. Quantitative comparisons among models have also been difficult due to the individual characteristics of each model under particular environmental conditions [2, 24, 25]. From a user point of view, it has not been clear which of the models would be best suited for a particular environment and application. Various research teams [18, 21, 26, 27] have developed models in the past decade to be used in environments that range from uniformly steady state to extremely transient and non-uniform. Models such as the Kansas State University model [26, 28], the Berkeley model [27], and the MU model [18] are in development to achieve such objectives. Even though these models incorporate more detail, they have their roots either in the Wissler [15] or the Stolwijk [14] models. All these models include heat transfer within the body as well as between the body and its environment, as well as sweating, shivering, and vasomotor capabilities.

This paper is organized as follows: section II provides a brief review of human thermal models, section III presents the additions made to the 41-Node Man and dynamic equations for numerical solutions, section IV reports the simulation results with discussion, and section V states the conclusions.

II. PROPOSED 2-D MODEL WITH EXTREMITIES

The thermal model presented in this paper, the MU Man model, incorporates many aspects of past human thermal models, especially the 41-Node Man [1] which is based on Stolwijk's six-segment, 25-node model [14]. The 14 major cylindrical segments include the head, torso, arms,

hands fingers, legs, feet and toes. The five fingers on each hand are represented as one cylinder and so are the five toes on each foot neither of which are present in the 41-Node Man. Similar to the 41-Node man, each segment contains four concentric layers representing the four layers the core, muscle, fat and skin regions.

The MU Man model also incorporates two-dimensional (radial and angular) heat conduction within the body as opposed to the radial-only in the 41-Node man model. Each body element in the model contains six angular sectors to account for these angular temperature variations. The model utilizes finite difference method (FDM) to solve the system of equations. The FDM approach was used as opposed to finite element method (FEM) to achieve faster execution for simulating a variety of input conditions [43]. Thermal modeling combining both FDM and FEM features has been successfully done [26], and could be an attractive alternative.

The MU Man model incorporates heat exchange between tissues and arteries/veins where the arterial and venous temperatures vary from element to element in contrast to a single blood pool used by the 41-Node Man model. In addition, the MU Man model incorporates the arteriovenous anastomoses (AVAs) in the digits along with the effects of cold-induced vasodilatation (CIVD), which will be important in studies dealing with extremity discomfort.

A. Two-dimensional Conduction

One-dimensional models cannot account for cases where disparate environmental conditions exist on different sides of the body. A study by Hall and Klemm showed that when the body was exposed to cold (-6.7°C) and hot (82ºC and 93.3°C) radiative temperatures on different sides of the body, skin temperature differences between the anterior and posterior sides ranged between 9-10ºC [4]. These experiments by Hall and Klemm were also validated through simulations of the two-dimensional model developed by Kuznetz where the environmental conditions of the

experiments were duplicated for the simulations [6]. Kuznetz's model also predicted different anterior and posterior temperatures for the same body element. For wall temperatures of -6.7° and 82º C, temperature differences between Kuznetz's model and Hall and Klemm's experiment never exceed 1.5º C. A one-dimensional model where temperature does not vary with the angle cannot predict such temperature differences on different sides of the same body element.

In addition, one-dimensional models cannot account for cases where non-uniform heat generation within body causes temperatures to vary for different sides of an element. Non-uniform heat generation can occur due to non-homogeneity of organs within an element. Also, non-uniform heat generation can occur within muscles during exercise. For example, a particular exercise could work the hamstrings, but not the quadriceps. This would cause more heat generation in the back of the leg than in the front.

B. Modeling the Digits

For the development of this model, explicit modeling of digits (fingers and toes) was incorporated, which has been suggested by NASA to be important. Studies have shown [5] that the digits, especially the fingers, respond to changes in the thermal environment quicker than all other locations of the body. Thus, a change in a digit temperature is a good indication of thermal imbalance in the body. Thus, a human thermal model that accurately predicts the digit thermal dynamics is important.

Accurate digit modeling is also important in extra-vehicular activity (EVA) applications. During EVA, astronauts encounter situations where they must handle objects with glove protected fingers and hands. If the object is at a different temperature than the glove, then heat transfer will occur between the glove and object. This will cause some kind of thermal

imbalance that will be detected first by the fingers. Thus, thermal comfort must still be insured during such heat exchanges.

C. Detailed Cardiovascular Model

In the past, many different techniques have been used to thermally model blood [1, 3, 14, 15, 16]. One technique is to use a single blood pool, which assumes that the blood temperature is the same throughout the body. This assumption greatly simplifies the circulatory system. Since, the arterial blood flow is so fast, it is assumed the blood temperature is homogeneous all throughout the body. However, this blood modeling technique does not incorporate the fact that blood entering the tissue will exit the arteries approximately at the tissue temperature. In addition, it is known that the blood temperature varies at different locations in the body. Therefore, there is a need to incorporate a blood model that includes the explicit modeling of arteries and veins where blood temperature can vary at different areas in the body as seen in the Wissler model [15]. In independently modeling arteries and veins, heat transfer occurs between the arteries and tissue, and between the veins and tissue. In addition, countercurrent heat exchange between arteries and veins approaches a realistic circulatory system. However, problems arise due to the difficulty in determining parameters such as the heat transfer coefficients between the arteries and veins, between the arteries and tissue, and between the veins and tissue.

D. AVA Modeling

The arteriovenous anastomoses are basically shunts which directly connect the arteries and venous plexuses, through which nutrient materials, metabolic products, and gases are not normally exchanged with the tissue fluids [36]. The AVAs are located in all major organs and its diameters vary depending upon the size of the vessel from which an AVA arises. In total length AVAs may vary form extremely short “side to side” shunts of only a few micrometers to true

vessels which may reach 2-4 mm, in length. They have a relatively large diameter, on an average 35 µm (20—70 µm) as compared to capillaries (5—10 µm) and are richly supplied with nerve fibers [37]. For heat exchange, most of this vasculature is located in the hands, feet, ears and hairless regions of the face [38, 39]. When they are open, large amounts of blood can pass through to the venous plexuses. It is estimated that blood flow into the subcutaneous venous plexuses can be as much as 30% of the total cardiac output [19]. Activation of sympathetic nerves leads to active vasoconstriction, and decrease in sympathetic activity leads to passive vasodilatation. In a moderately warm environment, the AVAs are open; and in the cold, the AVAs are almost closed. Thus, AVAs play a key role in regards to the thermal comfort of extremities [5]. A few published models [33, 34] have incorporated AVA vasomotor control to improve skin blood flow rate in limbs. Due to the importance of AVAs in human thermoregulation, the functions of the AVAs are included in this model, and its inclusion paves the way for future studies involving extremity discomfort.

E. Cold-Induced Vasodilatation

The phenomenon termed cold-induced vasodilatation (CIVD) most likely can be attributed to the AVAs. In CIVD, sufficient cold exposure causes temporary cyclic increases in blood perfusion to the fingers, which in turn increases finger temperatures. In general, CIVD is thought to be the body's way of preventing cold injuries [29] and improving manual dexterity in the cold. There have been a few noteworthy attempts to model a single digit during cold stress that include the CIVD phenomenon [30, 31]. For this study, the effects of CIVD on the finger will be modeled while using a whole-body simulation.

F. Model Equations

This model features three different clothing ensembles, nude, liquid cooling garment (LCG), and liquid cooling and ventilation garment (LCVG) with suit. For this paper, the equations for

the nude human will be the focus. However, the complete documentation of the model, including parameter values (which are too numerous to include in this paper), can be obtained if the reader desires further insight [18].

The human thermal system can be divided into two components. The first is the passive thermal system that includes non-decision making heat transfer processes. The second component is the active thermal system that includes all the decision-making processes such as sweating, shivering and vasomotor functions. These active systems attempt to update parameters or heat exchange rates on-line depending on the thermal state of the simulated subject.

Passive System

This human thermal model utilizes 14 cylindrical elements to represent the human body as shown in Figure 1a. Within each element are four concentric regions: the core, muscle, fat and skin layers as shown in Figure 1b. Each element contains radially and angularly varying temperature nodes. Each element contains six equally spaced angular sectors. Six angular sectors were used since it was shown that this enough to insure accurate temperature deviations in the angular direction [7]. Figure 1c shows the nodal spacing within each sector for the nude case. For the nude case, there are a total of 686 temperature nodes. The heat equation for two-dimensional conduction and heat generation is shown below.

$$C\frac{\partial T}{\partial t} = k\left[\frac{\partial^2 T}{\partial r^2} + \frac{1}{r}\frac{\partial T}{\partial r} + \frac{1}{r^2}\frac{\partial^2 T}{\partial \theta^2}\right] + \dot{Q}_{blood} + \dot{Q}_{gen} + \dot{Q}_{resp} \qquad (1)$$

The term on the left-hand side of Eq. 1 represents the heat storage, V represents the volume, C represents the thermal mass, the bracketed term on the right represents the conduction between

tissues, $\dot{Q}_{blood}$ represents the rate of heat addition due to blood, $\dot{Q}_{gen}$ represents the rate of heat generation, and $\dot{Q}_{resp}$ represents the rate of heat addition due to the respiratory system.

Eq. 1 is used for tissue nodes in the middle of a specific tissue region. However, there is a need for an equation for the temperature node at the interface between two distinct tissue regions. The following heat flux equality can be used for this purpose.

$$-k_{in}\frac{\partial T}{\partial r} = -k_{out}\frac{\partial T}{\partial r} \tag{2}$$

In Eq. 2, k_{in} represents the conductivity of the tissue layer on the inside of the interface and k_{out} represents the conductivity of the tissue layer on the outside of the interface.

In addition, at the edge of the skin layer, the following boundary condition must be imposed.

$$-k\frac{\partial T}{\partial r} = \dot{Q}''_{ext} \tag{3}$$

For the nude case

$$\dot{Q}_{ext} = \dot{Q}_{conv} + \dot{Q}_{rad} + \dot{Q}_{lat} \tag{4}$$

where $\dot{Q}_{conv}$, $\dot{Q}_{rad}$, and $\dot{Q}_{lat}$ represent the rate of heat transfer to due to convection, radiation and latent heat loss, respectively. It should be noted that $\dot{Q}_{lat}$ represents the latent heat loss for the entire body element.

Convection - The rate of heat transfer due to convection from the surrounding air to a skin temperature node is

$$\dot{Q}_{conv} = hA(T_{air} - T) \tag{5}$$

where h is the convection coefficient, A is the area of the skin surface and T_{air} is the ambient air temperature.

Radiation - The rate of heat transfer due to radiation from the surroundings to the skin surface is

$$\dot{Q}_{rad} = A\sigma F\left[(T_r + 273.15)^4 - (T + 273.15)^4\right] \tag{6}$$

where A is the skin surface area, σ is the Stefan-Boltzmann constant, F is the interchange factor and T_r is the radiant temperature.

4.1. **RESPIRATORY HEAT LOSS** - THE RATE OF RESPIRATORY HEAT LOSS HAS TWO COMPONENTS: SENSIBLE AND LATENT HEAT LOSS SUCH THAT

$$\dot{Q}_{resp} = \left(\dot{Q}_{resp,lat} + \dot{Q}_{resp,sens}\right)K_{resp} \tag{7}$$

where

$$\dot{Q}_{resp,lat} = MR\frac{G_1}{T_{air,abs}}\left(Pv_{air} - Pg_{resp}\right) \tag{8}$$

and

$$\dot{Q}_{resp,sens} = \frac{Cp_{air}P_{air,abs}MR \cdot G_2}{T_{air,abs}}\left(T_{air} - T_{resp}\right) \tag{9}$$

where K_{resp} is the percentage of the respiratory heat loss at a specific temperature node, MR is the metabolic rate, $T_{air,abs}$ is the absolute air temperature, Pv_{air} is water vapor pressure of air, Pg_{resp} is the saturation pressure of water at the respiratory temperature, Cp_{air} is the specific heat of air,

$P_{air,abs}$ is the absolute air pressure, T_{resp} is the respiratory temperature, and *G1* and *G2* are empirical constants .

Heat transfer due to blood - The rate of heat transfer due to the blood to each tissue node is

$$\dot{Q}_{blood} = hA_a(T_a - T) + (\dot{e}_b + hA_v)(T_v - T) \tag{10}$$

where $\dot{e}_b = \dot{m}_b Cp_b$, hA_a is the heat transfer coefficient between the tissue and artery, hA_v is the heat transfer coefficient between the tissue and vein, $\dot{e}_b$ is the thermal mass blood flow rate, and T_a and T_v are the artery and vein temperatures, respectively. In this model, blood flow is assumed to originate at the heart flowing to tissue layers through the arteries, which flow into the capillary bed and then exits the tissue layer through the veins. In this model, it is assumed that the blood entering tissue will exit the arteries approximately at the tissue temperature. Thus, blood entering the capillaries will approximately be at the tissue temperature. Thus, the term in Eq. 10 that involves $\dot{e}_b$ indicates perfect heat transfer within the capillary bed, or in other words that blood entering the capillary bed (at the tissue temperature) will exit at the vein temperature.

Active System

The active thermal system used in this thermal model utilizes the equations used for sweating, shivering and vasomotor actions from the 41-Node Man [1].

Latent heat transfer - The latent transfer of heat from the skin is comprised of two components: diffusion and active sweating such that

$$\dot{Q}_{lat} = \dot{Q}_{dif} + \dot{Q}_{sweat} \tag{11}$$

where $\dot{Q}_{dif} = AG_3\left(Pv_{air} - Pg_{skin}\right)^{-or\,0}$ and

$$\dot{Q}_{sweat} = -SK_{sweat}\,2^{(T-T_{set})_{skin}G_4} \tag{12}$$

where

$$S = (T_c - T_{set})^{+or\,0}_{head}\left(G_5 + G_6\sum_{i=1}^{14}\gamma_{sw}(T_i - T_{set})^{+or\,0}_{skin}\right) \tag{13}$$

where A is the diffusion area, Pv_{air} is the water vapor pressure of the environment, Pg_{skin} is the saturated pressure of water at the skin temperature, K_{sweat} is the sweat distribution, T_{set} is the setpoint temperature, T_c is the core temperature, γ_{sw} is the skin mass distribution, and G_4, G_5 and G_6 are empirical constants. In addition, active sweating is limited by the maximum evaporative capacity

$$\dot{Q}_{\max} = \left(1 - \exp\left(-\frac{\dot{Q}_{sweat}G_7T_{air}R_w}{H_mAh_{fg,air}(Pg_{skin} - Pv_{air})}\right)\right)\frac{H_{mass}Ah_{fg,air}(Pg_{skin} - Pv_{air})}{T_{air}R_w} \tag{14}$$

where H_{mass} is the mean mass transfer coefficient, $h_{fg,air}$ is the enthalpy of vaporization, R_w is the universal gas constant, and G_7 is an empirical constant. As state previously, $\dot{Q}_{lat}$ represents the latent heat loss from an entire body element. The superscript *"- or 0"* indicates that the preceding term must be either negative or zero and the superscript *"+ or 0"* indicates that the preceding term must be either positive or zero.

Shivering - The rate of heat production due to shivering is distributed within the muscle region of each element and is given by

$$\dot{Q}_{shiver} = \left(\sum_{i=1}^{14} (T_{set\,s} - T_s)_i^{+or0} \gamma_{sh,i} \right) (T_{set\,c} - T_c)_{head}^{+or0} G_8 K_{shiver} \frac{M_m}{M_{m0}} \tag{15}$$

where $T_{set,s}$ is the skin setpoint temperature, T_s is the skin temperature, γ_{sh} is the skin mass distribution, $T_{set,c}$ is the core setpoint temperature, T_c is the core temperature, K_{shiver} is the shiver distribution, G_8 is an empirical constant and M_m/M_{m0} is the muscle mass to nominal muscle mass ratio. The superscript *"+ or 0"* indicates that the preceding term must be either positive or zero.

Vasomotor functions - In this model, the vasomotor actions work either to increase or decrease the blood flow rate to the skin. During vasodilatation, the blood flow rate to the skin is increased to encourage heat loss to the environment. During vasoconstriction, the blood flow rate to the skin is decreased to inhibit heat transfer to the environment. Vasodilatation occurs when the simulated subject is too warm, and vasoconstriction when cold. The skin thermal mass blood flow rate is updated on-line using the following equation:

$$\dot{e}_{b\to s} = \frac{\dot{e}_{b\to s,basal} + \dot{e}_{dil}}{1 + \Re} \tag{16}$$

where $\dot{e}_{dil} = (T_c - T_{set\,c})_{head}^{+or0} G_9 K_{dil} \frac{M_s}{M_{s0}}$ and

$$\Re = \left((T_{set\,c} - T_c)_{head}^{+or0} + \sum_{i=1}^{14} \gamma_{cons} (T_{set\,i} - T_i)_{skin}^{+or0} \right) G_{10} K_{cons} \frac{M_s}{M_{s0}} \tag{17}$$

where K_{dil} is the vasodilatation distribution, K_{cons} is the vasoconstriction distribution, M_s/M_{s0} is the skin mass to nominal skin mass ratio, and G_9 and G_{10} are empirical constants. The superscript *"+ or 0"* indicates that the preceding term must be either positive or zero.

The AVA system – The AVA mechanism in our human thermal model is defined as a function of core temperature, mean skin temperature, and skin temperatures at the distal parts. The AVA model proposed here uses the framework developed by Takemori et al., which they used for modeling extremity blood perfusion in their own human thermal model [33]. Thus, the proposed AVA structure for our thermoregulatory model is

$$\dot{e}_{b\to s} = \dot{e}_{\max\_dil} \times AVA_{\lim b} \tag{18}$$

$$AVA_{\lim b} = a(T_{sk} - 34) + b(T_{core} - 36.8) + c \tag{19}$$

where $\dot{e}_{\max\_dil}$ is the maximum skin thermal mass blood flow in the hands, feet, fingers, or toes, AVA_{LIM} is a non-dimensional fraction related to the level of openness of the AVAs (0~1), a and b are weighting coefficients, and c is a constant.

During CIVD, $AVA_{limb} = 1$, if the skin temperature at the finger is less than T_{min}, where T_{min} is the lowest skin temperature at which CIVD begins and varies from one individual to the next [40]. Another parameter that can be specified in the model is the length of time that the CIVD occurs before the AVAs begin constricting again, which also varies from person to person. In reality, these parameters are based on individual characteristics (i.e. gender, age, level of cold acclimatization, genetics, etc.) as well as the thermal state (i.e. core and mean skin temperatures) of the simulated subject [40]. For instance, some studies have noticed a lower CIVD response in the elderly [41]. Gender studies have shown a greater hand and finger blood flow in men than in women, but gender studies involving CIVD have in general been inconclusive has to whether there are differences [40]. The CIVD response also appears to be more pronounced for cold

acclimatized persons [42]. The current model does not account for individual differences in regards to CIVD, but this will need to be accounted for in any future modeling endeavors.

C. Numerical Solution

The heat transfer equations are solved numerically using MATLAB™/SIMULINK™. Eqs.1-3 can be approximated using the following equation.

$$\begin{aligned}
\left.\frac{\partial^2 T}{\partial r^2}\right|_{r,\theta} &\approx \frac{T_{r+1,\theta} + T_{r-1,\theta} - 2T_{r,\theta}}{(\Delta r)^2} \\
\left.\frac{\partial T}{\partial r}\right|_{r,\theta} &\approx \frac{T_{r+1,\theta} - T_{r-1,\theta}}{2\Delta r} \\
\left.\frac{\partial^2 T}{\partial \theta^2}\right|_{r,\theta} &\approx \frac{T_{r,\theta+1} + T_{r,\theta-1} - 2T_{r,\theta}}{(\Delta \theta)^2} \\
\left.\frac{\partial T}{\partial t}\right|_{r,\theta} &\approx \frac{T_{r,\theta}^{p+1} - T_{r,\theta}^{p}}{\Delta t}
\end{aligned} \tag{20}$$

Thus, after substituting Eq. 20, Eq. 1 has the following numerical approximation.

$$\begin{aligned}
C\frac{T_{r,\theta}^{p+1} - T_{r,\theta}^{p}}{\Delta t} = {} & \frac{k\Delta\theta(R_r + R_{r+1})L}{2\Delta r}\left(T_{r+1,\theta}^{p} - T_{r,\theta}^{p}\right) + \frac{k\Delta\theta(R_r + R_{r-1})L}{2\Delta r}\left(T_{r-1,\theta}^{p} - T_{r,\theta}^{p}\right) \\
& + \frac{k\Delta r L}{R_r \Delta\theta}\left(T_{r,\theta+1}^{p} + T_{r,\theta-1}^{p} - 2T_{r,\theta}^{p}\right) + \dot{Q}_{blood} + \dot{Q}_{gen} + \dot{Q}_{resp}
\end{aligned} \tag{21}$$

In Eq. 21, R_r denotes the radius at the temperature node and L represents the length of the cylindrical segment.

Likewise, the heat flux equality at a tissue interface represented by Eq. 2 must also be numerically approximated. This approximation is shown below.

$$k_{in}\frac{T_{r,\theta}-T_{r-1,\theta}}{\Delta r}=k_{out}\frac{T_{r+1,\theta}-T_{r,\theta}}{\Delta r} \tag{22}$$

The boundary condition at the skin edge represented by Eq. 3 can be numerically approximated using Eq. 20. However, for this model, an energy balance equation at the skin surface was utilized to improve the accuracy [6]. Thus, the equation for the outer skin energy balance can also be numerically approximated as shown below.

$$C\frac{T_{r,\theta}^{p+1}-T_{r,\theta}^{p}}{\Delta t}=\frac{k\Delta\theta(R_r+R_{r-1})L}{2\Delta r}\left(T_{r-1,\theta}^{p}-T_{r,\theta}^{p}\right)+\frac{k\Delta rL}{2R_r\Delta\theta}\left(T_{r,\theta+1}^{p}+T_{r,\theta-1}^{p}-2T_{r,\theta}^{p}\right) + \dot{Q}_{blood}+\dot{Q}_{gen}+\dot{Q}_{ext} \tag{23}$$

As seen from inspection, Eq. 21 cannot be used to represent the central core temperature node. However, Osizik devised a finite-difference equation at the center of a cylindrical segment to be able to solve this particular problem [9]. Thus, an energy balance at the center of the core with radius $\Delta r/2$ can be formulated using Osizik's scheme. The numerical approximation at the central core temperature then can be written as

$$C\frac{T_0^{p+1}-T_0^{p}}{\Delta t}=\frac{k\,\Delta\theta\,L}{2}\left(T_1^{p}+.....+T_6^{p}-6T_0^{p}\right)+\dot{Q}_{blood}+\dot{Q}_{gen}+\dot{Q}_{resp} \tag{24}$$

where T_1, T_2, ..., T_6 represent six temperature nodes (since there are six angular sectors) radially spaced at distance of Δr from the central core temperature node. T_0 represents the temperature of the central core node.

III. RESULTS AND DISCUSSION

A. Verification of the Need for 2-D Modeling

The model was simulated using environmental conditions comparable to the experiments of Hall and Klemm [4]. For the simulation, the anterior and posterior sides of the body were exposed to 93.3 °C and –6.7 °C wall temperatures, respectively. The total simulation time was 30 minutes. The simulated subject was assumed to weigh about 70 kg with a 169 cm height. The subject was assumed to be resting, thus the metabolic rate was 81.4 W. The anterior temperatures were obtained by taking an average temperature of the frontal sectors (sectors 1-3). Similarly, the posterior temperatures were obtained by taking an average temperature of the rear sectors (sectors 4-6)

Figures 2a and 2b show results that justify modeling two-dimensional heat flow. The desired outputs were the anterior and posterior skin temperatures of the head, trunk, arm and leg. The results clearly show that the model can predict temperature variations on the same body element. As anticipated, the anterior side temperatures of each body element were greater than the posterior side temperatures.

Figure 3 shows a comparison of predicted posterior skin temperatures with the experimental results of Hall and Klemm. The model tracks the experimental data fairly well with the difference in temperatures never exceeding 0.7 °C. In general, the model predicts cooler posterior skin temperatures than the experiment, maybe due to over-prediction of heat loss due to active sweating. There are a few reasons that might possibly explain this finding. For one, the model assumes that latent heat loss for each body segment is evenly distributed to the front and back of the body. However, this assumption might be incorrect if the body is exposed to disparate radiant temperatures. In this particular case, where the back of the body is exposed to a cold radiant temperature, heat loss due to evaporation should occur more at the front of the body,

which is exposed to a hot radiant temperature. In addition, the shivering and active sweating functions in the model are driven mainly by the difference in head core (hypothalamic) setpoint temperature.

Figure 4 shows the predicted and experimental body core temperature results. Again, there is a strong agreement between the model and experimental results. As expected, the core temperature remains relatively constant throughout the simulation. This is consistent with reality in that the body actively attempts to maintain a constant core temperature using vasomotor functions. If the vasomotor functions aren't sufficient enough to maintain thermal comfort, then the body either sweats or shivers to insure a comfortable thermal state.

B. Prediction of Cold-induced Vasodilatation

The model was simulated to show the effects of CIVD on finger temperature and compared with experimental findings featured in a work by Shitzer et al. [30] that those authors used to validate their own extremity model. For the simulation, a bare hand is exposed to a 0°C ambient air temperature against negligible wind speed. The CIVD was initiated by an increase in blood flow in the AVAs to about 16 times the blood flowrate normally observed during full constriction in the finger. This increase in blood flowrate is a reasonable assumption [32] that was utilized to achieve some agreement with experimental data.

The comparison in CIVD response between predicted and measured finger temperatures is shown in Figure 5. Also shown is the predicted temperature response of a finger without the CIVD mechanism. There is a fairly good agreement between measured and predicted responses, indicating that the model is capable of showing CIVD responses in the fingers. As anticipated, the predicted response of finger temperature without CIVD is lower than the finger temperature

response with CIVD during the oscillatory stage. The obvious conclusion is that the CIVD mechanism reduces extremity discomfort and prevents injuries due to cold exposure.

C. Comparison with Experiments Done by Grahn et al. [19]

Grahn et al. [19] hypothesized and then validated through experimentation that the recovery from mild hypothermia can be achieved quickly by mechanically distending blood vessels in the hand with subatomic pressure, and then applying heat. They concluded that AVAs play a key role in this phenomenon in that applying subatomic pressure in conjuction with heat opens the AVAs to full capacity, which in turn allows a high blood flow through the venous plexuses in the hand. This blood is then heated and returns quickly to the core, thus somewhat directly heating the body core. The experiments conducted by Grahn et al. showed that their method resulted in a maximum rate of change in the external auditory meatus temperature (T_{EAM}) of 13.6 ± 2.1°C/h. This rate for the experimental group was 10 times faster than the maximum rate of the control group.

The MU Model was simulated in an attempt to predict the results of Grahn et al. to validate the AVA model formulated in this paper. The result of this simulation is shown in Figure 6. Here, the predicted T_{EAM} of the MU Model is compared to that of a single experimental subject. The model shows good agreement with the experimental data, but more importantly the model predicted a maximum rewarming rate of 12.11°C/h, which also agrees well with the results found by Grahn et al.

IV. CONCLUSIONS

The general structure for a two-dimensional human thermal model with extremities has been developed. The model included finger and toe temperature predictions along with countercurrent heat exchange involving arteries and veins. Arterial and venous countercurrent heat exchange is an especially nice feature in that it approaches a realistic representation of the human cardiovascular system especially when coupled with the modeling of the AVAs, which play a key role in thermoregulation. The AVA model that was implemented was able to produce CIVD responses due to cold exposure. In an example, many astronauts during EVA missions have reported extremity discomfort when handling cold objects in space; this is a psychological, as well as a physical distraction, most noticeably hindering manual dexterity. In controlling thermal comfort, finger temperatures could be important feedback variables necessary for fine tuning the thermal state of an astronaut. In presenting a general AVA model with CIVD, the model is made applicable for conducting extremity discomfort studies for persons subject to severe cold exposure at work or while participating in recreational activities.

Results from simulations indicated that the model could also predict varying temperatures on a body segment due to disparate environmental conditions. This is especially important, because astronauts are exposed to disparate environmental conditions during extra-vehicular activity (EVA) in space. Thermal comfort must be insured even in thermally disparate environments. The model predicted slightly lower posterior skin temperatures than the experimental findings reported in the literature [4].

Presently, the following features are being improved, now that the basic model has been successfully developed: shivering and sweating functions, heat transfer coefficients used in the cardiovascular model; better distribution of the AVA models throughout the body; and the

effects of fluid shifts due to microgravity. Further validation of the model will also be performed using a human thermal facility in our laboratory.

VII. NOMENCLATURE

$\dot{Q}$	Heat flow
ρ	Density
V	Volume
Cp	Specific heat capacity
T	Temperature
M	Mass
$\dot{m}$	Mass flow rate
$G_{empirical}$	Empirically derived gain
W	Work
$\Re$	Blood flow reduction via vasoconstriction
γ	Weighting parameter
K	Various distribution value
P	Pressure
Pv	Partial water vapor pressure
Pg	Adiabatic saturation pressure of water
A	Area
σ	Stefan-Boltzmann constant
F	Interchange factor
S	Drive for sweating
R_w	Universal Gas constant for water
H_{mass}	Mass transfer coefficient
h_{fg}	Heat of vaporization for water
V_{air}	Velocity of air
H	Height
L	Segment length
R	Radius
h	Convection coefficient
k	Thermal conductivity
r	Denotes radial direction in 2-D conduction
θ	Denotes angular direction in 2-D conduction
$\dot{e}_b$	Thermal mass blood flow rate
hA_a	Heat transfer coefficient between arteries and tissue
hA_v	Heat transfer coefficient between veins and tissue

VIII. REFERENCES

[1] G.C. Bue, *Computer Program Documentation: 41-Node Transient Metabolic Man Program*. Houston, TX: Lockheed Engineering and Sciences Company. LESC-27578, a.ka. CTSD-0425, 1989.

[2] C.G. Crandall, J.M. Johnson, V.A. Convertino, P.B. Raven, and K.A. Engelke, "Altered Thermoregulatory Responses after 15 Days of Head-Down Tilt, *J. Appl. Physiol*., 77(4), 1994, pp 1863-1867.

[3] A.P. Gagge, "A Two-Node Model of Human Temperature Regulation in Fortran", *Bioastronautics Data Book*, J.F. Parker, Jr. and V.R. West (editors), NASA SP-3006, Washington, D.C., 1973, pp. 142-148.

[4] J.F. Hall and F.K. Klemm, "Thermoregulatory Responses in Disparate Thermal Environments", *J. Appl. Physiol*. 23(4), 1967, pp 540-544.

[5] V.S. Koscheyev, S. Paul, G.R. Leon, D. Tanchida, T.J. Taylor and I.V. Koscheyev, "Body Surface Temperature Tuning as a Comfort Support System in Space and Other Extreme Environments", *SAE Technical Paper Series*, 1998.

[6] L.H. Kuznetz, "A Two-Dimensional Transient Mathematical Model of Human Thermoregulation", *American Journal of Physiology*, 237(5), 1979, pp R266-R277.

[7] T. Mungcharoen, *A Two-Dimensional Human Thermal Model for Execution on a Parallel Processor*, University of Texas-Austin, Ph.D Dissertation, 1989.

[8] P. Norsk, N. Foldager, F. Bonde-Petersen, B. Elmann-Larsen, and T.S. Johansen, "Central Venous Pressure in Humans During Short Periods of Weightlessness", *J. Appl. Physiol*., 63(6), 1987, pp 2433-2437.

[9] N.M. Ozisik, *Heat Conduction*, New York: Wiley, 1993.

[10] H.H. Pennes, "Analysis of Tissue and Arterial Blood Temperatures in the Resting Human Forearm", *J. Appl. Physiol*., 1, 1948, pp 93-122.

[11] J.K. Shoemaker, C.S. Hogeman, D.H. Silber, K. Gray, M. Herr, and L.I. Sinoway, "Head-Down Tilt Bed Rest Alters Forearm Vasodilator and Vasoconstrictor Responses", *J. Appl. Physiol.*, 84(5), 1998, pp 1756-1762.

[12] C.E. Smith, *A Transient, Three-Dimensional Model of the Human Thermal System*, Ph. D Dissertation, Kansas State University, 1991.

[13] J.A. Stolwijk and J.D. Hardy, "Control of Body Temperature", In: *Handbook of Physiology*, Sect. 9, edited by Lee, D. H. K., pp 45-68, American Physiological Society, Maryland, 1977.

[14] J.A. Stolwijk, *A Mathematical Model of Physiological Temperature Regulation in Man.* Washington, D.C.: NASA CR-1855, 1971.

[15] E.H. Wissler, "Mathematical Simulation of Human Thermal Behavior Using Whole Body Models", In: *Heat Transfer in Medicine and Biology*, ed. Avraham, Shitzer and Robert C. Eberhardt, 1:325-373. New York: Plenum Press, 1985.

[16] C.H. Wyndham and A.R. Atkins, "A Physiological Scheme and Mathematical Model of Temperature Regulation in Man", *Pflugers Archiv*., 303, 1968, pp 14-30.

[17] Y. Xue-jun, Y. Tian-de, "Ground-Based Studies on Thermoregulation at Simulated Microgravity by Head-Down Tilt Bed Rest", *Space Medicine & Medical Engineering*, Oct. 13(5), 2000, pp 382-385.

[18] A.E. Iyoho, *The Development of a 2-D Human Thermal Model for EVA Applications*, University of Missouri-Columbia, MS Thesis, 2002.

[19] D. Grahn, J.G. Brock-Utne, D.E. Watenpaugh, and H.C. Heller, "Recovery from Mild Hypothermia Can Be Accelerated by Mechanically Distending Blood Vessels in the Hand", *J. Appl. Physiol*., 85, 1998, pp 1643-1648.
[20] E. H. Wissler, "A mathematical model of the human thermal system," Bulletin of Mathematical Biophysics, vol 26, pp. 147-166, 1964.
[21] J. D. French, A. D. Viswanath, S. S. Nair, J. B. Miles and C. H. Lin, "Parameters and assumptions in human thermal modeling for EVA applications," SAE Transactions, Journal of Aerospace, vol. 106, pp. 579-586, SAE 972320, 1997.
[22] R. K. Jain, "Temperature distributions in normal and neoplastic tissues during normothermia and hyperthermia," Annals of the New York Academy of Sciences, vol. 335, pp. 98-106, 1980.
[23] R. B. Roemer and T. C. Cetas, "Application of bioheat transfer simulations to hyperthermia," Cancer Research, vol. 44, pp. 4788s-4798s, 1984.
[24] R. A. Haslam and K. C. Parsons, "Computer-based models of human responses to the thermal environment: Are their predictions accurate enough for practical use?," in Thermal Physiology, J.B. Mercer, Ed., 1989, pp. 763-768.
[25] C. L. Hwang and S. A. Konz, "Engineering models of the human thermoregulatory system: a review," IEEE Transactions on Biomedical Engineering, vol. 24(4), pp. 309-325, July 1977.
[26] G. Fu, A Transient, Three-Dimensional Mathematical Thermal Model for the Clothed Human. Ph.D. Thesis, Kansas State University, 1995.
[27] C. Huizenga, H. Zhang and E. Arens, "A model of human physiology and comfort for assessing complex thermal environments," Building and Environment, vol. 36, pp. 691-699, 2001.
[28] F. Hsu, *Modeling, Simulation, and Optimal Control of the Human Thermal System*, Ph.D. Thesis, Kansas State University, 1971.
[29] T. Idia, "Studies concerning vascular reaction to cold (Part 1). Physiological significance of vascular reaction to cold," *The Journal of thePhysiological Society of Japan*, vol. 11, pp. 73-78.
[30] A. Shitzer, L.A. Stroschein, R.R. Gonzalez, and K.B. Pandolf, "Lumped parameter finger tip model exhibiting cold induced vasodilatation," In: *Advances in Bioheat and Mass Transfer: Microscale Analysis of Thermal Injury Processes, Instrumentation, Modeling, and Clinical Applications*, HTD-Vol. 268, ASME, pp. 61-67, 1993.
[31] A. Shitzer, S. Bellomo, L.A. Stroschein, R.R. Gonzalez, and K.B. Pandolf, "Simulation of a cold-stressed finger including the effects of wind, gloves, and cold-induced vasodilatation," *Journal of Biomedical Engineering*, vol. 120, pp. 389-394, 1998.
[32] A.C. Burton, "The range and variablity of the blood flow in the human finger and the vasomotor regulation of body temperature," *American Journal of Physiology*, vol. 127, pp. 437-453.
[33] T. Takemori, T. Nakajima, and Y. Shoji, "A fundamental model of the human thermal system for prediction of thermal comfort," *Heat Transfer- Japanese Research*, vol. 24, no. 2, 1995.
[34] Y. Shoji, T. Takemori, H. Matsunami, and T. Nakajima, "A three-dimensional, clothed thermal model," *Heat Transfer-Japanese Research*, vol. 26, no. 8, 1997.
[35] K. Hirata, T. Nagasaka, M. Hirashita, and T. Takahata, "Increase in evaporative and non-evaporative heat loss from the forearm depends on venous return from the hand during

exercise," *Thermal Physiology*, Editor: J.B. Mercer, Excerpta Medica, International Congress Series 871, 1989.
[36] J. L. Sherman, Jr., "Normal arteriovenous anastomoses," *Medicine*, vol. 42, pp. 247-267, 1963.
[37] R.T. Grant and E.F. Bland, "Observation on arteriovenous anastomoses in human skin and in bird´s foot with special reference to the reaction to cold," *Heart*, vol. 15, pp. 385-411, 1991.
[38] M. Midttun and P. Sejrsen, "Blood flow rate in arteriovenous anastomoses and capillaries in thumb, first toe, ear lobe, and nose," *Clinical Physiology*, vol. 16: 275—289, 1996.
[39] H.A.M. Daanen, *Central and peripheral control of finger blood flow in the cold*, Thesis, Vrije University, 1997.
[40] H.A.M. Daanen, "Finger cold-induced vasodilation: a review," *European Journal of Applied Physiology*, vol. 89, pp. 411-426, 2003.
[41] S. Sawada, "Cold-induced vasodilation response of finger skin blood vessels in older men observed by using a modified local cold tolerance test," *Industrial Health*, vol. 34, pp. 561-556, 1996.
[42] J.D. Nelms and D.J.G. Soper, "Cold vasodilation and cold acclimation in the hands of British fish filleters," *Journal of Applied Physiology*, vol. 17, pp. 444-448, 1962.
[43] T Panczak, S. Ring, and M. Welch, "A CAD-based Tool for FDM and FEM radiation and conduction modeling," SAE Paper 981577, 28th International Conference of Environmental Systems, July 1998.
[44] J. Lefevre, *Engergétique et chaleur animale*, Masson, Paris, 1911.
[45] A.C. Brown, "Analog computer simulation of temperature regulation in man," Technical Report AMRL-TDR-63-116, Wright-Patterson A.F.B., 1963.

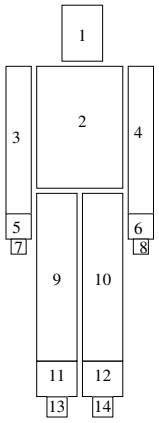

Figure 1a: Cylindrical representation of the human form with numbered elements.

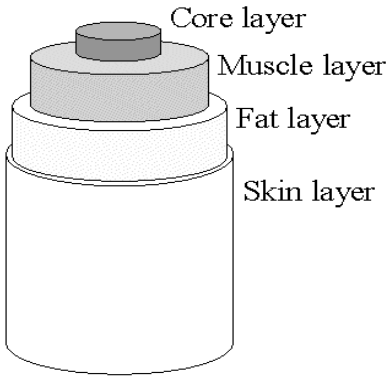

Figure 1b: Concentric regions in each element

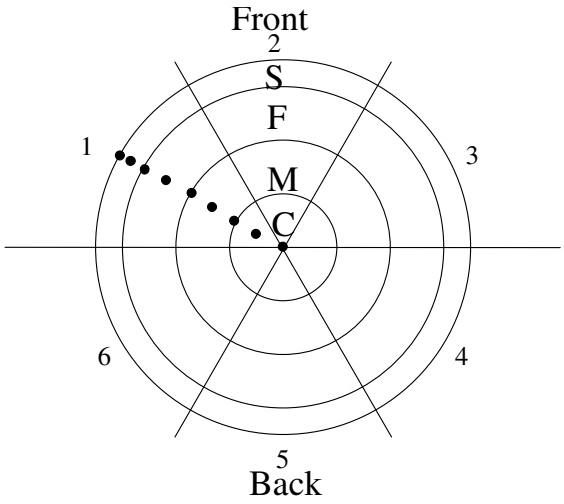

Figure 1c: Cross-sectional view of an element and nodal spacing for the nude case.

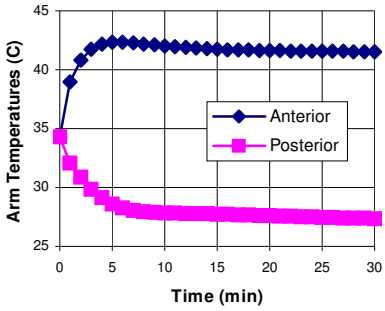

Figure 2a: Arm skin temperatures

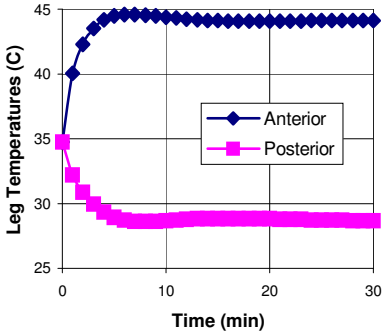

Figure 2b: Leg skin temperatures

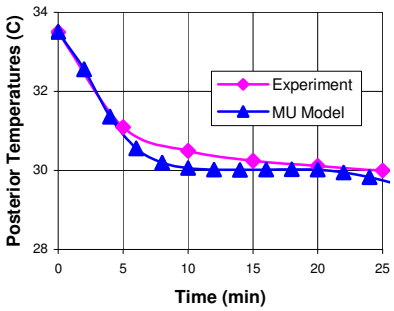

Figure 3: Comparison of MU Model predictions and experimental results for posterior skin temperature.

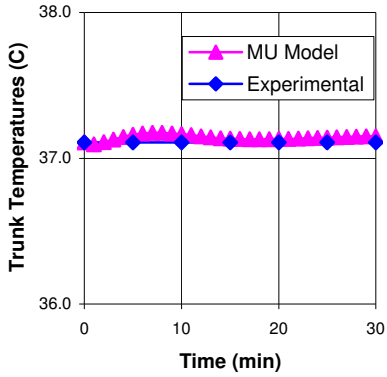

Figure 4: Comparison of MU Model predictions and experimental results for body core temperature.

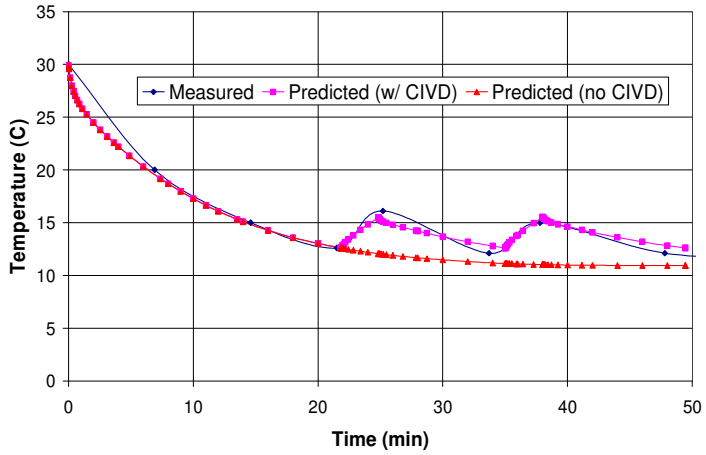

Figure 5: Comparison of model and experimental results for the effect of CIVD on finger temperature response during cold exposure.

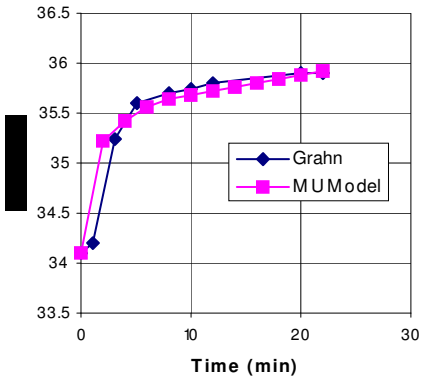

Figure 6: Comparison of MU Model predictions and experimental results for external auditory meatus temperature.

CHAPTER 7

SUMMARY, CONTRIBUTIONS AND FUTURE RESEARCH

7.1 Summary & Contributions

Mathematical techniques and frameworks to study two classes of bio-systems have been proposed including a consideration of the uncertainties involved. The approaches are illustrated by two real world Example Case systems, summarized below.

Example Case I:

- Cellular level modeling for neurons and networks, which is representative of complex nonlinear system with multiple inputs and outputs has been developed using two software platforms, GENESIS and Matlab/Simulink.
- The mechanisms of action of a drug on prefrontal cortical cells is elucidated with two possible hypotheses, and a systematic methodology to study the excitability of cells under inhibitory post synaptic currents is developed.
- Single cell models are developed for baroreceptor cells and it is shown to successfully model the conversion of an analog blood pressure signal to discrete firing patterns. Also investigated is whether spike frequency adaptation is mediated by a pre- or post-synaptic mechanism.
- At the network level, NTS cells which receive the baroreceptor afferents are modeled, and three specific network configurations are investigated as examples of the possible 'functional' circuitry that can implement the required 'signal transfer' from a pulse synchronous format (baroreceptors) at the input to one that lacks pulse-synchronocity in

the network (NTS neurons), back to a pulse synchronous format at the output (NTS output neuron).

Example Case II:

- Developed techniques to model and characterize the role of various subsystems and quantify the uncertainties, in a human thermal system, to capture inter-subject variations, to better understand variations in human thermal response under nominal (NASA astronauts) and extreme (warfighters and astronauts) environmental conditions.

- The MU 2-D human thermal model is a general purpose model that can predict thermal responses of human beings in transient environmental conditions. This model was enhanced using more accurate modeling of digits incorporating arterio-venous anastomoses mechanisms that the fingers and toes use for better control of heat transfer. Also, a novel black box model has been developed using artificial neural network techniques to predict the thermal response of supine subjects to transient environmental conditions, using a US Army data set.

Other Projects. The author was also involved in another project, mathematical modeling of optimal triage in pediatric trauma care using advanced modeling techniques, and that study resulted in two journal papers listed below:

- Burd, R. S., Jang, T., and Nair, S., "Evaluation of the relationship between mechanism of injury and outcome in pediatric trauma," *The Journal of Trauma* (accepted for publication).

- Burd, R. S., Jang, T. S., Nair, S. S., 2006, "Predicting hospital mortality among injured children using a national trauma database," *Journal of Trauma*, 60:792-801.

In addition, he participated in an extensive human thermal experimental study involving 7 male and 7 female subjects for a US Air Force project, and also developed a computer model for predicting thermal responses. All these have not been discussed in the dissertation, but mentioned here since it was performed during the author's Ph.D. program at MU.

7.2 Future Research

Cellular level:

- There is evidence indicating a complex interaction between the transmission of dopamine (DA) and norepinephrine (NE) in the noradrenergic and dopaminergic projections that converge in the medial prefrontal cortex (mPFC).
  A computational network model of PFC pyramidal cells with both the noradrenergic (e.g. $\alpha 1$ and $\alpha 2$) and dopaminergic receptors needs to be developed to study the complex interactions between various neurotransmitters such as DA, NE, glutamate, and their role in modulating signal to noise ratio..
- A systematic study needs to be performed to quantify the contribution of selected K+ currents on the excitability of functionally identified, barosensitive NTS neurons.
- The network model of NTS circuitry is a 'test-bed' for a host of studies including comparisons with normal and diseased (cardiovascular, etc.) cases, elucidation of 'design' sub-circuits within the circuitry, and characterization of robustness of the system.
- The single cell and network computational models, after extensive validation, provide a platform for a variety of predictions, many of which can be used to prioritize possible wet lab experiments to be pursued.

Systems level:

- Two statistical models using ANN have also been developed for the US Army and the US Air Force to predict individual human thermal responses under transient environmental conditions. As a next step, it is suggested that a 'hybrid model (see Fig. 7.1 below) be developed combining the existing first-principles human thermal models such as MU 2-D model with a carefully structured black box model of the ANN type to capture nonlinearities and uncertainties with improved precision, and subsequently improve overall prediction of human thermal responses.

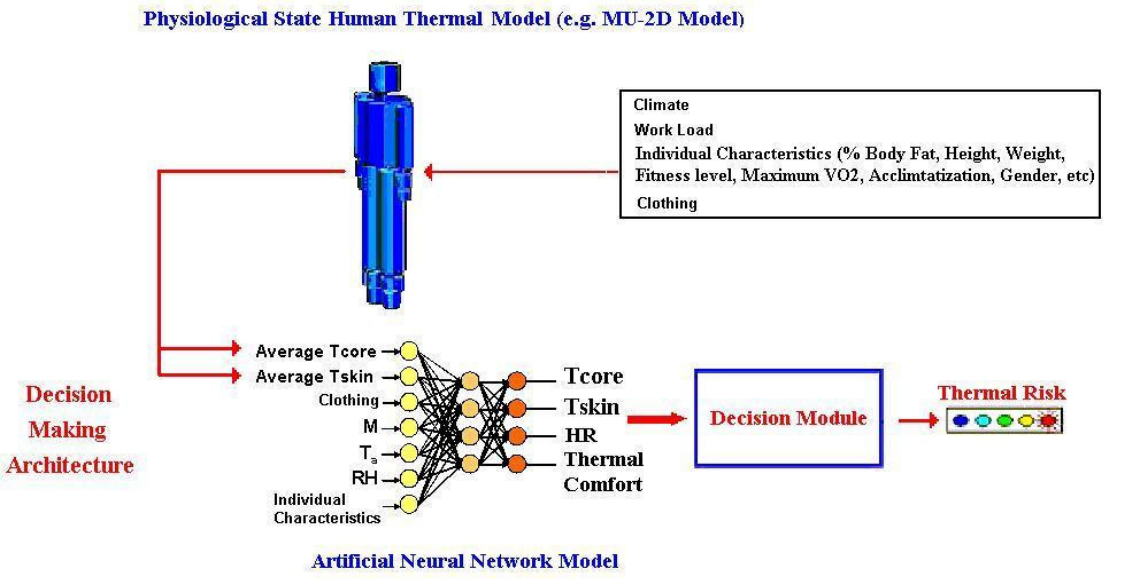

HR: heart rate Tcore: core temperature Tskin: mean skin temperatue Ta: air temp. RH: humidity M: heat production S: heat storage EV: evaporative heat loss T sensation: skin temperature sensation

Figure 7.1: Proposed hybrid human thermal model.

APPENDICES

APPENDIX 1 ---------- Air Force Project Model Users Manual

APPENDIX 2 ---------- SAE Journal Paper

APPENDIX 3 ---------- Pediatric Study Journal Paper

APPENDIX 4 ---------- Software Developed

4.1 Genesis Programming for Cellular Modeling

4.1.1 ADHD Single Cell and Network Model

4.1.2 NTS Single Cell and Network Model

4.2 Artificial Neural Network Program for DOD Project

4.3 Artificial Neural Network Program for Air Force Project

4.4 Artificial Neural Network Program for Pediatric Study

4.5 SAS Programs including ANOVA, Multiple Imputation for missing data, Logistic Regression Models, Multiple Linear Regression Models for Pediatric Study

4.6 GUI for DOD Project

4.7 GUI for NASA Space Suit Project

Appendix 1

Air Force Project Model - Users Manual

1.0 Range of applicability for the MU Heat Stress Model

Experimentation was conducted at the following conditions with 7 male subjects:

- 110 F, 20% RH (Desert)
- 95 F, 75% RH (Jungle)
- 75 F, 45% RH (Neutral)

The hybrid neural network model predictions are very good at temperature/humidity conditions that are near these conditions since only three points in the ambient temp/RH plane (see figure below) are available for generalization. The model interpolates well between these conditions in order to provide valid solutions within the triangular zone shown geometrically in Fig. 1 below:

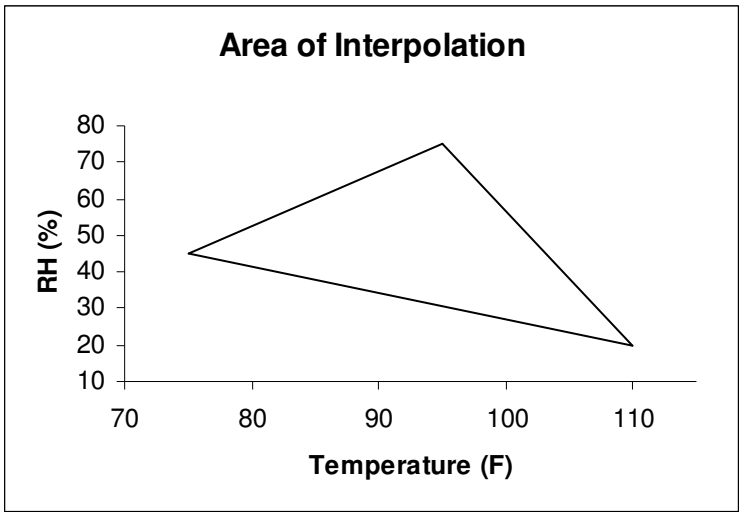

Figure 1. Ambient Temperature-RH region where model predictions hold best.

The model extrapolates reasonably well outside this triangular region so long as it is not too far, but the results are not guaranteed to be accurate too far outside this region. More tests are necessary to generalize reliably to longer distances outside this region.

Definition of the three typical subjects selected for the model predictions.

The prediction of the model are based on 7 young fit males from ages 19-26 who were our subjects for the experimental data gathered, and so is valid for that age group and for young generally-fit males. The model is valid for males within the following range:

- Age from 19-26 years
- Weight from 116-220 pounds
- Height 63-73 inches
- VO2 max from 33 to 54 ml/kg/min
- Body fat percentage from 20 to 31 percent

Among this group, we selected three typical subjects, labeled VERY FIT, FIT, and UNFIT in the program. The curves for very fit, fit and unfit subjects are taken from our experimental data where the following definitions hold for the three body types:

- VERY FIT subject has VO2max of 54 ml/kg/min, height of 180 cm, weight of 181 lb, and body fat of 21.1%
- FIT subject has VO2max of 43 ml/kg/min, height of 171 cm, weight of 177 lb, and body fat of 24%

- UNFIT subject has VO2 max of 36 ml/kg/min, height of 165 cm, weight of 129 lb, and body fat of 20.6%

It is emphasized that the subject types are based on our data on young males and not for the general population. More data are needed to generalize to other ages and body types.

Casualty %. The casualty % in the plot are based on the following ranges:

5% casualty	– corresponds to Core Temperature of 38 C
50% casualty	– corresponds to Core Temperature of 39.5 C
100% casualty	– corresponds to Core Temperature of 40 C

2.0 Computer Requirements to Run the Model

The PC should have the basic software described below to run the program.

- Microsoft .NET Framework 1.1
- Operating System
  - Microsoft Windows® Server 2003 (.NET is automatically installed), Windows XP Professional or Home Edition, Windows 2000, Windows Millenium Edition, Windows 98, or Microsoft Windows NT® 4.0 Service Pack 6a
  - Internet Information Services (IIS) must be installed prior to .NET Framework for Windows 2003, XP Professional and 2000.
- Processor
  - Client – 90-MHz Intel Pentium-class
  - Server – 133-MHz Intel Pentium-class
- Memory
  - Client – 32 MB of RAM, 96 MB recommended
  - Server – 128 MB of RAM, 256 MB recommended
- Hard Disk
  - 40 MB required for installation
  - 110 MB additionally required
- Microsoft Internet Explorer 5.01 or later
- Microsoft Data Access Components 2.6 is necessary for data scenarios, 2.8 is recommended
- Microsoft DirectX 9b is required to execute managed DirectX applications

3.0 How to run the program MU Heat Stress Model.EXE

- Predictive model – This is a three subject prediction of casualties based on Core Temperature values
- Model Files: Your computer should have a folder titled MU Heat Stress Model with the following:
  - MU Heat Stress Model.Exe – the file you need to doubleclick on.
  - Zedgraph.dll
  - Folder titled "Documentation for MU Heat Stress Model"
  - Helpfile1-GUI Help
  - Helpfile2-User's Manual
  - Helpfile3-Workload Reference
- Step by step procedure for running the model
  1. Doubleclick on the MU Heat Stress Model.EXE icon in the folder MU Heat Stress Model.
  2. Input the following parameters: ambient temperature, WBGT or relative humidity, MOPP, and activity level, as seen in the first column of Fig. 2.
  3. Hit 'Estimate'. This calculates the band of output tolerance time.

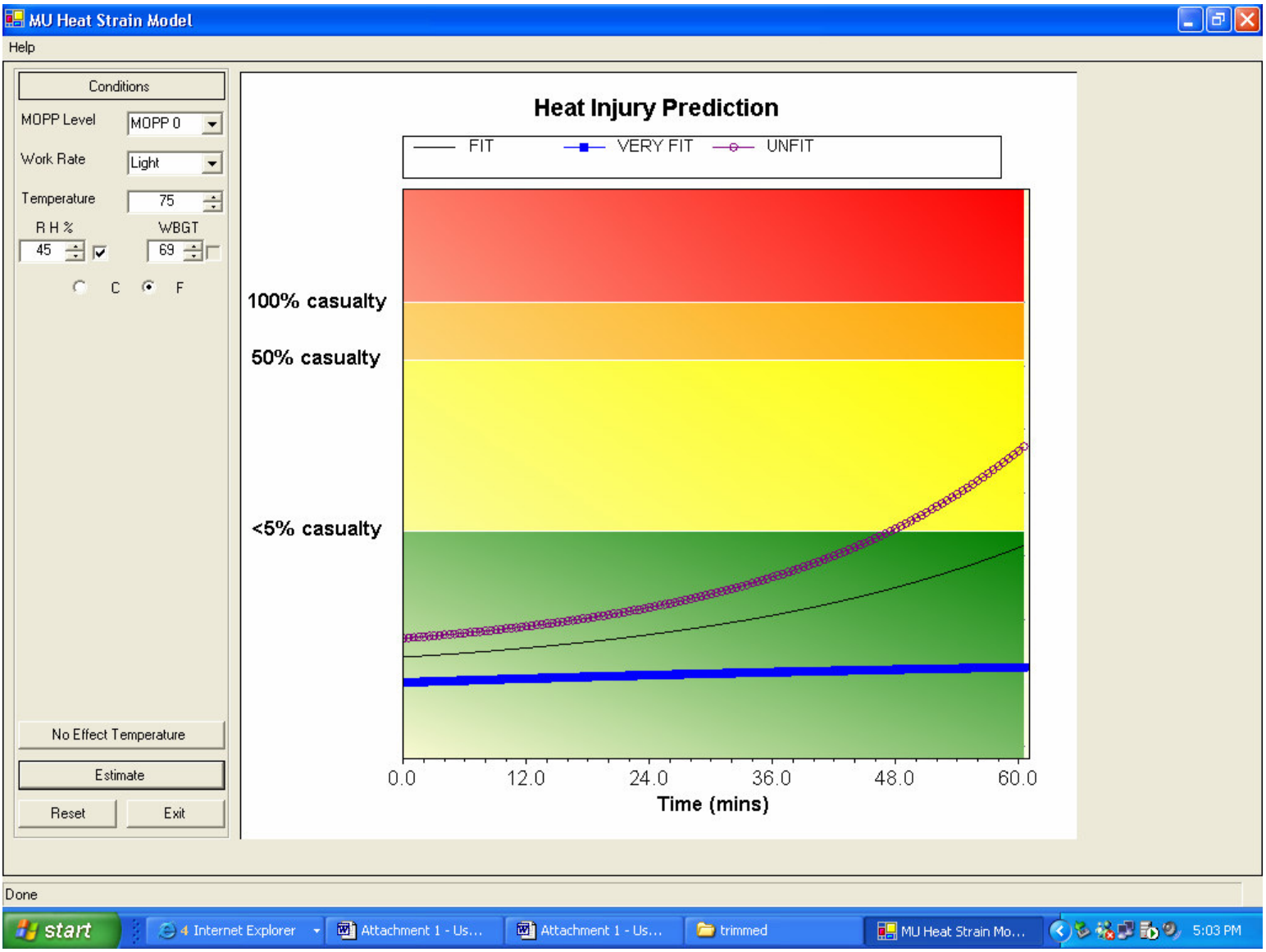

Figure 2: Main screen for the User Interface.

- Main screen (Fig. 2) inputs
  - Environment
    - Temperature (ºC or ºF)
    - WBGT (ºC or ºF) or Relative Humidity (%)
  - MOPP level (0,2,4)
  - Activity level
    - Light (200 W)
    - Heavy (425 W)
- Description of outputs
  - Core temperature v/s time assuming the person will continue exercising till core temperature reaches 40 C, or if time reaches 60 minutes. If the time reaches 60 minutes without the core reaching 40C, the user should look click on the 'No Effect Temperature' button to see what the No Effect Temperature is for the selected ambient temperature and RH/WBGT. The next bullet describes No Effect Temperature..
  - "No effect" temperature – Temperature at which for a given relative humidity, wind speed and low to moderate activity level (for example 200 W, 350 W, and 425 W), no critical levels of heat strain will occur over the span of a day's work while wearing MOPP 0,2,4. This has been obtained using the 39.5ºC core temperature criterion.

4.0 Corrections to prediction for individual characteristics (OPTIONAL SECTION)

In case the user desires to use this screen for evaluating subject thermal response for inputs not considered by our model (such as aerobic fitness, solar radiation, heat acclimation, hydration level, etc.), we provide some guidance on corrections to tolerance time that could be used. The following sections outline the corrections for differences in individual characteristics and solar radiation that can be used to correct the 'average' model predictions.

4.1 Physical Training & Aerobic Fitness

- For individuals of lower aerobic fitness (~ $\dot{V}o_2$ max = 46 ± 2.9 ml/kg/min or less) working at 250 W or less 22 min. could be deducted from predicted tolerance time of a fitter (~ $\dot{V}o_2$ max = 59.5 ± 4.1 ml/kg/min or more) individual, for MOPP-2 & MOPP-4 in jungle and desert climates.
- At 425 W, subtract only 5 min. at similar MOPP levels and environmental conditions.

4.2 Heat Acclimation and Acclimatization

- For corrections due to acclimation see Table 1 below.

Table 1: Corrections (min.) for non-acclimated individuals at a given threshold of core temperature (38.6 and 39.5°C) predicted by Givoni & Goldman at various MOPP, activity and environments for young, fit males. These values could be subtracted from the predicted tolerance time of an acclimated individual.

Neutral Environment (75 F, 45% rh)				
	Light Exercise, 200 W		Heavy Exercise, 425 W	
	38.6	39.5	38.6	39.5
MOPP 0	0	0	187*	0
MOPP 2	0	0	17	42
MOPP 4	56*	0	14	26
Jungle Environment (95 F, 75% rh)				
	Light Exercise, 200 W		Heavy Exercise, 425 W	
	38.6	39.5	38.6	39.5
MOPP 0	22	0	8	10
MOPP 2	16	0	8	9
MOPP 4	15	0	8	9
Desert Environment (110 F, 20% rh)				
	Light Exercise, 200 W		Heavy Exercise, 425 W	
	38.6	39.5	38.6	39.5
MOPP 0	165*	0	38	0
MOPP 2	34	86*	9	13
MOPP 4	27	101*	9	9

* – For this environment and MOPP, an acclimated individual never reached the threshold, thus an arbitrary 250 min. tolerance time was assumed for the acclimated individual. Thus, the value shown is equivalent to 250 minus the tolerance time of a non-acclimated individual.

4.3 Hydration Level

- For moderately and highly fit individuals, 19 and 9 min., respectively could be deducted from the predicted tolerance time due to a loss of ~2.5% body mass due to dehydration at a work rate of 250 W or less, and at MOPP-2 & MOPP-4 levels, jungle and desert.
- At 425, subtract only 4 min. at similar MOPP levels and environmental conditions.

4.4 Body Type

- Approximately 34 minutes could be deducted from the predicted tolerance time to account for individuals with higher body fat (>18.9% in comparison to <10.9%) content while in full chemical-defense posture exercising at low to moderate (<250 W) work rates.
- At 425 W, 6 min. could be deducted.

4.5 Gender

4.5.1 Corrections for Gender Differences

- At a low to moderate work rate (<250 W) the predicted tolerance time could be deducted by approximately 29 min. to account for gender differences when other individual characteristics (i.e. $\dot{V}_{2max}$, body mass, %body fat) are not matched at MOPP-2 and MOPP-4, and jungle and desert climates.
- At 425, 4 min. could be deducted for similar conditions.

4.5.2 Menstrual Cycle and Oral Contraceptives

- The data for the female model was obtained during the luteal phase of the menstrual cycle, thus approximately 21 min. could be added to the predicted tolerance time during the follicular phase for

female contraceptive non-users during light to moderate work (<250 W) for MOPP-2,4 in jungle and desert environments.

- At 425 W, the correction could be only 4 min. for similar MOPP levels and environments.
- No corrections should be made for contraceptive users.

4.6 Age

- It might be reasonable to approximate the correction (min.) due to age for persons unmatched in individual characteristics by using the equation, $Correction = 70.34 - (21.948 + 2.762x - 0.0395x^2)$, although care should be taken since the experimental study did not include males or chemical defense clothing; but it was an uncompensable heat stress study (48ºC, 10% RH).
- For example, for 35, 25, and 20 years of age, approximately 0, 4, and 9 min. should be deducted from the tolerance time prediction due to age.

4.7 Solar Load

- As expected, the addition of a solar load on an individual will cause increased body temperatures, and thus will decrease the tolerance time.
- For possible deductions in tolerance time due to solar load see Table 2 below.

Table 2: Corrections (min.) due to solar load at a given threshold of core temperature (38.6 and 39.5°C) predicted by Givoni & Goldman at various MOPP, activity and environments for young, fit males. These values should be subtracted from the predicted tolerance time of an individual working indoors.

Neutral Environment (75 F, 45% rh)				
	Light Exercise, 200 W		Heavy Exercise, 425 W	
	38.6	39.5	38.6	39.5
MOPP 0	0	0	0	0
MOPP 2	0	0	5	21
MOPP 4	0	0	3	11
Jungle Environment (95 F, 75% rh)				
	Light Exercise, 200 W		Heavy Exercise, 425 W	
	38.6	39.5	38.6	39.5
MOPP 0	17	64*	2	5
MOPP 2	11	94*	1	2
MOPP 4	9	89*	1	2
Desert Environment (110 F, 20% rh)				
	Light Exercise, 200 W		Heavy Exercise, 425 W	
	38.6	39.5	38.6	39.5
MOPP 0	0	0	13	0
MOPP 2	15	0	2	3
MOPP 4	11	0	1	0

***** – For this environment and MOPP, an individual working indoors never reached the threshold, thus an arbitrary 250 min. tolerance time was assumed for this individual. Thus, the value shown is equivalent to 250 minus the tolerance time of a individual working outdoors.

ADDITIONAL INFORMATION

- More details about modeling methodology, etc. can be found in several papers submitted to MACTEC as attachments to the Final Report.

USERS MANUAL – brief version

1.0 System Requirements

- Microsoft .NET Framework 1.1
- Operating System
    - Microsoft Windows® Server 2003 (.NET is automatically installed), Windows XP Professional or Home Edition, Windows 2000, Windows Millenium Edition, Windows 98, or Microsoft Windows NT® 4.0 Service Pack 6a
    - Internet Information Services (IIS) must be installed prior to .NET Framework for Windows 2003, XP Professional and 2000.
- Processor
    - Client – 90-MHz Intel Pentium-class
    - Server – 133-MHz Intel Pentium-class
- Memory
    - Client – 32 MB of RAM, 96 MB recommended
    - Server – 128 MB of RAM, 256 MB recommended
- Hard Disk
    - 40 MB required for installation
    - 110 MB additionally required
- Microsoft Internet Explorer 5.01 or later
- Microsoft Data Access Components 2.6 is necessary for data scenarios, 2.8 is recommended
- Microsoft DirectX 9b is required to execute managed DirectX applications

2.0 How to run the program

- Predictive models – There are two predictions running concurrently in this program: (i) 'subject' prediction of tolerance time using the experimental data obtained from this study, and so is limited to specific group of people (see next subsection); and (ii) 'average' prediction of tolerance times based on the Givoni & Goldman average man prediction, along with corrections to the prediction based on differences in individual characteristics.
    - Prediction based on the experimental data from this study
        - Input range
            - Male (Female is coming)
            - Age range – 19 to 26 years
            - $\dot{V}o_2$ max – 33 to 54 ml/kg/min
            - % Body fat range – 20 to 31%
            - Weight range – 116.6 to 220 lb
            - Height range – 63 to 73 in.
        - Outputs
            - Tolerance time (minutes)
            - Core temperature and heart rate response (v/s time)
    - Givoni & Goldman 'average' man prediction with corrections
        - Outputs
            - Tolerance time for average man and woman (minutes)
                - UPPER LIMIT is displayed if the subject can tolerate for a long period. See also NO EFFECT plots.
            - Suggested corrections to tolerance time of average prediction (minutes)
    - **SCREENSHOT**
- Step by step procedure for running the model
- Inputs
    - Environment
        - Neutral (75ºF, 45% RH)
        - Jungle (95ºF, 75% RH)
        - Desert (110ºF, 20% RH)
    - MOPP level (0 – 4)

- Activity level (200 or 425 W)
- Description of individual characteristics
  - $\dot{V}o_2$ max - The maximum volume of oxygen (ml/kg/min) consumed by the body during exercise. This value is an indication of the maximum capacity to do aerobic work.
  - Percent body fat – A measure of the amount of adipose (fat) tissue as a percentage of total body mass.
  - Weight (kg or lb), Height (cm or in.), and Age (years)
- Additional characteristics to correct average man predictions
  - Heat acclimation – Heat acclimation refers to building up heat tolerance in a controlled laboratory, whereas heat acclimatization occurs in a natural setting, but often these terms are used interchangeably. The average man prediction is for an acclimated individual, but a correction to the predicted tolerance for a non-acclimated individual is included.
  - Gender – A few studies in the past that looked into gender differences regarding heat stress response have concluded that females, when unmatched for individual characteristics, were more intolerant than their male counterparts. Thus, a correction due to gender for the average population is included.
  - Menstrual cycle phase – It has been observed that contraceptive non-users on average exhibit greater tolerance times in the early follicular phase in comparison to the mid-luteal phase during uncompensable heat stress, while contraceptive users have shown no significant differences in tolerance time between each phase. Thus, the appropriate correction due to menstrual cycle phase is provided.
  - Solar load – The average man prediction can be corrected to account for short wave radiation from the sun. This is accounted for when outdoor conditions are selected on the input screen.

- Description of outputs
  - Tolerance time – The time at which physical signs of heat stress make it impossible for an individual to continue with their activity; or when upper thresholds of core temperature (≥39.5°C) or heart rate (>180 b/min for 3 min.) are encountered.
  - Final core temperature and heart rate – The core temperature and heart rate upon cessation of activity due to severe heat strain. A graph of the core temperature and heart rate response is also provided.
  - Physiological Strain Index (PSI) – The physiological strain index (PSI) is based on rectal (core) temperature and heart rate, and indicates the level of strain from a scale of 0-10:
    - $PSI = 5[T_{re}(t) - T_{re0}] \times [39.5 - T_{re0}]^{-1} + 5[HR(t) - HR_0] \times [180 - HR_0]^{-1}$
  - "No effect" temperature – Temperature at which for a given relative humidity, wind speed and low to moderate activity level (for example 170 W and 250 W), no critical levels of heat strain will occur over the span of a day's work while wearing MOPP 2-4. This has been obtained using the 38.6ºC core temperature criterion.
  - Corrections – Suggested amount of time that should be subtracted from the predicted tolerance time of the average model based on differences in individual characteristics. This is explained in detail below.

3.0 Corrections to prediction for individual characteristics

If a prediction model per se was developed for a particular group of individuals, for example young, fit males, then some corrections to tolerance time would be needed to expand this prediction to include those of differing individual characteristics. The following sections outline the corrections for differences in individual characteristics and solar radiation, which can be used as a suggestion for correcting the prediction of the 'average' model.

3.1 Physical Training & Aerobic Fitness

- For individuals of lower aerobic fitness (~$\dot{V}o_2$ max = 46 ± 2.9 ml/kg/min or less) working at 250 W or less 22 min. could be deducted from predicted tolerance time of a fitter (~$\dot{V}o_2$ max = 59.5 ± 4.1 ml/kg/min or more) individual, for MOPP-2 & MOPP-4 in jungle and desert climates.
- At 425 W, subtract only 5 min. at similar MOPP levels and environmental conditions.

3.2 Heat Acclimation and Acclimatization

- For corrections due to acclimation see Table 1 below.

Table 1: Corrections (min.) for non-acclimated individuals at a given threshold of core temperature (38.6 and 39.5°C) predicted by Givoni & Goldman at various MOPP, activity and environments for young, fit males. These values could be subtracted from the predicted tolerance time of an acclimated individual.

Neutral Environment (75 F, 45% rh)				
	Light Exercise, 200 W		Heavy Exercise, 425 W	
	38.6	39.5	38.6	39.5
MOPP 0	0	0	187*	0
MOPP 2	0	0	17	42
MOPP 4	56*	0	14	26
Jungle Environment (95 F, 75% rh)				
	Light Exercise, 200 W		Heavy Exercise, 425 W	
	38.6	39.5	38.6	39.5
MOPP 0	22	0	8	10
MOPP 2	16	0	8	9
MOPP 4	15	0	8	9
Desert Environment (110 F, 20% rh)				
	Light Exercise, 200 W		Heavy Exercise, 425 W	
	38.6	39.5	38.6	39.5
MOPP 0	165*	0	38	0
MOPP 2	34	86*	9	13
MOPP 4	27	101*	9	9

* – For this environment and MOPP, an acclimated individual never reached the threshold, thus an arbitrary 250 min. tolerance time was assumed for the acclimated individual. Thus, the value shown is equivalent to 250 minus the tolerance time of a non-acclimated individual.

3.3 Hydration Level

- For moderately and highly fit individuals, 19 and 9 min., respectively could be deducted from the predicted tolerance time due to a loss of ~2.5% body mass due to dehydration at a work rate of 250 W or less, and at MOPP-2 & MOPP-4 levels, jungle and desert.
- At 425, subtract only 4 min. at similar MOPP levels and environmental conditions.

3.4 Body Type

- Approximately 34 minutes could be deducted from the predicted tolerance time to account for individuals with higher body fat (>18.9% in comparison to <10.9%) content while in full chemical-defense posture exercising at low to moderate (<250 W) work rates.
- At 425 W, 6 min. could be deducted.

3.5 Gender

3.5.1 Corrections for Gender Differences

- At a low to moderate work rate (<250 W) the predicted tolerance time could be deducted by approximately 29 min. to account for gender differences when other individual characteristics (i.e. $\dot{V}O_2max$, body mass, %body fat) are not matched at MOPP-2 and MOPP-4, and jungle and desert climates.
- At 425, 4 min. could be deducted for similar conditions.

3.5.2 Menstrual Cycle and Oral Contraceptives

- The data for the female model was obtained during the luteal phase of the menstrual cycle, thus approximately 21 min. could be added to the predicted tolerance time during the follicular phase for female contraceptive non-users during light to moderate work (<250 W) for MOPP-2,4 in jungle and desert environments.
- At 425 W, the correction could be only 4 min. for similar MOPP levels and environments.
- No corrections should be made for contraceptive users.

3.6 Age

- It might be reasonable to approximate the correction (min.) due to age for persons unmatched in individual characteristics by using the equation, $Correction = 70.34 - (21.948 + 2.762x - 0.0395x^2)$, although care should be taken since the experimental study did not include males or chemical defense clothing; but it was an uncompensable heat stress study (48ºC, 10% RH).
- For example, for 35, 25, and 20 years of age, approximately 0, 4, and 9 min. should be deducted from the tolerance time prediction due to age.

3.7 Solar Load

- As expected, the addition of a solar load on an individual will cause increased body temperatures, and thus will decrease the tolerance time.
- For possible deductions in tolerance time due to solar load see Table 2 below.

Table 2: Corrections (min.) due to solar load at a given threshold of core temperature (38.6 and 39.5°C) predicted by Givoni & Goldman at various MOPP, activity and environments for young, fit males. These values should be subtracted from the predicted tolerance time of an individual working indoors.

Neutral Environment (75 F, 45% rh)				
	Light Exercise, 200 W		Heavy Exercise, 425 W	
	38.6	39.5	38.6	39.5
MOPP 0	0	0	0	0
MOPP 2	0	0	5	21
MOPP 4	0	0	3	11
Jungle Environment (95 F, 75% rh)				
	Light Exercise, 200 W		Heavy Exercise, 425 W	
	38.6	39.5	38.6	39.5
MOPP 0	17	64*	2	5
MOPP 2	11	94*	1	2
MOPP 4	9	89*	1	2
Desert Environment (110 F, 20% rh)				
	Light Exercise, 200 W		Heavy Exercise, 425 W	
	38.6	39.5	38.6	39.5
MOPP 0	0	0	13	0
MOPP 2	15	0	2	3
MOPP 4	11	0	1	0

***** – For this environment and MOPP, an individual working indoors never reached the threshold, thus an arbitrary 250 min. tolerance time was assumed for this individual. Thus, the value shown is equivalent to 250 minus the tolerance time of a individual working outdoors.

Appendix

- More details can be found in the Final Report submitted to MACTEC.

WORKLOAD INFORMATION

A list of activities and the work rates associated with those are provided below (based on the 2000 ACGIH, TLVs and BEIs). Note: The MU Heat Stress Model uses 200 W for 'Light' workload and 425 W for 'Heavy' workload.

Light workloads

Light Workloads are those that require less than 230 Watts. The No Effect Temperature plot in the MU Heat Stress Model uses 200 Watts for Light workload.

ACTIVITY	JOB DESCRIPTION
Sitting with moderate arm and leg movements	Administrative/paper work
Standing with light work at a machine or bench and some walking	Ground and aircraft maintenance personnel
Hand and arm activities	Administrative/paper work
Prolong standing and some walking	Century Duty
Tow-tractors (i.e. missile/bomb towing)	Munitions Specialists
Troop transport	Transportation/deployed personnel
Fueling aircraft, vehicles	Fueling Specialist
Towing Aircraft	Aircraft maintenance/support

Moderate workloads

Moderate workloads require between 230 and 400 Watts. The No Effect Temperature plot in the MU Heat Stress Model uses 300 Watts for Moderate workload.

ACTIVITY	JOB DESCRIPTION
Moderate lifting and pushing (i.e. supplies, boxes, miscellaneous items)	Crew Chiefs, Flight Chiefs, AGE, Load masters Ground and aircraft maintenance, mission support personnel
Walking	All deployed members
Carrying items (i.e. around shoulder, and hips)	All deployed members
Performing mechanical work with hands	Ground and aircraft maintenance personnel
Decontamination of patients	Hospital Augmentees
Hand and arm activities (heavy equipment operators)	Civil Engineering/RED HORSE

Heavy workloads

Heavy Workloads require more than 400 Watts. The No Effect Temperature plot in the MU Heat Stress Model uses 425 Watts for Heavy workload.

ACTIVITY	JOB DESCRIPTION
Heavy lifting and pushing (i.e. bomb loading)	Crew Chiefs, Flight Chiefs, AGE, Load masters, Ground and aircraft maintenance, munitions, mission support personnel
Running	All deployed members
Carrying large and heavy objects	All deployed members
Filling sand bags	All deployed members
Carpentry work	Civil Engineering
Assembly work	All deployed members
Trench digging (Pick and Shovel)	All deployed members
Erecting tent cities	All deployed members
Transport and carrying patients/casualties on stretchers.	Hospital Augmentees

Appendix 2

SAE Journal Paper

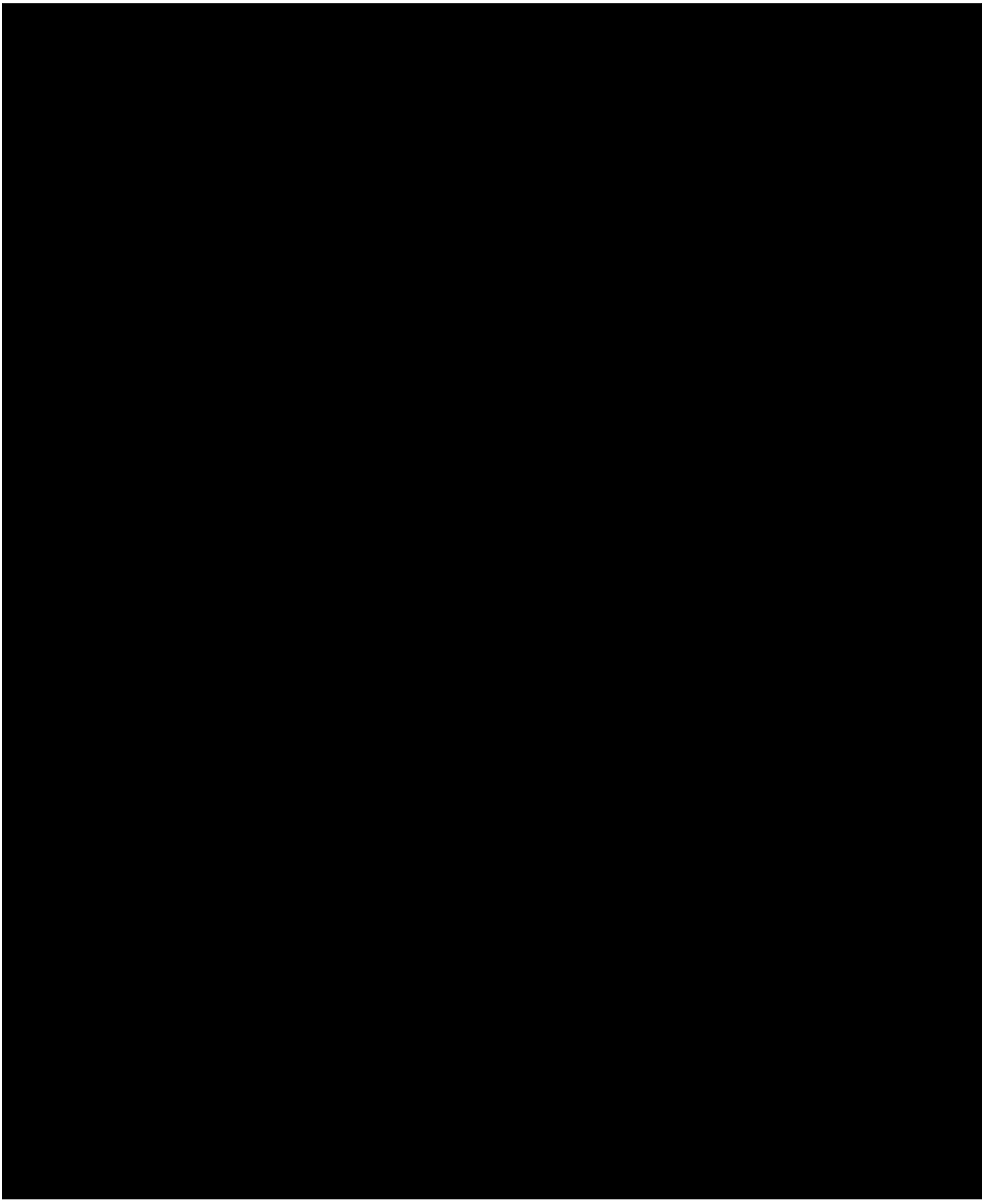

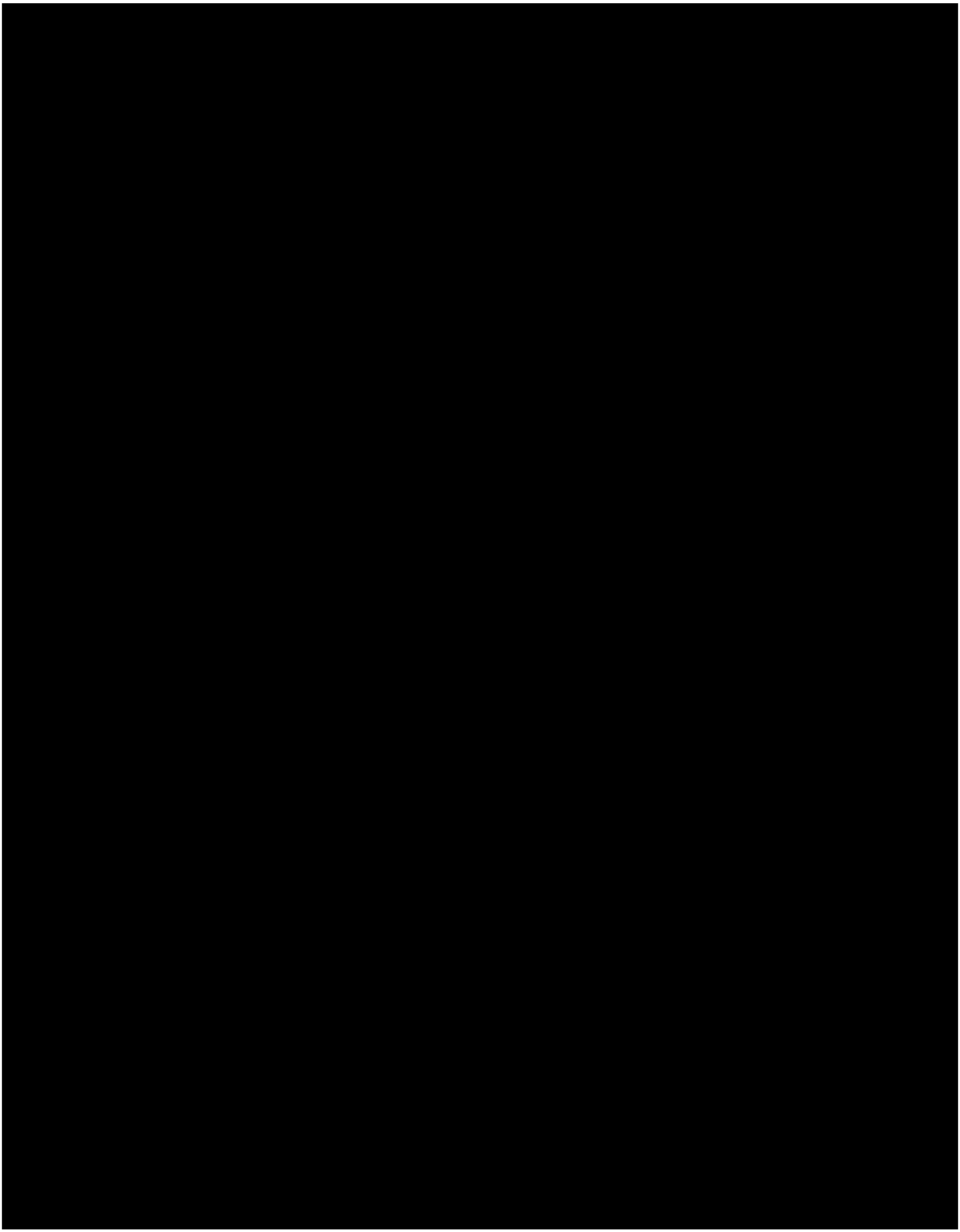

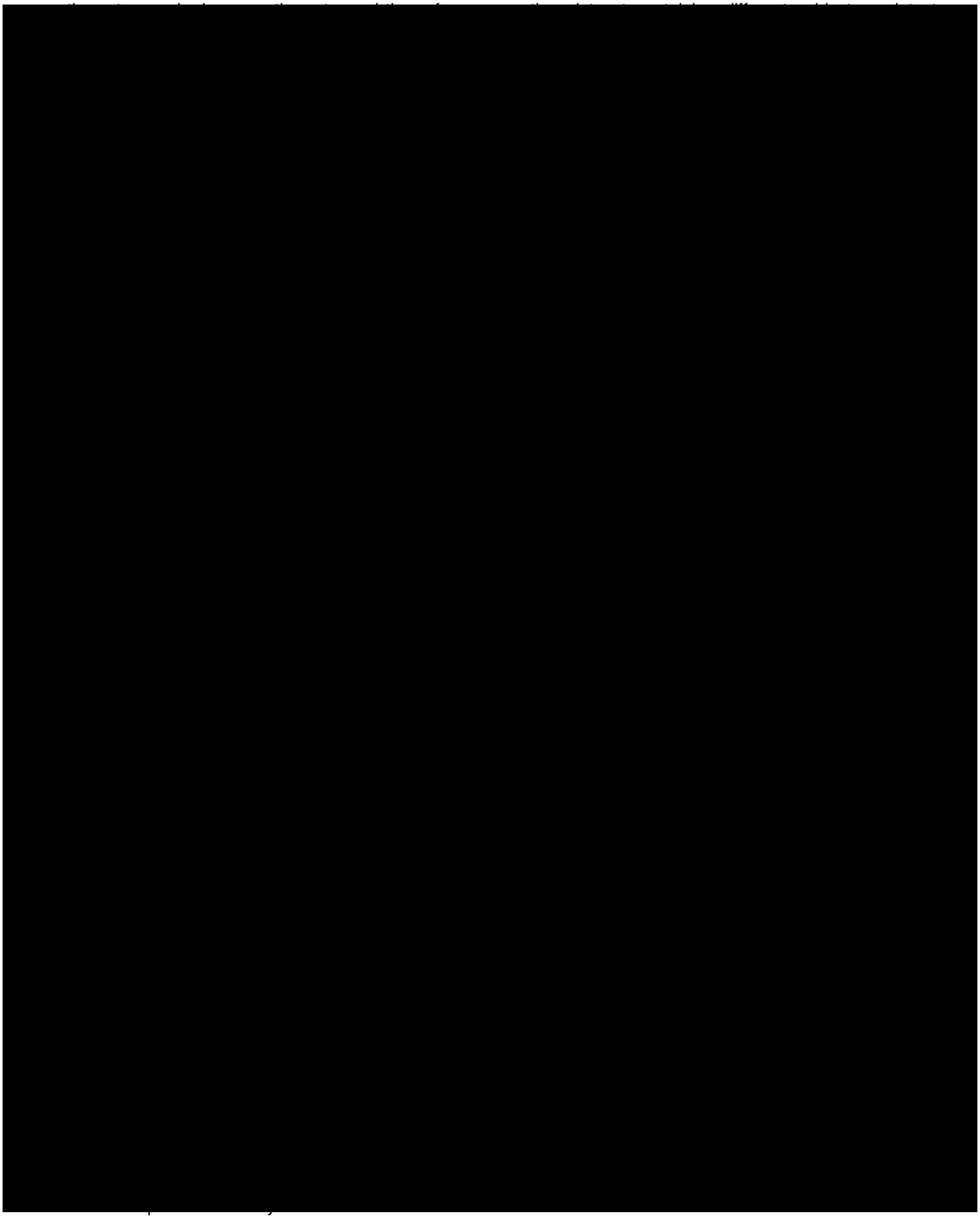

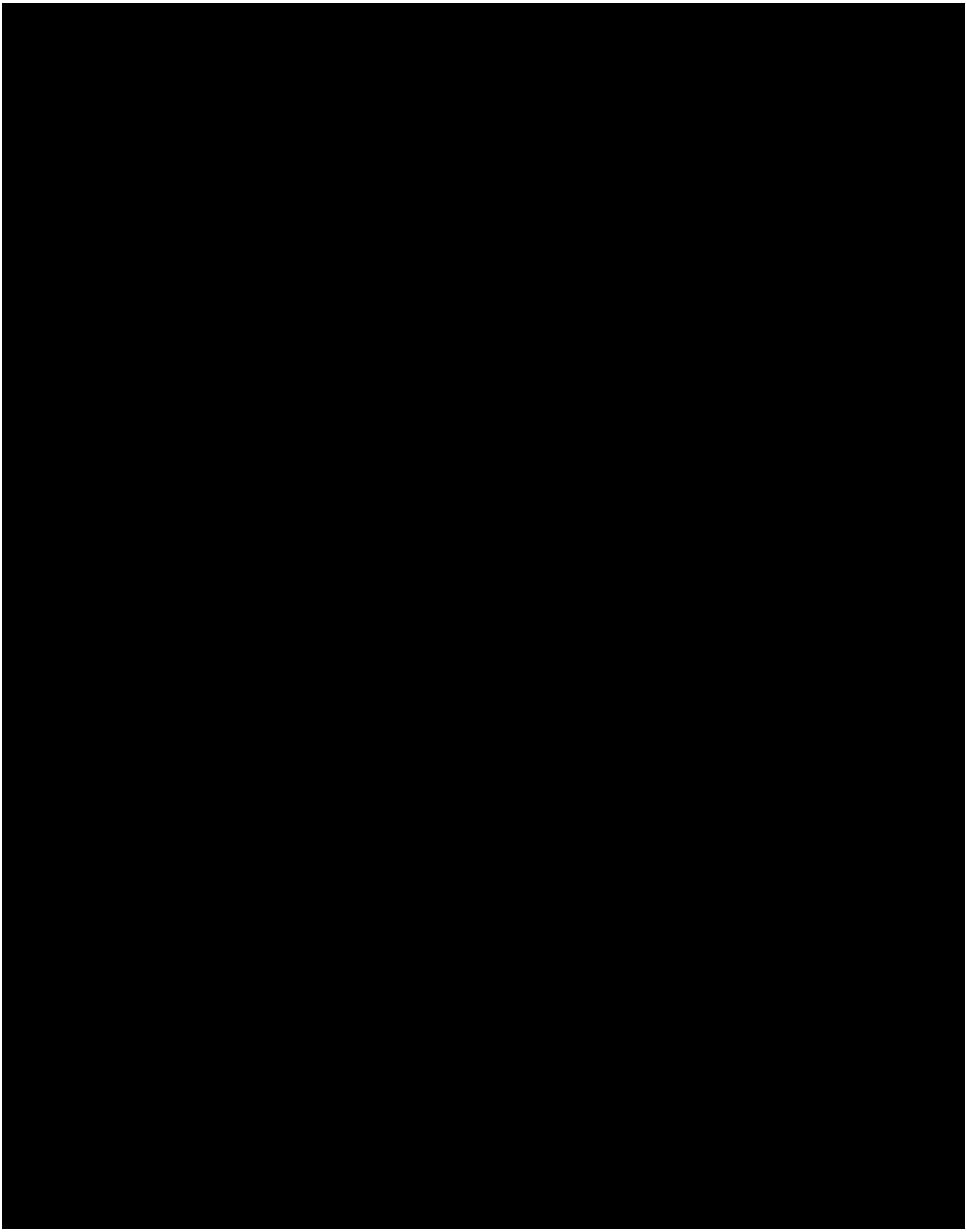

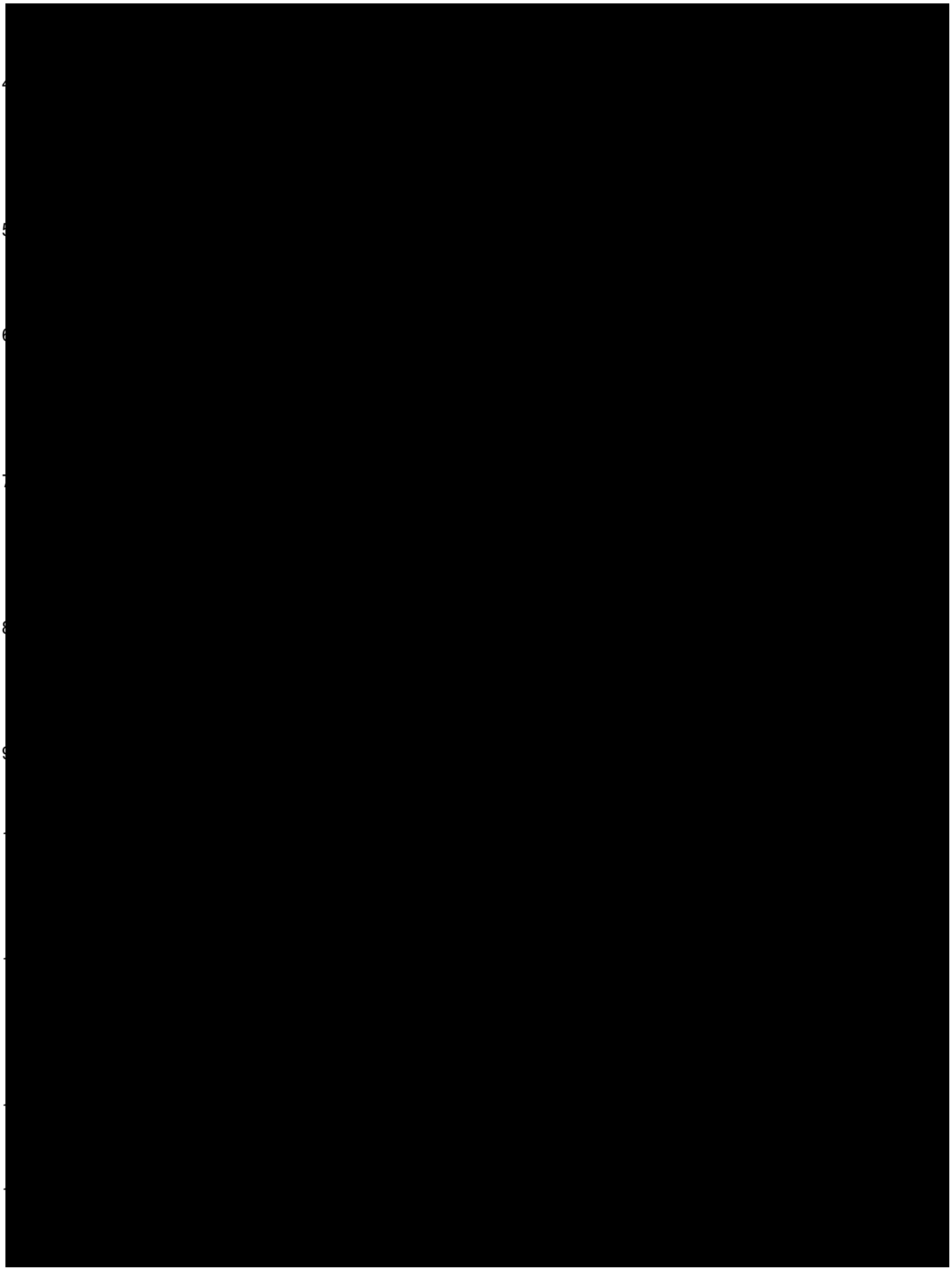

Table 1. Physical characteristics of the Natick dataset 1.

Gender	Group	N^{o} of Subjects	Age (years)	Surface Area of Body (Cm^2 $Kg^{-1)}$	Maximum Aerobic Capacity(VO2 max) ml/(min-kg)
Female	1	5	11.7 ± 1.6	321.3 ± 21.4	43.8 ± 1.3
	2	5	22.5 ± 2.3	307.3 ± 36.4	49.8 ± 1.3
	3	3	40.0 ± 6.0	279.3 ± 11.1	35.8 ± 1.3
	4	2	61.8 ± 2.0	290.3 ± 9.4	30.9 ± 1.3
Male	1	5	11.8 ± 2.8	319.3 ± 35.9	47.8 ± 2.4
	2	5	22.3 ± 2.9	270.3 ± 14.2	47.1 ± 2.1
	3	5	34.0 ± 5.6	252.3 ± 11.9	44.4 ± 2.2
	4	5	60.2 ± 5.0	253.3 ± 18.6	27.7 ± 1.5

Table 2. Descriptions of the parameters in dataset 1.

	Variables	Description	Unit
Individual Characteristics	**Subject**	Identifier	
	Group	I to IV	
	Age	Age of a subject	Years
	A_D	Surface area	m^2
	Gender	Male or Female	
	VO_2 Max	Max. aerobic capacity	ml/(min-kg)
	Height		Inches
	Weight		Kg
	M initial	Initial Metabolic Production	$W*m^{-2}$
	HR initial	Initial Heart Rate	Beat/min
Controlled Variables	**Time**	A total of 140 min	Min
	Ta	Air Temperature	C
	Pa	Ambient Vapor Pressure	Torr=mmHg
Measured Variables	**Tsk**	Skin Temperature	C
	Tes	Core Temperature	C
	HR	Heart Rate	Beat/min
	Evg	Evaporative Loss	g/min
	m_s	Sweating rate sweat capsule	$mg/(min*cm^2)$
	K_{chest}	Skin Conductance in Chest	$W/(m^2C)$
	K_{arm}	Skin Conductance	$W/(m^2C)$
	M	Metabolic Free Energy production	$W*m^{-2}$
	Disc	Discomfort Index	
	Tsens	Temperature Sensation Magnitude	
Calculated Variables	**Esk**	Heat Transfer via evaporation from the skir	$W*m^{-2}$
	Tb	Mean body temp.	C
	w	Skin wettedness	
	R+C	Dry Heat Loss	$W*m^{-2}$
	$\Delta Tb / \min$	Mean body temp. rate	$W*m^{-2}$
	S	Body Heat Storage Rate	$W*m^{-2}$
	Req. Esk	Required Evaporative Heat Loss	$W*m^{-2}$
	ET	Effective Temp.	C
	HRR	Heart Rate Ratio	

Table 3. Profiles of 'typical' subjects used for validation tests for dataset 1

	Male1	Male2	Male3	Male4	Male5	Female1	Female2	Female3	Female4
Age	8	25	21	39	64	10	26	32	60
Ad	0.963	1.89	1.86	1.97	1.88	1.3	1.45	1.72	1.45
VO2max	55.2	46.77	53.3	37.8	26.8	45.1	35.8	49.1	37.9
HRinitial	72	64	68	84	76	80	84	72	76
Minitial	56.9	51.2	55	48.6	40	54.8	62.7	45.9	46.9

Table 4. Coefficients of correlation (R) of predicted values with experimental values for each output (values with low R are marked in red.), for dataset 1.

	Male1	Male2	Male3	Male4	Male5	Female1	Female2	Female3	Female4
Tsk	0.995	0.984	0.987	0.992	0.987	0.957	0.99	0.985	0.981
R+C	1	0.969	0.999	0.999	0.999	0.994	0.999	0.999	0.985
M	0.983	0.548	0.903	0.927	0.823	0.955	0.774	0.941	0.777
Esk	0.943	0.875	0.918	0.871	0.949	0.849	0.943	0.915	0.92
Wett.	0.98	0.882	0.893	0.943	0.896	0.849	0.939	0.956	0.949
Karm	0.91	0.87	0.772	0.931	0.77	0.897	0.949	0.948	0.938
Kchest	0.955	0.985	0.895	0.94	0.788	0.827	0.915	0.948	0.835
Tcore	0.967	0.902	0.951	0.91	0.911	0.921	0.962	0.938	0.977
HR	0.954	0.924	0.928	0.762	0.904	0.963	0.91	0.964	0.905
S	0.975	0.998	0.99	0.998	0.995	0.992	0.997	0.997	0.964
Tsens	0.952	0.936	0.962	0.989	0.855	0.944	0.959	0.936	0.974
Disc	0.852	0.839	0.912	0.874	0.631	0.862	0.883	0.854	0.0854

Table 5. Descriptions of the parameters in dataset 2.

	Variables	Description	Unit
Individual Characteristics	**Subject**	Identifier	Non-dim
	Age	Age of a subject	Years
	Ad	Body surface area	m^2
	Gender	Male or Female	Non-dim
	VO_2 Max	Max. aerobic capacity	ml/(min-kg)
	% BF	Percentage of Body Fat	Non-dim
	Lean Body Mass	Mass without fat	kg
	VO2 Max (LBM)	Maximum VO2 for lean body Mass	ml/(min-kg)
	BSA/Wt	The ratio of BSA and Weight	Non-dim
	Height		Inches
	Weight		Kg
	M initial	Initial Metabolic Production	$W*m^{-2}$
	HR maximum	Maximum Heart Rate	Beat/min
Controlled Variables	**Time**	Time limit for heat tolerance	Min
	Ta	Air Temperature 40 C. Constant	C
	Air Velocity	Air Velocity 0.4 m/s Constant	M/s
	Clo	Clothing level Clo=2. Constant	M^2K/W
Output	**Tsk**	Skin Temperature	C
	Tcore	Core Temperature	C
	Evg	Evaporative Loss	g/min

Table 6. Correlation between parameters in dataset 2: Female group

	Age	height	Weight	VO2max	BSA	%BF	HR max	LBM	VO2 LBM	BSA/Wt	Time
Age	1.00										
Height	-0.05	1.00									
Weight	-0.24	0.79	1.00								
VO2max	0.21	0.41	-0.10	1.00							
BSA	-0.18	0.91	0.97	0.10	1.00						
%BF	0.13	-0.76	-0.94	-0.11	-0.92	1.00					
HR max	-0.70	-0.17	0.00	-0.24	-0.06	0.17	1.00				
LBM	-0.23	0.79	1.00	-0.08	0.97	-0.95	-0.02	1.00			
VO2 (LBM)	0.23	0.30	-0.24	0.99	-0.04	0.03	-0.21	-0.22	1.00		
BSA/Wt	0.33	-0.54	-0.94	0.30	-0.84	0.88	-0.11	-0.94	0.43	1.00	
Time	0.52	0.44	0.09	0.85	0.23	-0.33	-0.36	0.12	0.80	0.08	1.00

Table 7. Comparison of the individual time limit for heat tolerance between experimental and calculated values for dataset 2: Female group. R=0.91, Error SD =12.19

	Fem1	Fem2	Fem3	Fem4	Fem5	Fem6	Fem7	Fem8	Fem9
Experimental	130	130	180	140	130	105	90	90	120
Calculated	130	150	180	130	130	125	90	115	120
Error	0	+20	0	-10	0	+20	0	+25	0

Table 8. Comparison of the individual time-limit (min) for heat tolerance between experimental and calculated values for dataset 2: Male group. R=0.69, Error SD =18.44

	M1	M2	M3	M4	M5	M6	M7	M8	M9	M10	M11	M12	M13
Experimental	135	155	145	150	180	105	180	150	105	155	135	130	120
Calculated	125	145	145	145	145	125	180	145	125	145	135	165	125
Error	-10	-10	0	-5	-35	+20	0	-5	+20	-5	0	+35	+25

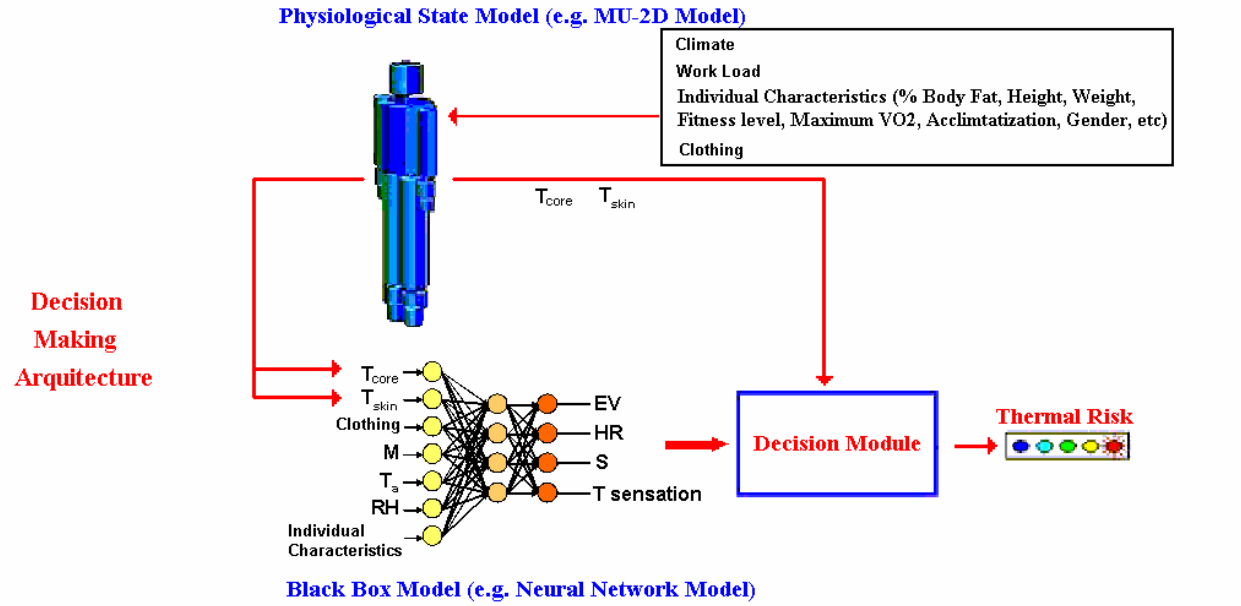

HR: heart rate Tcore: core temperature Tskin: mean skin temperatue Ta: air temp. RH: humidity M: heat production S: heat storage EV: evaporative heat loss T sensation: skin temperature sensation

Figure 1. Schematic of the proposed decision making model for thermal risk.

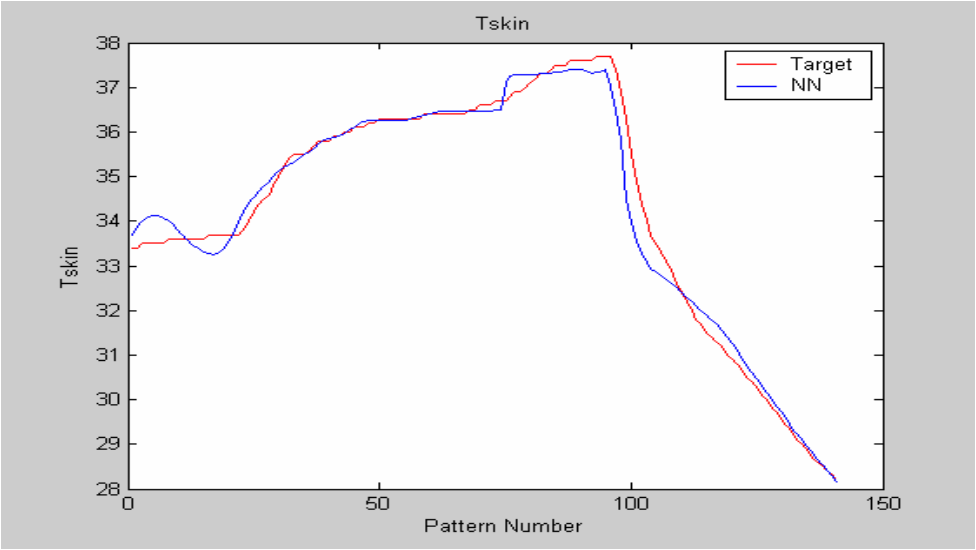

Figure 2. Representative plot for the prediction of T skin (Male 4 from dataset 1)

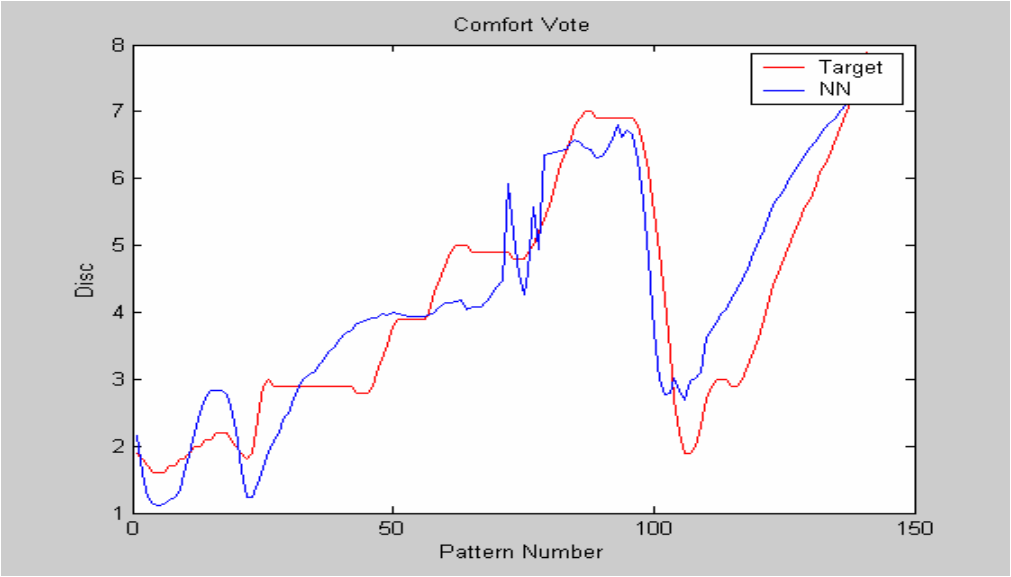

Figure 3. Representative plot for the prediction of Comfort Vote (Male 4 from dataset 1).

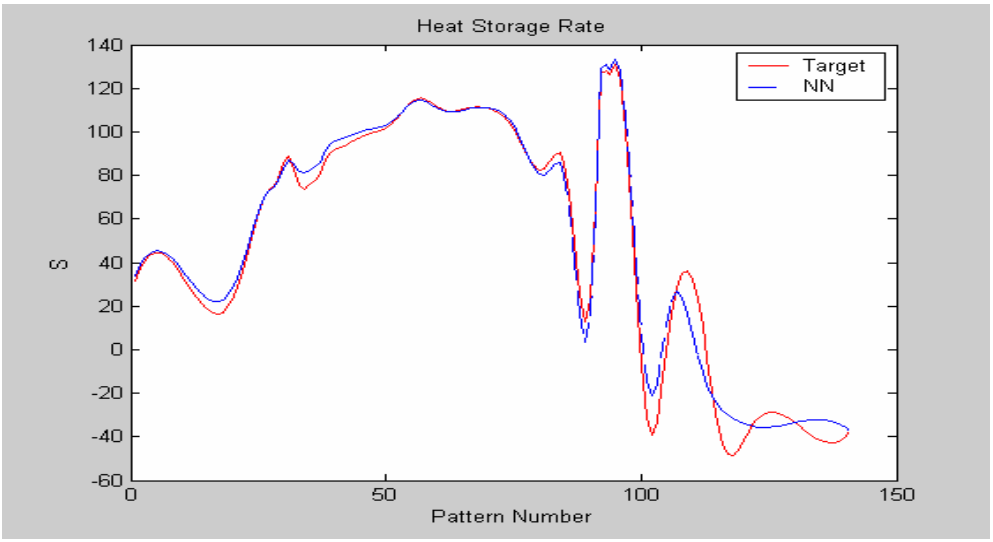

Figure 4. Representative plot for prediction of Heat Storage Rate (Female 1 from dataset 1).

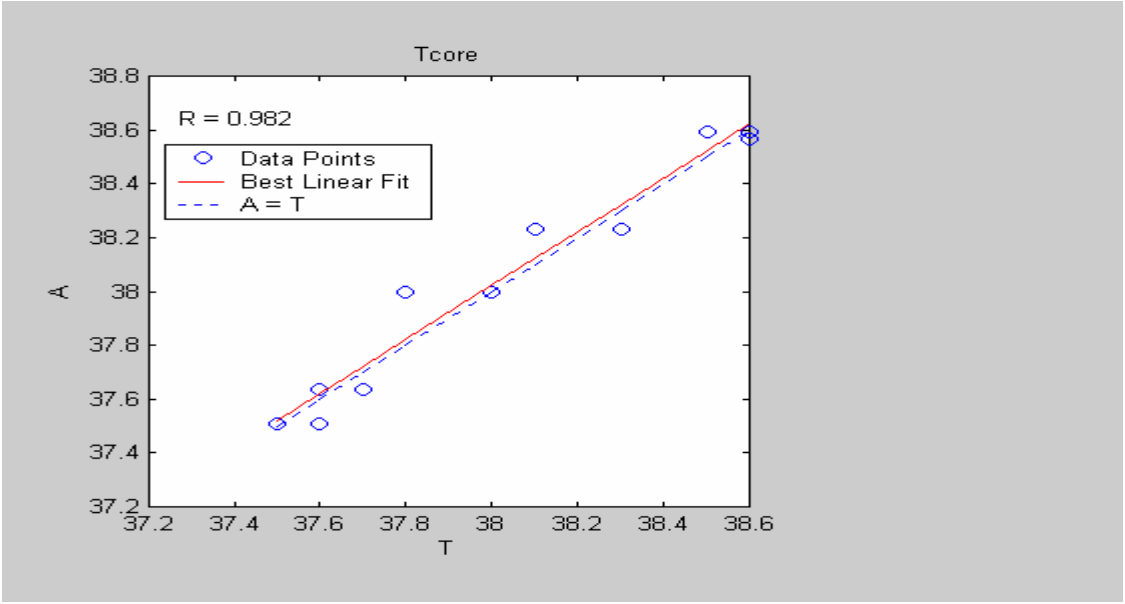

Fig 5. Plot for the correlation analysis between experimental against calculated values of Tcore with R=0.982 (Female 7 from dataset 2).

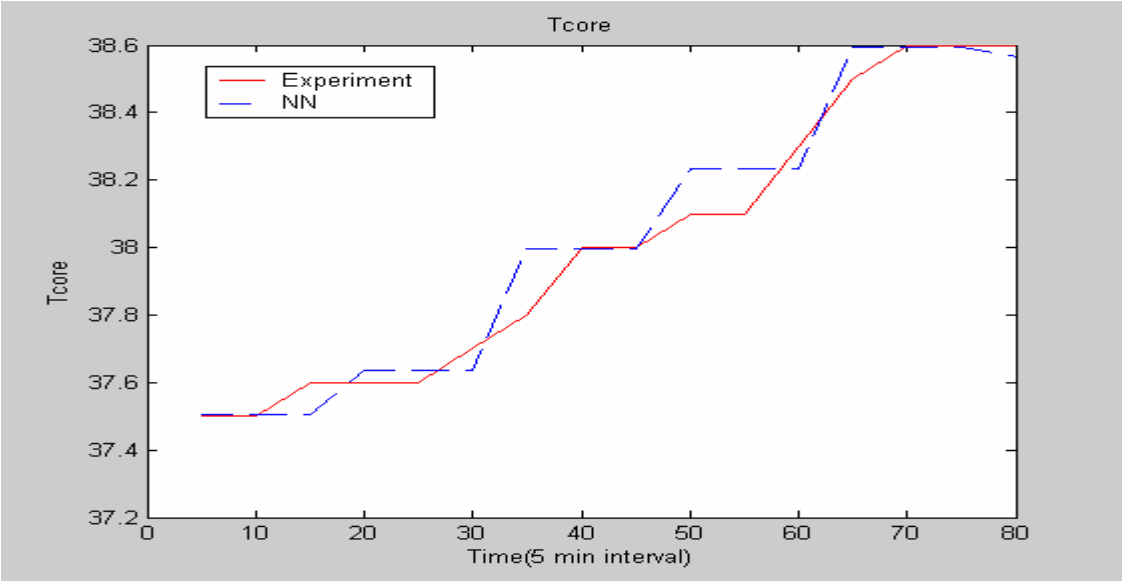

Fig 6. Plot for the predication of Tcore with R=0.982 (Female 7 from dataset 2).

Appendix 3

Pediatric Study Journal Papers

3.1 Journal of Trauma (2006): Predicting Hospital Mortality Among Injured Children Using a National Trauma Database (in pdf)

3.2 PREDICTION OF EARLY MORTALITY IN PEDIATRIC TRAUMA

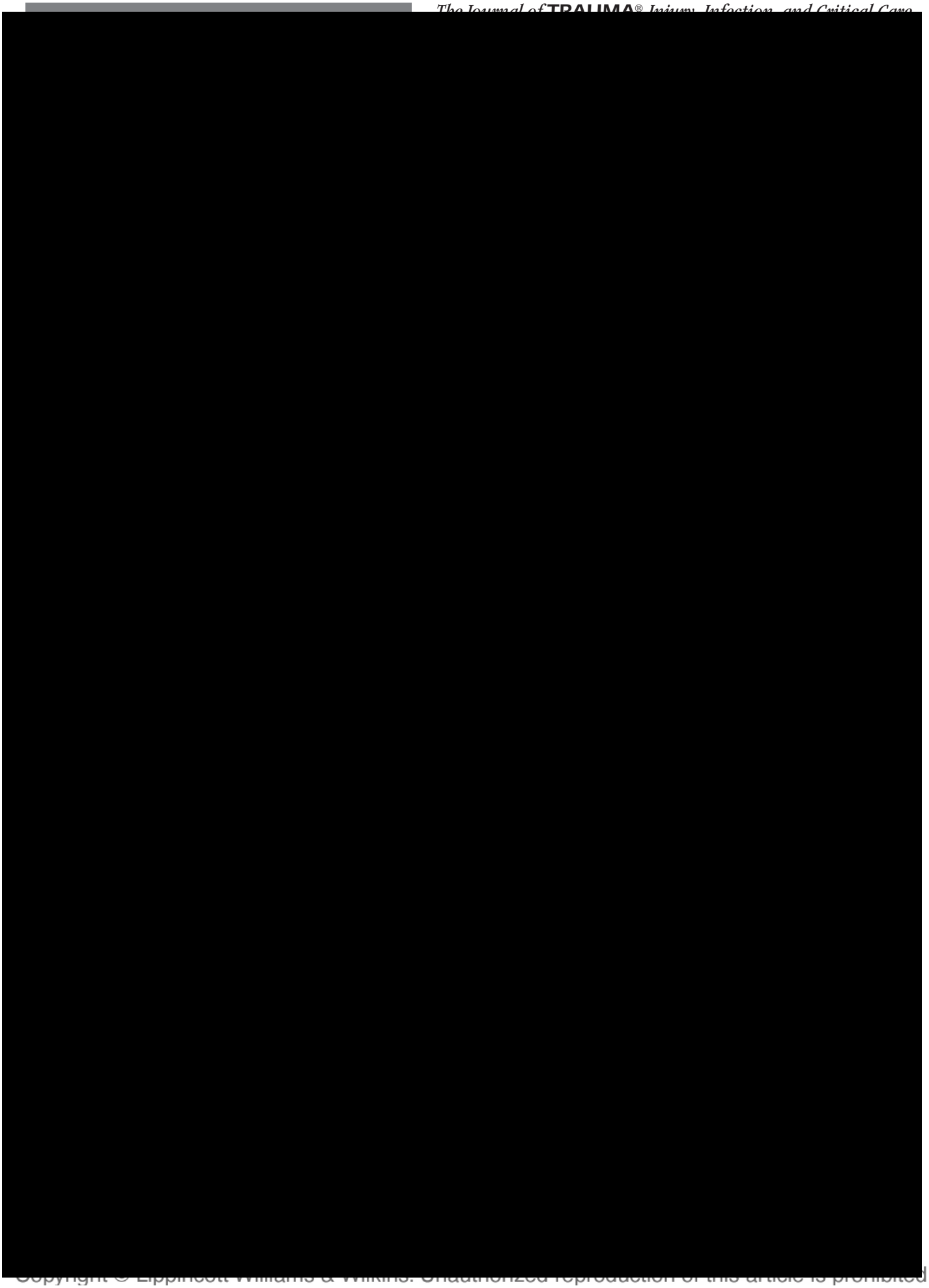

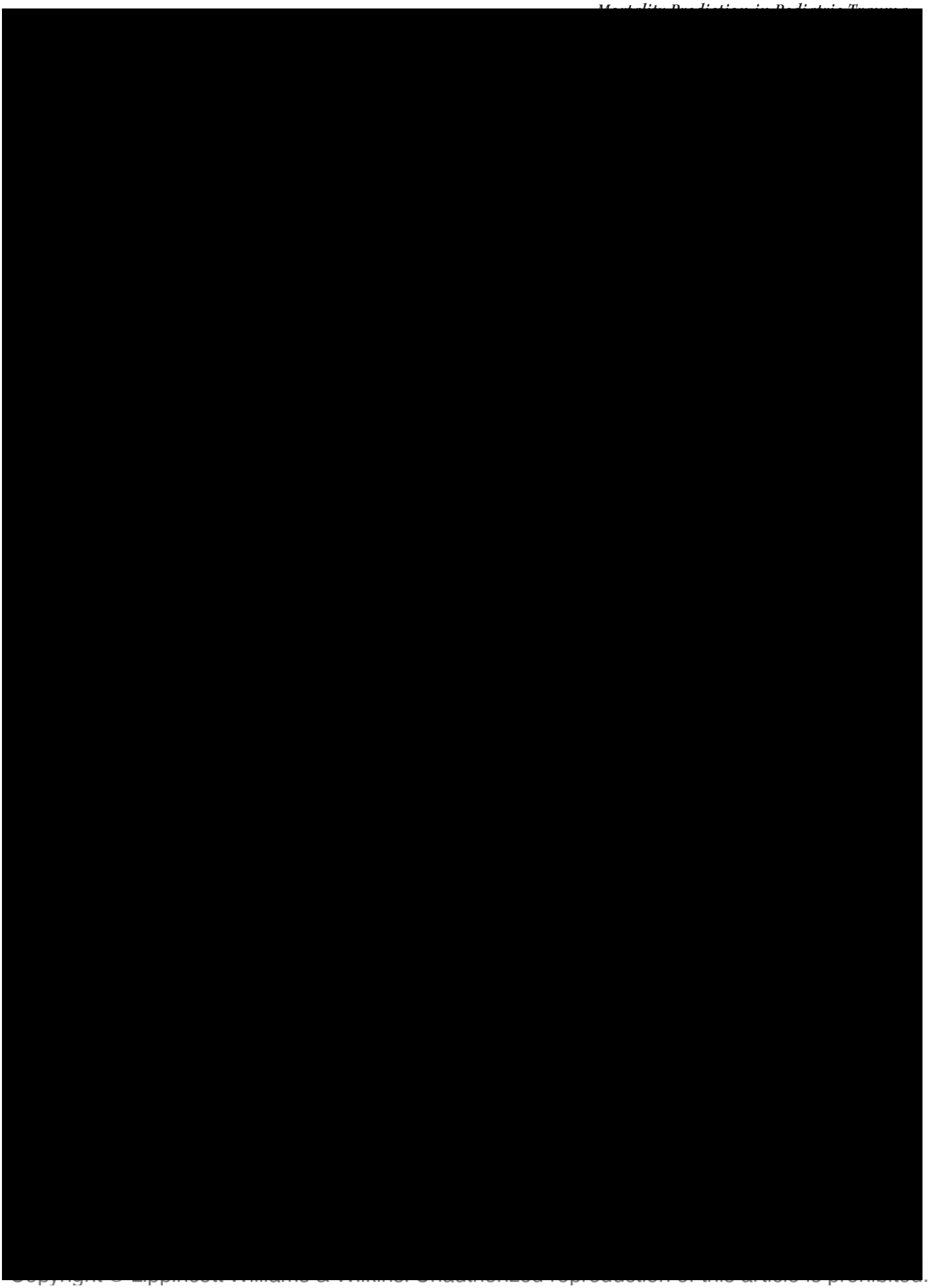

[redacted]

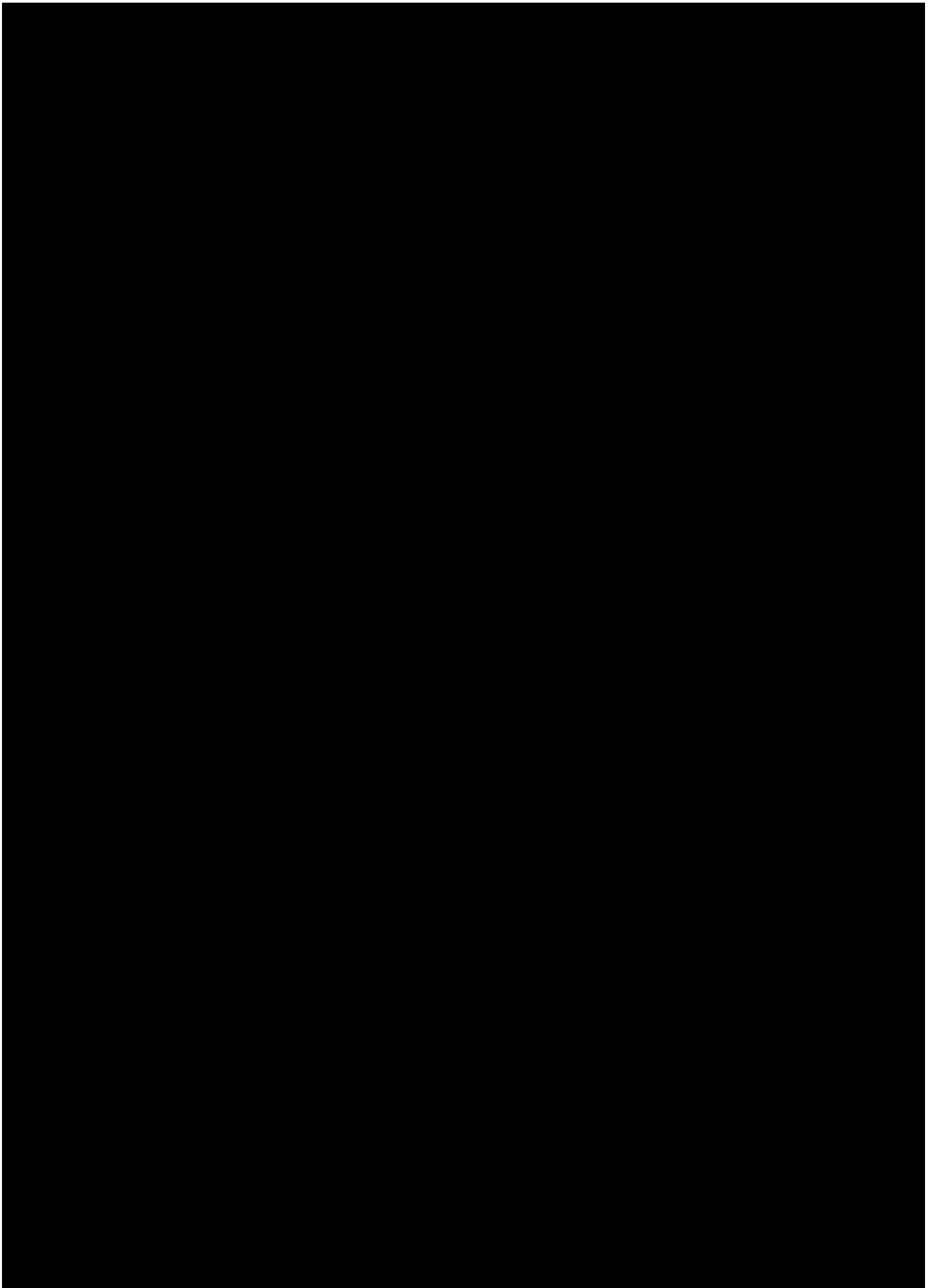

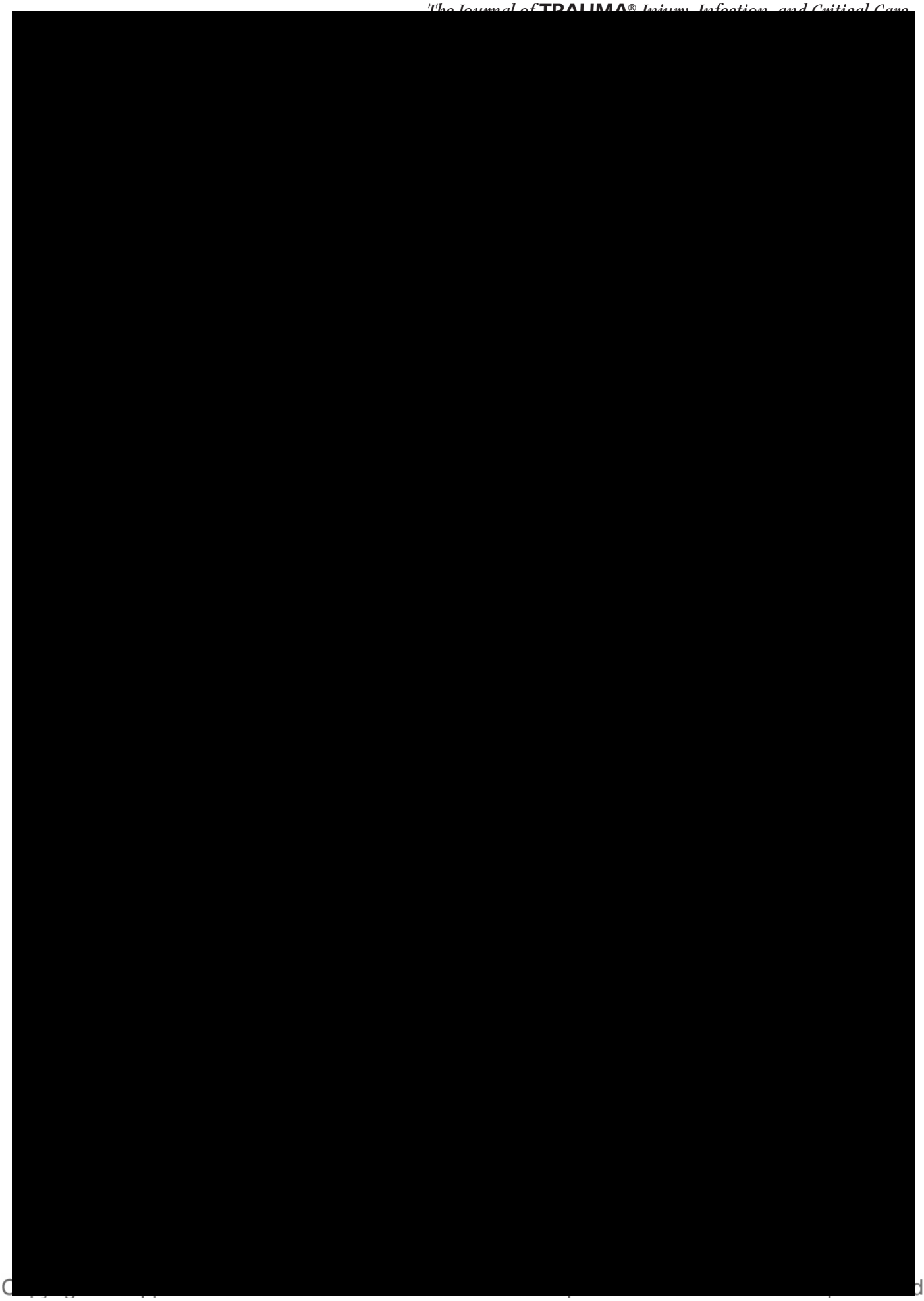

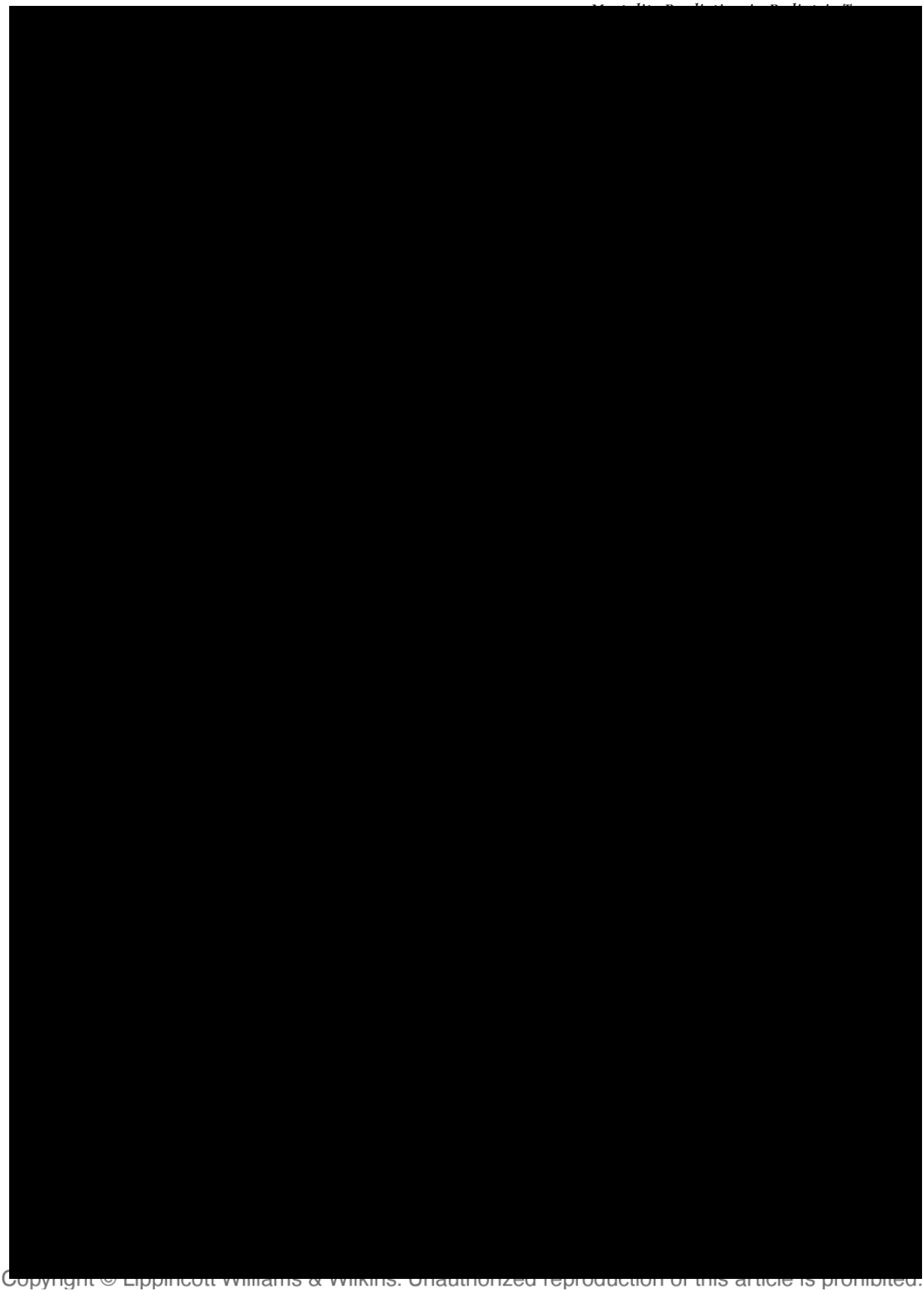

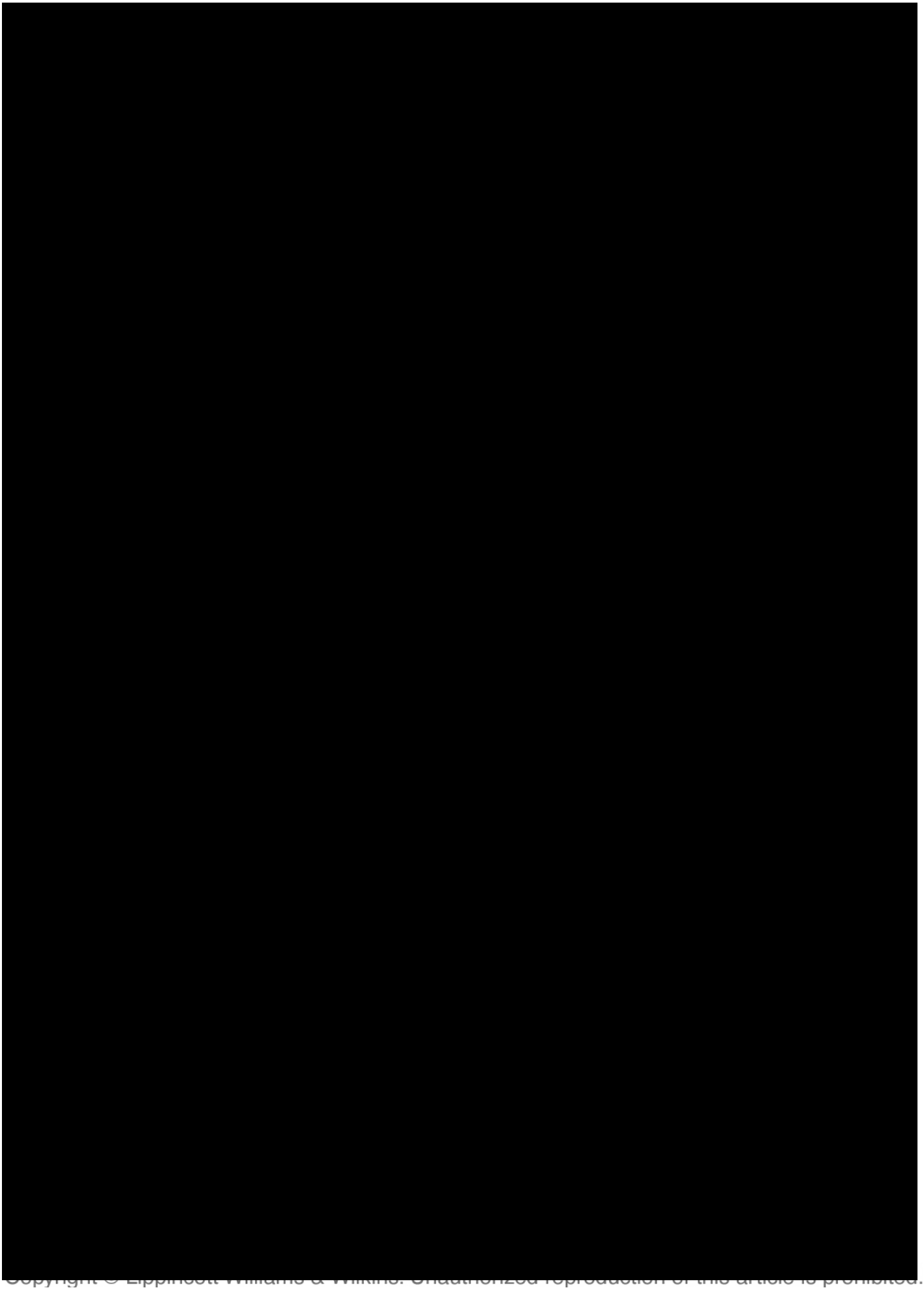

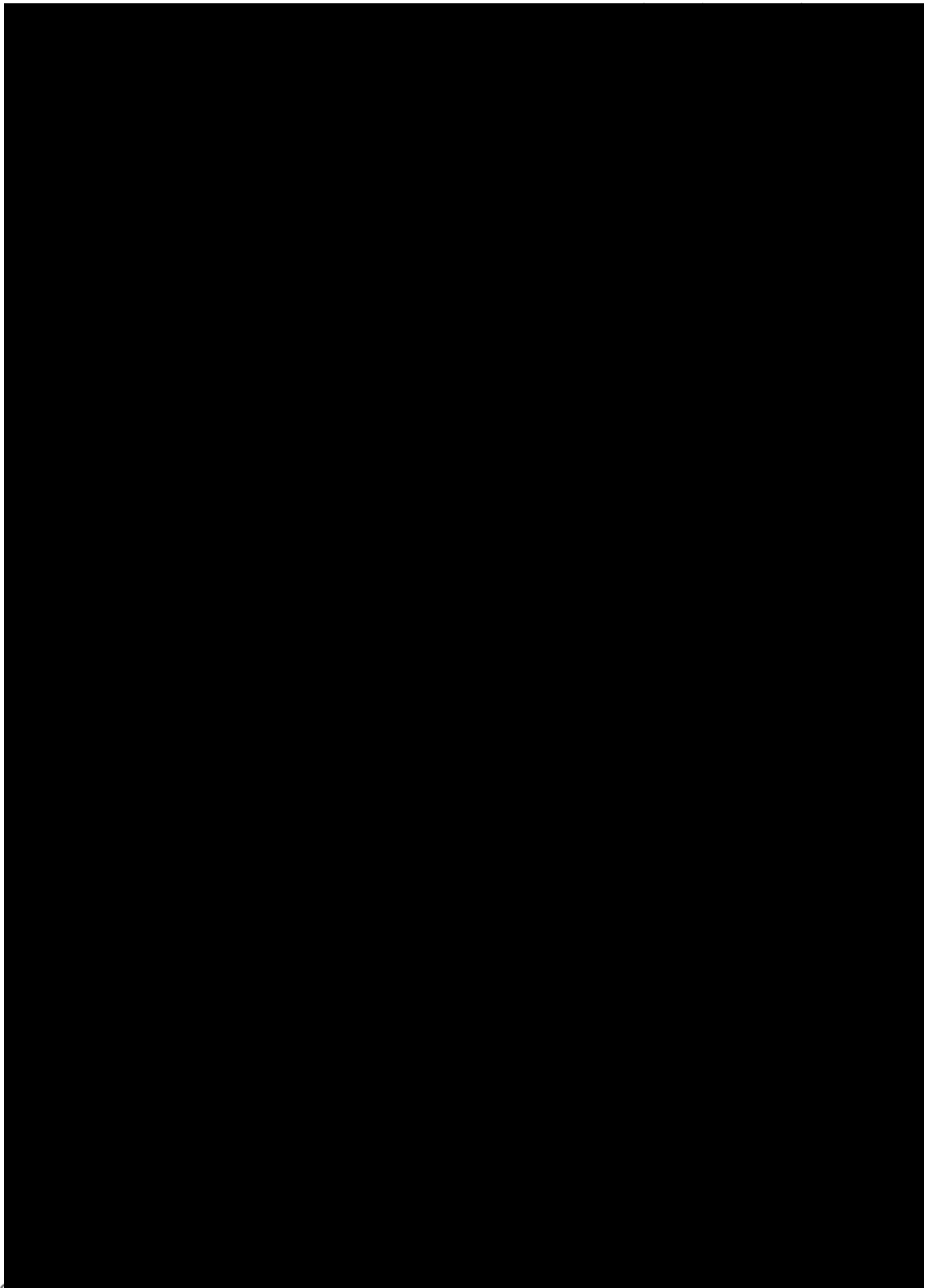

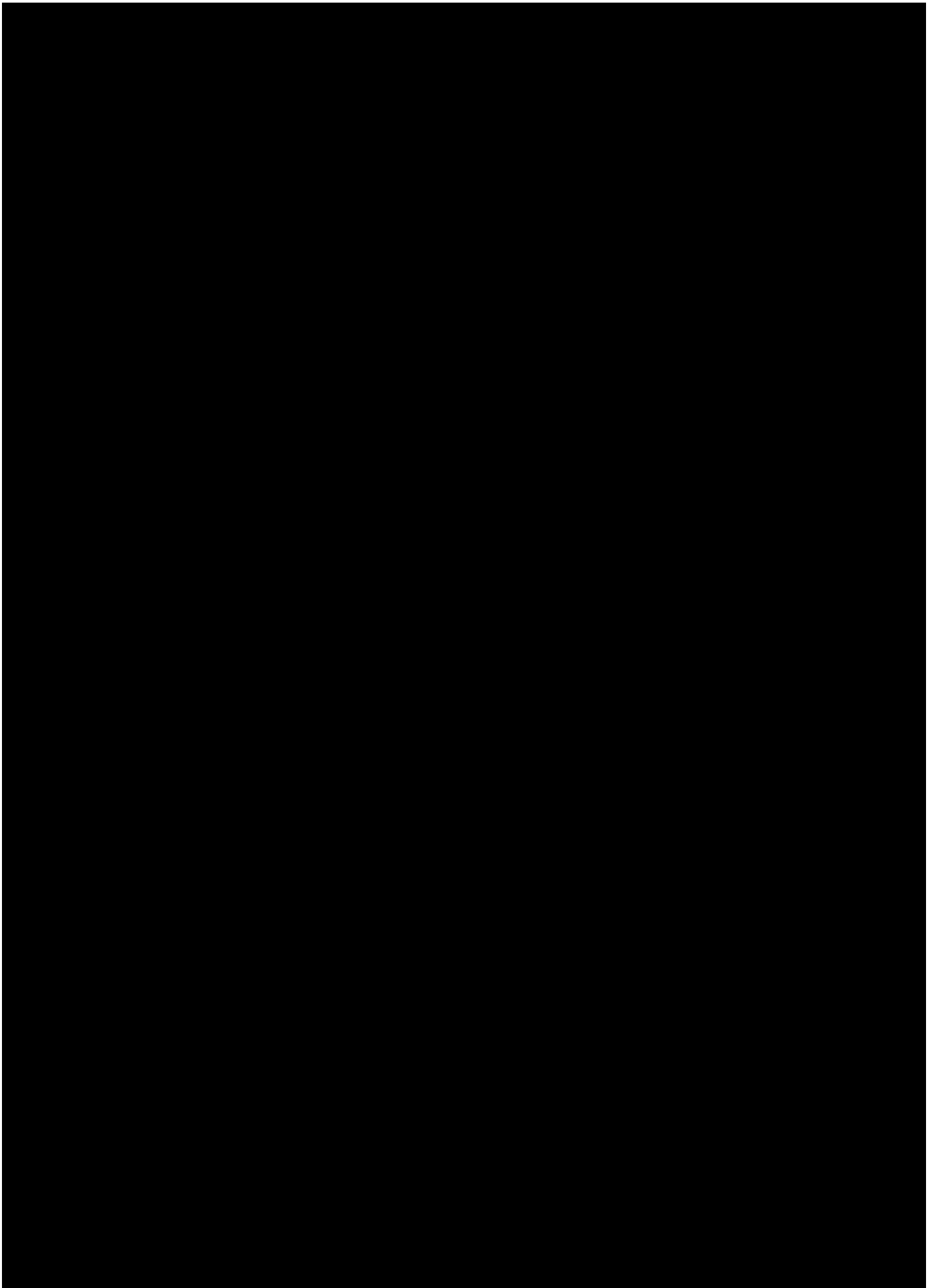

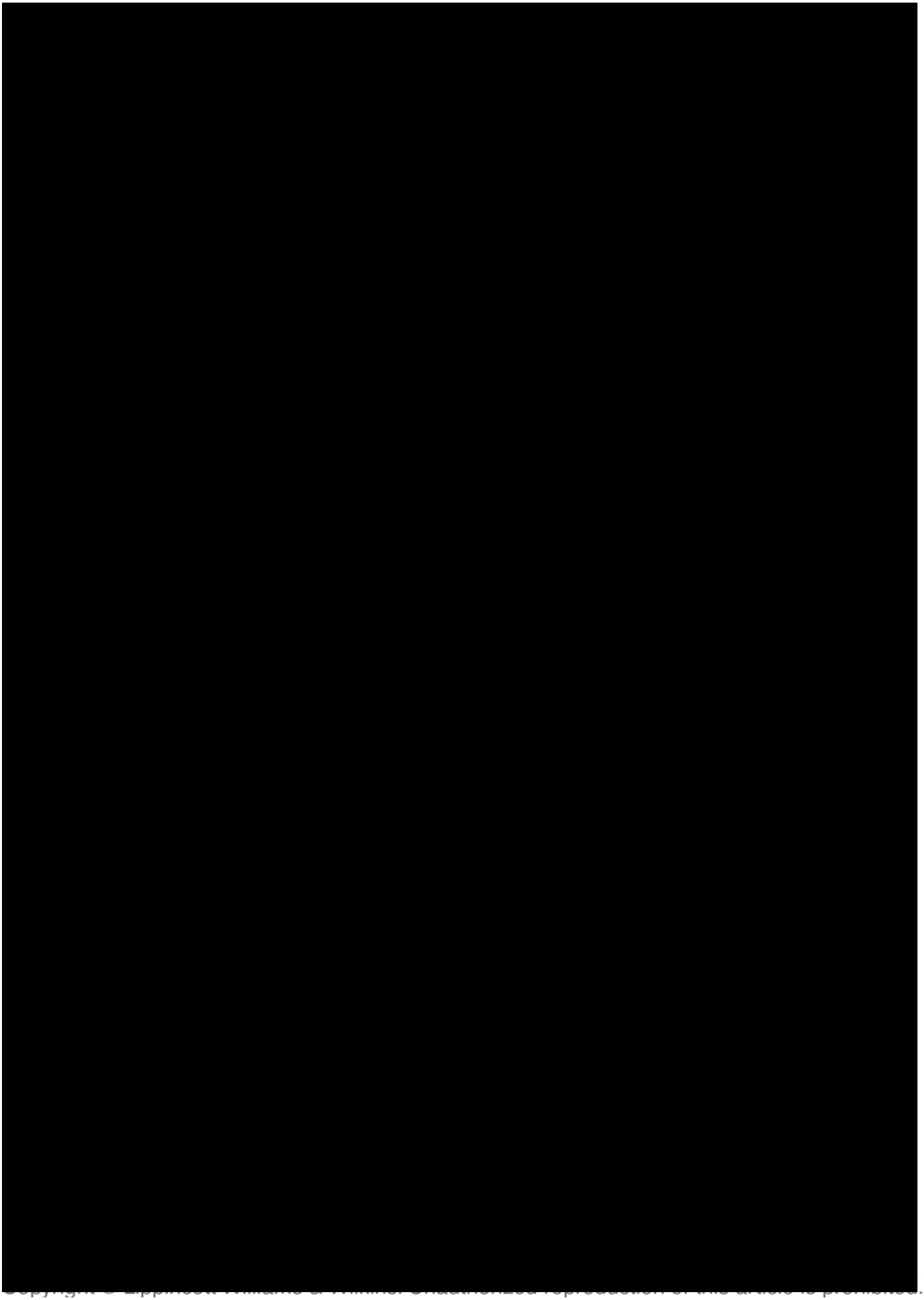

RUNNING HEAD

PREDICTION OF EARLY MORTALITY IN PEDIATRIC TRAUMA

REASSESSMENT OF THE RELATIONSHIP BETWEEN TYPE, INTENT AND MECHANISM OF INJURY AND RESOURCE UTILIZATION AND OUTCOME IN PEDIATRIC TRAUMA

Randall S. Burd, M.D., Ph.D.

Tai S. Jang, M.S.

Jeffrey S. Hammond, MD

Satish S. Nair, Ph.D.

Randall S. Burd, M.D., Ph.D.*

Tai S. Jang, M.S.+

Jeffrey S. Hammond, MD*

Satish S. Nair, Ph.D. +

From the Department of Surgery, UMDNJ- Robert Wood Johnson Medical School, New Brunswick, New Jersey* and the Department of Mechanical and Aerospace Engineering, University of Missouri-Columbia, Columbia, Missouri+

Supported by grant R03/HD042561 from the National Institute of Child Health and Human Development, National Institutes of Health

Address correspondence/reprints: Randall S. Burd, M.D., Ph.D., UMDNJ-Robert Wood Johnson Medical School, Department of Surgery, Division of Pediatric Surgery, One Robert Wood Johnson Place, PO Box 19, New Brunswick, NJ 08903, telephone 732-235-7821, Fax: 732-235=8878, e-mail: burdrs@umdnj.edu

We, the below authors, have no financial or proprietary interest in the subject matter or materials discussed in the manuscript, including (but not limited to) employment, consultancies, stock ownership, honoraria, and paid expert testimony.

Randall S. Burd _____

Tai S. Jang _____

Jeffrey S. Hammond _____

Satish S. Nair _____

ABSTRACT

Purpose: Most prehospital triage strategies are based on physiologic, anatomic and mechanism-related variables. Measurement variability and prehospital provider interpretation can affect the accuracy of physiologic variables such as Glasgow coma score and vital signs, while prehospital provider interpretation can affect the accuracy of anatomic site assessment. The purpose of this study was to develop a model predicting early hospital mortality based on non-physiologic and non-anatomic prehospital variables.

Methods: Patients <18 yrs (n=34,338) included in the National Pediatric Trauma Registry (NPTR) Phase III were used to develop a logistic regression model to predict early mortality (<4 hrs after arrival). Covariates used in the model included mechanism of injury, scene vs. hospital transfer status, and prehospital treatment. Multiple imputation was used to handle missing values. NPTR Phase IV (n=14,200) data was used to test the model. Discrimination was tested using area under the ROC curve (ROC) and calibration using the Hosmer-Lemeshow (H-L) h-statistic and calibration curve R^2.

Results: Early hospital mortality was observed in 0.8% of subjects in the training dataset and 0.7% in the testing dataset. Significant (p<0.05) predictors of increased mortality included assault (OR 2.4), pedestrian accident (OR 2.9), gunshot wound (OR 5.6), transfer from the scene (OR 4.4), prehospital intubation (OR 10.1) and prehospital CPR (OR 45.6). Injury by a fall had a significantly lower risk of early mortality (OR 0.2, p<0.05). Other mechanisms had no significant association with mortality including motor vehicle, motorcycle, bike or ATV crash and stab injury. The model had excellent discrimination (ROC 0.945) and calibration (H-L statistic 5.2, p>0.05; R^2=0.96) on data in the testing set.

Conclusion: Non-physiologic and non-anatomic prehospital data can accurately predict early

hospital mortality among injured children. This model may be a useful adjunct to current triage tools for rapidly identifying a high risk subgroup of injured children who may benefit from early trauma center interventions.

KEY WORDS: wounds and injury; child; hospital mortality; models, statistical

INTRODUCTION

Previous studies suggest that severely injured children have better outcomes when treated at trauma centers, particularly those with a pediatric expertise. The reasons for these observations have not been studied but likely relates to the resources and experience available at trauma centers. These

Advantages of trauma center:

1. Improved quality of care by virtue of experience, QI, verification and maintenance of a broad range of servies
2. Rapid availability of resources: CT scan, OR staff, in house trauma surgeons

The prehospital decision of where to direct injured patients is complex. (to trauma center, to adult trauma center, to nearest hospital, by what mode (ground vs air). Trauma triage decisions are complex and based on:

1. Criteria established using local, regional or national standards—also, the interpretation of these standards by prehospital providers is relevant
2. Nearest hospital (even though this is used prehospital, the need for ER to other hospital transfer should be considered)
3. Prehospital provider biases: belief of appropriate hospital for patient, practice pattern of prehospital provider, relationships of ambulances with hospital

Cooper ME: patients triage based on ACS mechanism criteria alone (those without any anatomic or physiologic criteria) uncommonly had severe injury (ISS>15) (was this article only adults?)

Esposito TE: mechanism as a sole predictor of mortality was variable: high yield for pedest struck and those with vhenicular occu death and low for vehicular rollover. (was this article only adults?)

Santaniello: mechanism of injury alone resulted in 'appreciable' undertriage with respect to mortality and severity of injury. In contrast, using mechanism has a high yield for identifying patients who are resource intensive: i.e., transfor from ED to OR or to ICU.
Another point by Santaniello: many operations may potentially be able to be performed at the outlying hospital before transfer. The time delay associated with transport and reevaluation may be important in selected patients' outcome. **urged evaluation of mechanism, anatomic and physiologic criteria based on "resource utilization and functional/operational issues".

Farrell LS: most children with severe injuries in NY treated at hospitals with a PICU (evidence that appropriate triage is being applied). (This article also has important review of the advantages of pediatric trauma centers).

Previous evaluation of triage systems has been primarly based on severity of injury (as measured by ISS) and hospital death. Few have looked at the need for trauma center resources (ICU, operating room). Also, few have looked at pediatric triage specifically. E.g., the physiologic criteria need to be modified to be pediatric specific, the importance of difference mechanism criteria may be different in kids.

The reality is that ACS trauma triage criteria may be poorly followed. Most (60%) of adult trauma pts meeting at least one ACS criteria were transported to a non-trauma hospital. More importantly, about 25% of those with an ACS criteria and severe injury (ISS>15) were treated at non-trauma centers (Baez AA).

The importance of appropriate initial triage has been shown by a long waiting time before transfer even among those rapidly identified at the referring hospital early on who would require transfer to a trauma facility. Factors such as communication delays between facilities,

availability as an appropriate transport team are factors which influence transport time even when a rapid decision to transfer is made (Ammon AA)

The use of the NPTR is helpful: includes time until death. Also, in addition to ECODE, provides a brief written description of the injury that permits more detailed study of features of the injury than possible using ECODE alone.

METHODS

Data Sources and Subject Selection

This study has been approved by the Institutional Review Board at UMDNJ-Robert Wood Johnson Medical School. The National Pediatric Trauma Registry (NPTR) is a database started in 1985 that tracks the management and outcome of injured children treated at participating pediatric trauma centers or pediatric hospitals. Data (n = 50,199) from the registry obtained between 1995 and 2001 were used. Variables available in the database included age, gender, type of injury (blunt, penetrating or other), external cause of injury (E-code), Injury Severity Score (ISS), emergency department and discharge disposition, length of ICU stay, total length of stay (LOS), mortality, time until death and cause of death (central nervous system injury-related, hypoxia, hypovolemia or hemorrhage, multiple organ failure or other/unknown). The NPTR also includes a brief description of the injury provided by the reporting hospital. E-codes were used to assign a mechanism and intent (assault, self-inflicted, unintentional or undetermined/other) using the framework recommended by the Centers for Disease Control (CDC) for presenting injury mortality data.[16] Because of their importance as a mechanism of

injury among children, falls were further classified as previously described into falls from a building, falls fro furniture, falls from playground equipment, falls from stairs, other falls from stairs, other falls from heights, falls on the same level and other/unspecified falls. Children with injuries related to an off-road motor vehicle (E821) were identified among those injured by other modes of transportation ('transport, other') based on the high morbidity and mortality associated with this mechanism in children. Patients >14 yrs old (n = 7,202) and those with an E-code representing injury by poisoning, drowning, overexertion or burn (n = 31) were not included in the analysis.

Statistical Software

SPSS 12.0 (SPSS Inc., Chicago, IL) was used for all statistical calculations. Differences between groups were compared using Fisher's exact test with significance defined as $p<0.05$. Kaplan-Meier product limit method was also used to analyze mortality. Time until death was a variable available in the database. Survivors were censored when discharged from the hospital. Survival rates were compared using the log rank test with significance defined as $p<0.005$ to account for multiple comparisons. Continuous variables were analyzed using the Student's t-test.

RESULTS

Overview of Data

In the study, 42,966 injured children were identified, 63.6% of whom were male. The average age was 6.8 ± 4.2 yrs. The distribution of the type of injury among different mechanisms of injury is shown in Table 1. More injuries were due to blunt than either penetrating or other mechanisms. Penetrating injuries were most frequent among children injured by a cut/pierce, firearm, machinery or natural/environmental mechanism. Penetrating machinery injuries were most commonly from a saw (14/46, 30.3%), while penetrating injuries due to a

natural/environmental mechanism were most commonly from dog (606/748, 81.0%) or snake bites (77/748, 10.3%). The distribution of the intent of injury among different mechanisms of injury is shown in Table 2. Unintentional injuries were more frequent than injuries due to other intents (93.1%). Assaults were most common among children injured by a firearm, those being struck by a non-falling object and child abuse. Self-inflicted injuries were most frequent among those injured by a firearm or by suffocation.

Type, Intent and Mechanism of Injury and Mortality

There were 1,232 deaths (2.9%). Children who died were younger (5.9 ± 4.4 vs. 6.7 ± 4.2 yrs, $p<0.001$) and more commonly male (40.0% vs. 36.6%, $p=0.02$) than those how survived. Central nervous system injury was the leading cause of death followed by hypoxia, hemorrhage or hypovolemia, multiple organ failure and other or unknown causes (Table 3). While a similar percentage of deaths among children sustaining either a blunt or penetrating injury were due to a central nervous system cause (73.4% vs. 67.5%, $p>0.05$), death among children sustaining a penetrating injury were more commonly due to hypovolemia or hemorrhage than those dying from a blunt injury (16.9% vs. 5.8%, $p<0.001$). Compared to deaths due to other intents, deaths due to a self-inflicted injuries were less commonly from a central nervous system cause and more commonly from hypovolemia or hemorrhage (Table 3), consistent with the high percentage (45%) of penetrating injuries among children with self-inflicted injuries. More than 25% of deaths cause by a cut/pierce, machinery and motorcycle mechanism were due to hypovolemia or hemorrhage (Table 3). Death occurred most rapidly in children dying of hypovolemia or hemorrhage (Fig. 1). Mean survival was 17 hrs (95% CI, 5 to 29 hrs) for children dying of hypovolemia or hemorrhage, 29 hrs (95% CI, 17 to 42) for those dying of other or unknown causes, 52 hrs (95% CI 43 to 60) for those dying of CNS injury, 59 hrs (95% CI, 38 to 81) for

those dying of hypoxia and 73 hrs (95% confidence interval [CI], 29 to 117) for those dying of multiple organ failure.

Blunt and penetrating injuries had a similar mortality (Table 4) and time until death (Fig. 2). Patients injured by a penetrating or blunt mechanism had a lower mortality ($p<0.001$, Table 4) and died later after injury (Fig. 2) than those with other types of injury. Self-inflicted injuries had a higher mortality than injuries due to other intents ($p<0.001$, Table 4), with 76% (22/29) of deaths occurring within the 24 hrs after admission (Fig. 3). Unintentional injuries had the lowest mortality ($p<0.001$, Table 4).

Deaths were observed for firearm injuries and suffocations in each intent category. Children sustaining a firearm injury that was either self-inflicted or due to an undetermined intent had a higher mortality than those injured in an assault or injured unintentionally ($p<0.001$, Table 4). Seventy-five percent (11/13) of deaths due to a self-inflicted firearm injury and 66% (4/6) of deaths due to a firearm injury of undetermined cause occurred within the first 24 hrs after admission (Fig. 4A). Self-inflicted firearm injuries leading to death were most commonly gunshot wounds to the head (10/13, 77%). CNS injury was the most common cause of death among children sustaining a self-inflicted or undetermined intent firearm injury (15/19, 79%). No significant difference in mortality was observed among suffocations due to each intent ($p>0.05$, Table 4). All self-inflicted suffocations (n = 31) were due to hanging. Sixty-nine percent (11/16) of deaths due to self-inflicted suffocations and 48% (10/21) of those due to unintentional suffocations occurred within the first 24 hrs after admission (Fig. 4B).

Mechanisms were further analyzed after grouping by intent. Assaults due to either firearms or child abuse had a higher mortality than assaults due to other mechanisms (Table 4). Ninety-one percent (21/23) of deaths due to an assault by a firearm and 48% (108/227) of deaths

due to child abuse occurred with the first 24 hrs after admission (Fig 5A). Firearm injury and suffocation generally had the highest mortality among children injured by self-inflicted, unintentional or undetermined intent. The mortality of firearm and suffocation injuries was similar among those with self-inflicted and undetermined intents, while the mortality of unintentional suffocation injuries was higher than unintentional firearm injuries (Table 4, Fig. 5B to 5D).

Resource Utilization and Outcome by Type, Intent and Mechanism of Injury

Children injured by a penetrating injury more frequently went to the operating room directly from the emergency department ($p<0.001$) and more frequently required surgery during their hospitalization ($p<0.001$) than those injured by a blunt or other mechanism (Table 5). Patients with unintentional injuries more commonly went to the operating room directly from the emergency department than those injured by an assault or undetermined cause ($p<0.001$, Table 5). No difference in the need for immediate surgery was observed between those sustaining either an unintentional or self-inflicted injury. Children sustaining an unintentional injury more commonly required surgical treatment during hospitalization than those sustaining injury by any other intent ($p<0.005$). Depending on the mechanism, the percentage of children requiring immediate surgery ranged from 0% to 50.8% and requiring surgery at any time during hospitalization ranged from 4.1% to 69.3% (Table 3). Mechanisms associated with a higher percentage of penetrating injury (including cut/pierce, firearm, machinery and natural/environmental mechanisms) more often required either immediate surgery or surgery at any time during hospitalization. Among mechanisms due only to a blunt type of injury, falls from playground equipment most often required immediate or delayed surgery ($p<0.001$).

Patients injured by a penetrating mechanism had a shorter ICU LOS (0.8 ± 3.5 vs. 1.0 ± 3.5 days, p=0.013) but longer total LOS (4.2 ± 6.5 vs. 3.8 ± 6.6 days, p=0.003) than those with a blunt mechanism. The ICU and total LOS were longer among children injured in an assault compared to those injured by undetermined or unintentional intent (p<0.001), but were not significantly different compared to those sustaining a self-inflicted injury (Table 5). Compared to children sustaining an unintentional injury, children sustaining a self-inflicted injury had a longer ICU LOS (p=0.017) but not longer total LOS (p>0.05). Children injured by a firearm, suffocation and child abuse had the longest ICU LOS, while those injured by a firearm, machinery or child abuse had the longest total LOS (Table 5).

Children injured by a penetrating injury less commonly had an ISS ≥15 than those injured by a blunt mechanism (7.9% vs. 16.0%, p<0.001). Fewer children injured unintentionally had an ISS ≥15 than those injured by other intents (p<0.001). No difference in the percentage of children with an ISS ≥15 was observed among those injured by an assault, self-inflicted or undetermined intent (Table 5). Severe injuries was highest among children injured by firearms (27.2%), unspecified motor vehicle traffic accidents (28.0%), suffocation (25.9%) and child abuse (48.4%) and lowest among those injured by a cut/pierce (3.3%) mechanism or by a fall related to playground equipment (2.8%).

No difference in emergency department or operating room or hospital mortality was observed among children with either a blunt or penetrating type of injury. Children sustaining a self-inflicted injury had a higher emergency department and overall mortality than those injured by other intents (p<0.001, Table 5). No differences were observed in the percentage of children dying in the operating room after injury by any intent. Injuries due to firearms, pedestrian accidents and suffocation had the highest emergency department mortality, while injuries due to

firearms, child abuse and suffocation had the highest hospital mortality (Table 5). The highest percentages of deaths in the operating room were observed among children injured by a firearm or in a motorcycle accident (Table 5).

Among survivors, discharge to a rehabilitation facility was more common among children sustaining a blunt compared to penetrating injury ($p<0.001$, Table 5). Children with self-inflicted injuries more commonly required inpatient rehabilitation care after discharge than those with injuries by other intents ($p<0.02$). No differences were observed among those injured by other intents. Children injured by a firearm or in a motor vehicle traffic accident generally had the highest rates of transfer to a rehabilitation facility, while those injured in a fall had the lowest (Table 5).

DISCUSSION

In the current study, we observed that the features of the injury (type, intent and mechanism) provide important insight into patient outcome and resource utilization. While hospital mortality, site of mortality and time until death were similar between children injured by blunt and penetrating mechanisms, other measures of outcome and utilization differed. Compared to those sustaining penetrating injuries, children sustaining blunt injuries were more severely injured, required more acute care days and were more likely to require rehabilitation after discharge. Patients injured by a penetrating mechanism, however, more frequently required immediate or delayed surgical care and had a longer total LOS.

Differences in resource utilization and outcome were also observed among children injured by different intents. Unintentional injuries were more frequent than those due to other intents, with most being due to a motor vehicle traffic accident. Children sustaining unintentional injuries were less severely injured and required fewer critical care days but more commonly

required either immediate or delayed surgical care. Self-inflicted injuries were associated with a higher mortality than those due to other intents with most deaths occurring either in the emergency department or on the first day of admission. A high mortality of self-inflicted injuries has also been described using data from the National Trauma Database. The reason for the high mortality of self-inflicted injuries most likely relates to the mechanism of these injuries—gunshot wounds to the head and suffocation by hanging. In addition to being associated with high, early hospital mortality, self-inflicted injuries more often required inpatient rehabilitation after discharge showing the long-term impact of these injuries. While resource utilization and severity of injury were similar between self-inflicted injuries and assaults, the early and overall mortality of self-inflicted injuries were higher.

Diverse patterns of resource utilization and outcome among the 28 different mechanisms of injury considered in this study were observed. To facilitate comparison, we considered a classification according to the level of trauma center resources required (e.g., need for surgical care or ICU days) and the severity of injury (ISS or mortality rate). For example, firearm injuries required significant trauma center resources and were associated with a high ISS and mortality, while falls on stairs required fewer resources and were associated with less severe injury. While suffocation injuries were associated with severe injury and high mortality, resource utilization was not the highest among different mechanism, likely related to early mortality among these patients. While cut/pierce injuries were more likely to be less severe and less likely to result in death, these injuries frequently required immediate or delayed surgical care. Using classification based on resource utilization and injury severity, we have proposed initial recommendations about the appropriateness of immediate or delayed triage to a trauma center.

Similar to previous studies, more deaths were due to blunt injuries and unintentional injuries reflecting the high frequency of these categories of injury. CNS injury most common cause of death: previously observed in other studies

Deaths related to penetrating injuries were more commonly attributed to volume loss than other mechanisms.

With regards to type, blunt injuries were most common-consistent with previous observations-and were correspondingly the most common cause of death.

ACS triage criteria (Cook C)

Includes criteria based on mechanism: ejection, prolonge extrication, rollover, high-speed crash, survivor w. fatality fall>15 ft, auto vs. pedest, motorcycle>20mph. and based on type (penetrating with neurovascular compromise).

Baystate: all penetrating of torso, head, neck and groin (type) and mechanism=fall >3x ght, survivor w. fatality, ejected, high speed and unrestrained, pedes vs. auto: Simon B

The priorities of prehospital triage need to be established. The immediate need is appropriate availiabity of resources for treatment in 'the golden hour'. As a measure of this outcome, need for transfer to the OR directly from the ER or death in the ER or death after transfer from the ER to OR (death in OR) are most important. Severity of injury may also be important. Triage decisions that focus on the need for trauma center expertise are critical but have a lesser urgency. Measures that may predict the need for trauma center facilities include the severity of injury, the need for ICU, the need for a surgical procedure during admission, LOS and overall hospital mortality. The time until death is a measure of the need for triage. Patients that die early in the

hospital course (ER or OR) need immediate trauma center care. Equally important are those children not dying immediately (ER or OR) but who die early during hospitalization (e.g., <24 hrs). These patients require a facility equipped to manage complex critically ill patients around the clock.

REFERENCES

FIGURE LEGENDS

Figure 1. Overall survival rates according to cause of death (Kaplan-Meier estimates). Overall: $p<0.001$. Pairwise: CNS vs. hypovolemia/hemorrhage, $p<0.001$; hypoxia vs. hypovolemia/hemorrhage, $p<0.001$; multiple organ failure (MOF) vs. hypovolemia/hemorrhage, $p<0.001$, other/unknown vs. hypovolemia/hemorrhage, $p=0.03$; CNS vs. other/unknown, $p<0.001$; hypoxia vs. other/unknown, $p=0.009$; MOF vs. other/unknown, $p=0.03$; $p>0.05$ for other combinations.

Figure 2. Overall survival rates according to type of injury (Kaplan-Meier estimates). Blunt vs. penetrating, $p>0.05$; blunt vs. other and penetrating vs. other, $p<0.001$.

Figure 3. Overall survival rates according to intent of injury (Kaplan-Meier estimates). Assault vs. unintentional, $p<0.001$; assault vs. self-inflicted, $p<0.001$; assault vs. undetermined, p=NS; undetermined vs. self-inflicted, $p<0.001$; unintentional vs. self-inflicted, $p<0.001$; unintentional vs. undetermined, $p<0.001$.

Figure 4. Overall survival rates among children sustaining firearm (*A*) or suffocation (*B*) injuries (Kaplan-Meier estimates). Firearm injuries (*A*): assault vs. self-inflicted, $p<0.001$; assault vs. undetermined, $p<0.001$; unintentional vs. self-inflicted, $p<0.001$; unintentional vs. undetermined, $p<0.001$; p=NS for other combinations. Suffocation injuries (*B*): assault vs. unintentional, $p<0.001$; assault vs. undetermined, $p<0.001$; assault vs. self-inflicted, $p<0.001$; self-inflicted vs. unintentional, $p<0.001$; $p>0.05$ for other combinations.

Figure 5. Overall survival rates among children injured by assault (*A*), self-inflicted (*B*), unintentional (*C*) or undetermined (*D*) intent (Kaplan-Meier estimates). Graphs for mechanisms without mortality are not shown. Assault: cut/pierce vs. firearm, p=0.03; other struck vs. firearm, p<0.001; cut/pierce vs. child abuse, p=0.01; other struck vs. child abuse, p<0.001; other struck vs. unspecified, p<0.001; p>0.05 for other combinations. Self-inflicted: firearm vs. suffocation, p>0.05. Unintentional: suffocation vs. all other mechanisms, p<0.001; firearm vs. pedestrian, other, p=0.02; firearm vs. all other mechanisms, p<0.005; firearm vs. suffocation, p<0.001. Undetermined: firearm vs. unspecified, p<0.001; suffocation vs. unspecified, p=0.009; firearm vs. suffocation, p>0.05.

.

Table 1. Distribution of Type of Injury Among Different Mechanisms of Injury*

	Blunt	Penetrating	Other
Mechanism of injury			
Cut / pierce	27 (2.1)	1,237 (97.7)	2 (0.2)
Fall			
Building	1,273 (100)	--	--
Furniture	2,242 (100)	--	--
Playground equipment	2,459 (100)	--	--
Stairs	1,206 (100)	--	--
Other falls from height	3,267 (100)	--	--
Falls on the same level	2,002 (99.8)	4 (0.2)	--
Other and unspecified	2,057 (100)	--	--
Firearm	7 (1.4)	510 (98.6)	--
Machinery	125 (69.8)	46 (25.6)	8 (4.5)
MV traffic			
Occupant	7,871 (100)	--	--
Motorcyclist	217 (100)	--	--
Pedal cyclist	1,553 (100)	--	--
Pedestrian	4,618 (100)	--	--
Other	94 (100)	--	--
Pedal cyclist, other	2,268 (100)	--	--
Pedestrian, other	910 (99.7)	2 (0.21)	--
Transport, other			
All-terrain vehicle	612 (100)	--	--
Other transport	735 (98.5)	10 (1.3)	1 (0.1)
Natural / environmental	275 (26.4)	748 (71.9)	16 (1.5)
Struck by, against			
Struck by falling object	549 (100)	--	--
Other struck	336 (71.7)	87 (18.5)	45 (9.6)
Suffocation	56 (87.5)	--	8 (12.5)
Other specified, classifiable			
Child abuse	1,736 (98.6)	18 (1.0)	5 (0.3)
Other	2,541 (94.4)	148 (5.5)	--
Other specified, not classifiable	100 (78.1)	27 (21.0)	1 (0.8)
Unspecified	434 (97.9)	7 (1.6)	2 (0.5)
TOTAL	3,9570 (93.1)	2,844 (6.7)	88 (0.2)

*percentage of all deaths shown in parentheses

Table 2. Distribution of Intent of Injury Among Different Mechanisms of Injury *

	Assault	Self-inflicted	Unintentional	Undetermined
Mechanism of injury				
Cut / pierce	91 (7.2)	1 (0.1)	1,175 (92.5)	3 (0.2)
Fall				
Building	--	--	1,273 (100)	--
Furniture	--	--	2,242 (100)	--
Playground equipment	--	--	2,459 (100)	--
Stairs	--	--	1,206 (100)	--
Other falls from height	9 (0.3)	14 (0.4)	3,258 (99.2)	1 (0.1)
Falls on the same level	--	--	2,006 (100)	--
Other and unspecified	--	--	2,057 (100)	--
Firearm	260 (47.5)	18 (3.3)	257 (46.9)	12 (2.2)
Machinery	--	--	179 (100)	--
MV traffic				
Occupant	--	--	7,871 (100)	--
Motorcyclist	--	--	217 (100)	--
Pedal cyclist	--	--	1,553 (100)	--
Pedestrian	--	--	4,618 (100)	--
Other	--	--	94 (100)	--
Pedal cyclist, other	--	--	2,268 (100)	--
Pedestrian, other	--	--	912 (100)	--
Transport, other				
All-terrain vehicle	--	--	612 (100)	--
Other transport	--	--	746 (100)	--
Natural / environmental	--	--	1,039 (100)	--
Struck by, against				
Struck by falling object	--	--	549 (100)	--
Other struck	263 (13.8)	--	1,636 (86.1)	--
Suffocation	4 (4.1)	31 (31.6)	60 (61.2)	3 (3.1)
Other specified, classifiable				
Child abuse	1,759 (100)	--	--	--
Other	20 (4.3)	1 (0.2)	442 (95.2)	1 (0.2)
Other specified, not classifiable	53 (33.3)	15 (9.4)	75 (47.1)	16 (10.0)
Unspecified	21 (2.6)	--	428 (53.7)	348 (43.6)
TOTAL	2,480 (5.8)	80 (0.2)	40,022 (93.1)	384 (0.9)

*percentage of cases for each intent shown in parentheses

Table 3. Cause of Death Among Children Dying of Each Mechanism

	Central Nervous System Injury	Hypoxia	Hypovolemia/ hemorrhage	Multiple Organ Failure	Other or Unknown
Type of Injury					
Blunt	838 (73.3)	96 (8.4)	66 (5.8)	50 (4.37)	92 (8.1)
Penetrating	52 (67.5)	4 (5.2)	13 (16.8)	1 (1.3)	7 (9.1)
Other	4 (30.7)	5 (38.4)	--	--	4 (30.7)
Intent of injury					
Assault	196 (76.8)	13 (5.1)	21 (8.2)	5 (2.0)	20 (7.8)
Self-inflicted	15 (51.7)	1 (3.4)	9 (31.0)	1 (3.4)	3 (10.3)
Undetermined	17 (73.9)	3 (13.0)	1 (4.3)	--	2 (8.7)
Unintentional	666 (72.0)	62 (6.7)	74 (8.0)	45 (4.9)	78 (8.4)
Mechanism of injury					
Cut / pierce	2 (50)	--	2 (50)	--	--
Fall					
Building	19 (82.6)	1 (4.3)	1 (4.3)	--	2 (8.7)
Furniture	4 (100)	--	--	--	--
Playground equipment	3 (100)	--	--	--	--
Stairs	5 (83.3)	--	--	--	1 (16.7)
Other falls from height	5 (55.6)	2 (22.2)	1 (11.1)	--	1 (11.1)
Falls on the same level	5 (71.4)	1 (14.3)	--	--	1 (14.3)
Other and unspecified	2 (66.7)	--	--	--	1 (33.4)
Firearm	46 (69.7)	3 (4.6)	9 (13.7)	1 (1.6)	7 (10. 7)
Machinery	3 (75)	--	1 (25)	--	--
MV traffic					
Occupant	298 (76.1)	28 (7.2)	19 (4.9)	16 (4.1)	31 (7.9)
Motorcyclist	5 (62.5)	1 (12.5)	2 (25)	--	--
Pedal cyclist	50 (75.8)	3 (4.5)	5 (7.6)	3 (4.5)	5 (7.6)
Pedestrian	159 (73.6)	8 (3.7)	18 (8.3)	16 (7.4)	15 (6.9)
Other	2 (100)				
Pedal cyclist, other	7 (87.5)	--	1 (12.5)	--	--
Pedestrian, other	33 (68.8)	3 (6.25)	1 (2.0)	4 (8.3)	7 (14.6)
Transport, other					
All-terrain vehicle	9 (60)	1 (6.7)	2 (13.4)	1 (6.7)	2 (13.3)
Other transport	8 (66.7)	--	1 (8.3)	1 (8.3)	2 (16.7)
Natural / environmental	11 (78.6)	1 (7.1)	2 (14.3)	--	--
Struck by, against					
Struck by falling object	7 (46.7)	5 (33.3)	1 (6.7)	1 (6.7)	1 (6.7)
Other struck	6 (54.5)	3 (27. 3)	1 (9.1)	--	1 (9.1)
Suffocation	11 (29.0)	19 (50)	--	3 (7.9)	5 (13.2)
Other specified, classifiable					
Child abuse	179 (78.9)	18 (7.9)	8 (3.5)	5 (2.2)	17 (7.5)

Other	1 (9.1)	5 (45.5)	1 (9.1)	--	4 (36.4)
Other specified, not classifiable					
Unspecified	14 (70)	3 (15)	3 (15)	--	--
TOTAL	894 (72.6)	105 (8.5)	79 (6.4)	51 (4.1)	103 (8.4)

*percentage of deaths for each mechanism shown in parentheses

Table 4. Type, Mechanism and Intent of Injury and Hospital Mortality Among Pediatric Trauma Patients*

	Assault	Self-inflicted	Unintentional	Undetermined	Total
Type of injury					
Blunt	11.0	29.1	4.6	2.4	2.9
Penetrating	6.5	52.0	18.9	1.3	2.6
Other/undetermined	16.7	--	0	14.6	14.4
Mechanism of injury					
Cut / pierce	2.2	0.0	0.2	0.0	0.3
Fall	--	--	--	--	
Building	--	--	1.8	--	1.8
Furniture	--	--	0.2	--	0.2
Playground equipment	--	--	0.1	--	0.1
Stairs	--	--	0.5	--	0.5
Other falls from height	0.0	0.0	0.3	0.0	0.3
Falls on the same level	--	--	0.3	--	0.3
Other and unspecified	--	--	0.0	--	0.0
Firearm	8.8	72.2	10.1	50.0	12.4
Machinery	--	--	2.2	--	2.2
MV traffic	--	--	--	--	
Occupant	--	--	5.0	--	5.0
Motorcyclist	--	--	3.7	--	3.7
Pedal cyclist	--	--	4.2	--	4.2
Pedestrian	--	--	4.7	--	4.7
Other	--	--	2.1	--	2.1
Pedal cyclist, other	--	--	0.4	--	0.4
Pedestrian, other	--	--	5.3	--	5.3
Transport, other	--	--	--	--	
All-terrain vehicle	--	--	2.5	--	2.5
Other transport	--	--	1.6	--	1.6
Natural / environmental	--	--	1.3	--	1.3
Struck by, against	--	--	--	--	
Struck by falling object	--	--	2.7	--	2.7
Other struck	0.4	--	0.6	--	0.6
Suffocation	0.0	51.6	35.0	33.3	38.8
Other specified, classifiable	--	--	--	--	
Child abuse	12.9	--	--	--	12.9
Other	0.0	0.0	2.0	0.0	1.9
Other specified, not classifiable	0.0	0.0	0.0	0.0	0.0
Unspecified	9.5	--	0.5	5.5	2.9
TOTAL	10.3	36.3	2.3	6.8	2.9

Table 5. Resource Utilization and Outcome by Intent and Mechanism of Injury

	ER to Operating Room (%)	Any Operating Room (%)	# of ICU Days (mean±SD)	# Hospital Days (mean±SD)	ISS ≥15 (%)	Died in ER (%)	Died in OR (%)	Mortality (%)	Discharge to Rehabilitation Facility (%)
Type of injury									
Blunt	17.9	37.3	3.8 ± 6.6	1.0 ± 3.5	16.0	0.6	0.1	2.9	3.0
Penetrating	46.5	64.3	4.2 ± 6.6	0.9 ± 3.6	7.9	0.7	0.1	2.6	1.9
Other	22.2	34.4	4.4 ± 8.0	1.0 ± 3.5	16.0	6.7	0.0	14.4	3.9
Intent of injury									
Assault	11.1	25.6	2.0 ± 4.7	6.4 ± 8.9	38.7	0.9	0.2	10.3	5.1
Self-inflicted	12.5	23.8	2.0 ± 4.1	6.1 ± 11.1	36.8	8.8	0.0	36.3	13.7
Undetermined	12.5	32.6	1.9 ± 3.1	1.1 ± 5.8	25.9	1.3	0.3	6.0	3.6
Unintentional	20.4	40.1	0.9 ± 3.4	3.7 ± 6.4	13.9	0.6	0.1	2.3	2.8
Mechanism of injury									
Cut / pierce	55.0	75.0	0.4 ± 2.9	3.7 ± 5.3	3.3	0.2	0.0	0.3	0.9
Fall									
Building	9.3	21.8	0.9 ± 1.9	2.9 ± 3.8	16.7	0.3	0.0	1.8	2.5
Furniture	20.4	43.3	0.2 ± 1.0	1.8 ± 2.4	10.8	0.0	0.0	0.2	0.4
Playground equipment	39.9	68.6	0.1 ± 0.6	1.8 ± 2.4	2.8	0.0	0.0	0.1	0.1
Stairs	10.9	23.1	0.4 ± 1.5	2.0 ± 2.9	11.1	0.0	0.0	0.5	0.5
Other falls from height	18.3	34.7	0.5 ± 1.6	2.4 ± 3.9	14.0	0.0	0.0	0.3	0.8
Falls on the same level	27.3	56.8	0.2 ± 0.8	2.3 ± 3.2	4.9	0.0	0.0	0.3	0.4
Other and unspecified	25.7	51.6	0.2 ± 1.2	2.3 ± 3.5	6.3	0.0	0.0	0.1	0.4
Firearm	36.2	51.9	2.4 ± 5.5	6.8 ± 9.7	27.2	2.7	0.5	12.4	7.0
Machinery	50.8	67.0	1.3 ± 5.3	5.9 ± 9.8	12.6	0.0	0.0	2.2	3.5
MV traffic									
Occupant	11.3	27.8	1.7 ± 4.9	5.0 ± 8.5	21.9	1.0	0.1	5.0	5.8
Motorcyclist	27.2	43.3	1.1 ± 2.4	4.8 ± 5.3	17.0	0.9	0.9	3.7	3.3
Pedal cyclist	14.4	32.3	1.6 ± 4.4	5.4 ± 9.5	21.4	0.8	0.2	4.2	6.8
Pedestrian	12.1	31.1	1.6 ± 4.9	5.4 ± 9.0	19.1	1.4	0.2	4.7	6.5
Other	16.0	35.1	2.2 ± 5.7	5.5 ± 8.6	28.0	0.0	0.0	2.1	3.3
Pedal cyclist, other	19.7	39.3	0.6 ± 1.9	3.0 ± 4.0	12.5	0.0	0.0	0.4	0.7
Pedestrian, other	13.6	27.0	1.4 ± 4.1	4.6 ± 7.2	18.6	2.5	0.0	5.3	2.7
Transport, other									
All-terrain vehicle	23.2	45.6	1.3 ± 3.6	4.9 ± 6.6	17.7	0.7	0.2	2.5	4.6
Other transport	24.4	42.0	1.0 ± 3.3	4.3 ± 6.3	17.3	0.4	0.1	1.6	3.2
Natural / environmental	33.8	50.9	0.7± 2.5	3.5 ± 6.6	7.0	0.3	0.0	1.3	1.2
Struck by, against									
Struck by falling object	22.0	43.2	1.0 ± 3.3	4.0 ± 5.7	13.8	0.9	0.0	2.7	2.6
Other struck	18.3	37.5	0.4 ± 1.3	3.0 ± 4.1	8.9	0.2	0.1	0.4	0.9
Suffocation	0.0	4.1	2.3 ± 4.3	4.1 ± 7.0	25.9	13.3	0.0	38.8	11.4
Other specified, classifiable									
Child abuse	6.8	20.9	2.4 ± 4.9	7.3 ± 9.5	48.4	0.9	0.2	12.9	5.1

Other	50.0	69.3	0.7 ± 2.9	3.4 ± 5.8	2.9	1.1	0.0	1.9	1.1
Other specified, not classifiable	23.3	42.8	0.5 ± 2.4	2.8 ± 4.8	4.5	0.0	0.0	0.0	1.3
Unspecified	20.7	48.0	0.6 ± 2.2	3.7 ± 5.3	14.2	0.1	0.1	2.4	1.8
TOTAL	19.8	39.1	1.0 ± 3.5	3.8 ± 6.6	15.5	0.6	0.1	2.9	2.9

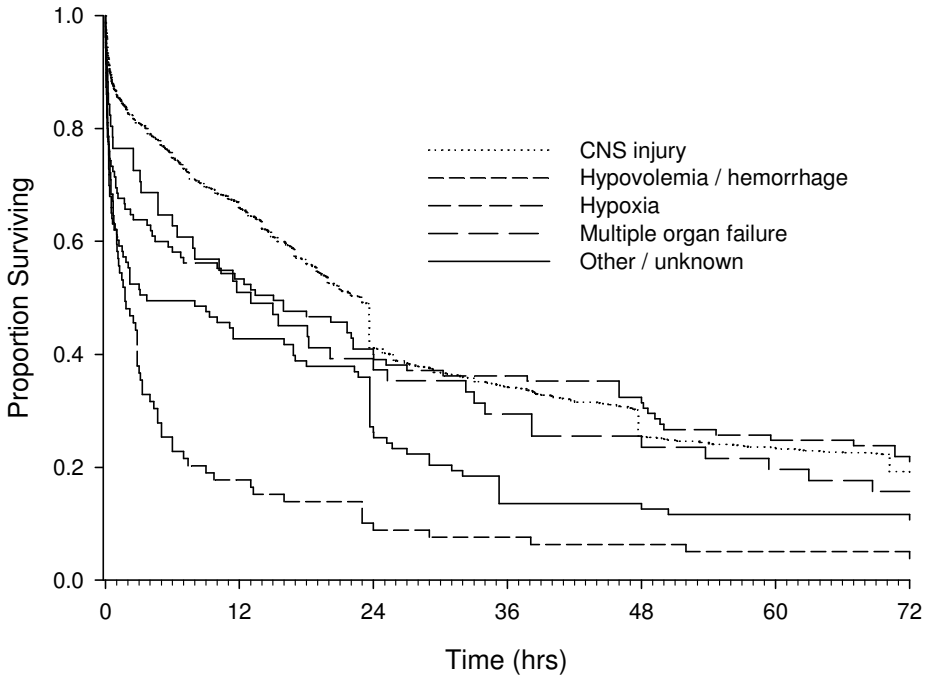

FIGURE 1

A.

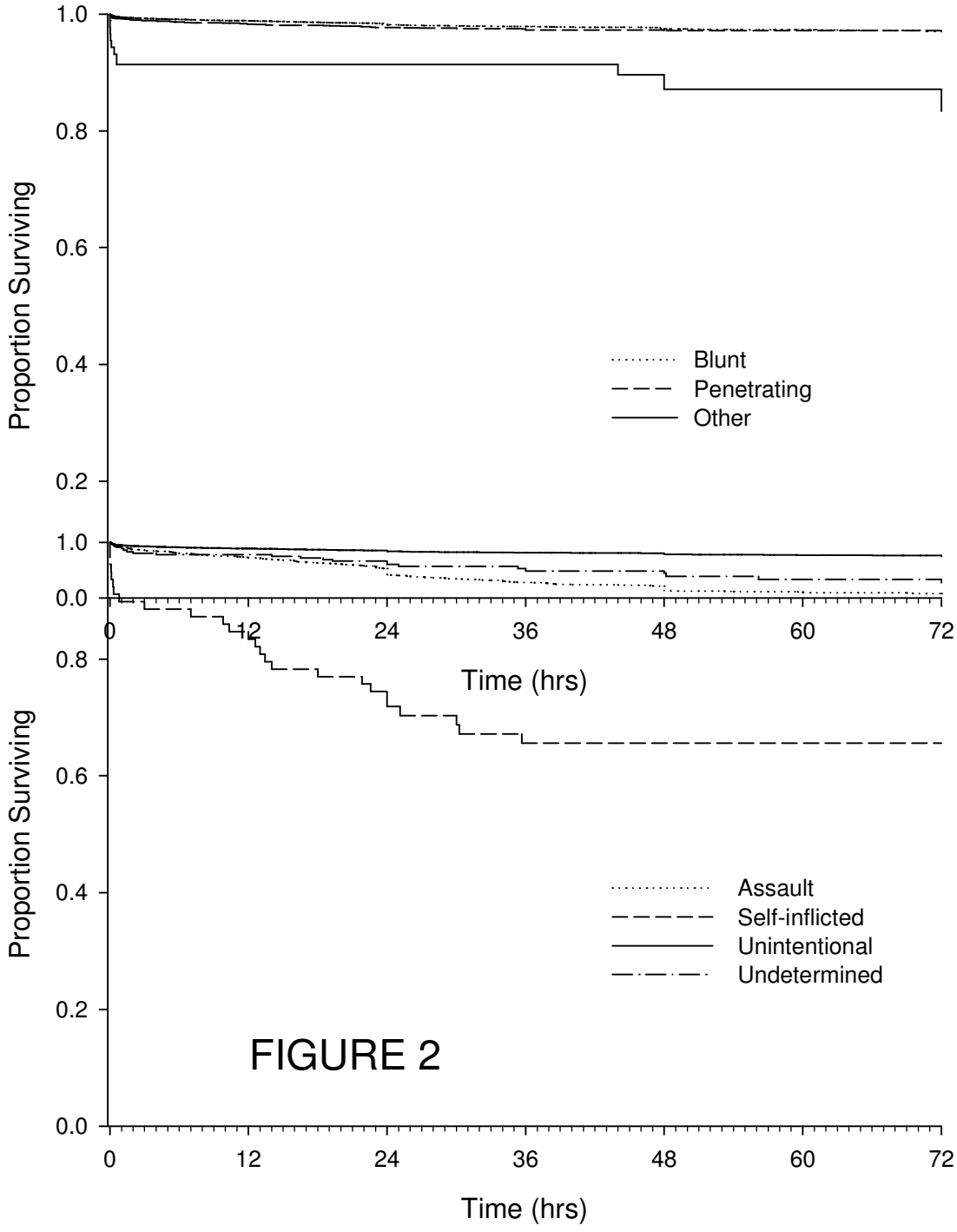
1.0
0.8
0.6
0.4
0.2
0.0
Proportion Surviving
Blunt
Penetrating
Other
0
12
24
36
48
60
72
Time (hrs)

B.

1.0
0.8
0.6
0.4
0.2
0.0
Proportion Surviving
Assault
Self-inflicted
Unintentional
Undetermined
0
12
24
36
48
60
72
Time (hrs)

FIGURE 2

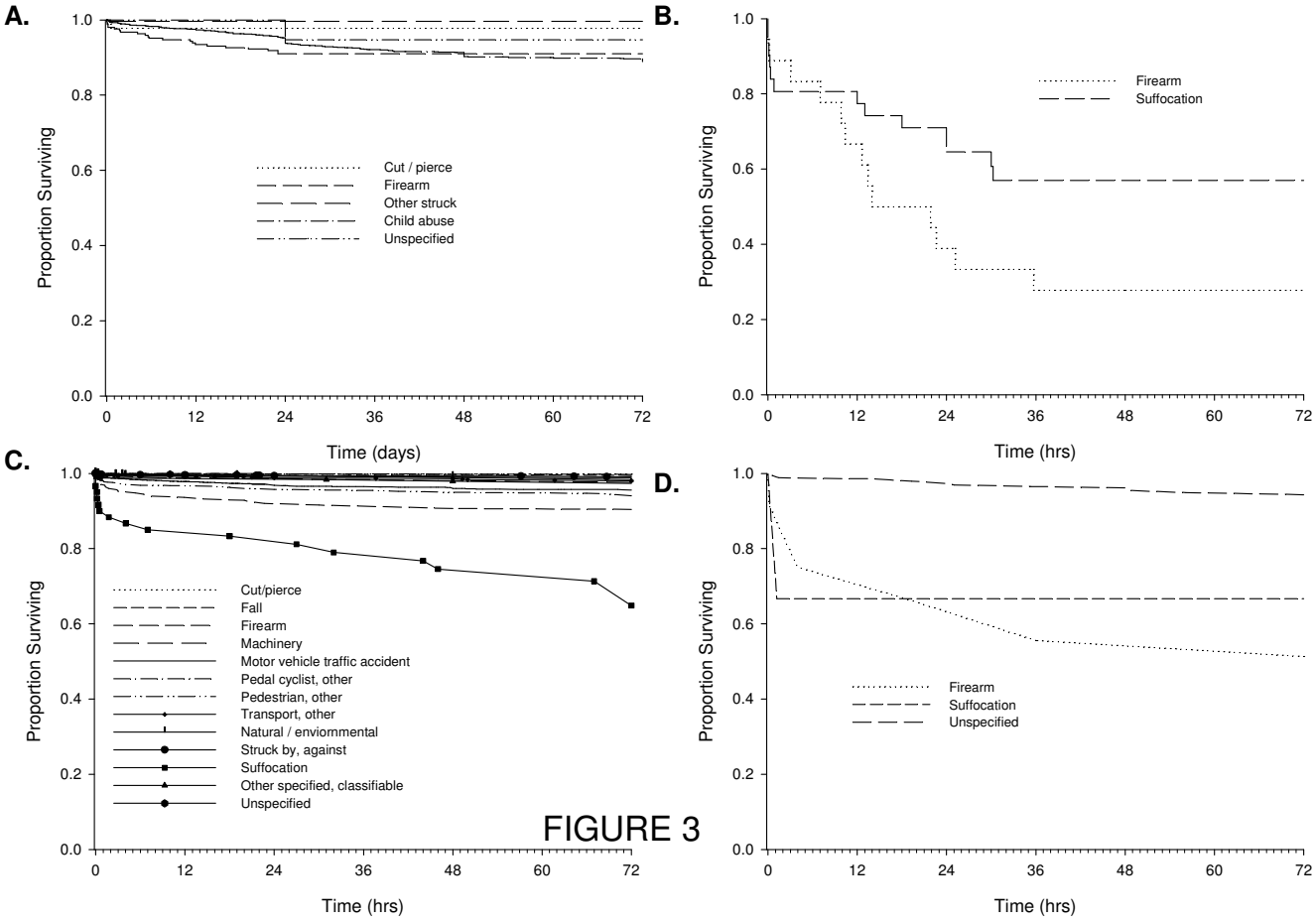
A.
Proportion Surviving
Time (days)
Cut / pierce
Firearm
Other struck
Child abuse
Unspecified
B.
Proportion Surviving
Time (hrs)
Firearm
Suffocation
C.
Proportion Surviving
Time (hrs)
Cut/pierce
Fall
Firearm
Machinery
Motor vehicle traffic accident
Pedal cyclist, other
Pedestrian, other
Transport, other
Natural / enviornmental
Struck by, against
Suffocation
Other specified, classifiable
Unspecified
D.
Proportion Surviving
Time (hrs)
Firearm
Suffocation
Unspecified

FIGURE 3

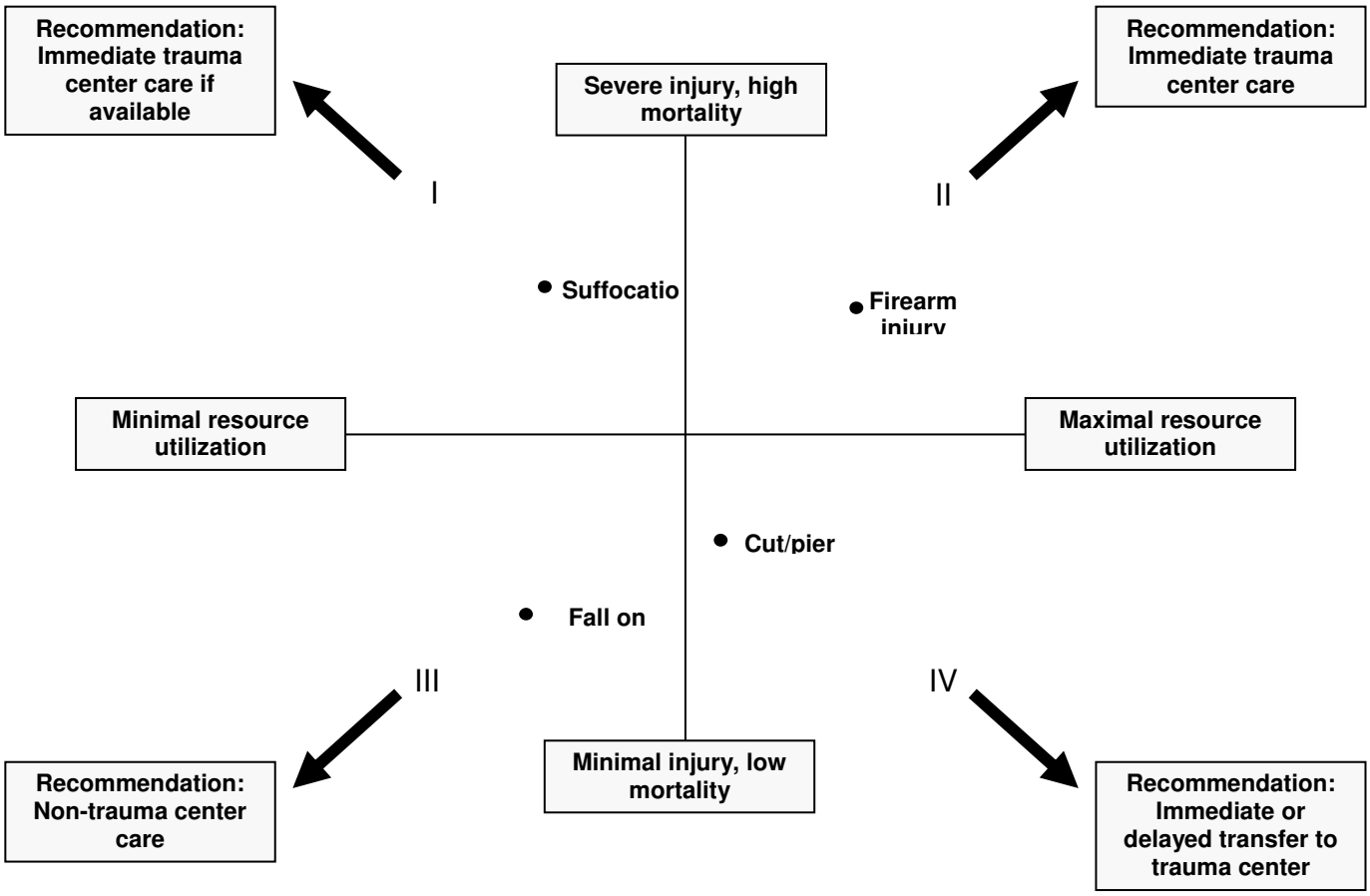
Recommendation: Immediate trauma center care if available
Severe injury, high mortality
Recommendation: Immediate trauma center care
I
II
Suffocatio
Firearm injury
Minimal resource utilization
Maximal resource utilization
Cut/pier
Fall on
III
IV
Recommendation: Non-trauma center care
Minimal injury, low mortality
Recommendation: Immediate or delayed transfer to trauma center

FIGURE 4

Appendix 4

Software Developed – provided separately

Appendix 4 items are provided separately on a CD which contains the following programs;

4.1 Genesis Programming for Cellular Modeling
4.1.1 ADHD Single Cell and Network Model
4.1.2 NTS Single Cell and Network Model
4.2 Artificial Neural Network Program for DOD Project
4 .3 GUI for NASA Space Suit Project
4.4 Artificial Neural Network Program for Air Force Project

PUBLICATIONS

REFERRED JOURNAL PAPERS

- Jang, Tai S., Iyoho, Anthony E., S., Nair, S. S., "Study on Individual Differences in Thermal Stress Using Black Box Models," Transactions of the Society of Automotive Engineers, Journal of Aerospace, July 2005.

- Jang, T. S., Iyoho, A., Nair, S. S., and Berglund, L., "Modeling individual variations in thermal stress response for humans in transient environments," ASHRAE Transactions (in review).

- Burd, R. S., Jang, T., and Nair, S., "Evaluation of the relationship between mechanism of injury and outcome in pediatric trauma," The Journal of Trauma (accepted for publication).

- Burd, R. S., Jang, T. S., Nair, S. S., 2006, "Predicting hospital mortality among injured children using a national trauma database," Journal of Trauma, 60:792-801.

- Iyoho, A., Jang, T. S., Thornton, S. B., and Nair, S. S., "Quantifying modeling uncertainties for the human thermal system," ASHRAE Transactions, 2006 (to appear).

- Iyoho, A., Jang, T. S., Gall, A., and Nair, S. S., "Predicting individual differences in human thermal strain using computational models," ASHRAE Transactions, 2006 (to appear).

IN PREPARATION

- Jang, Tai S., Nair, J., Nair, S., and Lavin, A, "Computational Model of the mechanisms of action of the Alpha 2 agonist clonidine in the PFC" to be submitted to Journal of Computational Neuroscience.

- Jang, Tai S., Iyoho, Anthony E., S., Nair, S. S., "Arteriovenous Anastomoses (AVA) Mechanism and Modeling," to be submitted to the ASHRAE Transactions.

- Jang, Tai S., Iyoho, Anthony E., S., Nair, S. S., "Hybrid System to Predict Individual Thermal Responses," ASHRAE Transactions.

CONFERENCE PAPERS & REPORTS

- Jang, T.S., Nair, J., Nair, S.S., and Lavin A, "Computational model of the mechanism of action of the α2 agonist clonidine in the PFC,"Annual Meeting of the Society for Neuroscience (SfN), Oct 14-18, 2006, Atlanta, GA (poster)

- Jang, T., Nair, J., Lavin, A., and Nair, S.S., "Modulation of PFC pyramidal cell excitability by clonidine - A computational modeling study," Proceedings of the Dynamic Systems and Control Division, ASME International Mechanical Engineering Congress and Exposition, Chicago, IL, IMECE06-82349, pp.1-10, 2006.

- Jang, Tai S., Iyoho, Anthony E., S., Nair, S. S., “Alternative Approach in Forecasting Individual Thermal Responses using Artificial Neural Network”, International Conference on Environmental Systems, Colorado, 2004.

- Jang, Tai S., Iyoho, Anthony E., S., Nair, S. S., Gonzalez R. R., “Effect of Individual Differences on Transient Modeling and Thermal Risk”. American Control Conference, Boston, MA, pp. 4266-4371, 2004

- Jang, Tai S., Nair, S. S., “Development of a Neural Network Model for Forecasting Thermal Risk by Age and Gender Applicable to Warfighter Performance “ USARIEM project report, 2003. Grant Number DAAD16-03-P-0119

- Jang, Tai S., Nair, S.S., Pediatric Trauma Study Report, 2003 Robert Wood Johnson Medical School, New Jersey.

- Iyoho, A. E., Jang, T. S., Nair, S. S., “Human Thermal Model with Extremities For Asymmetric Environments”, American Controls Conference, Boston, MA, pp.4266-4371, 2004.

- Iyoho, A., Jang, T. S. and Nair, S. S., 2004, “Human Thermal Model with Extremities for Asymmetric Environments,” American Control Conference, Boston, pp. 4366-4371.

- Iyoho, A., Jang T-S., and Nair, S. S., 2002, “The Development of a 2-Dimensional Human Thermal Model,” International Conference on Environmental Systems, San Antonio, TX, SAE Paper No. 2002-01-2540.

- Iyoho, A. E., Jang, T. S., Nair, S. S., “The development of a 2-dimensional human thermal model,” Presented to the 32nd Annual International Conference on Environmental Systems”, San Antonio, TX, on July 15-18, SAE 2002-01-2540, 2002

VITA

Tai Seung Jang was born October 27, 1971 in South Korea. He left Korea in 1986 and immigrated with his family to Argentina. He came to the United States in 1996. He received his B.S. in Mathematics from the Missouri State University, Springfield, Missouri and M.S. in Mechanical Engineering from the University of Missouri-Columbia in 2001 and 2003, respectively. He continued his Ph.D. program in the same department, and received a Ph.D. degree in 2006. His academic background includes automatic control, dynamic system modeling, heat transfer, analysis and design. His personal interests include invention, the guitar, robotics, soccer, and Taekwondo.